HAL
open science

Suivi des flux d'eau et de matières en suspension dans les cours d'eau par profileurs acoustiques Doppler horizontaux

Stéphanie Moore

▶ **To cite this version:**

Stéphanie Moore. Suivi des flux d'eau et de matières en suspension dans les cours d'eau par profileurs acoustiques Doppler horizontaux. Sciences de la Terre. Université de Grenoble, 2011. Français. NNT : 2011GRENU043 . tel-00680090

HAL Id: tel-00680090

https://theses.hal.science/tel-00680090v1

Submitted on 17 Mar 2012

HAL is a multi-disciplinary open access archive for the deposit and dissemination of scientific research documents, whether they are published or not. The documents may come from teaching and research institutions in France or abroad, or from public or private research centers.

L'archive ouverte pluridisciplinaire **HAL**, est destinée au dépôt et à la diffusion de documents scientifiques de niveau recherche, publiés ou non, émanant des établissements d'enseignement et de recherche français ou étrangers, des laboratoires publics ou privés.

UNIVERSITÉ DE GRENOBLE

THÈSE

Pour obtenir le grade de

DOCTEUR DE L'UNIVERSITÉ DE GRENOBLE

Spécialité : **Sciences de la Terre, Univers, Environnement**

Arrêté ministériel : 7 août 2006

Présentée par

Stephanie Astrid Moore

Thèse dirigée par **André Paquier et David Hurther**
et codirigée par **Jérôme Le Coz**

préparée au sein du **Cemagref Lyon, Unité Hydrologie–Hydraulique**
et de **l'Ecole Doctorale Terre, Univers, Environnement**

Monitoring flow and fluxes of suspended sediment in rivers using side-looking acoustic Doppler current profilers

Thèse soutenue publiquement le **16 décembre 2011**,
devant le jury composé de :

Dr. M. Estèves
Directeur de Recherche IRD, LTHE, Grenoble, Président
Dr. C. D. Rennie
Professeur, Université d'Ottawa, Canada, Rapporteur
Dr. P. D. Thorne
Professeur, Proudman Oceanographic Laboratory, Royaume-Uni, Rapporteur
Dr. M. Parlange
Professeur, Ecole Polytechnique Fédérale de Lausanne, Suisse, Examinateur
Dr. A. Paquier
HDR, ICPEF, Cemagref Lyon, Directeur de thèse
Dr. D. Hurther
Chargé de Recherche CNRS, LEGI, Grenoble, Directeur de thèse
Dr. J. Le Coz
IPEF, Cemagref Lyon, Co-Directeur de thèse
G. Pierrefeu
Compagnie Nationale du Rhône, Invité
Dr. F. Gottardi
Electricité de France, Invité

To Fred, though I'm sure you could have seen this one coming, I wonder if you knew I'd end up in France.

And to Wes Paul, thanks for all the good times in the lab during my MSc. You are dearly missed.

CONTENTS

List of Tables . . . . . **v**

List of Figures . . . . . **vii**

Abstract . . . . . **xiv**

List of Abbreviations and Symbols Used . . . . . **xv**

Acknowledgements . . . . . **xix**

Résumé de la thèse . . . . . **xxi**

Chapter 1 Introduction **1**

Chapter 2 Theory **6**

2.1 Velocity Measurements 6

2.1.1 The Doppler effect 6

2.1.2 The principles of operation of RD Instruments BroadBand ADCPs 7

2.1.3 Measuring the three components of velocity 7

2.2 Echo Intensity Measurements 9

2.2.1 Sound waves and their propagation 9

2.2.2 Sound scattering 10

2.2.3 Scattering from a single spherical particle 11

2.2.4 Scattering from a suspension of spherical particles 13

2.2.5 The form function 14

2.2.6 Attenuation 15

2.3 Principles of laser grain sizing 19

Chapter 3 Study Sites and Instrumentation **24**

3.1 Romans-sur-Isère 28

3.1.1 Instrumentation 28

3.1.2 Hydrological conditions 33

3.1.3 Concentration and grain size of the suspended sediment 35
3.2 Saint-Georges 46
3.2.1 Study site and instrumentation 46
3.2.2 Grain size distributions of the suspended sediment 49
3.2.3 Complementary data 53
3.3 Montélimar 53
3.4 Tricastin 56
3.5 Conclusion 58

Chapter 4 Influence of the H-ADCP positioning on the profiles of velocity and intensity 59
4.1 The impact of scattering from obstacles 60
4.2 Observations at Romans-sur-Isère 63
4.3 Modelling scattering from the air-water interface 68
4.4 Comparison of model results to data at Romans-sur-Isère 74
4.5 Comparison to data from Montélimar and Saint-Georges 80
4.6 Conclusions 83

Chapter 5 Velocity data analysis 85
5.1 Validation of the form of the velocity profiles 87
5.2 Validation of the velocity measurements 92
5.2.1 300 kHz H-ADCP data at Romans-sur-Isère 94
5.2.2 600 and 1200 kHz H-ADCP data at Romans-sur-Isère 101
5.2.3 Results at Montélimar 104
5.3 Conclusions 111

Chapter 6 Inversion methods and their application to suspended sediment surveys 113
6.1 Theory 113
6.1.1 Inversion of the backscattered intensity to concentration 114
6.1.2 A novel inversion of the acoustic attenuation to concentration 116
6.1.3 Measuring grain size with multi-frequency attenuation data 120
6.2 Application of the backscattered intensity inversion 123
6.2.1 Saône river at Saint-Georges 124
6.2.2 Isère river at Romans-sur-Isère 130

6.2.3 Rhône Canal at Montélimar 132
6.2.4 Rhône Canal at Tricastin 134
6.3 Application of the attenuation inversion 135
6.3.1 Saône River at Saint-Georges 135
6.3.2 Isère river at Romans-sur-Isère 135
6.3.3 Rhône Canal at Montélimar and Tricastin 140
6.4 Conclusion 145

Chapter 7 Application of the Attenuation Inversion Method to Specific Hydrological Events 147
7.1 Studying the Propagation of a Spring Flood 148
7.2 Variations in suspended sediment grain size throughout the flood 155

Chapter 8 Conclusions 159
8.1 Positioning 160
8.2 Measuring velocity 160
8.3 Measuring suspended sediment concentrations and grain size 161
8.4 Application of the method 162
8.5 Perspectives 163

Appendix A Laser Grain Sizer Results for Romans-sur-Isère Suspended Matter . . 165

Appendix B ADCP velocity data collected at Romans-sur-Isère prior to the thesis 181

Bibliography 183

LIST OF TABLES

3.1 A summary of the positioning and specifications of the horizontal ADCPs at Romans-sur-Isère. 29

3.2 Relevant information for the samples collected at Romans-sur-Isère March 31, 2010 and analysed using the laser grain sizer. 39

3.3 The theoretical attenuation parameters for the grain size distributions measured in the samples collected at Romans-sur-Isère March 31, 2010. 39

3.4 Relevant information from the grain size analysis of samples collected at the surface near the right bank of the Romans-sur-Isère study site. 43

3.5 The theoretical attenuation parameters for the grain size distributions measured in the samples collected at Romans-sur-Isère. 44

3.6 The theoretical attenuation parameters for the grain size distributions measured in the samples collected at Romans-sur-Isère using both Fraunhofer and Mie theory. 46

3.7 Relevant information for the samples collected on the Saône river and analysed using the laser grain sizer. 52

3.8 A summary of the positioning and instrument specifications for the H-ADCPs used at Saint-Georges, Montélimar and Tricastin. 58

4.1 The positioning of the 300 and 600 kHz horizontal ADCPs at Romans-sur-Isère before and after December 14, 2010. 77

5.1 Summary of the ADCP gauging campaigns at the Saint-Georges study site that are analyzed in this chapter. 88

5.2 Summary of the ADCP gauging campaigns at the Montélimar study site analyzed in this chapter. 91

A.1 Relevant information for the grain size analysis results of the samples collected at Romans-sur-Isère between January, 2009 and June, 2010 and analysed using the laser grain sizer. 166

A.2 Relevant information for the grain size analysis results of samples collected at Romans-sur-Isère in June, 2010 and analysed using the laser grain sizer. 167

A.3 Relevant information for the grain size analysis results of samples collected at Romans-sur-Isère between June and October, 2010 and analysed using the laser grain sizer. 168

A.4 Relevant information for the grain size analysis results of samples collected at Romans-sur-Isère between October, 2010 and January, 2011 and analysed using the laser grain sizer. 169

LIST OF FIGURES

2.1 Geometry of the horizontal ADCPs (top-view). 8

2.2 Images of the various H-ADCPs used in this study. 8

2.3 The coordinate system of the transducers. 12

2.4 The attenuation coefficient due to viscous absorption (solid curves) and scattering (dashed-dotted curves) as a function of particle radius for sound waves having the operating frequencies of the H-ADCPs. 18

2.5 The attenuation coefficient due to viscous absorption (solid curves) and scattering (dashed-dotted curves) as a function of median radius, a_{50}, for sound waves having the operating frequencies of the H-ADCPs. 19

2.6 Grain size distributions measured using the low-angle laser light scattering technique for water samples collected at Romans-sur-Isère interpreted using either Fraunhofer or Mie theory. 23

3.1 Map of France indicating the three rivers that are studied in this thesis. . . 25

3.2 Map of the Rhône drainage basin. 26

3.3 Upstream view of the Romans-sur-Isère study site. 28

3.4 The Romans-sur-Isère study site. 29

3.5 The theoretical directional response of the 300 kHz H-ADCP at Romans-sur-Isère. 30

3.6 Relationship between suspended sediment concentration measured in water samples and optical turbidity at Romans-sur-Isère. 33

3.7 The average velocity magnitude measured on January 9, 2009 using a 600 kHz Workhorse RioGrande ADCP at Romans-sur-Isère overlayed on the average bathymetry from its bottom-tracking function. 34

3.8 Grain size distributions measured using the laser grain sizer for water samples collected at Romans-sur-Isère March 31, 2010. 40

3.9 Grain size distributions measured using the laser grain sizer for water samples collected at Romans-sur-Isère March 31, 2010. 41

3.10 Grain size distributions measured using the Fraunhofer method for water samples collected at Romans-sur-Isère throughout 2009 and 2010. 43

3.11 Probability density distributions of the volume size for the samples previously presented in Figure 3.10. 45

3.12 Aerial photograph of the Saint-Georges study site. 47

3.13 Upstream view of the Saint-Georges study site. Velocity and bathymetry data were obtained during moving-boat gauging. 48

3.14 Calibration curve for the turbidity meter at Saint-Georges. 49

3.15 Grain size distributions measured for water samples collected from the Saône at the Saint-Georges study site and at the Koenig bridge. 51

3.16 Aerial photograph of the Montélimar study site on the Rhône canal. 54

3.17 Upstream view of the velocity field at the Montélimar study site. 55

3.18 Aerial photograph of the Tricastin study site on the Donzère-Mondragon canal. 57

3.19 Upstream view of the velocity field at the Tricastin study site. 57

4.1 Fifteen minutes of intensity data from the downstream beam of the 300 kHz H-ADCP at the Saint-Alban study site. 61

4.2 Example of fifteen minutes of data from the downstream beam of the 300 kHz H-ADCP at Saint-Georges. 62

4.3 Echo intensity in counts measured with the central transducer of the H-ADCP at Saint-Georges on June 11, 2006 during a period of heavy boat traffic. 63

4.4 Velocity magnitude measured during ADCP gauging January 9, 2009 at Romans. 65

4.5 Comparaison between ADCP (red) and H-ADCP velocity data measured by the 300 kHz (black) and 600 kHz (gray) H-ADCPs at Romans-sur-Isère on March 5, 2009. 66

4.6 (a,b) Average streamwise velocity, v_x, measured by the 300 kHz (black) and 600 kHz (gray) H-ADCPs (a) November 25, 2009 between 18:15 and 18:30 (UTC+1) and (b) May 4, 2010 between 23:15 and 23:30 (UTC+1); (c,d) the corresponding range-corrected intensities measured by the central beam of each H-ADCP. 67

4.7 The relevant geometry for scattering from the air-water interface. 68

4.8 The relevant geometry in the vertical plane for a transducer installed at a depth z_0 below the surface. 70

4.9 Top view of the geometry of Figure 4.8. 71

4.10 The theoretical intensity incident on the air-water interface for the central transducer of the 300 kHz H-ADCP at Romans-sur-Isère, relative to I_*. . . 73

4.11 The theoretical intensity detected by the 300 kHz H-ADCP for scattering from the air-water interface, normalized by I_*. 74

4.12 Theoretical profiles of the range-corrected intensity for scattering from the air-water interface in the far field of the transducers (solid lines) compared to measurements (dotted solid lines) for (a) the 300 and (b) the 600 kHz H-ADCPs for water levels of 0.09 m (black) and 0.21 m (gray) on the staff gauge. 76

4.13 Positioning of the 300 and 600 kHz H-ADCPs at the Romans-sur-Isère study site before and after December 14, 2010. 77

4.14 Theoretical profiles of the range-corrected intensity for scattering from the air-water interface in the far field of the central transducer of (a) the 300 kHz H-ADCP and (b) the 600 kHz H-ADCP at Romans in the old (solid line) and new (dashed-dotted line) positioning. 78

4.15 Along-stream velocity profiles (top panels) and range-corrected intensity profiles (bottom panels) measured with the 300 kHz (black) and 600 kHz (gray) instruments at Romans-sur-Isère. 80

4.16 Three 15-minute averaged profiles of range-corrected intensity measured with the 300 kHz H-ADCP at Montélimar. 81

4.17 Two 15-minute averaged profiles of range-corrected intensity measured by the central transducer of the H-ADCP at Saint-Georges. 82

5.1 Saint-Georges: horizontal profiles of along-stream velocity normalized by the maximum value of each profile. 89

5.2 Montélimar: examples of the horizontal profiles of along-stream velocity averaged over 15 minutes and normalized by the maximum velocity of each profile. 91

5.3 The percent error in the discharge velocity that would be calculated using a unique index-velocity relationship for the 300 kHz H-ADCP at Romans-sur-Isère using data collected between November, 2009 and July, 2010 in measurement **cell 3 (8 m from the H-ADCP)**. 95

5.4 The percent error in the discharge velocity that would be calculated using a unique index-velocity relationship for the 300 kHz H-ADCP at Romans-sur-Isère using data collected between November, 2009 and July, 2010 in measurement **cell 6 (14 m from the H-ADCP)**. 97

5.5 The percent error in the discharge velocity that would be calculated using a unique index-velocity relationship for the 300 kHz H-ADCP at Romans-sur-Isère using data collected between November, 2009 and July, 2010 in measurement **cell 9 (20 m from the H-ADCP)**. 98

5.6 The percent error in the discharge velocity that would be calculated using a unique index-velocity relationship for the 300 kHz H-ADCP at Romans-sur-Isère using data collected between November, 2009 and July, 2010 in measurement **cell 12 (26 m from the H-ADCP)**. 99

5.7 The percent error in the discharge velocity that would be calculated using a unique index-velocity relationship for the 300 kHz H-ADCP at Romans-sur-Isère using data collected between November, 2009 and July, 2010 in measurement **cell 15 (34 m from the H-ADCP)**. 100

5.8 The percent error in the discharge velocity that would be calculated using a unique index-velocity relationship for the **600 kHz H-ADCP** at Romans-sur-Isère using data collected between November, 2009 and July, 2010 in **measurement cell 13 (14 m from the wall)**. 102

5.9 The percent error in the discharge velocity that would be calculated using a unique index-velocity relationship for the **1200 kHz H-ADCP** at Romans-sur-Isère using data collected between November, 2009 and July, 2010 in measurement **cell 27 (14 m from the right bank)**. 103

5.10 The percent error in the discharge velocity that would be calculated using a unique index-velocity relationship for the 300 kHz H-ADCP at Montélimar using data collected between January, 2010 and December, 2010 in **cell 3 (3.2 m from the H-ADCP)**. 106

5.11 The percent error in the discharge velocity that would be calculated using a unique index-velocity relationship for the 300 kHz H-ADCP at Montélimar using data collected between January, 2010 and December, 2010 in **cell 10 (41.2 m from the H-ADCP)**. 107

5.12 The percent error in the discharge velocity that would be calculated using a unique index-velocity relationship for the 300 kHz H-ADCP at Montélimar using data collected between January, 2010 and December, 2010 in **cell 18 (73.2 m from the H-ADCP)**. 108

5.13 The percent error in the discharge velocity that would be calculated using a unique index-velocity relationship for the 300 kHz H-ADCP at Montélimar using data collected between January, 2010 and December, 2010 in **cell 24** (**101.2 m** from the H-ADCP). 109

5.14 Index velocity error measured at Montélimar (blue) and Romans-sur-Isère (black) as a function of the backscattered intensity. 110

6.1 Reproduction of Figure 37 of *Thevenot et al.* (1992). 116

6.2 An example of the raw and range-corrected intensity profiles for data collected with the downstream beam of the 1200 kHz H-ADCP at Romans-sur-Isère for a concentration of 2.3 g/L. 118

6.3 The relationship between sediment attenuation and concentration of suspended sediment for the three H-ADCPs at Romans-sur-Isère on June 30, 2010 (circles for 300 kHz, squares for 600 kHz and triangles for 1200 kHz data). 119

6.4 Variation of the sediment absorption ratios with particle radius for the three frequency combinations: 300/600 kHz (solid line), 600/1200 kHz (dotted line), 300 kHz/1200 kHz (dash-dotted line). 121

6.5 ϵ_{ij} versus particle size calculated using fifteen minutes of attenuation data at Romans. 122

6.6 Fifteen-minute average time series of (a) concentration data from the optical turbidity meter at Saint-Georges and (b) the backscattered intensity recorded at the cell located 14 m from the 300 kHz H-ADCP. 125

6.7 Concentration of suspended sediment versus the backscattering level BL measured at 14 m from the H-ADCP at Saint-Georges. 126

6.8 Concentration of suspended sediment versus the backscattering level BL measured at 26 m from the H-ADCP at Saint-Georges. 127

6.9 Box and whisker plots of the data presented in Figure 6.7: concentration of suspended sediment versus the range-corrected average backscatter measured 14 m from the H-ADCP at Saint-Georges. 128

6.10 Box and whisker plots of the data presented in Figure 6.8: concentration of suspended sediment versus the range-corrected average backscatter measured 26 m from the H-ADCP at Saint-Georges. 129

6.11 (a) Concentration from turbidity and (b) acoustic calibration data for the 1200 kHz H-ADCP at Romans-sur-Isère using intensities recorded 3 m from the instrument. 131

6.12 Daily-averaged values of suspended sediment concentration at Arles versus the daily-averaged backscattering level BL measured at 14 m from the H-ADCP at Montélimar for all available data in 2010. 133

6.13 Daily-averaged values of suspended sediment concentration at Arles versus the daily-averaged range-corrected beam-averaged backscatter measured at 14 m from the H-ADCP at Tricastin for 2008. 134

6.14 Relationship between concentration from optical turbidity and sediment attenuation measured with the 300 kHz (blue), 600 kHz (magenta) and 1200 kHz (red) H-ADCPs between May 31 and June 3, 2010 at Romans-sur-Isère. 137

6.15 Relationship between concentration from optical turbidity and sediment attenuation measured with the 300 kHz (blue), 600 kHz (magenta) and 1200 kHz (red) H-ADCPs between June 16 and 20, 2010 at Romans-sur-Isère. 138

6.16 Relationship between concentration from optical turbidity and sediment attenuation measured with the 300 kHz (blue), 600 kHz (magenta) and 1200 kHz (red) H-ADCPs on between June 30 and July 1, 2010 at Romans-sur-Isère. 139

6.17 Time series of concentration measured by filtration at Arles and by the attenuation of the 300 kHz H-ADCP data at Montélimar for 2010. 141

6.18 Time series of concentration measured by filtration at Arles and by the attenuation of the 300 kHz H-ADCP data at Tricastin for 2008. 142

6.19 Time series of concentration measured by filtration at Arles and by the attenuation of the 300 kHz acoustic data at Tricastin for 2010. 143

6.20 Time series of concentration measured by filtration at Arles (black) and by the attenuation of the 300 kHz acoustic data at Montélimar (blue) and Tricastin (magenta) for 2010. 145

7.1 A time series of the concentration data at Romans-sur-Isère measured by the turbidity meter (black line) and by in-situ sampling (red triangles). . . 148

7.2 (a) Concentration of suspended sediment at Romans-sur-Isère measured with the turbidity meter (black) and the 300 kHz (blue), 600 kHz (magenta) and 1200 kHz (red) H-ADCPs. (b) Along-stream velocity measured at 14 m from the right bank with the three H-ADCPs and (c) the resulting sediment transport rates in tonnes per second. 151

7.3 Sediment transport rates calculated using data from the various H-ADCPs at Romans-sur-Isère, the turbidity meter at Beaumont-Monteux combined with the discharge at the Beaumont-Monteux dam, the H-ADCP at Montélimar combined with the discharge at the Montélimar dam and water samples at Arles combined with values of the maximum daily discharge. . 153

7.4 Sediment transport rates plotted on a logarithmic scale. 154

7.5 (a) Attenuation data measured with the 300 kHz (blue), 600 kHz (magenta) and 1200 kHz (red) H-ADCPs at Romans-sur-Isère. (b) The median grain radius obtained using the multi-frequency attenuation inversion method. 156

7.6 Four examples of the multi-frequency size estimation method based on the acoustic attenuation data. 157

A.1 Grain size distributions measured using a laser sizer for water samples collected at Romans-sur-Isère between January and March, 2009. 170

A.2 Grain size distributions measured using a laser sizer for water samples collected at Romans-sur-Isère during May and June, 2010. 171

A.3 Grain size distributions measured using a laser sizer for water samples collected at Romans-sur-Isère during June, 2010. 172

A.4 Grain size distributions measured using a laser sizer for water samples collected at Romans-sur-Isère during June, 2010. 173

A.5 Grain size distributions measured using a laser sizer for water samples collected at Romans-sur-Isère during June, 2010. 174

A.6 Grain size distributions measured using a laser sizer for water samples collected at Romans-sur-Isère during June, 2010. 175

A.7 Grain size distributions measured using a laser sizer for water samples collected at Romans-sur-Isère during June, 2010. 176

A.8 Grain size distributions measured using a laser sizer for water samples collected at Romans-sur-Isère during June and July, 2010. 177

A.9 Grain size distributions measured using a laser sizer for water samples collected at Romans-sur-Isère between July and September, 2010. 178

A.10 Grain size distributions measured using a laser sizer for water samples collected at Romans-sur-Isère between September and December, 2010. . 179

A.11 Grain size distributions measured using a laser sizer for water samples collected at Romans-sur-Isère during December, 2010 and January, 2011. 180

B.1 Across-stream velocity profiles measured during ADCP gauging at Romans-sur-Isère. 182

ABSTRACT

Suspended sediment in rivers has important impacts on fluvial biota, fate of nutrients and pollutants, erosion controls, and engineering issues from sediment infilling. However, the study of sediment transport has been hampered by lack of equipment for continuous field monitoring of sediment concentration and velocity. Side-looking or horizontal acoustic Doppler current profilers (H-ADCPs) are a potential tool for this purpose. Installed facing across-stream, discharge rates can be calculated from the river-wide velocity profile and suspended sediment concentrations estimated from the backscattered intensity. A multi-year measurement campaign on three rivers in southeastern France was used to determine potential uses and limitations of commercially available H-ADCPs under various river morphology, sediment content, boat traffic, seasonal variation, and flow conditions. Standard water samples and optical turbidity measurements establish a baseline for comparison of the concentration estimates while ADCP gauging and discharge stations establish a baseline for the velocity measurements. Grain size analysis was performed on suspended sediment samples from one study site using a laser grain sizer. The distributions were lognormal and the sediments were predominantly silts and clays.

Low sediment load conditions resulted in underestimating velocities. When the H-ADCP measurement volume was close to the surface, the sound reflected from the surface dominated the signal from the particles in the water, even when the incident angle was low. In measurement cells unaffected by the surface, flow velocity was also underestimated when the backscattered intensity from the water was low due to low sediment concentrations, whereas velocity estimates appeared accurate when the backscattered intensity was low due to attenuation by high concentrations of sediment. Relationships between velocity underestimation and (1) concentration and (2) intensity are presented for the 300, 600 and 1200 kHz H-ADCPs used in this study. These relationships can be used to correct the biased velocity measurements from the H-ADCPs.

At the range of frequencies of these instruments, viscous absorption by silt-sized particles leads to substantial attenuation when concentrations exceed 100 mg/L. Excellent agreement was found between concentrations from attenuation and standard methods of water samples and optical turbidity meters when concentrations ranged from 100 mg/L to 10 g/L. The median grain size of the suspended sediment was determined from multi-frequency attenuation data by assuming lognormal size distributions. The sizes estimates were 20 times greater than what was predicted assuming monosized particles. The median radius measured by laser grain sizer was in between the two acoustic estimates. This highlights the need for laboratory experiments with controlled size distributions to determine whether multi-frequency attenuation data can provide accurate measurements of grain size.

This study shows that once the limits of accurate velocity measurements are established for a given site and instrument, the H-ADCP is a valuable tool for regional fluvial sediment transport surveys, especially for monitoring concentration and qualitatively characterizing changes in grain size during flood events. This is a significant finding, since the majority of sediment transport is believed to occur during floods or dam flushing events and most other monitoring techniques fail under these extreme conditions.

List of Abbreviations and Symbols Used

a	radius of the scatterer
a_n	nth percentile grain radius
a_t	radius of the transducer
A	wetted area
BL	backscattering level
c	sound speed
c_0	speed of compression waves in a vacuum
d	particle diameter
d_n	nth percentile grain diameter
D	transducer directivity
E	intensity in counts
E_{noise}	noise level in counts
E_0	elasticity of the medium
E_1	elasticity of the scatterer
f	acoustic frequency
f_r	reflection form function
f_{receive}	received frequency of a Doppler-shifted signal
f_∞	far field form factor
F_d	Doppler frequency shift
FCB	fluid-corrected backscatter
g	ratio of the density of the scatterers to the density of the medium
i	$\sqrt{-1}$
I	intensity
I_{bs}	backscattered intensity
I_{dB}	intensity in decibels
I_{detected}	Intensity detected by the transducer

I_i	incident intensity
I_s	scattered intensity
I_*	intensity at distance r_*
J_1	first order cylindrical Bessel function
k	acoustic wavenumber
k_c	conversion factor from counts to decibels
K	index velocity constant
m	relative refractive index
M	mass concentration of particles
M_h	mass concentration from H-ADCP data
n	real refractive index
n'	imaginary refractive index
n_m	real refractive index of the medium
n_p	real refractive index of a particle
n'_p	imaginary refractive index of a particle
$n(a)$	size spectral density defined such that $N = \int_0^\infty n(a)da$
N	number of particles per unit volume
NGF	Nivellement Général de la France
p	pressure
p_d	detected pressure
p_i	incident pressure
p_{ref}	reference pressure
p_s	scattered pressure
p_*	pressure at distance r_*
Q	discharge
r	distance from the point of observation to the scatterer
r_n	far field distance of a transducer
r_*	reference distance
R	correlation coefficient
$\vec{r}$	x and y component of $\vec{R}$
$\vec{r_0}$	x and y component of $\vec{R_0}$
$\vec{R}$	vector between the origin of the transducer and a point on the surface

$\vec{R}_0$	vector coincident with the axis of the transducer
SL	source level of the transducer
t	time
T	temperature
T_e	temperature of the electronics of a transducer
u	particle velocity
u^*	complex conjugate of u
v	relative radial velocity between a particle and the transducer
$v_{1,2,3}$	radial velocity measured by transducer 1, 2 or 3
v_x	flow velocity in the x-direction, the along-stream velocity
v_y	flow velocity in the y-direction, the across-stream velocity
V_h	velocity measured with the H-ADCP
V_i	index velocity
V_q	discharge velocity; cross-sectional averaged velocity
x	non-dimensional wavenumber in the medium; ka
z_0	depth of the transducer
α	attenuation
α_{dB}	attenuation in decibels
α_s	sediment attenuation
$\alpha_{s,\,\text{visc}}$	viscous sediment attenuation
$\alpha_{s,\,\text{scat}}$	scattering sediment attenuation
α_w	attenuation by the water
β	angle between the scatterer and the axis of the transducer
β_0	half-power angle of the transducer, i.e. transducer beamwidth
γ	angle between the relative velocity vector and the axis of the transducer
$\epsilon_{i,j}$	difference between the ratios of observed and expected attenuation at frequencies i and j
ζ	theoretical attenuation constant
ζ_{exp}	experimental attenuation constant
ζ_s	theoretical scattering attenuation constant
ζ_v	theoretical viscous attenuation constant
θ	angle between the observer's line of sight and the surface normal
θ_i	angle between the incident wave and the surface normal

θ_s	scattering angle
κ	horizontal separation angle between the axes of the transducers
λ	acoustic wavelength
μ	Lambert scattering parameter
μ_x	location parameter of a lognormal probability distribution
ν	kinematic viscosity
ρ	density of the medium
ρ_s	density of the scatterer
σ_X	shape parameter of a lognormal probability distribution
σ_s	differential scattering cross section
Σ_s	total scattering cross section
τ	acoustic pulse duration
χ	normalized total scattering cross-section
ψ	near field correction factor
Ψ_h	sediment transport rate calculated from H-ADCP measurements
ω	angular frequency
Ω	solid angle
$\langle\cdot\rangle$	ensemble average, $\int_0^\infty \cdot\, n(a)da$

ACKNOWLEDGEMENTS

Tout d'abord je souhaite remercier la Compagnie Nationale du Rhône (CNR) et l'Electricité de France (EDF). Merci pour l'utilisation de vos instruments et de vos données. Merci pour le financement qui a rendu cette thèse possible. Un grand merci à Xavier Martin qui m'a aidé infiniment sur le terrain comme au bureau. Merci à Serge Doucet, Serge Françon, Thibault Grenier, Laetitia Grimaldi, Thierry Pantel et Olivier Tisseur. Merci à Gilles Pierrefeu pour les échanges et pour l'opportunité d'intervenir à un congrès international au tout début de la thèse. Je remercie Christian Perret, Frédéric Gottardi, Anne-Laure Besnier et Damien Sevrez d'EDF. Je souhaite également remercier la Station Observatoire du Rhône en Arles pour les données de concentration et de débit.

Merci à Guillaume Dramais, Mickaël Lagouy, Fabien Thollet et Laurent Dramais pour toutes les heures passées sur le terrain et dans le labo. Merci à André pour les retours sur l'organisation du temps et du manuscrit et à David pour les échanges sur des thèmes acoustiques. Jérôme, merci pour la patience que tu m'as accordée au début quand je découvrais la vie en France et pour l'encouragement que tu m'as donné à la fin. C'était un vrai plaisir de travailler avec toi au quotidien.

A special thanks to my Master's supervisor, Alex Hay. Your experience and knowledge guided me both through this degree and the last. Thank you very much for the office that you provided me and the time that you spent with me during the spring of 2010. The fruit of this "séjour" was the resolution a question that had plagued me since the start of my thesis: just what was causing the data at Romans to be so wonky? The resolution of this question permitted me to move forward with my research, and for that I am grateful.

I am truly grateful to Colin Rennie and Peter Thorne who reviewed this thesis with such attention to detail. The points that you raised, both for correction and discussion were invaluable. Merci and thank you aux autres membres du jury, ainsi qu'aux membres du comité de pilotage. Je vous remercie pour votre suivi de cette étude et pour l'encouragement que vous m'avez accordé tout au long de ce travail.

Merci mille fois à toutes les filles de LOU water polo, votre énergie m'inspire et me détend. Dommage que j'ai mis trois ans avant de vous trouver! Jérôme et Flora, merci pour l'accueil chaleureux dès mon arrivée à Lyon. Grâce à vous j'ai découvert la beauté de la campagne

française, les régals de la cuisine française, et les traditions d'ici et d'ailleurs.

Lastly, I would like to thank my family, both blood relatives and adopted. Mom, Dad and Eric, thanks for the moral support. Craig, though it may have taken me two years to open the wireless mouse, I have never looked back. Joanne, thanks for being exactly what a godmother should be: a friend, a counsellor and a motivator. Thank you to the rest of my family and to my friends and partners, past and present, you know who you are, and you know in what ways you have helped.

Résumé de la Thèse

Cadre de l'étude

Le suivi en continu des flux d'eau et de matières en suspension dans les cours d'eau est important pour de nombreuses raisons. Les études de l'envasement des retenues de barrage, les études géomorphologiques et les études du transport des nutriments et des polluants nécessitent des mesures en continu car les concentrations peuvent varier de plusieurs ordres de grandeur lors des crues. Le suivi en continu des débits est important pour l'optimisation de la production hydro-électrique et, entre autres, l'étude des crues et des ressources en eau. Afin de quantifier le transport solide en suspension, les mesures de débit sont en général combinées avec des prélèvements d'eau ou des mesures optiques de la concentration en sédiments, mais seuls les instruments acoustiques sont capables de fournir des mesures simultanées de vitesse et de concentration. Cette thèse est une étude de l'applicabilité d'une nouvelle configuration d'un instrument commercial, le profileur acoustique Doppler horizontal (H-ADCP), pour le suivi des flux d'eau et de matières en suspension dans les rivières.

Un profileur acoustique Doppler (ADCP) est un instrument conçu pour mesurer un profil de vitesse. Les ADCPs fonctionnent sur le principe qu'il y a des particules en suspension dans l'eau qui se déplacent à la vitesse de l'eau. Cette hypothèse est appropriée loin du lit, dans la couche de suspension homogène des rivières car les particules en suspension se déplacent avec les mêmes direction et vitesse que l'écoulement, surtout sur les courtes échelles temporelles des mesures acoustiques. Un ADCP mesure la vitesse de l'écoulement dans la direction parallèle à l'axe du transducteur en envoyant des signaux acoustiques dans l'eau et en analysant le son qui est rétrodiffusé par les particules en suspension. En utilisant des transducteurs avec des axes dans plusieurs directions, les instruments fournissent des mesures de vitesse de l'écoulement en deux ou trois dimensions.

L'intensité acoustique qui est rétro-diffusée par les matières en suspension peut être exploitée pour déterminer leur concentration. La majorité de la matière en suspension dans les rivières est composée de limons, d'argiles et de sables fins. La concentration des sables peut être déterminer à partir de l'intensité rétrodiffusée (e.g. *Hay*, 1983; *Thorne and Hanes*, 2002). Pour les fréquences des H-ADCPs, l'intensité rétrodiffusée par les limons et argiles est faible, mais l'atténuation est importante. L'atténuation sédimentaire peut-être exploitée pour determiner la concentration des

sédiments fins en suspension (e.g. *Urick*, 1948; *Flammer*, 1962; *Topping et al.*, 2007; *Wright et al.*, 2010).

Dans une application fluviale typique, un H-ADCP est installé sur une berge de la rivière à quelques mètres de profondeur, visant la rive opposée. L'instrument mesure un profil de vitesse à travers la section avec un espacement de cellule de mesure compris entre 0.5 m et 4 m. L'avantage de ces instruments pour le suivi des vitesses par rapport à un jaugeage avec un ADCP vertical est qu'ils fournissent des mesures en continu. Avec un modèle approprié, on peut relier leurs mesures de vitesse à la vitesse débitante, c'est-a-dire la vitesse moyenne sur la section. Il suffit ensuite d'une mesure de la surface mouillée pour déterminer un débit. L'application de ces instruments pour suivre les débits en continu est très prometteur. Ceci dit, des études préliminaires par *Le Coz et al.* (2008) et *Pierrefeu* (2008) ont montré que les vitesses mesurées avec des H-ADCPs sont sous-estimées quand le débit est faible. Cette observation n'était pas inattendue car il faut une certaine concentration de particules en suspension pour avoir une mesure fiable, mais il faut pouvoir quantifier de combien les instruments sous-estiment les vitesses et en quelles circonstances. C'est d'autant plus important que les utilisateurs principaux des H-ADCPs en France sont des compagnies hydro-électriques. Pour assurer le respect du débit réservé et pour optimiser la production, par exemple, il est impératif qu'ils aient des mesures fiables pendant des périodes de faible vitesse.

Objectifs

Avec un grand jeu de données acquis sur des sites d'étude avec des bathymétries et des conditions de forçage contrastées, le premier objectif de cette étude était de déterminer la cause de la sous-estimation de vitesse par les H-ADCPs et de déterminer les conditions sous lesquelles ces instruments fournissent des mesures fiables de vitesses. Le deuxième objectif était d'établir une méthode robuste pour obtenir la concentration de la matière en suspension à partir des données d'intensité.

Plan du manuscrit

Une introduction à la théorie des mesures hydro-acoustiques de vitesse et de concentration est présentée dans le Chapitre 2. Chapitre 2 aborde la diffusion ainsi que l'atténuation acoustique

par une suspension de sédiments à des fréquences élévées (100 kHz - 1 MHz). Une méthode innovante pour déterminer la granulométrie à partir de mesures multi-fréquences d'atténuation est introduite. Les sites d'étude sont détaillés dans le Chapitre 3 ; ils appartiennent soit à l'Electricité de France (EDF), soit à la Compagnie Nationale du Rhône (CNR). Les mesures ont été réalisées principalement sur quatre sites d'étude sur trois cours d'eau : la Saône à Lyon, passerelle Saint-Georges (CNR), l'Isère à Romans-sur-Isère (CNR) et le Rhône à Montélimar (CNR) et au Tricastin (EDF). Les instruments, qui sont tous construits par Teledyne RD Instruments, ont une fréquence porteuse de 300, 600 ou 1200 kHz. A Romans-sur-Isère se trouve un instrument de chaque fréquence, mais les autres sites d'étude comportent uniquement un H-ADCP de 300 kHz. Une description des conditions hydro-sédimentaires pour chaque site est aussi donnée dans le Chapitre 3.

A travers ce travail, nous avons observé que la profondeur limitée de certaines rivières peut compromettre les mesures de vitesse et de concentration à travers la section. L'objectif du Chapitre 4 est de mettre en évidence et d'analyser ce problème. Les mesures de vitesse sont présentées dans le Chapitre 5 et les facteurs qui influencent la justesse des mesures sont discutés. Des relations de type "index-velocity" sont établies pour les trois H-ADCPs de Romans et pour le H-ADCP de Montélimar. Ces relations permettent une correction des débits, qui seraient autrement sous-estimés. Montélimar est considéré comme le site d'étude idéal car la position de l'instrument est assez profonde et horizontale, la rivière est profonde et il n'y a pas de passage de bateaux devant l'instrument. Les méthodes d'inversion en concentration sont détaillées et appliquées dans le Chapitre 6. Dans le Chapitre 7, nous combinons les mesures de vitesse avec les mesures de concentration pour calculer les flux de matières en suspension pendant une crue naturelle sur l'Isère et le bas-Rhône. Les principaux résultats de cette thèse sont détaillés dans les quatre sections ci-dessous.

Le positionnement des instruments

Dans le Chapitre 4, nous montrons que les profils d'intensité des H-ADCPs de 300 et de 600 kHz de Romans ne sont pas cohérents avec la diffusion par une suspension homogène de sédiment quand la concentration de la matière en suspension est en dessous de $\sim$20 mg/L (ce qui est le cas la majorité de l'année). A part dans les premières quelques cellules de mesures où les valeurs sont crédibles, les intensités sont fortes et variables malgré des concentrations de diffuseurs faibles et constantes. De plus, les vitesses sont quasi-nulles et fluctuent autour de zéro dans ces mêmes

cellules.

D'habitude, on simplifie le fonctionnement d'un ADCP en considérant qu'il mesure ce qui se passe dans un volume cylindrique à une distance donnée de l'instrument. Mais en réalité, l'intensité qui est détectée correspond à toutes les ondes qui ont parcouru la même distance. C'est-à-dire qu'à chaque distance supérieure ou égale à la profondeur d'immersion de l'instrument, il y aura une contribution de la diffusion par la surface. L'explication la plus probable pour les observations d'intensités et vitesses abhérentes est donc la diffusion par la surface. Les particules à la surface de l'eau se déplacent à la vitesse de l'eau, mais les ondes capillaires créées par la macroturbulence en rivière se propagent dans tous les sens et leur vitesse moyenne devrait être proche de zéro. Pour une onde acoustique incidente sur une surface présentant des ondes capillaires, la vitesse détectée serait donc nulle, mais l'intensité rétrodiffusée pourrait être importante par rapport à l'intensité renvoyée par les particules en suspension quand l'eau est peu chargée.

Pour déterminer l'effet de la diffusion par la surface sur les mesures d'intensité, nous modélisons la surface comme un diffuseur lambertien. Dans le cas de la rétrodiffusion (angle de diffusion égal à l'angle d'incidence), l'intensité diffusée par une surface lambertienne dépend linéairement du cosinus carré de l'angle d'incidence. Cette représentation de la surface libre est valable si nous supposons que l'échelle caractéristique des rugosités de la surface est du même ordre de grandeur que la longeur d'onde acoustique, ce qui est vrai pour des ondes capillaires. Nous montrons que les irrégularités observées dans les profils d'intensité mesurés avec les H-ADCPs de 300 et de 600 kHz à Romans-sur-Isère pendant des périodes de faible concentration ont la même forme que ce qu'on attend de la diffusion par la surface libre. Ces résultats montrent que quand les ondes acoustiques interceptent la surface libre, les mesures de concentration et de vitesse peuvent être fortement perturbées, même quand les ondes sont incidentes avec un faible angle d'incidence. Ceci contraste avec ce qui est écrit dans le guide utilisateur qui est fourni avec les H-ADCPs ainsi qu'avec les déclarations de *Hoitink et al.* (2009) selon lesquelles la réflexion du lobe principal sur la surface libre ne pose aucun problème pour les mesures de vitesse.

Les H-ADCPs de 300 et de 600 kHz à Romans ont été repositionnés en décembre 2010 dans le but d'éviter le problème de la réflexion par la surface, mais en raison de la faible profondeur de la section (profondeur maximale de 4 m), aucune position n'a été trouvée dans laquelle ni la surface, ni le fond ne posent problème. Il n'est, donc, pas possible de profiler correctement les vitesses à travers la section entière à Romans ($\sim$85 m). La possibilité que les mesures acoustiques soient perturbées par la diffusion par la surface à Montélimar et à Saint-Georges a aussi été étudiée à l'aide du modèle lambertien. La conclusion est qu'en raison du bon positionnement du H-ADCP

à Montélimar et de la profondeur importante de ce site d'étude, ni la réflexion par la surface, ni la réflexion par le fond ne posent problème pour les mesures du transport des sédiments en suspension. Par contre, il semble que la réflexion par le fond pose un léger problème pour les mesures à Saint-Georges à des distances au-delà de 40 m.

La modélisation simple qui a été effectuée dans cette thèse est un outil pertinent pour de futures études. Comme le problème de la surface libre n'est pas apparent quand l'eau est suffisamment chargée, le problème ne sera pas détecté si l'installation est faite un jour où les concentrations sont suffisantes (typiquement supérieures à 20 mg/L).

Les mesures de vitesse

La justesse des mesures de vitesse faites avec les H-ADCPs a été étudiée sur trois sites d'étude. La forme des profils de vitesse mesurés avec les H-ADCPs de Saint-Georges et de Montélimar a été comparée aux données des jaugeages ADCP réalisés avec un ADCP vertical fixé à un bateau à moteur. Nous observons que les H-ADCPs sous-estiment la vitesse quand les vitesses – et donc probablement les concentrations – sont faibles. La sous-estimation s'aggrave avec la distance de mesure depuis l'instrument car l'intensité diminue avec la distance de propagation.

Les données de débit du barrage de Pizançon (EDF) sont utilisées pour calculer une vitesse débitante à Romans (débit divisé par la surface mouillée) et le débit du barrage de Châteauneuf (CNR) est utilisé pour calculer une vitesse débitante à Montélimar. Le barrage de Pizançon est situé 2 km en amont de Romans et le barrage de Châteauneuf est situé 500 m en aval du H-ADCP de Montélimar. Pour les deux sites d'étude l'écart entre la vitesse débitante et la vitesse mesurée par les H-ADCPs à une distance donnée est évalué en fonction de (1) la vitesse débitante, (2) de l'intensité rétrodiffusée et (3) de la concentration de matières en suspension, quand disponible. Plus de six mois de données en continu sont utilisées pour effectuer une comparaison avec des données de plusieurs cellules de mesure. Si les H-ADCPs mesuraient correctement les vitesses, le rapport de la vitesse débitante à la vitesse locale du H-ADCP devrait être une constante à une distance de mesure donnée, c'est-à-dire que le rapport ne devrait pas dépendre de la concentration, ni de la vitesse. Au contraire, on trouve que la vitesse mesurée par les H-ADCPs est sous-estimée quand l'intensité rétrodiffusée est faible en raison d'une charge en matières en suspension faible, mais pas lorsque l'intensité est faible en raison de l'atténuation acoustique due à de fortes concentrations. Nous observons un comportement similaire à Montélimar, mais comme il n'y a pas de mesures de concentration à ce site d'étude, on ne peut pas définir une valeur de concentration

en-dessous de laquelle les mesures sont faussées. L'explication pour la sous-estimation en raison de trop faible concentration est que les H-ADCPs amplifient trop le signal. Quand il y a peu de sédiment ce signal est que du bruit, ce qui contribue une vitesse nulle, mais quand il y a beaucoup de sédiment, ce signal vient des particules et donc leurs vitesses sont répresentatives de la vitesse de l'écoulement.

Les mesures de turbidité à Romans-sur-Isère sont utilisées pour montrer que quand la concentration est inférieure à $\sim$70 mg/L, le H-ADCP de 300 kHz sous-estime la vitesse. La sous-estimation s'aggrave et l'écart dans les mesures de vitesse augmente avec une concentration décroissante. Par exemple, à 14 m depuis l'instrument la sous-estimation peut atteindre 50%. En revanche, quand les concentrations sont supérieures à 100 mg/L, même si l'intensité est très faible, les valeurs du H-ADCP sont à 10% des vraies vitesses. Une sous-estimation de vitesse a également été observée dans les données du H-ADCP de 600 kHz de Romans pour des concentrations $\lesssim$70 mg/L. Comme avec le H-ADCP de 300 kHz, l'écart des données et la sous-estimation de vitesse s'aggravent quand l'intensité diminue. Les mesures de vitesse effectuées avec le H-ADCP de 1200 kHz sont plutôt correctes, mais l'écart des données augmente légèrement quand l'intensité décroît. Malgré ses mesures de vitesse justes, un H-ADCP de 1200 kHz ne peut pas profiler à des distances supérieures à 20 m à cause de l'atténuation importante du signal. Nos observations montrent donc que l'utilisateur doit décider s'il a besoin de mesures justes sur de courtes distances, auquel cas il utilisera un H-ADCP de 1200 kHz, ou s'il a besoin de mesures moins justes, mais sur des distances plus importantes, auquel cas il utilisera un H-ADCP de 600 kHz, voire 300 kHz.

Des relations de type "index-velocity" sont établies pour les trois H-ADCPs de Romans et pour le H-ADCP de Montélimar en fonction de l'intensité rétrodiffusée et de la concentration. Ces relations permettent une correction des débits, qui seraient autrement sous-estimés. Pour obtenir des mesures justes de vitesse avec les données des H-ADCPs, il faut d'abord déterminer s'il y a de l'atténuation acoustique liée à la présence de la matière en suspension, car les vitesses sont justes quand le signal est faible en raison de fortes concentrations. S'il y a de l'atténuation, cela veut dire que la charge en matières en suspension est importante. En ce cas, la vitesse débitante est toujours le même ratio de la vitesse mesurée par le H-ADCP à une distance donnée, indépendamment de l'intensité. S'il n'y a pas d'atténuation, il peut y avoir relativement peu de sédiment et donc une relation index-velocity qui dépend de l'intensité acoustique doit être utilisée.

Les mesures de concentration et de granulométrie

Deux méthodes sont présentées pour établir les concentrations de matières en suspension avec les mesures acoustiques : l'inversion directe de l'intensité retrodiffusée ou l'inversion de l'atténuation acoustique qui est obtenue à partir des profils d'intensité. Les sédiments en suspension dans l'Isère, la Saône et le Rhône sont surtout des limons accompagnés d'argiles et, de temps en temps, de sables fins. Pour les fluctuations de granulométrie observées sur nos sites d'étude, la méthode d'inversion de l'atténuation est plus robuste que la méthode d'inversion de l'intensité retrodiffusée. Ceci vient du fait que les sables dominent la rétrodiffusion à des fréquences de 300 kHz - 1200 kHz, alors que c'est justement la proportion de sables fins qui est susceptible de changer lors des crues. Nos observations sont en accord avec les travaux de *Topping et al.* (2007) et de *Wright et al.* (2010) avec des H-ADCPs de type Sontek, qui montrent que l'intensité rétrodiffusée dépend surtout de la concentration des sables, tandis que l'atténuation est dominée par l'atténuation visqueuse au voisinage des sédiments fins.

En effet, dans la gamme de fréquence 300 - 1200 kHz, l'atténuation visqueuse dans la couche d'eau qui entoure les sédiments fins (limons et argiles) est beaucoup plus importante que l'atténuation due à la diffusion par les particules. L'atténuation dépend de la concentration d'une manière linéaire et elle est notable sur des distances de l'ordre d'un mètre quand les concentrations en sédiments fins sont supérieures à $\sim$100 mg/L. Une relation entre l'atténuation sédimentaire et la concentration (issue du turbidimètre optique calibré) a été établie pour les H-ADCP de 300, 600 et 1200 kHz à Romans-sur-Isère pour plusieurs évènements. La pente de cette rélation donne la valeur expérimentale de la constante d'atténuation. Les relations linéaires sont très nettes. Des valeurs théoriques de la constante d'atténuation sont calculées pour les distributions granulométriques des échantillons d'eau mesurées en laboratoire avec un granulomètre à diffraction laser. L'accord entre les observations et les calculs théoriques est bon pour les données du H-ADCP de 300 kHz. Pour le H-ADCP de 600 kHz, la valeur expérimentale est à peu près les deux tiers de la valeur théorique et pour le H-ADCP de 1200 kHz, c'est la moitié. Le désaccord entre théorie et observations pourrait être parce que les distributions granulométriques qui sont utilisées dans les calculs sont les distributions des particules primaires, alors que les sédiments pourraient être floculés en rivière (*Droppo and Ongley*, 1994), surtout quand les concentrations sont de l'ordre de 1 g/L. Par contre, c'est sûrement aussi liée à l'incertitude sur les mesures de granulométrie pour les particules les plus fines, ainsi qu'au fait que la théorie s'applique aux particules sphériques.

Une méthode est également introduite pour déterminer la granulométrie à partir de données multi -fréquences d'atténuation. Cette méthode se fonde sur les méthodes de *Hay and Sheng*

(1992) et *Crawford and Hay* (1993) pour l'inversion du signal rétrodiffusé en taille moyenne. Elle s'applique seulement pendant des périodes de fortes concentrations ($\gtrsim$ 100 mg/L) car elle nécessite une atténuation sédimentaire substantielle. Pour l'inversion, des distributions granulométriques volumiques log-normales ont été supposées. L'inversion multi-fréquence donne alors une valeur de la taille médiane des particules en suspension. Nous montrons que si une taille unique est supposée au lieu d'une distributions lognormale, le diamètre médian des particules obtenu peut différer d'un facteur 20. La valeur médiane obtenue avec le granulomètre laser se trouve entre les deux estimations de taille.

Les concentrations sont aussi obtenues à partir des données H-ADCP à Montélimar et Tricastin. Comme il n'y a de mesures ni de concentration ni de granulométrie sur le Rhône à Montélimar ou au Tricastin, on a supposé que les particules en suspension ont la même granulométrie moyenne qu'à Romans. Cette hypothèse semble réaliste au vu des données disponibles sur le bas-Rhône, à la station d'Arles notamment. L'atténuation sédimentaire obtenue à partir des profils d'intensité est divisée par la constante d'atténuation sédimentaire observée dans les données de 300 kHz de Romans-sur-Isère pour obtenir des séries temporelles de concentration pendant une succession de crues. L'accord temporel entre les concentrations obtenues avec les données H-ADCPs à Montélimar et Tricastin est cohérent avec la propagation déduite des vitesses mesurées.

La mesure des flux de sédiments

Les méthodes qui sont détaillées dans cette thèse pour obtenir des mesures fiables de vitesse et de concentration par H-ADCP sont appliquées dans le Chapitre 7 pour analyser les flux de sédiments en suspension pendant une crue naturelle sur l'Isère et le bas-Rhône. Les concentrations obtenues avec l'inversion de l'atténuation sont multipliées par la surface mouillée et la vitesse débitante (obtenue à partir de la vitesse mesurée à 14 m des H-ADCPs) pour obtenir un flux de sédiments en suspension. Les mesures acoustiques sont comparées avec des mesures de concentration par turbidimètre optique combinées avec des mesures de débit classiques pour étudier la propagation spatio-temporelle de la crue solide entre Romans-sur-Isère et Arles. L'accord entre les concentrations obtenues avec des mesures acoustiques, optiques et physiques est encourageant. Cette thèse montre qu'une fois que les limites d'applicabilité des H-ADCPs sont bien établies, l'ADCP horizontal peut être un outil puissant pour les mesures en continu de transport des sédiments pendant des périodes de fortes concentration. Des mesures mono-fréquences peuvent fournir vitesse et concentration et des mesures multi-fréquences peuvent en outre fournir

l'évolution de la granulométrie intra et inter-évènements. C'est un résultat très encourageant car la majorité du transport de sédiments en rivière a lieu pendant les évènements les plus chargés.

Perspectives

Les perspectives peuvent être divisées en trois catégories. Les perspectives pour les mesures de vitesse, celles pour les mesures de concentration et celles pour les mesures de granulométrie. Pour les mesures de vitesse, la première perspective pour la suite de ce travail est la validation des relations "index-velocity" qui ont été établies. L'application de la méthode à un jeu de données autre que celui qui était utilisé pour le calage permettrait de s'assurer que la méthode peut être appliquée pour obtenir des vitesses justes à partir des mesures faites avec des ADCPs horizontaux. Si la méthode est jugée robuste, elle pourra être appliquée lors de l'acquisition des données pour fournir des mesures de vitesse en continu avec les H-ADCPs qui sont déjà en place.

Le site d'étude de Montélimar a été trop peu étudié pendant cette thèse, mais il y a des données acoustiques qui donnent l'impression que la concentration et/ou la granulométrie ne sont pas homogènes à travers la section pendant certaine manœvres d'ouvrages. Comme le positionnement et les conditions hydrauliques à Montélimar sont a priori idéals pour des mesures H-ADCPs, des mesures de la distribution spatiale de la concentration et de la granulométrie, ainsi que des séries temporelles de concentration à un point donné pourraient permettre de mieux explorer les capacités des H-ADCPs. Si, en effet, le H-ADCP peut être utilisé pour distinguer des changements de concentration ou de granulométrie à travers son profil de mesure, il constituerait un outil intéressant pour l'étude des confluences ou des courants de turbidité par exemple.

Une autre perspective pour une étude future est l'investigation du rôle des flocs sur les mesures acoustiques. Le bon accord entre les observations et les calculs théoriques pour des particules primaires pourraient suggérer qu'il n'y avait pas de flocculation des particules pendant nos campagnes de mesure, mais des mesures de granulométrie in-situ avec un granulo-laser de type LISST permettraient de mieux élucider cette question. Finalement, cette étude souligne l'intérêt d'instruments acoustiques capables de fonctionner à plusieurs fréquences. Il existe désormais des ADCPs dévéloppés pour des mesures fluviales qui sont capables de fonctionner sur deux fréquences. Cette étude montre que ces instruments offrent la possibilité de fournir des mesures de granulométrie, même pendant des périodes de fortes concentrations, telles que des crues.

CHAPTER 1

INTRODUCTION

The sediment that is transported in rivers is divided into two categories: suspended load and bedload. Suspended load is the sediment that is dispersed in the flow by turbulence, it is typically composed of fine sand, silt and clay. Bedload is the coarser material that moves along the bed, either by rolling, sliding or saltating. In this thesis we are only concerned with the suspended load, but a comprehensive overview of the sampling, monitoring and prediction of both suspended load and bedload can be found in *Hicks and Gomez* (2003).

The study of suspended sediments and their transport in rivers is important for a number of reasons. Environmental reasons include the study of pollutant and nutrient transport. Hydrophobic pollutants, such as polychlorinated biphenyls (PCBs), chlorinated pesticides such as hexachlorobenzene, and dry-cleaning products such as tetrachloroethylene can adsorb to fine sediments (e.g. *Bero and Gibbs*, 1990; *Lick*, 2009). These particles can then be transported, deposited, and eventually resuspended. Nutrients such as nitrogen and phosphate can also be transported on suspended sediment in rivers (*Walling et al.*, 1997).

In rivers used for the production of hydroelectricity, sediments are often trapped upstream of dams, resulting in infilling which eventually results in the reduction of reservoir storage. Sediments can be flushed out regularly, but in order to understand how far they are transported, real-time measurements of sediment fluxes are imperative. In addition, flow regulation by dams severely alters fluvial morphology, changing patterns of erosion and deposition (e.g. *Howard and Dolan*, 1981). Although it could be argued that suspended load is negligible for geomorphology compared to bedload, the suspended load can be transformed to bedload when the flow encounters deposits or bars or is encroached by vegetation. Therefore the study of suspended sediment transport enables us to study patterns of erosion and deposition which can then be used to better understand past rock records and to predict future changes.

Quantifying suspended sediment fluxes requires continuous measurements because of the high temporal variability in sediment fluxes in rivers. Throughout the course of a flood, concentrations may vary by three orders of magnitude. A variety of techniques exist for measuring sediment transport. Frequent collection of water samples across the river and subsequent filtration is the most robust method for measuring suspended sediment load. Nonetheless, this method only provides information about a given location at a given point in time, and intensive sampling is time consuming. As such, sediment rating curves have been widely used since the mid 1900s (e.g. *Campbell and Bauder*, 1940; *Miller*, 1951). Using a limited number of samples and a record of discharge, a relationship is established between sediment concentration and discharge. This relationship can then be used to estimate sediment transport for future events. Distinct rating curves often exist for the rising and falling limbs of floods because there is often a time lag, or hysteresis, between the peak in suspended sediment concentration and the peak in discharge. However, the relationship between suspended sediment concentration and discharge also depends on sediment supply (e.g. *Wood*, 1977) and seasonality and there is significant uncertainty associated with this technique, especially on small time scales. If the wrong rating curve is used for a given event, or if all possible scenarios have not been sampled, then sediment transport rates estimated from a rating curve can be quite erroneous (*Walling*, 1977). What is needed, therefore, is a robust and reliable technique to continuously monitor suspended sediment concentration. If such a technique can be combined with flow velocity measurements, continuous monitoring of sediment transport rates can be provided.

Two possibilities currently exist for continuous measurements of suspended sediment concentration: the use of (1) optical or (2) acoustical instruments, with optical instruments being the most commonly used. Optical instruments include transmissometers or optical backscatter sensors that typically operate at infrared frequencies. A transmissometer measures the transmissivity between an emitter and a receptor, whereas an optical backscatter sensor, which is also known as a turbidity meter, measures the scattered signal at an angle typically ranging from 90° to 180° to the incident direction (*Downing*, 2006). The measurement is typically made a few centimeters in front of the instrument. Depending on the instrument and the size of particles in suspension, the detectable range of concentrations can be anywhere from 1 mg/L to 200 g/L (*Hicks and Gomez*, 2003). There is typically a distinct linear relationship between concentration of suspended sediment and turbidity (optical scattering), but a calibration must be done with water samples collected at the site of interest since the optical scattering is a function of the refractive index and

particle grain size (*Foster et al.*, 1992). A disadvantage of optical instruments is that they must be cleaned frequently since biological material can colonize the lens and severely impact the measurements; this is known as bio-fouling. Furthermore, they cannot measure flow velocity, which eliminates the possibility of sediment flux monitoring with these instruments alone.

Unlike optical instruments, acoustic instruments are practically insensitive to bio-fouling. A second difference is that they can provide co-incident and co-located measurements of velocity and concentration across a profile. With the use of an acoustical backscatter system, such as the commercially available acoustic Doppler current profiler (ADCP), one has measurements of the velocity field at a range of distances from the instrument. Depending on the instrument, either two or three components of the flow field can be measured. In addition, the intensity of the backscattered signal can be used to determine the concentration of sediment in the measurement volume. Classical ADCPs have been used for quantitative measurements of suspended sediment by *Holdaway et al.* (1999) and *Reichel and Nachtnebel* (1994), among others. The simultaneous measurements of flow speed and concentration made with ADCPs can be used to determine fluxes of suspended sediment. The use of instruments which operate at different frequencies can also provide information on the grain size of particles in suspension. Multi-frequency acoustics have been applied successfully in fine-scale flow and sediment transport studies in order to profile sediment size (*Hay and Sheng*, 1992; *Thorne and Hardcastle*, 1997) as well as sediment fluxes across the highly concentrated benthic flow region (*Hurther et al.*, 2011).

This thesis focuses on the use of a new form of ADCP, the side-looking, or horizontal, acoustic Doppler current profiler (H-ADCP). These instruments are marketed as an ideal tool for high-accuracy continuous measurements of flow in rivers. They are intended to be installed facing horizontally across the river in order to continuously measure a profile of flow speed. The interest in using horizontal ADCPs for gauging as opposed to the more traditional method with a motor boat and a vertically-oriented ADCP is that H-ADCPs can provide continuous measurements, whereas gauging with a vertically-oriented ADCP is limited to the number of hours per day a person can spend in a boat. The work of *Huang* (2006), *Le Coz et al.* (2008), *Nihei and Kimizu* (2008) and *Hoitink et al.* (2009) focused on the use of H-ADCPs for discharge measurements in river. They showed that with the use of a suitable model, the discharge could be determined from the horizontal profile of velocity. However, at a number of study sites used in this thesis it was found that when flow speeds, and presumably concentrations of suspended sediment, were low the H-ADCPs underestimated velocity (*Le Coz et al.*, 2008; *Pierrefeu*, 2008).

To the best of our knowledge there have been no publications that explore the validity of the velocity measurements made using H-ADCPs as a function of scatterer concentration, even though this is of crucial importance for operators. The predominant users of horizontal-ADCPs in France are hydroelectric companies. They have a vested interest in having accurate measurements of velocity during low flow conditions since they aim to optimize production while respecting compensation water regulations ("débit réservé"). Since preliminary studies showed that velocity measurements made using H-ADCPs were not accurate during low flow conditions, the first goal of this study was to determine the hydrological and suspended sediment conditions under which H-ADCPs accurately measure cross-river profiles of flow speed. This was done using data from a number of different study sites with different instruments and instrument configurations. The second objective was to develop a robust method for determining suspended sediment concentrations from the backscattered intensity data in order to measure fluxes of suspended sediment at the various study sites. Previous researchers had investigated the use of side-looking ADCPs for concentration measurements in rivers (*Topping et al.*, 2007; *Wright et al.*, 2010). They showed that the backscattered intensity was most sensitive to sand-sized particles, while the attenuation was most sensitive to silt-sized particles.

The layout of the thesis is the following. The theory pertaining to velocity and concentration measurements is presented in Chapter 2. This includes an introduction to the theory of high frequencies (100 kHz - 1 MHz) acoustic scattering from suspensions of sand (*Hay*, 1983) as well as the theory of acoustic attenuation from suspensions of silt-sized particles (*Urick*, 1948; *Hay*, 1983). The method that is used to determine particle grain size in this study is also presented. The various study sites are presented in Chapter 3. This includes a description of the flow and suspended sediment conditions at each site as well as a detailed description of the acoustic instruments and their configurations.

Throughout this dissertation it will be seen that the limited depth in medium-sized rivers poses a problem for accurately measuring flow speed and concentration across the profile. Chapter 4 discusses the negative effects of scattering from obstacles on the measurement of concentration and flow speed. The main focus of this chapter is an investigation of the impact of scattering from the free surface of the flow. Chapter 5 presents velocity measurements made with the various H-ADCPs. The form of the profiles are compared to measurements from moving-boat gauging. The validity of the velocity measurements is explored as a function of flow speed, echo intensity, and suspended sediment concentration. An index-velocity type relationship is

developed to relate the velocity measured by the H-ADCP at a given distance to the mean flow velocity. The relationships developed in this thesis can be used to obtain accurate measurements of discharge from the H-ADCP velocity data.

In Chapter 6 we present the methods that are used to determine the concentration of suspended sediment. Two methods exist: direct inversion of the backscattered intensity, or determination of the attenuation and subsequent inversion of the attenuation data. We also present a method for determining grain size using multi-frequency attenuation data. In terms of innovative science, our use of the multi-frequency attenuation measurements is the principal contribution of our study to the field of fluvial sediment transport measurements. Lastly, Chapter 7 focuses on the application of H-ADCPs to suspended sediment discharge measurements during floods. Using the velocity data from the H-ADCPs and the concentration from the attenuation, we calculate the flux of suspended sediment for a natural flood. Multiplying the flux by the wetted area gives the suspended sediment discharge, or the mass of suspended sediment moving past a given river cross section per unit time. We look at the downstream propagation of the event and compare the acoustic data to optical data and water samples from a number of different study sites. The evolution of grain size throughout the event is also investigated. Finally, Chapter 8 summarizes the content of this manuscript and presents perspectives for future work.

CHAPTER 2

THEORY

This chapter is divided into three main sections. The first section describes the manner in which the horizontal acoustic Doppler current profilers use the backscattered sound to measure velocity. The second section presents the theory of acoustic scattering and attenuation from a suspension of particles. The third section is devoted to the theory of laser grain size analysis, which is the grain sizing technique employed in our study.

2.1 Velocity Measurements

Our ability to use sound scattering to measure currents is based on two assumptions: (1) that there are particles in the water that will scatter sound; and (2) that these particles are passive flow tracers, moving at the same velocity as the water. Both statements are typically true in the homogeneous suspension layer in rivers. The suspension layer represents more than 90% of the water column, as opposed to the bedload layer which represents the remaining 10%. Although sediments can move at a lower velocity than the flow in the bedload layer, horizontal ADCPs are positioned well above the bottom, profiling a part of the river that is well within the suspension layer. This means that the above two assumptions are true in our measurements.

2.1.1 The Doppler effect

When a wave is incident on an object, the frequency of the wave perceived by the object differs from the emitted frequency if there is a relative radial velocity between the source and the obstacle. If the object is moving towards the source, the perceived frequency is higher than the emitted frequency, and if it is moving away from the source, the perceived frequency is lower. The change in frequency or Doppler shift that is observed by the object is $F_d = f_{\text{receive}} - f$ where

f_{receive} is the received frequency and f is the emitted frequency. The Doppler shift depends on the relative radial velocity v in the following manner (*Doppler*, 1842)

$$F_d = \frac{fv}{c} \tag{2.1}$$

where c is the speed of sound in the medium (1484 m/s in fresh water at 20 °C) and positive radial velocity indicates the object moving towards the source.

Acoustic Doppler Current Profilers (ADCPs) are composed of transducers which both emit and receive waves. They therefore detect the sound that is scattered at $180°$ to the incident direction, which is known as the backscattered sound. This setup is commonly called the monostatic configuration. Since the sound must travel from source to obstacle and back again, the Doppler frequency shift of the scattered wave at the transducer is doubled, i.e. it is $2fv/c$. In the case where the relative motion between the obstacle and the transducer is not along the radial axis of the transducer, the Doppler frequency shift of the received sound is (*RD Instruments*, 1996):

$$F_d = \frac{2fv\cos\gamma}{c} \tag{2.2}$$

where γ is the angle between the relative velocity vector and the axis of the transducer. By using transducers positioned at different angles to the flow, we can measure the different components of velocity.

2.1.2 The principles of operation of RD Instruments BroadBand ADCPs

The horizontal ADCPs used in this study are composed of what RD Instruments refers to as BroadBand transducers. Velocity is measured using the Doppler principle, but instead of measuring velocity based on information contained in a single backscattered wave, the transducers transmit two consecutive identical packets of waves, or pulses, and measure velocity from the phase shift of the consecutive pulses that are scattered back to the transducer. When the time lag between consecutive pulses is too large, phases of n degrees and $(360 + n)$ degrees are indistinguishable. In order to avoid this problem of phase ambiguity, two long pulses consisting of a number of phase coded pulses are emitted, and the phase shift or propagation delay is determined by computing the autocorrelation between these two pulse trains.

2.1.3 Measuring the three components of velocity

The 300 kHz and 600 kHz H-ADCPs employed in this study are composed of three transducers, while the 1200 kHz H-ADCP is composed of two transducers. It is common to refer to the

transducers and the sound that they emit as beams, in reference to the main lobe of the radiation pattern emitted by each transducer. A sketch of a horizontal-ADCP installed on the right bank of a river is shown in Figure 2.1. Beam 1 faces downstream and beam 2 faces upstream and both beams form a horizontal angle κ with the instrument's axis. For the 600 and 1200 kHz instruments, the three transducers are in the same horizontal plane, whereas beam 3 of the 300 kHz H-ADCP is slightly raised from the plane of beams 1 and 2 (see Figure 2.2). The horizontal separation angle between the beams is 20° for the 300 kHz instrument, 40° for the 1200 kHz and 30.2° for the 600 kHz instrument. The x-axis is parallel to the central transducer and the y-axis is perpendicular. The instruments are positioned such that the positive x-direction is downstream and the positive y-direction is across-stream, as shown in Figure 2.1.

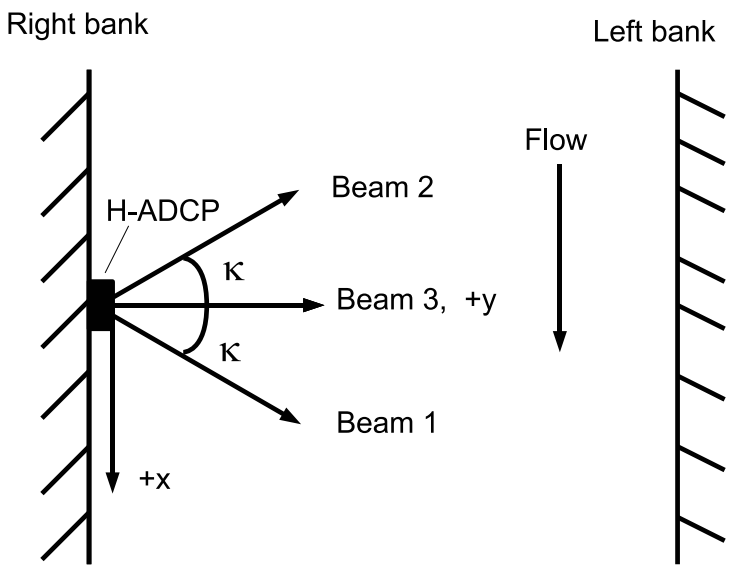

Figure 2.1: Top view of the geometry of a horizontal ADCP installed on the right bank of a river.

300 kHz Workhorse 600 kHz Workhorse 1200 kHz Channel Master

Figure 2.2: Images of the various H-ADCPs used in this study.

The radial velocities v_1, v_2, and v_3 measured by each of the transducers can be combined to yield v_x and v_y. The velocity in the x direction, v_x is (*RD Instruments*, 2007):

$$v_x = \frac{1}{2\sin\kappa}\left(v_2 - v_1\right). \tag{2.3}$$

If there are only two beams, then:

$$v_y = \frac{-1}{2\cos\kappa}\left(v_1 + v_2\right). \tag{2.4}$$

While, in the case of a three beam instrument,

$$v_y = \frac{-\cos\kappa}{1 + 2\cos^2\kappa}\left(v_1 + v_2\right) - \frac{v_3}{1 + 2\cos^2\kappa}. \tag{2.5}$$

Although Equation 2.4 is also valid for three beam H-ADCPs, RD Instruments does the above calculation, using the redundant data from beam 3 to improve the estimate of across-stream velocity.

If the instruments are installed with zero pitch and roll and facing perpendicular to the main flow, then v_x is simply the along-stream velocity while v_y is the across-stream velocity. However, if the pitch and/or roll are non-negligible, then a correction for these terms must be included in order to calculate the along-stream and across-stream velocities. The rotation matrix that must be applied to convert from instrument co-ordinates to the so-called ship or Earth coordinates can be found on page 18 of the ADCP Coordinate Transformation Manuel (*RD Instruments*, 2007). A non-negligible pitch and roll is undesirable since the accuracy of our velocity estimates relies on the flow being uniform over the distance separating the three beams. When the H-ADCPs are horizontal, this is a fair assumption if we are far from any obstacles or confluences, however, if there is rotation about the axis of the instrument (roll), then the beams measure the velocity at different heights above the bottom.

2.2 Echo Intensity Measurements

2.2.1 Sound waves and their propagation

A sound wave is a density disturbance that travels through a medium. If the medium is homogeneous, then the wave travels at a constant speed, c. For a sound wave emitted from a spherical source having pressure p_* at distance r_*, the complex pressure, p, and particle velocity, u, at

distance r and time t are (*Clay and Medwin*, 1977, p.81)

$$p(r,t) = \frac{p_* r_*}{r} e^{i(\omega t - kr)} \tag{2.6}$$

and

$$u(r,t) = \frac{p_* r_*}{r\rho c}\left(1 + \frac{1}{ikr}\right) e^{i(\omega t - kr)} \tag{2.7}$$

where ρ is the density of the medium. The average power passing through a unit area, which is equivalent to the average intensity of the wave, is equal to the real part of the time average of pu^* where u^* is the complex conjugate of u. Therefore, the intensity, I, is

$$I = \frac{{p_*}^2 {r_*}^2}{r^2 \rho c} = \frac{|p|^2}{\rho c}, \tag{2.8}$$

so we see that the intensity of an acoustic wave is proportional to the square of the pressure amplitude.

2.2.2 Sound scattering

The sound scattering and attenuation from a suspension of particles depend not only on their concentration, but also on a combination of the incident frequency and the size of the scatterers. Therefore, the scattering and attenuation parameters are often expressed as functions of the non-dimensional wave number, $x = ka$ where $k = 2\pi/\lambda$ is the wave number, λ is the wavelength and a is the particle radius. Depending on the value of x, different physical processes result in the scattering (re-direction), or attenuation (decrease in amplitude) of the incident sound. For the operating frequencies of the horizontal ADCPs and the grain encountered in this study which are predominantly silts with some fine sands from time to time, the value of ka is always below 1. For example, for a particle with a 100 μm radius (sand), a frequency of 1228.8 kHz and a sound speed of 1500 m/s, the ka value is 0.51. Sand-sized particles are rarely observed in suspension at our study sites; a more typical radius would be 10 μm, which yields a ka value of 0.05. When the non-dimensional wavenumber is much less than one, we say that we are in the long wavelength, or Rayleigh frequency regime. The geometric regime refers to $ka > 1$. In the following sections we shall present the theory as it applies to the full range of ka values.

The development of the theory of sound scattering from suspensions of particles began with the work of *Lord (J. W. Strutt) Rayleigh* (1945). Lord Rayleigh presented the theory for acoustic

scattering from a single fluid sphere, treating it as an elastic movable target in an inviscid, non-heat conducting fluid. *Faran* (1951) later extended this theory to describe scattering from a solid elastic sphere, taking into account both the shear and compressional waves that can exist within a solid body.

Since the mid-1900s, research - primarily in the field of oceanography - has progressed to the point where we now have a good theoretical and experimental understanding of how sound scatters from suspensions of both spherical particles and natural sediments. The majority of this work has focused on scattering from sand-size particles and has been primarily conducted by Hay, Schaafsma and Thorne and their respective collaborators. The data published on sound scattering and attenuation from suspensions of sand-sized particles cover the non-dimensional wavenumber range x = 0.2 - 50 (see review paper by *Thorne and Meral* (2008)). As previously mentioned, the ka values encountered in the present study are at and below the lower range of these measurements. Although sand-sized particles of are primary interest in most oceanographic applications, silts are the primary particles in suspension in medium-sized rivers such as those studied throughout this thesis. The manner in which sound scatters from finer sediments is currently being explored by other researchers (*B. Moate and P.D. Thorne, Personal Communication, June 2011*). In terms of the attenuation of sound by fine sediments, the early theoretical and experimental work of *Urick* (1948) provides the background for this study.

2.2.3 Scattering from a single spherical particle

The presentation of equations which follows is based primarily on the formulations of *Sheng and Hay* (1988). To begin with, we consider the simple case of a plane wave incident on a homogeneous particle of radius a surrounded by water. The scattered pressure, p_s, at a distance r from the particle can be expressed as

$$p_s = p_i \frac{f_\infty a}{2r} \exp\left[-\alpha_w r\right] \exp\left[i\left(kr - \omega t\right)\right] \tag{2.9}$$

where p_i is the incident pressure amplitude, f_∞ is the far field form function which describes the scattering properties of the particle, α_w is the attenuation by the water in m^{-1}, ω is the angular frequency and t is time. Using Equation 2.6 and accounting for (a) the directivity pattern of the transducer, D, and (b) the near field correction function, ψ, the amplitude of the incident pressure wave at a distance r from the source is generally expressed as:

$$p_i = \frac{p_* r_*}{\psi r} D \exp\left[-\alpha_w r\right]. \tag{2.10}$$

The near field correction accounts for the complicated range dependence of the pressure at distances close to the transducer, it is equal to one in the far field of the transducer. For a transducer of radius a_t and wavelength λ, the distance to the far field is defined to be $r_n = 2\pi {a_t}^2/\lambda$. The directivity accounts for the angular dependence of the radiated power of a transmit transducer or the sensitivity of a receive transducer, as applicable. For the monostatic piston transducers used in this study, the directivity is the same on emission as on reception. The directivity of a circular piston transducer of radius a_t depends on the angle β between the scatterer and the axis of the transducer (see Figure 2.3 for geometry) as (*Clay and Medwin*, 1977, p.454):

$$D = \frac{2J_1(ka_t \sin\beta)}{ka_t \sin\beta} \tag{2.11}$$

where J_1 is the first-order cylindrical Bessel function. A clear and succinct introduction to transducers and their directionality can be found in Section 5.2 and Appendix A5 of *Clay and Medwin* (1977). An example of the radiation pattern of the transducers used in this study shall be presented in Chapter 3. The directivity on transmission is also referred to as the radiation pattern, while the directivity on reception is often called the directional response.

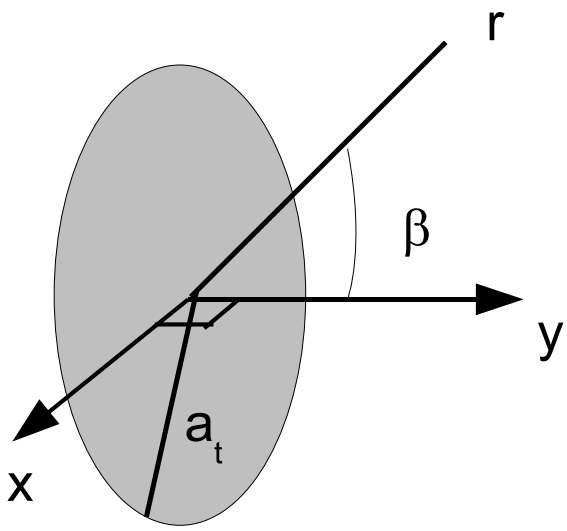

Figure 2.3: The coordinate system of the transducers. The x axis is parallel to the transducer face and the y axis is normal.

Combining equations 2.9 and 2.10, the amplitude of the pressure that is detected by the transducer, p_d, for backscattering from a spherical particle can be written as

$$p_d = \frac{p_* r_* f_\infty a}{2\psi r^2} D^2 \exp[-2\alpha_w r] \tag{2.12}$$

where we have accounted for the transducer's directivity upon reception and the attenuation loss of the scattered wave.

2.2.4 Scattering from a suspension of spherical particles

When sound is scattered from a suspension of spheres in turbulent motion, the phases of the scattered waves are random and uniformly distributed over 2π. This means that the phases of the scattered waves add incoherently and the ensemble mean-square pressure for scattering from a large number of particles, $\langle {p_s}^2 \rangle$, is the sum of the wavelets scattered from each particle (*Morse and Ingard*, 1968, p. 438). When concentrations are sufficiently low that there is no multiple scattering, the ensemble mean-square pressure depends linearly on the number of particle per unit volume N (e.g. *Hay*, 1991). Multiple scattering refers to the process whereby the wave scattered by one particle influences the wave that is incident on another particle. It occurs when concentrations exceed 1% by volume (*Ma et al.*, 1984), which is equivalent to 26.5 kg/m^3 for quartz particles in water. Since the concentrations encountered at our study sites never exceeded 10 kg/m^3, multiple scattering is not an issue.

When the particles in suspension have more than one grain size, we must average over the contributions from all particles of all sizes. The ensemble average for a suspension of particles with a probability number size distribution $n(a)$ is the integral over the size distribution times the parameter of interest: $\int_0^\infty \cdot\, n(a)da$. In the remainder of this thesis, it is expressed as $< \cdot >$. In the far-field of the transducers, the ensemble mean-square pressure for scattering from a suspension of particles with a size spectral density $n(a)$ can be expressed as

$$\begin{aligned} \langle {p_s}^2 \rangle &= \int_V N \left[\int_0^\infty p_s {p_s}^* n(a) da \right] dV \\ &= \frac{{p_*}^2 {r_*}^2}{4} \int_V N \left[\frac{D^4}{r^2} \exp[-4\alpha r] \int_0^\infty |f_\infty|^2 a^2 n(a) da \right] dV, \end{aligned} \tag{2.13}$$

where ${p_s}^*$ is the complex conjugate of p_s, dV is the detected volume and $\alpha = \alpha_w + \alpha_s$ is the sum of the attenuation due to water and that due to the suspended sediment. Since the mass concentration of particles, M, can be measured more easily than the number concentration of particles, it is substituted for N, in Equation 2.13 using the relationship

$$M = N\rho_s \frac{4}{3}\pi \int_0^\infty a^3 n(a) da, \tag{2.14}$$

where ρ_s is the particle density. Equation 2.13 then becomes

$$\langle {p_s}^2 \rangle = \frac{3M{p_*}^2{r_*}^2}{16\pi\rho_s} \frac{\int_0^\infty |f_\infty|^2 a^2 n(a) da}{\int_0^\infty a^3 n(a) da} \int_V \frac{D^4}{r^2} \exp[-4\alpha r]\, dV \tag{2.15}$$

for a narrow beamwidth transducer (*Sheng and Hay*, 1988).

2.2.5 *The form function*

The reflection form function, f_r, is a dimensionless parameter which describes the scattering properties of a particle. It was originally introduced by *Neubauer et al.* (1974) in order to describe the relationship between the incident and scattered pressure for acoustic scattering from elastic spheres. At distances much greater than the radius of the sphere, the reflection form function is equivalent to the far field form function, f_∞, which is a simplified version of f_r. It is defined as

$$|f_\infty| = \frac{2r}{a}\frac{|p_s|}{|p_i|}, \tag{2.16}$$

or equivalently,

$$\sigma_s = \frac{|f_\infty|^2 a^2}{4} \tag{2.17}$$

where σ_s is the differential scattering cross-section. This is a measure of the power that is scattered into the solid angle $d\Omega$ at a given angle, θ_s relative to the incident intensity.

Although the nomenclature of the form function was first introduced by *Neubauer et al.* (1974), the theory for sound scattering from solid spheres was primarily developed by *Faran* (1951), *Hickling* (1962) and *Hay and Mercer* (1985). Since then, a number of experiments have been performed on sound scattering from suspensions of glass beads and natural sand particles in order to compare experimental results with the theory for suspensions of spherical particles. *Thorne and Hanes* (2002) and *Thorne and Meral* (2008) provide comprehensive reviews of these studies. In *Thorne and Meral* (2008), a general expression is provided for the far field form function of suspensions of sand-sized particles based on data that covered the range $x = ka = 0.2 - 30$. Their expression, which is given below, predicts something close to the theoretical scattering by

a suspension of spheres in both the Rayleigh and geometric regimes:

$$f_\infty = \frac{x^2\left(1 - 0.35\exp^{-((x-1.5)/0.7)^2}\right)\left(1 + 0.5\exp^{-((x-1.8)/2.2)^2}\right)}{1 + 0.9x^2}. \tag{2.18}$$

The expression for the backscatter form function in the Rayleigh regime is given by *Clay and Medwin* (1977) as

$$f_\infty = 2x^2\left[\frac{e-1}{3e} + \frac{g-1}{2g+1}\right] \tag{2.19}$$

where $e = E_1/E_0$ is the ratio of the elasticity of the scatterers to the elasticity of the medium and g is the ratio of the density of the scatterers to the density of the medium. For quartz spheres suspended in water, $e = 39$ and $g = 2.65$, yielding $f_\infty = 1.17x^2$. In comparison, Equation 2.18 gives $f_\infty = 1.25x^2$ when $x << 1$.

In the geometric regime, as the name suggests, the scattering is dependent on the shape of the particle. In this regime, the total power that is scattered by a sphere is equal to twice its cross-sectional area, $2\pi a^2$, the backscattering cross section, $\sigma_s(180°)$, is equal to $a^2/4$ and f_∞ is therefore equal to 1. Since it has been found that the scattering from a suspension of natural sand grains is enhanced compared to scattering from a suspension of spheres (e.g. *Hay*, 1991), Equation 2.18 tends to 1.1 when $x >> 1$.

2.2.6 Attenuation

In underwater acoustics, the term attenuation is used to describe the portion of the reduction in amplitude of the acoustic waves that is not dependent on geometrical spreading (*Clay and Medwin*, 1977, p. 78 - 79). When a sound wave travels through a fluid medium such as fresh water, the amplitude of the signal decreases due to viscous losses as the acoustic energy is transformed into heat. The expression for the attenuation due to freshwater that will be employed in the following analysis is:

$$\alpha_w = \left(55.9 - 2.37T + 4.77\times10^{-2}T^2 - 3.48\times10^{-4}T^3\right)10^{-15}f^2\,[\mathrm{m}^{-1}] \tag{2.20}$$

where T is the water temperature in degrees Celsius and f is the frequency in Hz (*Fisher and Simmons*, 1977). The pressure term proposed by *Fisher and Simmons* (1977) has been neglected in Equation 2.20 since it is negligible in our measurements, where the maximum measurement

depth is 5 m. As an example, α_w is 0.0035 m^{-1} at 10°C and 307.2 kHz, which is the frequency of an RD Instruments 300 kHz H-ADCP.

When particles are present in the water, there is additional attenuation due to their presence. This sediment attenuation, α_s, can be the result of two different phenomena, but in both cases it is linearly proportional to the mass concentration of suspended sediment and must be averaged over the number size distribution of the particles. The total sediment attenuation can be written as

$$\alpha_s = \alpha_{s,\,\text{visc}} + \alpha_{s,\,\text{scat}} = M\left\langle \zeta_v \right\rangle + M\left\langle \zeta_s \right\rangle \tag{2.21}$$

where $\alpha_{s,\,\text{visc}}$ and $\alpha_{s,\,\text{scat}}$ are the viscous and scattering attenuation, respectively, angular brackets continue to represent an average over the number size distribution and ζ_v and ζ_s are what we refer to as the viscous and scattering attenuation constants.

If the particles are small, there is viscous absorption in the boundary layer surrounding the particles. If the particles are larger, the incident wave is scattered from the particles which also results in loss, this is known as scattering attenuation. The scattering attenuation, $\alpha_{s,\,\text{scat}}$, can be written as

$$\alpha_{s,\,\text{scat}} = \frac{3M\left\langle a^2\chi \right\rangle}{4\rho_s\left\langle a^3 \right\rangle} = M\left\langle \zeta_s \right\rangle \tag{2.22}$$

where the expression that we use for χ is taken from *Thorne and Meral* (2008):

$$\chi = \frac{0.29x^4}{0.95 + 1.28x^2 + 0.25x^4}\,. \tag{2.23}$$

The above expression was established using measurements made with suspensions of sand at MHz frequencies.

The attenuation due to viscous absorption for a suspension of particles with a range of sizes is (*Hay*, 1983)

$$\alpha_{s,\,\text{visc}} = M\langle \zeta_v \rangle. \tag{2.24}$$

The viscous attenuation constant is based on the theory of *Urick* (1948), from which we get :

$$\zeta_v = \frac{k\,(g-1)^2}{2\rho_s}\left[\frac{s}{s^2+(g+\delta)^2}\right] \tag{2.25}$$
$$s = \frac{9}{4ba}\left[1+\frac{1}{ba}\right]$$
$$g = \frac{\rho_s}{\rho}, \quad \delta = \frac{1}{2}\left[1+\frac{9}{2ba}\right], \quad b = \sqrt{\frac{\omega}{2\nu}},$$

ρ is the density of the fluid (water), ρ_s is the density of the sediment, ν is the kinematic viscosity of water, which is 1.2×10^{-6} m^2/s at 14°C (*Clay and Medwin*, 1977) and ω is the angular frequency.

Viscous absorption is the dominant source of attenuation at and below megahertz frequencies for small particles, but for sand sized particles the scattering attenuation dominates. To demonstrate this, Figure 2.4 is a plot of the attenuation due to both scattering and viscous absorption as a function of grain size for the three operating frequencies of the H-ADCPs used in this study. This plot was inspired by Figure 1b of *Ha et al.* (2011). It can be seen from Figure 2.4 that the attenuation due to viscous absorption (solid curves) dominates the sediment attenuation constant when particle radii are less than ∼50 μm for the 1200 kHz instrument, ∼90 μm for the 600 kHz instrument, and ∼160 μm for the 300 kHz instrument.

While instructive, Figure 2.4 is too simplistic, since natural sediments are not a unique size, but have a distribution of sizes. Consequently, in order to determine the theoretical attenuation for a suspension of particles we must average over the grain size distribution. The size frequency distributions of natural sediments are commonly interpreted as lognormal (e.g. *Middleton*, 1970). The probability density function of a variable X with a lognormal distribution is defined as

$$\text{pdf}(X) = \frac{1}{X\sigma_X\sqrt{2\pi}}\,\exp\left[-\frac{(\ln X-\mu_X)^2}{2{\sigma_X}^2}\right] \tag{2.26}$$

where the median value of X, X_{50}, is $\exp^{\mu_X}$ and the parameter σ_X controls the shape of the distribution. *Sengupta* (1979) found that suspended sediment tended towards a lognormal grain size distribution for a particular combination of bed material, flow velocity and height above the bed. He found that the higher the flow velocity, the more likely the particles were to have a lognormal distribution. In our observations of grain size which will be presented in Section 3.1.3 of Chapter 3, we found that the volume size distributions that we observed were reasonably well modelled by a lognormal distribution with $\mu_X = \ln d_{50}$ and $\sigma_X = 1$, when plotted with diameter.

As such, we compute the theoretical attenuation as a function of a_{50} smoothing over the number size distribution $n(a)$ that corresponds to a lognormal volume size distribution with $\mu_X = \ln a_{50}$ and σ_X = 1. The resulting theoretical attenuation constants are shown in Figure 2.5. The validity of these theoretical values rests on the assumption that the volume size distributions of the grains continue to be lognormal across a range of grain sizes from 0.01 μm to 1 mm.

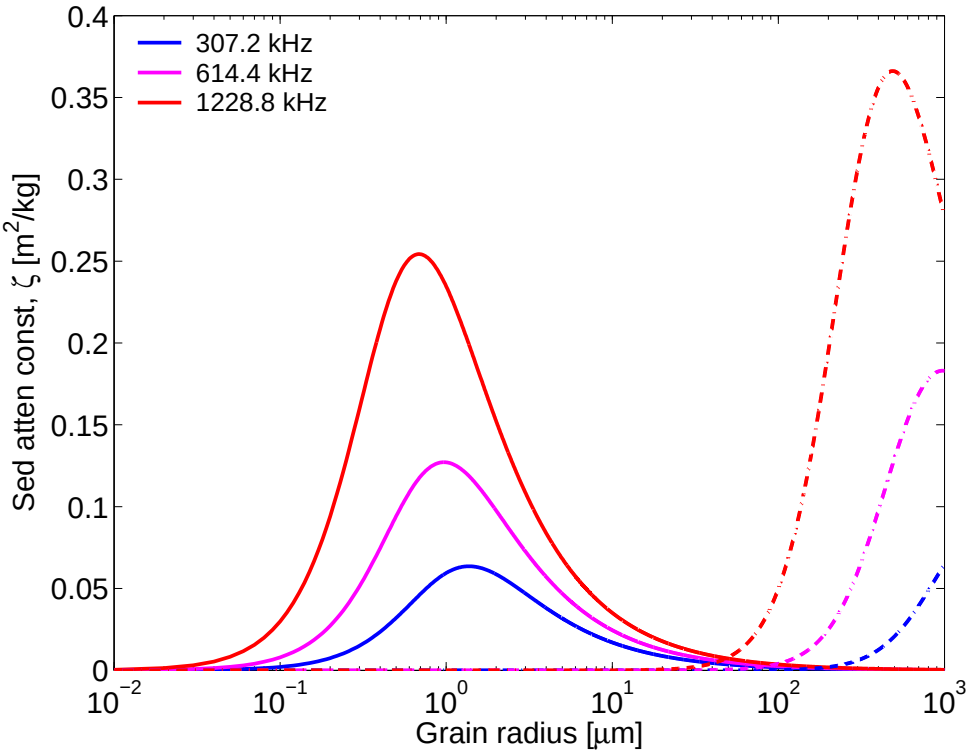

Figure 2.4: The attenuation coefficient due to viscous absorption (solid curves) and scattering (dashed-dotted curves) as a function of particle radius for sound waves having the operating frequencies of the H-ADCPs.

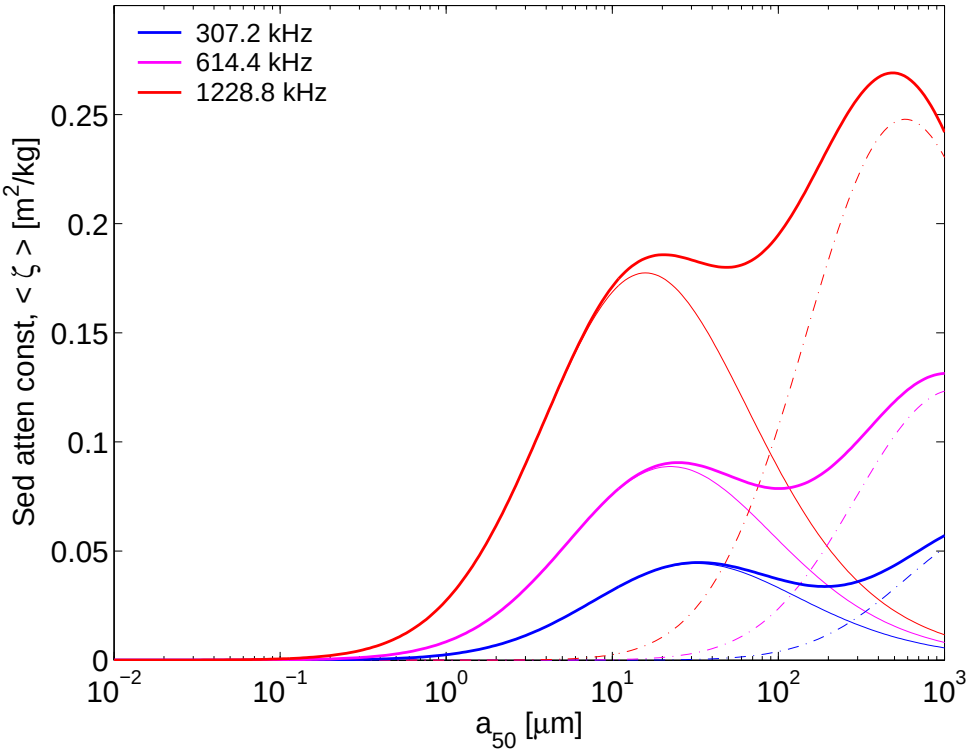

Figure 2.5: The attenuation coefficient due to viscous absorption (thin solid curves) and scattering (dashed-dotted curves) calculated for lognormal volume size distributions with $\mu_X = \ln a_{50}$ and $\sigma_X = 1$ as a function of median radius, a_{50} for the operating frequencies of the H-ADCPs. The thick solid lines are the total attenuation constant.

It can be seen that incorporating size distributions into the calculation of the sediment attenuation constants flattens both the viscous absorption and scattering peaks compared to the single size case (notice the different y scales). It also shifts the peaks in the viscous absorption constants to much higher grain sizes and there is overlap of the two processes for a given a_{50}.

2.3 Principles of laser grain sizing

The method of grain size analysis used in this study was the low-angle laser light scattering technique. The decision to use this sizing method was primarily motivated by instrument availability, however, it is also one of the few sizing methods capable of precisely measuring micron and sub-micron particles. Although the suspended particulate matter of the Isère, Saône and lower Rhône can contain sand-sized particles during floods (*Bravard* (1987) for upper-Rhône, *Astrade* (2005) for Saône, *O. Radakovitch, personal comm., May 2011* for lower-Rhône), the suspended matter tends to be primarily composed of silts (> 2 μm) with some clays.

When light is scattered from a suspension of particles, the diffraction pattern that is created depends on the size of the scatterers. If particle concentrations are sufficiently low that multiple scattering does not occur, i.e., the scattered light from one particle does not influence the incident light on any other particles, then the scattering pattern from a suspension of particles is equal to the sum of their individual scattering patterns. Laser grain sizers calculate the size distribution of the illuminated particles by matching the diffraction pattern that is measured to the diffraction pattern that would be created by a certain size distribution of particles.

The laser grain sizer used in this work was a Mastersizer 2000 manufactured by Malvern instruments. This instrument has the advantage that either one of two optical models can be applied in the interpretation of the scattering pattern: either Fraunhofer or Mie (*Malvern*, 2005). Historically, Fraunhofer theory was preferred due to the restrictive computation time of the full Mie theory, but at present computation time is no longer a deciding factor and one must carefully weigh one's choice of model based on the available knowledge of particle size and composition. The basis of the two theories and the assumptions made in their application are outlined below.

The Fraunhofer method is distinctive in its simplicity, as it does not require any knowledge of the optical properties of the particles. However, it does require that the particles be spherical and that they be much larger than the wavelength of the incident light. If this is the case, then the extent to which the particle attenuates light through scattering and absorption (its extinction efficiency), is equal to twice its geometrical cross-section. According to the ISO standard for particle size analysis by laser diffraction methods (NF ISO 13320-1, 2000), the Fraunhofer method can be used when the particle diameter is at least 40 times the wavelength of the incident light. The wavelength of the He-Ne laser used by the Malvern Mastersizer 2000 is 632 nm. This implies that the Fraunhofer model should be suitable when particles exceed 26 μm in diameter. If the particles are opaque compared to the solution in which they are suspended, the Fraunhofer theory can be used without error for particles smaller than this limit; if however, the sample contains small, optically transparent particles, use of the Fraunhofer model may predict a substantially larger amount of small particles than what is actually present (NF ISO 13320-1). Mie theory, on the other hand, is suitable for all sizes of particles. However, the assumptions of particle sphericity and homogeneity still apply and the complex refractive index of the particles is required as input for the model. Any error in the assumption of this value will introduce error into the measured grain size distributions.

The refractive index of a medium is a measure of the speed of light in that medium. The real

refractive index, n, quantifies the ratio of the phase speed *in vacuo*, c_0, to that in the medium, c, as (e.g. *Morel and Bricaud*, 1986):

$$n = c_0/c. \tag{2.27}$$

The imaginary part of the refractive index, n', quantifies the absorption, or reduction of intensity of the incident light by the medium. Since it is the difference in refractive index from one medium to another which induces scattering and/or absorption, the parameter of interest is the relative refractive index of the particles to that of the medium. The relative refractive index, m, of a particle in water is expressed as:

$$m = \frac{n_p - i\, n'_p}{n_m} \tag{2.28}$$

where the subscripts p and m refer to particle and medium, respectively, and in water n_m equals 1.33 and n'_m = 0. Typically the refractive index of natural sediments is taken to be that of quartz, with n_p =1.544, and $n'_p = 0.008$ (*Campbell*, 2003). The relative refractive index of the quartz is therefore 1.16, since the imaginary part of the refractive index is negligible compared to the real part.

While the optical properties of quartz are well understood, water samples collected in rivers often contain some organic particles. There were problems with algae colonising the area around the suction tube of the automatic sampler at the Romans-sur-Isère study site, especially during periods of low flow. As such, most samples collected with the automatic sampler during quiescent periods contained some algae. Samples collected by hand during the summer months also contained algae, likely because the samples were collected near the wall of the right bank, which tends to be colonised by algae. On the Saône river, algae was even observed in samples that were collected during periods of high flow.

We do not have a measure of the proportions of organic to inorganic material in our samples, nor do we know the origins of the algae, but we can assume that they were freshwater cyanobacteria. According to a study by *Morel and Bricaud* (1986), the relative refractive index of algal cells ranges from 1.02 to 1.08 and, due to the high water content of algal material, the relative refractive index of algal strands is closer to 1.0 than the value for the individual cells. If the samples are not treated prior to grain size analysis to kill the organic particles, as was the case in our study, then there is ambiguity in the value of the relative refractive index. The ISO guidelines

suggest using the Fraunhofer method for all particles greater than 50 μm, no matter their refractive index, and for medium sized particles (1 μm - 50 μm) with $n_p/n_m > 1.1$. The majority of particles encountered in this study fall within the latter size range. Although the relative proportion of organic to inorganic material in each sample was unknown, we expect that n_p/n_m likely exceeded 1.1. Thus, we applied the Fraunhofer method to all samples, keeping in mind that the fraction of finer particles may be overestimated as a result.

The laser grain sizer provides a measure of the projected area of the particles. By making the assumption of particle sphericity and homogeneity, the laser grain sizer outputs the size distributions as volume size distributions, giving the fraction of the total volume of particles occupied by particles of each size class. We refer to the fraction of particles in size class i as volFrac$_i$. Since the scattering power of particles that are much larger than the wavelength of incident light is proportional to two times their geometric cross section, the representation in terms of volume is logical (*Wedd*, 2003). Nevertheless, number size distributions are required for the acoustic calculations. For a given size class, i, the volume fraction is converted to number fraction, numFrac$_i$, as follows:

$$\text{numFrac}_i = \frac{\text{volFrac}_i/\text{vol}_i}{\sum_i (\text{volFrac}_i/\text{vol}_i)} \tag{2.29}$$

where vol$_i$ is the volume of a spherical particle with radius a_i: $4\pi {a_i}^3/3$. In Figure 2.6, grain size distributions are represented as both volume and number fractions in order to highlight the differences in these two representations of the data. This is an interesting exercise as it demonstrates how a few large particles can completely skew the volume size distributions.

In order to explore the difference between the application of the two optical theories, roughly 10% of the samples were processed using both Fraunhofer and Mie theory. The default settings for glass beads (a real refractive index of 1.52 and an imaginary refractive index of zero) were used for the optical parameters, since they are very close to the properties of quartz. The volume size distributions obtained using the two theories for three different samples are shown in Figure 2.6(a). The Fraunhofer results are shown as circles, and the Mie results are shown as triangles. It can be seen that the Fraunhofer theory predicts a significant amount of particles with a diameter less than 2 μm, while the Mie theory does not. In the conversion from volume size distributions to number size distributions, this leads to differences between the results of the two methods that are much larger than the observed variability between samples.

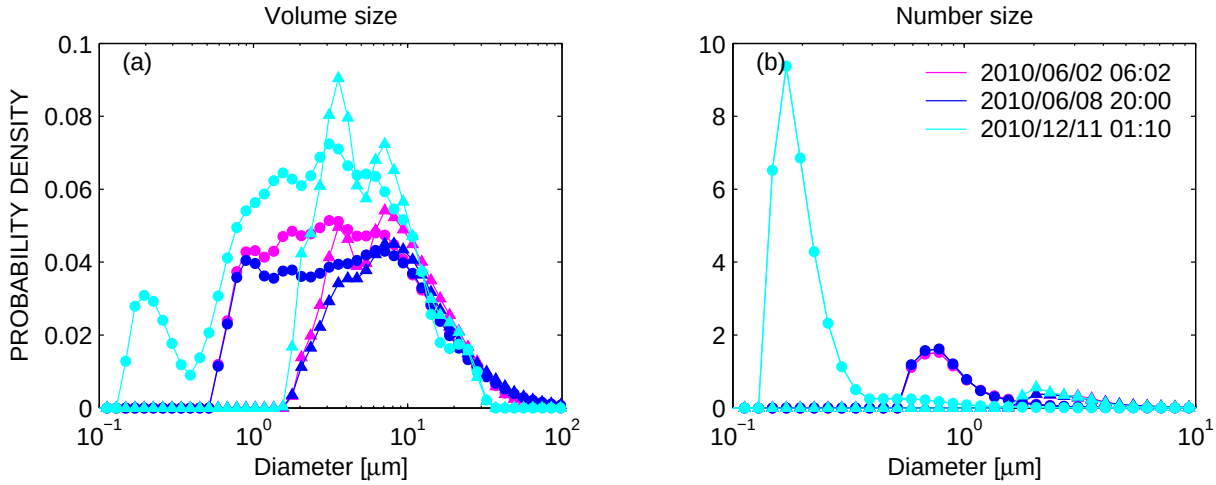

Figure 2.6: Grain size distributions measured using the low-angle laser light scattering technique for water samples collected at Romans-sur-Isère interpreted using either Fraunhofer (circles) or Mie (triangles) theory.

Few studies have been done investigating the accuracy of laser sizing of natural sediments, but it appears that the method may overestimate the amount of larger particles due to the non-sphericity of natural sediments (*Campbell*, 2003). The work of *Xu and Di Guida* (2003) showed that as the shape of the particles was less and less spherical, measurements with a laser diffraction system yielded progressively larger mean sizes and broader distributions compared to results from electrical sensing zone and dynamic image analysis.

CHAPTER 3

STUDY SITES AND INSTRUMENTATION

In the following chapter we provide pertinent information on the various study sites from which data will be presented in this thesis, including details of the instrumentation, the hydrological conditions and the concentration and grain sizes of the suspended sediment, when available. The three rivers which are studied in this thesis, the Saône, the Rhône and the Isère, are indicated on the map of France presented in Figure 3.1. A depiction of the Rhône river catchment is shown in Figure 3.2, with the study sites listed. The four study sites are Saint-Georges (Saône), Romans-sur-Isère (Isère), Montélimar (Rhône canal) and Tricastin (Rhône canal). The Saint-Georges study site, which is located in Lyon on the right bank of the Saône river, is 2 km upstream of the confluence with the Rhône river. The Romans-sur-Isère study site is 20 km upstream of the confluence of the Isère and Rhône rivers. The Montélimar and Tricastin study sites are on different parts of the Rhône canal. The Isère and Rhône rivers are used for hydroelectric production and therefore have dams which regulate their discharge and flow rates. The Saône and Rhône rivers are used for navigation, meaning that there are navigation canals on certain parts of the rivers.

Since Romans-sur-Isère was the primary site of investigation of this thesis, the details of this site shall be presented first and then the other sites shall be compared and contrasted with it. There are a number of reasons for which Romans-sur-Isère was our main study site. To begin with, the ranges of concentration and velocity observed at this site are much larger than what is observed at the other sites. As an example, between November 2009 and July 2010 the cross-sectional averaged velocity at Romans-sur-Isère ranged from 0.25 m/s to 3.5 m/s and the concentration ranged from 5 mg/L to 8.5 g/L. In contrast, the cross-sectional averaged velocity at Saint-Georges ranges from $\sim$ 0.1 m/s to 2.3 m/s (*Le Coz et al.*, 2008) and the concentration

of suspended sediment ranges from 5 mg/L to 150 mg/L during floods. The maximum concentration observed at Saint-Georges is an order of magnitude less than the values that have been observed at Romans.

Figure 3.1: Map of France indicating the three rivers that are studied in this thesis.

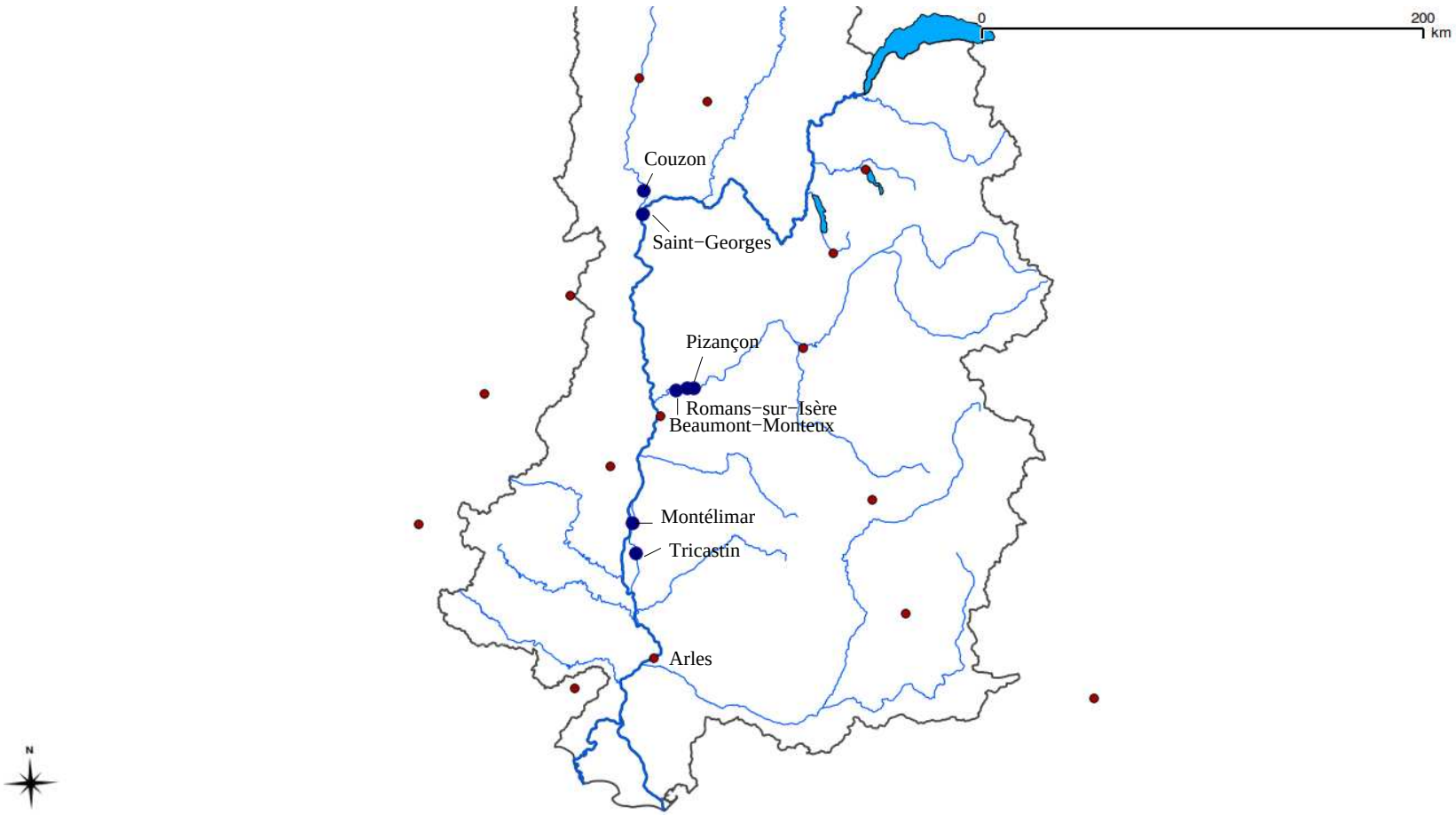

Figure 3.2: Map of the Rhône drainage basin. The sites used in this thesis are labeled. The red dots mark cities and the lake in the top right corner is Lake Léman.

The Montélimar study site is on a canal of the Rhône river, 12 km downstream of the diffluence between the Rhône canal and the old Rhône, and 500 m upstream of the Châteauneuf dam. Due to the H-ADCP's proximity to the dam and the diversion of water the old Rhône at the upstream diffluence, the flow speeds at Montélimar are fairly low, even during floods: the maximum section-averaged velocity observed in 2010 was 1.2 m/s, as opposed to 3.5 m/s at Romans. The concentrations are also less than at Romans-sur-Isère. This is because the Rhône river is less concentrated than the Isère river and their confluence 60 km upstream of Montélimar dilutes the water. Based on acoustic attenuation data from the H-ADCP at Montélimar (cf. Section 6.2.3), the maximum concentration observed in 2010 was 1 g/L. The range of velocity values observed at Tricastin was also less than at Romans-sur-Isère and the concentration did not exceed 2 g/L during floods. Daily concentration data collected on the Rhône at Arles ($\sim$ 90 km downstream of Tricastin) confirm that the Rhône is less concentrated than the Isère.

The second reason for which Romans-sur-Isère was the primary focus of this thesis is related to the difficulties that were faced making accurate measurements of velocity across the entire profile. These problems shall be detailed in Chapter 5, but essentially the Compagnie Nationale du Rhône (CNR) purchased and installed two 300 kHz H-ADCPs in the hopes of profiling across the whole width of the river. The aspect ratio limitation of a 300 kHz Workhorse H-ADCP is 19:1, range to total depth (*Teledyne RD Instruments*, 2007). This means that at Romans-sur-Isère, where the depth is 4 m, these instruments should provide accurate measurements of velocity up to 76 m from the instrument. Instead, the instruments underestimated velocities at distances much closer to the instrument than what was expected. It was hypothesized that this was due to the difficulty with properly positioning the instruments in such a shallow site. Thus, in order to have a better understanding of the possibilities and limitations of using side-looking ADCPs to make discharge measurements at shallow sites, RD Instruments Europe lent CNR a 600 kHz Workhorse H-ADCP prototype and a 1200 kHz ChannelMaster H-ADCP. In addition, this thesis was launched around the same time. Since few side-looking ADCPs had been employed in rivers prior to this study, we decided to use Romans-sur-Isère as a worst-case scenario to explore the conditions under which measurements are accurate, and the conditions under which they are not. An additional and major reason to focus on this site is that the quasi simultaneous measurements at three frequencies provide data that can be used to determine the grain size of the sediment in suspension. For all of these reasons, Romans-sur-Isère became our principle study site.

3.1 Romans-sur-Isère

3.1.1 Instrumentation

Acoustic Instruments

The study site is equipped with three RD Instruments H-ADCPs which operate at 307.2 kHz, 614.4 kHz and 1228.8 kHz, they shall be referred to as the 300 kHz, 600 kHz, and 1200 kHz instruments in the remainder of the thesis. The 300 kHz instrument is a Workhorse model, the 600 kHz instrument is a Workhorse prototype and the 1200 kHz instrument is a Channel Master model. The depth, pitch and roll of each instrument are listed in Table 3.1 and depicted in Figure 3.3 (NB. Only the pitch can be discerned from the figure). An image of the right bank of the study site is provided in Figure 3.4. For instruments installed on the right bank, beam 1 faces downstream, beam 2, upstream, and beam 3 across stream (see Figure 2.1).

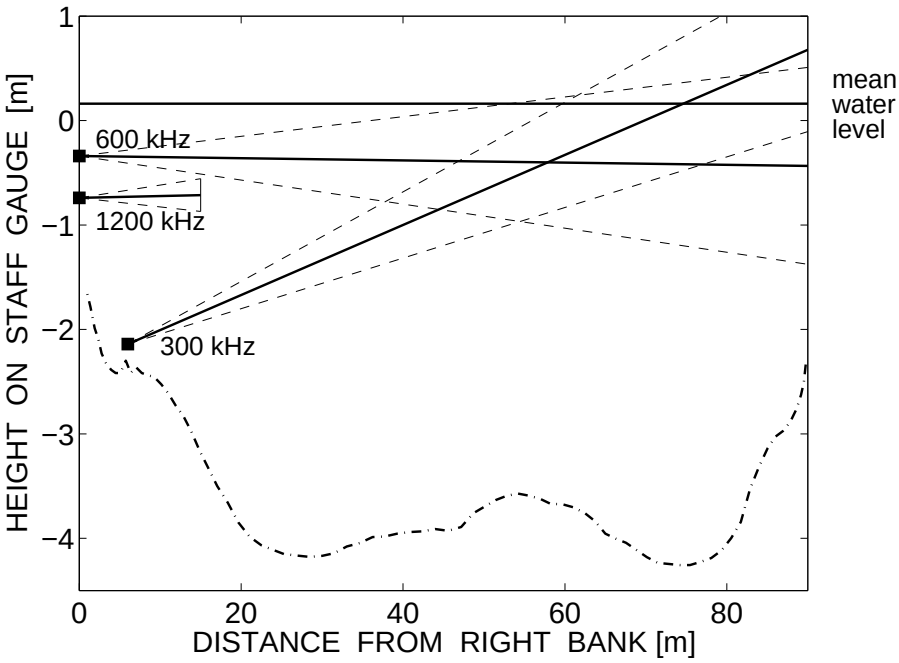

Figure 3.3: Upstream view of the Romans-sur-Isère study site. The solid horizontal line at 0.16 m indicates the mean water level and the dashed-dotted line is the river bathymetry. The horizontal ADCPs are indicated as squares. The solid lines represent the projections of the “central” beam of each instrument and dashed lines represent their beam widths (-3dB level of the transmitted power).

Table 3.1: A summary of the positioning and specifications of the horizontal ADCPs at Romans-sur-Isère. Depth is given with respect to the zero on the staff gauge, positive pitch indicates upward inclination, positive roll means the downstream beam faces the surface and the upstream beam faces the bottom. The beam width (β_0) and nominal maximum profiling range are based on information provided by the manufacturer. Beam width corresponds to the full width half maximum of the transmitted power (-3dB level of the directivity squared). The distance to the far field of each instrument, r_n is also listed.

Instrument	depth (m)	pitch (°)	roll (°)	max range (m)	β_0 (°)	r_n (m)
300 kHz	-2.16	1.8	0.1	250	1	12.8
600 kHz	-0.36	-0.1	-0.4	85	1.2	4.5
1200 kHz	-0.76	0.1	-0.7	15	1.5	2.2

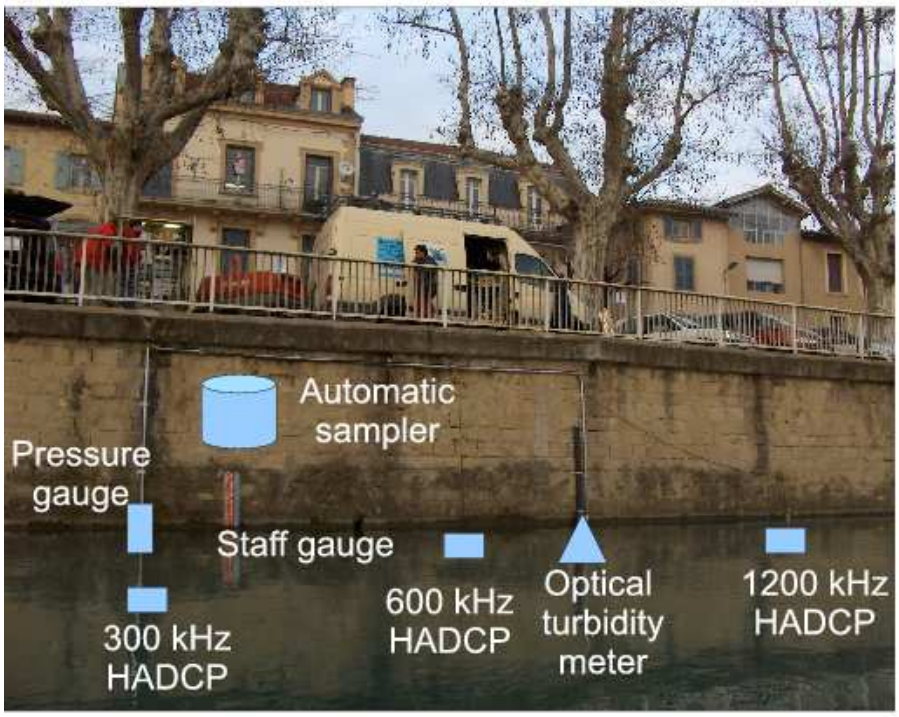

Figure 3.4: The Romans-sur-Isère study site. All instruments are installed along the wall of the right bank except the 300 kHz H-ADCP which is attached to a 6-m long arm. To give an idea of scale, the thick vertical bars of the railing are separated by 2 m.

Each instrument is composed of either two or three monostatic piezoelectric transducers. Images of the three different H-ADCPs are shown in Figure 2.2. The axis of each transducer and the sound that they emit are often referred to as “beams”, in reference to the main beam of their lobed radiation pattern. The term “beam width” is also commonly used, this is the full width at

half maximum of the directivity, D^2, of the transducer in degrees. If both the beam width and the radius of the active area of a circular piston transducer are known, then Equation 2.11 can be used to calculate the directivity of the transducer. The beam widths provided by the manufacturer for the 300, 600, and 1200 kHz instruments at Romans are 1°, 1.2° and 1.5°, respectively. The theoretical directional response of the 300 kHz H-ADCP used at Romans is shown in Figure 3.5 as an example. Directivity is plotted as a function of β, the angle between the axis of the transducer and a field point (recall Figure 2.3).

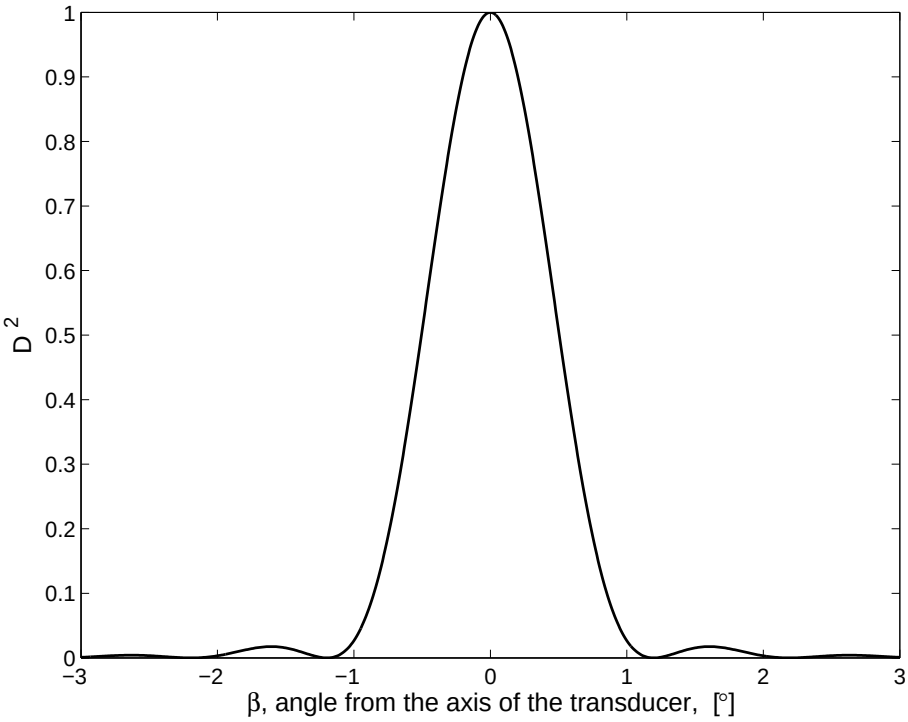

Figure 3.5: The theoretical directional response of the 300 kHz H-ADCP at Romans-sur-Isère. The directivity, D, is calculated for a 307.2 kHz transducer with a 14 cm radius and a beam width of 1° using Equation 2.11.

The 300 kHz and 600 kHz instruments each have three transducers: one points downstream (beam 1), one points upstream (beam 2), and one points across stream (beam 3). For the 600 kHz instrument, all three transducers are in the same plane, separated by 30.2° and the axis of the instrument is the axis of beam 3. For the 300 kHz instrument, beam 3 is parallel to, but slightly raised from the plane of beams 1 and 2 (see Figure 2.2), which are both at an angle of 20° to the instrument axis. The 1200 kHz instrument has two beams: beam 1 faces 20° downstream and beam 2 faces 20° upstream. The horizontal ADCPs are equipped with temperature sensors

in order to calculate the sound celerity. Their sampling rate is typically 2 Hz (*RD Instruments*, 2008).

In order to avoid interference between the various H-ADCPs, they are programmed to ping in turn, with each instrument transmitting 15 pings and then lying dormant until a total of 75 seconds has passed. The profiles of velocity and intensity measured by each transducer are internally averaged and the final result is one profile of intensity and one of velocity for each beam every 75 seconds. The transmit pulse length and size of the range gates that were used corresponded to the manufacturer's recommendations for our specific site. The cell size was 2 m for the 300 kHz H-ADCP, 1 m for the 600 kHz H-ADCP and 0.5 m for the 1200 kHz instrument, and the blank distance was 1.75 m, 1.00 m, and 0.50 m, respectively. All instruments at Romans-sur-Isère were operated in narrow bandwidth mode. In this mode of operation a bandwidth filter of 6.25% of the central frequency of the transducer is applied to the signal on reception (*RD Instruments*, 2008, p. 162).

Turbidity Meter

A SOLITAX sc optical turbidity meter constructed by Hach Lange provides a continuous measure of suspended sediment concentration at Romans-sur-Isère. It is installed at a depth of 0.5 m on the right bank of the river as shown in Figure 3.4. For all data presented in this thesis, the turbidity meter was operated in Total Suspended Solids (TSS) mode. This mode of operation is to be used when particle concentrations are high, although the manufacturer does not specify a concentration. While concentrations at this site are typically on the order of 0.01 kg/m^3 (10 mg/L), the high concentration mode of operation was selected because concentrations may exceed 1 kg/m^3 (1 g/L) during floods. The turbidity meter functions by emitting light with a light-emitting diode and detecting the scattered light with a photoreceptor. In Total Suspended Solids mode it detects the light that is scattered at 140° to the incident direction and the optical turbidity is recorded in units of mg/L TSS (p.9 *Hach Lange*, 2006). Water samples are required in order to relate this unit to mass concentration.

An ISCO 6712 peristaltic pump automatic sampler is also installed along the right river bank (see Figure 3.4). The water intake of the sampler is at the same depth as the optical sensor, 0.5 m, and at the same along-stream position as the 300 kHz H-ADCP. The automatic sampler is linked to the turbidity meter and can be programmed to sample when triggered by events, sampling say once an hour when the turbidity exceeds a certain value. Alternatively, it can be programmed to sample regularly over a fixed time period. When triggered to sample, a plastic bottle is filled

with 700 mL of water.

In order to calibrate the turbidity meter, water samples were also collected by hand by submerging 1-l plastic bottles just below the surface. In total, 128 samples were collected between April 2009 and January 2011 for the calibration of the turbidity meter. Figure 3.6 is a plot of the concentration of suspended particles versus turbidity at the time of sampling. The concentrations that were measured ranged from 0.0047 kg/m^3 to 8.3 kg/m^3 while the turbidity values encountered ranged from 8.8 mg/l TSS to 8.3 g/l TSS. It can be seen from Figure 3.6 that a clear linear relationship exists between concentration and optical turbidity over a range of concentration values that spans three orders of magnitude. A major observation is that there appeared to be no grouping of the points by events. In addition, the turbidity meter appeared to be relatively insensitive to the differences in the size distributions of the primary particles that were observed at this study site, at least relative to the other sources of scatter on a log-log plot (*Moore et al.*, 2011). (These grain size distributions shall be presented later in this chapter.) Thus, in the remainder of our analysis we calculate the concentration of suspended sediment from the turbidity data using the linear relationship that is provided in Figure 3.6. Nevertheless, we can see that use of this linear relationship will have a tendency to overestimate the concentration when it exceeds 200 mg/L (see points below the line).

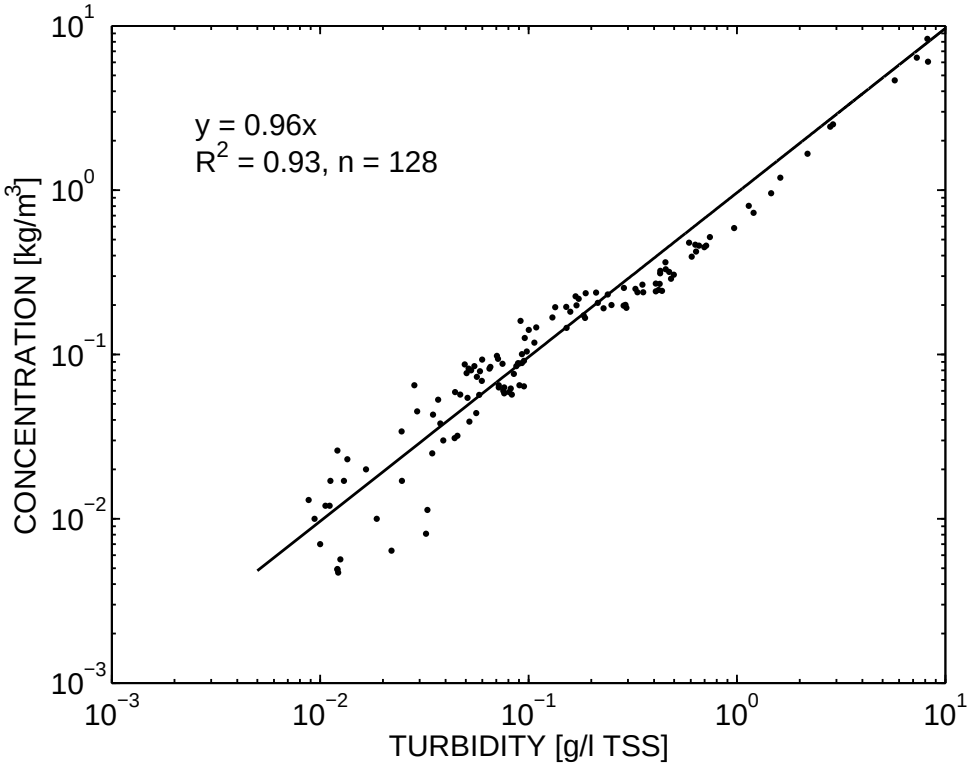

Figure 3.6: Relationship between suspended sediment concentration measured in water samples and optical turbidity at Romans-sur-Isère. Units of turbidity are g/l Total Suspended Solids. The linear regression between concentration and turbidity was forced through the zero crossing of both variables. The number of data points used for the fit and the coefficient of determination, R^2 are given.

3.1.2 Hydrological conditions

The Romans-sur-Isère study site is 6 km upstream of the La Vanelle dam (EDF) and 2 km downstream of the Pizançon dam (EDF). At this location, the river is roughly 90 m wide and the maximum depth is about 4 m. A pressure gauge that is independent from the acoustic instruments is used to measure the water level. The average bathymetry measured during river gauging January 9, 2009 is shown in Figure 3.7, using the actual aspect ratio of the site in the top panel and a more legible aspect ratio in the bottom panel. The velocity magnitude normal to the axis of the 300 kHz instrument, as measured with ADCP gauging is overlayed on the bathymetry. These measurements were made with a 600 kHz RD Instruments Workhorse RioGrande ADCP. These values have been averaged over six transects and interpolated onto a grid with regular spacing. Since the ADCP cannot measure velocity within ∼50 cm of the surface and bottom due to ringing and side lobe effects, respectively, the velocity field presented in Figure 3.7 has been extrapolated to fill the water column. The values near the bottom have been extrapolated using a

linear regression to zero at the bottom. Although it may have been better to use a log law, these figures are purely for illustrative purposes. From Figure 3.7 we see that the velocity field has the form that we would expect considering the site is along a relatively straight reach of the river, far from any confluences and is not too near a dam. That is, the maximum velocity occurs towards the centre of the river and the flow field is nearly symmetric about the centre.

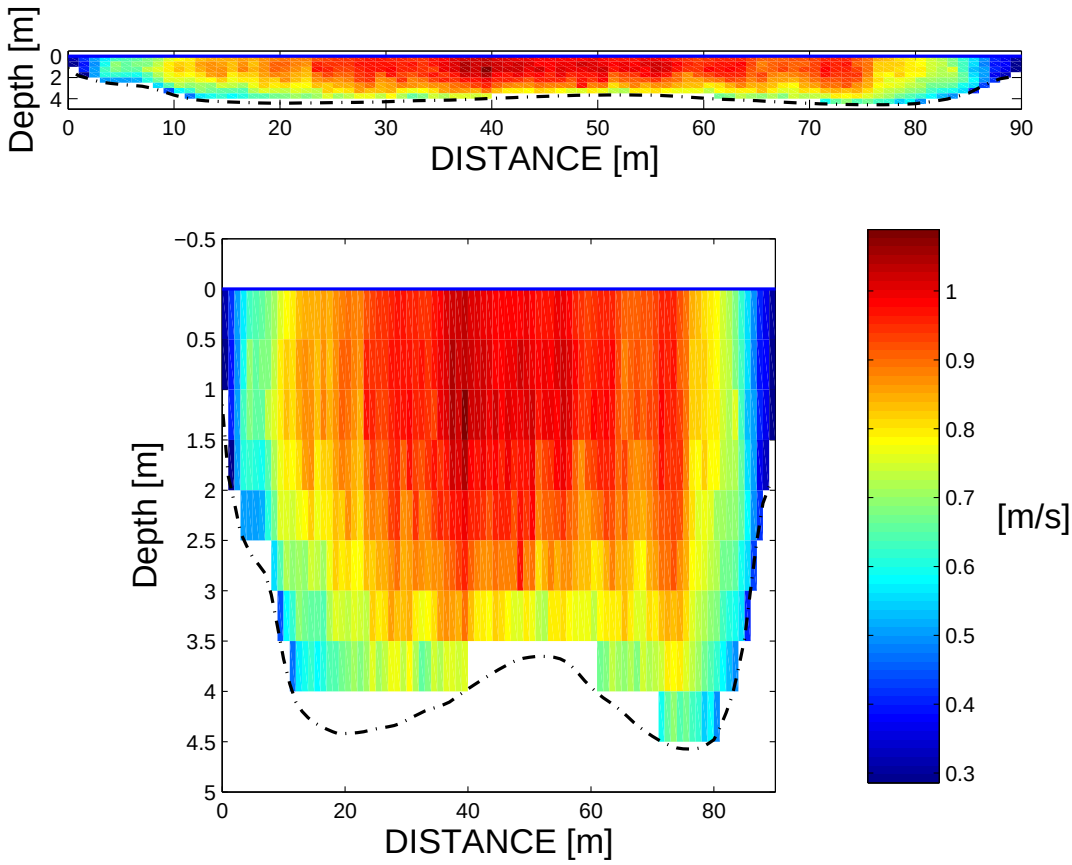

Figure 3.7: The average velocity magnitude [m/s] measured on January 9, 2009 by moving-boat gauging using a 600 kHz Workhorse RioGrande ADCP at Romans-sur-Isère overlayed on the average bathymetry from its bottom-tracking function. The velocity data are the average of six transects with velocities extrapolated to fill the water column.

During most of the year, the cross-sectional averaged flow speed at Romans-sur-Isère typically ranges from 0.25 m/s to 1.5 m/s. The concentration of suspended sediment ranges from 10 mg/L to 30 mg/L. Floods tend to occur during the spring snowmelt since there are a number of mountains in the catchment basin of the Isère river, but they can also occur due to rain storms. During these events, the mean discharge and particle concentration can exceed 1000 m^3/s and 1 g/L. Nevertheless, the conditions at this site depend heavily on the operations of the neighbouring dams.

There can be high concentrations of suspended sediment during floods when the dam gates can be opened wider than usual. This permits the sediment from further upstream to continue downstream and it often results in a sort of dam flushing of the fine sediments that can be retained behind the dam. The downstream dam controls the mean water level and hence the mean flow velocity. During floods or dam opening events upstream, the downstream dam is opened wider than usual which results in a decrease in water level. This means that velocity values at this site are more telling of hydrological conditions than are water level or discharge values alone.

In this study the output discharge from the Pizançon dam is used in combination with the water level measured by the pneumatic water level sensor at Romans-sur-Isère to determine the cross-sectional averaged velocity. The cross-sectional averaged velocity is also referred to as the discharge velocity, V_q, since it is calculated as

$$V_q = \frac{Q}{A}, \tag{3.1}$$

where Q is the discharge and A is the wetted area at the site. The latter is calculated using the water level and bathymetry data. The range of discharge velocity values measured at this site between November 2009 and July 2010 was between 0.25 m/s and 3.5 m/s.

3.1.3 Concentration and grain size of the suspended sediment

Measurement procedure

In terms of the suspended sediment at Romans-sur-Isère, over one hundred water samples have been analysed for concentration following the ISO 11923 (1997) standard. To begin with, 47 mm diameter glass fiber filters were washed. They were then dried for 90 - 120 minutes in an oven at 105 °C and weighed with a scale that has a precision of 10^{-5} g. A volume of 500 mL of the sample was filtered through the clean filter and the sediment-laden filter was then dried and weighed. The difference between the weight of the filter before and after filtration divided by the sample volume gives the concentration of suspended sediment, which is typically quoted in kg/m^3 or equivalently g/L.

Grain size analysis was performed using a Malvern Mastersizer, as indicated in Section 6.1.3, following the procedure outlined by the manufacturer for two phase samples. To begin with the system was flushed with distilled water twice. The samples were then added to the recirculation tank and, if needed, water was added (1) to increase volume to cover the recirculation valves and permit recirculation or (2) to dilute the suspension if heavily concentrated. The amount of

water to be added was determined using the obscuration value output by the instrument. This is a measure of the light that is diverted or absorbed by the particles. Although it is recommended that this value be kept between 5 and 20% of the incident light, this was not always possible since many of the samples were not sufficiently concentrated. This means that the obscuration was often less than the recommended 5%.

In between sample collection and size analysis, the samples were stored in a refrigerator at 14°C. Before commencing the grain size measurements, ultrasonic waves were typically applied to the solution in order to break up any flocs that may have existed in the river or that may have formed since the time of collection. As such, our grain size analysis was performed on the primary particles in suspension in the river, and we have no information of the presence or lack thereof of flocs. During the measurements, the solution was kept in motion by a stirrer which maintained homogeneity in the recirculation tank and a pump permitted the solution to circulate through the measurement volume. The stirrer speed was 500 rpm and the pump speed was 20 000 rpm. A measurement run lasted 15 seconds, and three consecutive runs were performed on each sample. In between the analysis of each sample, one cleaning cycle was run. For samples which were analysed using both Fraunhofer and Mie theory, the measurements were performed consecutively without any alterations to the sample.

Assessing the quality of the measurements

A large number of water samples have been analysed by a variety of different users on a number of different days. Only a selection of the data shall be shown in the main text, but a list of all the samples and the corresponding figures can be found in Appendix A. The tables that summarize the laser grain sizer results (Tables 3.2 and 3.4) include the location and date of sampling, the concentration measured by filtration and the optical theory used in the interpretation of the results. The percentage optical obscuration recorded by the grain sizer is also listed. If this value is less than 5% there may be insufficient sediment to have accurate measurements, and if the value is greater than 20 %, multiple scattering may occur, thereby leading to error in the results.

The grain sizer essentially measure the cross-sectional of the particles. Using the obscuration value plus a number of other values (p.15 *Wedd*, 2003), the instrument calculates a volume concentration of particles assuming spherical particles. This value is converted to a mass concentration by assuming that all particles have the density of quartz, 2650 kg/m^3. The volume and mass concentration from the laser grain sizer are also provided in Tables 3.2 and 3.4. The agreement, or lack thereof, between the actual concentration of the sample and the concentration

from the laser grain sizer provides a measure of whether or not the selected model does a suitable job of representing the data (NF ISO 13320-1). Since we did not note when the samples were diluted, we cannot compare absolute values of concentration, but when the concentration from the laser grain sizer is greater than the actual concentration, there is likely a problem with the grain size measurements.

We found that for samples analysed with both Mie and Fraunhofer theory, analysis using Mie theory provided slightly higher values of concentration than Fraunhofer theory for the same sample (see Section 6.1.3 for a description of the two theories and the tables in Appendix A for a summary of the measurements). However, the agreement between the actual concentration and the concentration from the laser grain sizer did not differ significantly for the two methods. This suggests that neither theory is better suited to our samples. When the samples appeared to contain only inorganic particles, the agreement between the actual concentration and the concentration from the laser grain sizer was good. However, when the samples contained algae there were substantial differences between the actual concentration and the optical concentration regardless of the method that was used (see Table A.3). This points to the inability of both models to represent the optical scattering from the organic that can be present in our water samples. The final value given in Tables 3.2 and 3.4 is the residual error. This is a measure of the difference between the modelled and the measured diffraction patterns; the higher it is, the worse the agreement between the observations and the theoretical optical diffraction for the size distribution that is determined. Ideally this value should be less than 1%. Although a small residual value indicates that the modelled diffraction pattern closely resembles the observations, it should not be used as the sole criterion of good measurements, since the modelled diffraction pattern for the wrong distribution could closely resemble the data.

Spatial homogeneity of grain size and concentration

In order to verify that the concentration and grain size of particles were homogeneous throughout the measurement volume of the side-looking ADCPs, an experiment was performed March 31, 2010 during which water samples were collected throughout the river cross-section. Water samples were collected with a 1-L Niskin bottle at depths of 0 m, 1 m, 2 m, 3 m and ranges of 10 m, 30 m, 50 m, 70 m, and 90 m from the right bank at the along-stream position of the staff gauge, for a total of 20 samples. The mean velocity during the experiment was 0.8 m/s. No noticeable trend in concentration or grain size was seen with either depth or distance across the river. The mean concentration for all samples was 0.031 kg/m^3 and the standard deviation from the mean

was 0.002 kg/m^3, which is the typical uncertainty for the filtration method. It should be noted that no samples were collected near the bed and the details of the grain size of the bed material are unknown.

Since the homogeneity experiment was performed before the Fraunhofer theory was selected as the method of choice, Mie theory was applied. The results are shown in Figures 3.8 and 3.9 as probability density distributions of volume and number size (Equation 2.29 is used to go from volume size distributions to number size distributions) and the relevant information is summarized in Table 3.2. From these figures we see that the probability density functions of the volume size are either unimodal or slightly bimodal distributions that are positively skewed. The particles are mainly silts with some clays. The median diameter, d_{50}, of the volume size distributions ranges from 5 to 9 μm, while the median diameter of the number size distributions ranges from 2 to 4 μm. There is good agreement between the actual concentration and the concentration measured by the laser grain sizer. Nevertheless, the laser obscuration values were below the recommended 5% level and the residual errors were fairly high (see Table 3.2). This implies that caution must be used when interpreting the data.

Using the Equations laid out in Chapter 2 we calculate theoretical values of the ensemble average of the scattering attenuation constant $\langle \zeta_s \rangle$ and of the viscous attenuation constant $\langle \zeta_v \rangle$ for the various grain size distributions that were observed. These values are calculated for the three operating frequencies of the horizontal ADCPs at Romans-sur-Isère. They are summarized in Table 3.3. The first thing to notice from Table 3.3 is that the viscous attenuation constant is always orders of magnitude larger than the scattering attenuation constant, as we would expect for these fine particles (recall Figure 2.4). It can be seen that the viscous attenuation constant varies negligibly with the slight changes in the grain size distributions that are observed from one sample to the next. The scattering attenuation constant, on the other hand, varies substantially: the presence of slightly larger particles in samples V1 1-m and V4 2-m (see Figures 3.8(c) and 3.9(a)) leads to a substantial increase in the scattering attenuation constant, since larger particles dominate the scattering losses.

Table 3.2: Relevant information for the samples collected at Romans-sur-Isère March 31, 2010 and analysed using the laser grain sizer. This includes the sizing method (Fraunhofer or Mie theory), the laser obscuration, the concentration measured by filtration, the sizer concentration in percent volume and mass and the residual error. The across-stream positions relative to the right bank are abbreviated as V1 ($\sim$ 10 m), V2($\sim$ 30 m), V3 ($\sim$ 50 m), V4 ($\sim$ 70 m) or V5 ($\sim$ 90 m).

Sample	Method	Sample Conc (mg/L)	Obscuration (%)	Sizer Conc (% volume)	Sizer Conc (mg/L)	Residual Error (%)	Notes
31/03/2010 R bank surface	Mie	31	2.4	0.0016	42	4.8	-
31/03/2010 V1 surface	Mie	31	3.1	0.0022	58	6.2	-
31/03/2010 V2 surface	Mie	30	3.2	0.0025	66	5.5	-
31/03/2010 V3 surface	Mie	30	2.0	0.0014	37	6.1	-
31/03/2010 V4 surface	Mie	30	2.1	0.0014	37	4.8	-
31/03/2010 V5 surface	Mie	31	1.9	0.0011	29	4.7	-
31/03/2010 V1 1-m	Mie	31	3.0	0.0026	69	4.1	-
31/03/2010 V2 1-m	Mie	32	1.8	0.0014	37	4.3	-
31/03/2010 V3 1-m	Mie	33	2.7	0.0018	48	11.0	-
31/03/2010 V4 1-m	Mie	30	2.6	0.0018	48	2.3	-
31/03/2010 V5 1-m	Mie	30	2.2	0.0015	40	5.7	-
31/03/2010 V1 2-m	Mie	32	1.7	0.001	27	5.5	-
31/03/2010 V2 2-m	Mie	30	1.3	0.0007	19	7.9	-
31/03/2010 V3 2-m	Mie	32	1.5	0.0009	24	9.8	-
31/03/2010 V4 2-m	Mie	30	3.0	0.0029	77	1.8	-
31/03/2010 V5 2-m	Mie	29	1.9	0.0012	32	4.0	-
31/03/2010 V1 3-m	Mie	30	1.6	0.001	27	7.0	-
31/03/2010 V2 3-m	Mie	37	1.3	0.0008	21	4.9	-
31/03/2010 V3 3-m	Mie	31	2.4	0.0016	42	10.6	-
31/03/2010 V4 3-m	Mie	31	2.2	0.0015	40	3.0	-
31/03/2010 V5 3-m	Mie	31	2.0	0.0015	40	4.9	-

Table 3.3: The theoretical attenuation parameters for the grain size distributions measured in the samples collected at Romans-sur-Isère March 31, 2010. The viscous and scattering attenuation parameters, $\langle\zeta_v\rangle$ and $\langle\zeta_s\rangle$, are calculated for the three operating frequencies of the ADCPs at Romans-sur-Isère.

Sample	307.2 kHz		614.4 kHz		1228.8 kHz	
	$\langle\zeta_v(a)\rangle$ (m^2/kg)	$\langle\zeta_s(a)\rangle$ (m^2/kg)	$\langle\zeta_v(a)\rangle$ (m^2/kg)	$\langle\zeta_s(a)\rangle$ (m^2/kg)	$\langle\zeta_v(a)\rangle$ (m^2/kg)	$\langle\zeta_s(a)\rangle$ (m^2/kg)
31/03/2010 R bank surface	0.059	2.53e-008	0.111	4.05e-007	0.190	6.47e-006
31/03/2010 V1 surface	0.058	3.20e-008	0.110	5.12e-007	0.189	8.18e-006
31/03/2010 V2 surface	0.058	4.44e-008	0.108	7.09e-007	0.183	1.13e-005
31/03/2010 V3 surface	0.056	1.01e-008	0.095	1.62e-007	0.151	2.59e-006
31/03/2010 V4 surface	0.057	1.11e-008	0.101	1.77e-007	0.165	2.84e-006
31/03/2010 V5 surface	0.059	1.82e-008	0.111	2.91e-007	0.189	4.66e-006
31/03/2010 V1 1-m	0.058	4.67e-006	0.109	7.00e-005	0.186	9.14e-004
31/03/2010 V2 1-m	0.057	2.92e-008	0.104	4.66e-007	0.173	7.45e-006
31/03/2010 V3 1-m	0.058	2.82e-008	0.112	4.51e-007	0.194	7.21e-006
31/03/2010 V4 1-m	0.058	2.97e-008	0.109	4.74e-007	0.185	7.58e-006
31/03/2010 V5 1-m	0.058	2.82e-008	0.110	4.52e-007	0.189	7.22e-006
31/03/2010 V1 2-m	0.058	1.28e-008	0.107	2.05e-007	0.180	3.27e-006
31/03/2010 V2 2-m	0.059	1.18e-008	0.113	1.88e-007	0.195	3.01e-006
31/03/2010 V3 2-m	0.059	1.60e-008	0.113	2.57e-007	0.197	4.10e-006
31/03/2010 V4 2-m	0.058	1.22e-005	0.108	1.77e-004	0.184	0.0021
31/03/2010 V5 2-m	0.059	2.65e-008	0.112	4.24e-007	0.192	6.77e-006
31/03/2010 V1 3-m	0.059	2.25e-008	0.111	3.60e-007	0.190	5.75e-006
31/03/2010 V2 3-m	0.058	9.56e-009	0.103	1.53e-007	0.170	2.45e-006
31/03/2010 V3 3-m	0.058	2.86e-008	0.112	4.58e-007	0.194	7.32e-006
31/03/2010 V4 3-m	0.058	1.67e-008	0.105	2.67e-007	0.174	4.27e-006
31/03/2010 V5 3-m	0.058	3.74e-008	0.109	5.99e-007	0.186	9.56e-006

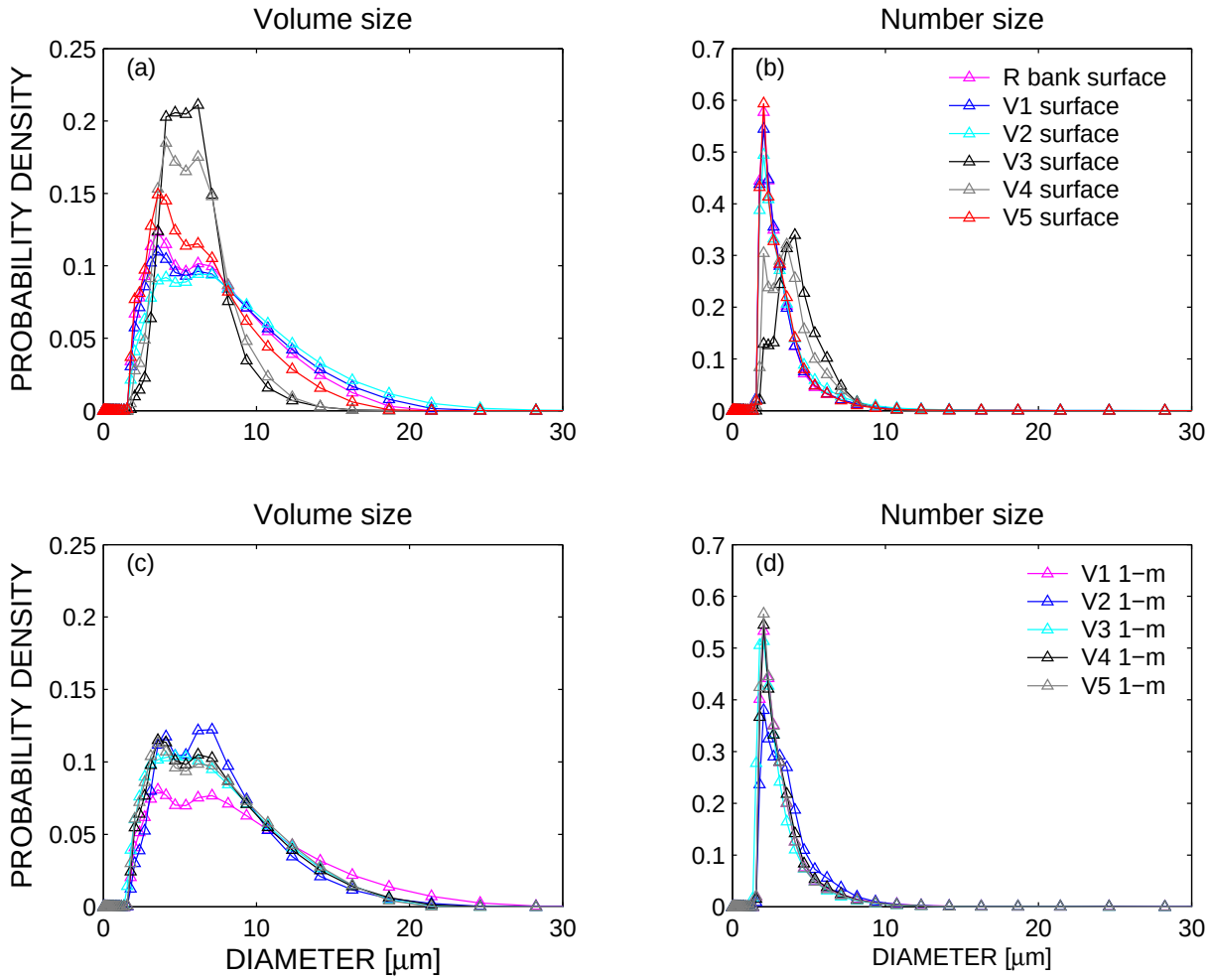

Figure 3.8: Grain size distributions measured using the laser grain sizer for water samples collected at Romans-sur-Isère March 31, 2010 represented as probability density functions of (a,c) volume and (b,d) number size. Samples were collected **either just below the surface, or at a depth of 1 m,** as indicated. The across-stream positions relative to the right bank are V1 (∼ 10 m), V2(∼ 30 m), V3 (∼ 50 m), V4 (∼ 70 m) or V5 (∼ 90 m). Concentrations were 30 mg/L

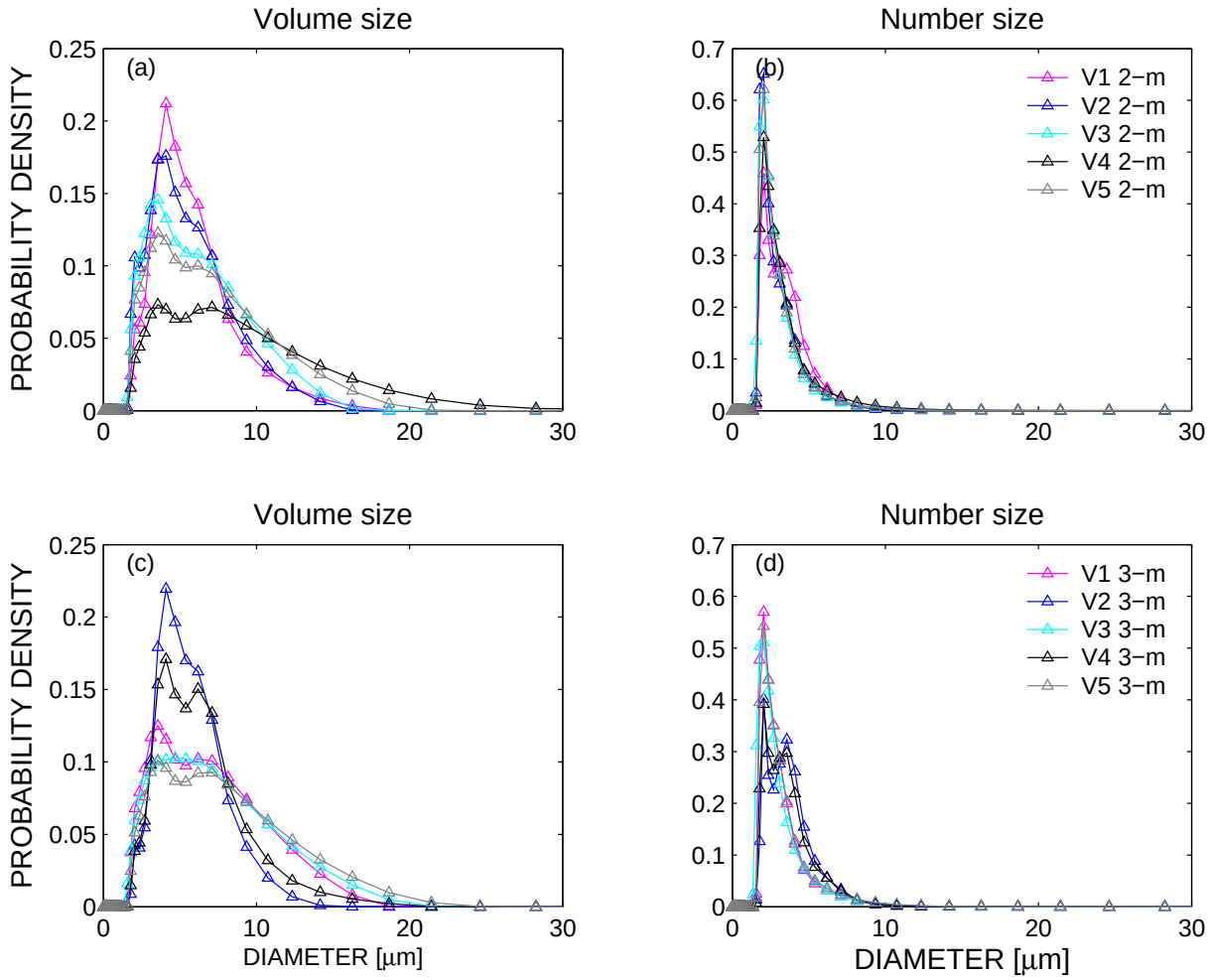

Figure 3.9: Grain size distributions measured using the laser grain sizer for water samples collected at Romans-sur-Isère March 31, 2010 represented as probability density functions of (a,c) volume and (b,d) number fractions. Samples were collected **either at 2 or 3 m depth,** as indicated. The across-stream position relative to the right bank are V1 (∼ 10 m), V2 (∼ 30 m), V3 (∼ 50 m), V4 (∼ 70 m) or V5 (∼ 90 m). Concentrations were 30 mg/L

The results of our test of the spatial distribution of wash load at Romans-sur-Isère imply that the grain size and concentration of suspended sediment were homogeneous across the river cross-section. While these results may only be representative of the velocities and concentrations encountered March 31 2010, in the acoustical analysis that is presented in Chapters 6 and 7, it will be assumed that the grain size distributions and concentration are homogeneous throughout the ensonified volume. We believe this to be a fair assumption considering the study site is along a relatively straight and uniform reach of the river and is far from any confluences.

Variability with hydraulic conditions

The grain size distributions measured in five surface water samples collected during various flow conditions at various times in the year are shown in Figure 3.10 and the relevant information is summarized in Table 3.4. These samples, which were all analysed in Fraunhofer mode illustrate the variety of grain size distributions that were observed at Romans-sur-Isère. They include both samples collected by hand (open circles) and by the automatic sampler (filled circles) and cover a range of concentration values from 8 mg/L to almost 5 g/L. No organic particles were seen by the naked eye in these samples, but organic content was not assessed quantitatively. The sample from January 9, 2009 corresponds to a period of low flow (5 mg/L, $V_q < 1$ m/s). The sample collected May 11, 2010 corresponds to two days of relatively high concentrations and flow rates (100 mg/L, 1.5 m/s). The sample from June 1 was collected near the peak of a large spring flood (5 g/L, 2.5 m/s), while the sample from June 3 was collected on the falling limb of this flood (200 mg/L, $\sim$ 1.5 m/s) and the sample collected in December 2010 was collected on the descent of a small winter flood (velocity unknown, concentration 62 mg/L). We believe that the differences in the grain size distributions that are observed between these five samples are representative of the differences that can be observed at Romans-sur-Isère at different times in the year [1].

[1]The grain size distributions of the samples collected May 11, 2010 and June 1, 2010 were presented in *Moore et al.* (2011). Instead of plotting the data in terms of the probability density functions, as was done here, the data were plotted in terms of the fraction of the total sample occupied by grains of a given size class. This resulted in more noticeable differences between the different samples, and it appeared that the size distributions were unimodal, bimodal and trimodal. With the current representation of the data, the differences in the grain size distributions between the various samples are less noticeable.

Table 3.4: Relevant information from the grain size analysis of samples collected at the surface near the right bank of the Romans-sur-Isère study site. This includes the sizing method (Fraunhofer or Mie theory), the laser obscuration, the concentration measured by filtration, the concentration from the laser sizer in percent volume and mass and the residual error.

Sample	Method	Measured Conc (mg/L)	Obscuration (%)	Sizer Conc (% volume)	Sizer Conc (mg/L)	Residual Error (%)
2009-01-09 10:20	Fr	8	0.9	0.0014	37	0.4
2010-05-11 04:31	Fr	104	4.9	0.0042	111	4.0
2010-06-01 12:04	Fr	4937	15.2	0.0158	419	2.0
2010-06-03 15:02	Fr	200	8.2	0.008	212	2.7
2010-12-11 05:10	Fr	62	7.1	0.0043	114	1.8

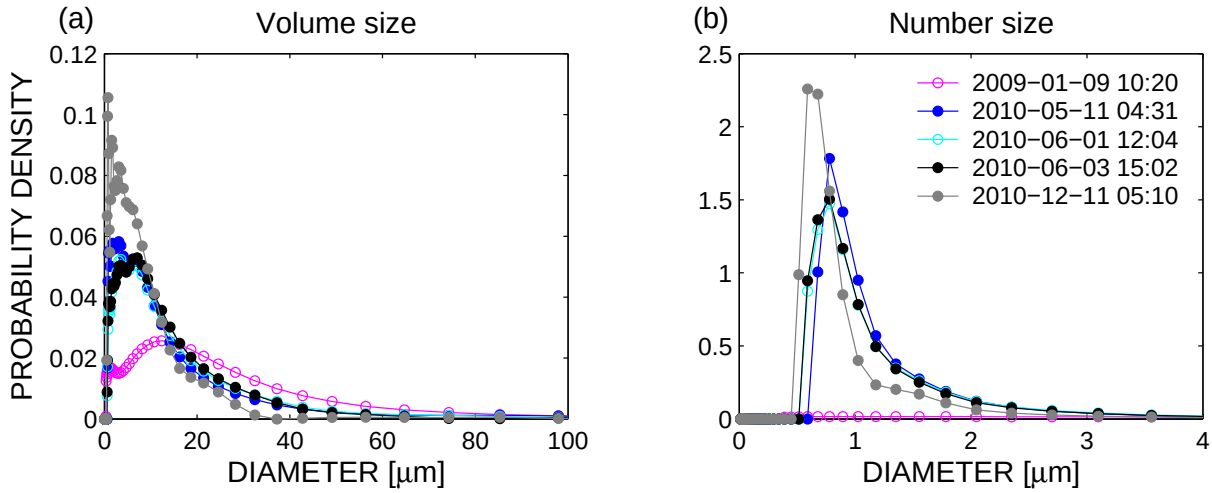

Figure 3.10: Grain size distributions measured using the Fraunhofer method for water samples collected at Romans-sur-Isère throughout 2009 and 2010. Samples collected by hand are represented as open circles while those collected by the automatic sampler are represented as closed circles.

From Table 3.4, we see that the laser obscuration value for the sample collected in January 2009 was very low ($< 1\%$), as we would expect for such a dilute sample. In addition, the sizer concentration was 4.5 times the actual concentration. We are therefore skeptical of the low residual error that was output by the laser grain sizer and of the grain size distribution that was measured (see data in magenta in Figure 3.10). Apart from this sample, the form of the grain size distributions of the other samples are all very similar: they all appear to be lognormal, and the main mode in the volume size distributions and the only mode in the number size distributions change little from sample to sample. The volume size distributions from Figure 3.10(a) are reproduced in Figure 3.11 on both a linear and logarithmic scale in order to better visualize the form of the profiles at micron and submicron diameters. For all samples but the one collected January 9, peaks in the size distributions are seen around 1, 2 and 3 microns. We suspect that these

modes are an artifact of the use of the Fraunhofer method (see Figure 2.6 and the corresponding discussion in Chapter 2).

Recalling the discussion from Chapter 2, Section 2.2.6, the size frequency distributions of natural sediments are commonly interpreted as lognormal. Overlayed on the data in Figure 3.11 are lognormal distributions computed using $\mu_X = \ln d_{50}$ and $\sigma_X = 1$ for each sample (N.B. These curves are not fitted to the data). It can be seen that there is relatively good agreement between the data and the theoretical curves, except at diameters less than a few microns. We conjecture that the discrepancy between theory and observations at low diameters is an artifact of the Fraunhofer method overpredicting the fine particles. Consequently, lognormal grain size distributions shall be used in the theoretical calculations of the acoustic scattering and attenuation later on in this thesis.

As with the data collected during the homogeneity test, the viscous and scattering attenuation constants are calculated for the grain size distributions shown in Figures 3.10 and 3.11 for incident frequencies of 307.2, 614.4 and 1228.8 kHz. These values are summarized in Table 3.5. Apart from the values for the sample collected January 9, 2009, of which we are skeptical, the values of the viscous attenuation constant for all samples at all frequencies are very similar. In contrast, the scattering attenuation constant changes significantly with the different size distributions due to the different amounts of larger particles. As an example, the scattering attenuation constants for the sample collected in December, 2010 are about an order of magnitude lower than the values for the other samples due to the lack of large particles in this sample.

Table 3.5: The theoretical attenuation parameters for the grain size distributions measured in the samples collected at Romans-sur-Isère and shown in Figures 3.10 and 3.11. The viscous and scattering attenuation parameters, $\langle\zeta_v\rangle$ and $\langle\zeta_s\rangle$, are calculated for the operating frequencies of the H-ADCPs used in this study.

Sample	307.2 kHz		614.4 kHz		1228.8 kHz	
	$\langle\zeta_v(a)\rangle$ (m^2/kg)	$\langle\zeta_s(a)\rangle$ (m^2/kg)	$\langle\zeta_v(a)\rangle$ (m^2/kg)	$\langle\zeta_s(a)\rangle$ (m^2/kg)	$\langle\zeta_v(a)\rangle$ (m^2/kg)	$\langle\zeta_s(a)\rangle$ (m^2/kg)
2009-01-09 10:20	0.0181	9.7×10^{-5}	0.0540	1.10×10^{-3}	0.1514	8.7×10^{-3}
2010-05-11 04:31	0.0358	3.4×10^{-6}	0.0937	5.3×10^{-5}	0.2208	7.5×10^{-4}
2010-06-01 12:04	0.0347	2.0×10^{-6}	0.0902	3.1×10^{-5}	0.2135	4.6×10^{-4}
2010-06-03 15:02	0.0340	1.0×10^{-6}	0.0893	1.6×10^{-5}	0.2130	2.5×10^{-4}
2010-12-11 05:10	0.0266	4.4×10^{-7}	0.0753	7.0×10^{-6}	0.1953	1.1×10^{-4}

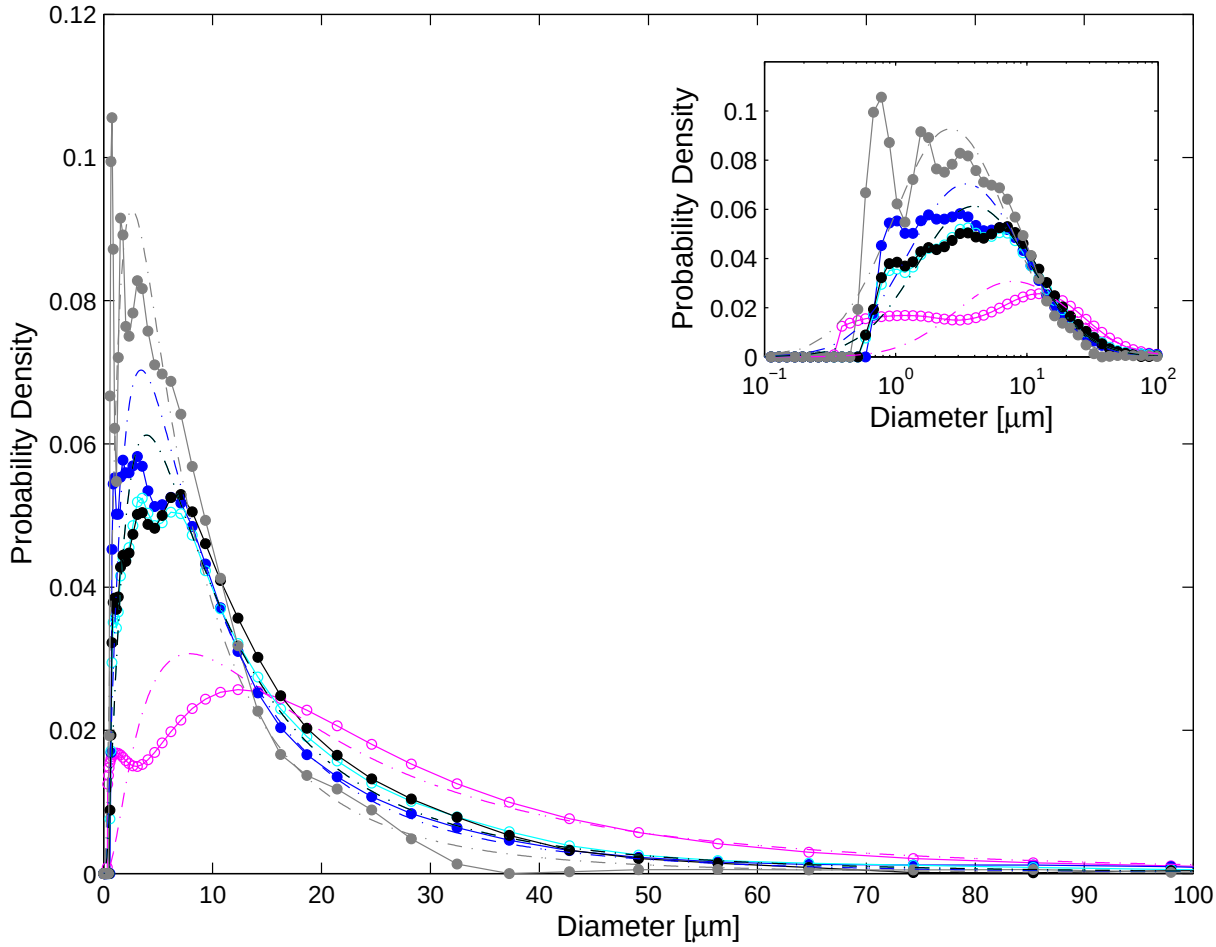

Figure 3.11: Probability density distributions of the volume size for the samples previously presented in Figure 3.10. The distributions are shown on both linear and logarithmic scales. Lognormal distributions with $\mu_X = \ln d_{50}$ and $\sigma_X = 1$ are plotted as dashed lines for each sample. Samples collected by hand are represented as open circles while those collected by the automatic sampler are represented as closed circles.

3.1.3.1 Variability of the results depending on the theory that is used

In terms of the implications of the grain size analysis results for our acoustic study, we have previously seen and discussed the fact that the viscous attenuation parameter is controlled by the fine particles. This implies that the overprediction of clay-sized particles when using the Fraunhofer method may impact the theoretical values of the scattering and attenuation parameters that are calculated. This would in turn affect the concentration estimates that are calculated with these values. In order to quantify these differences, we have calculated the viscous and scattering attenuation constants for all samples that have been analysed using the two different theories. These values are summarized in Table 3.6. It can be seen that, for the most part, there is little

difference between the values calculated from the grain size distributions from the two methods.

Table 3.6: The theoretical attenuation parameters for the grain size distributions measured in the samples collected at Romans-sur-Isère using both Fraunhofer and Mie theory. The viscous and scattering attenuation parameters, $\langle\zeta_v\rangle$ and $\langle\zeta_s\rangle$, are calculated for the operating frequencies of the H-ADCPs used in this study.

Sample	Method	307.2 kHz		614.4 kHz		1228.8 kHz	
		$\langle\zeta_v(a)\rangle$ (m^2/kg)	$\langle\zeta_s(a)\rangle$ (m^2/kg)	$\langle\zeta_v(a)\rangle$ (m^2/kg)	$\langle\zeta_s(a)\rangle$ (m^2/kg)	$\langle\zeta_v(a)\rangle$ (m^2/kg)	$\langle\zeta_s(a)\rangle$ (m^2/kg)
01/06/2010 11:34	Fr	0.033	1.6×10^{-6}	0.088	2.6×10^{-5}	0.212	4.0×10^{-4}
01/06/2010 11:34	Mie	0.058	2.4×10^{-6}	0.107	3.9×10^{-5}	0.182	5.8×10^{-4}
02/06/2010 06:02	Fr	0.033	7.5×10^{-7}	0.088	1.2×10^{-5}	0.212	1.9×10^{-4}
02/06/2010 06:02	Mie	0.057	5.6×10^{-7}	0.103	8.9×10^{-6}	0.170	1.4×10^{-4}
08/06/2010 20:00	Fr	0.032	2.1×10^{-6}	0.086	3.2×10^{-5}	0.211	4.9×10^{-4}
08/06/2010 20:00	Mie	0.056	2.0×10^{-6}	0.102	3.2×10^{-5}	0.170	4.9×10^{-4}
09/06/2010 20:00	Fr	0.033	1.4×10^{-6}	0.088	2.1×10^{-5}	0.213	3.3×10^{-4}
09/06/2010 20:00	Mie	0.058	1.4×10^{-6}	0.109	2.27×10^{-5}	0.185	3.5×10^{-4}
11/06/2010 02:00	Fr	0.032	2.9×10^{-6}	0.086	4.5×10^{-5}	0.211	6.9×10^{-4}
11/06/2010 02:00	Mie	0.057	3.2×10^{-6}	0.107	5.1×10^{-5}	0.182	7.6×10^{-4}
10/10/2010 04:00	Fr	0.054	2.0×10^{-2}	0.115	1.02×10^{-1}	0.220	2.69×10^{-1}
10/10/2010 04:00	Mie	0.057	1.6×10^{-2}	0.103	9.4×10^{-2}	0.169	2.74×10^{-1}
11/12/2010 01:10	Fr	0.006	1.2×10^{-7}	0.019	1.9×10^{-6}	0.058	3.0×10^{-5}
11/12/2010 01:10	Mie	0.058	1.2×10^{-7}	0.109	2.0×10^{-6}	0.186	3.1×10^{-5}

3.2 Saint-Georges

3.2.1 Study site and instrumentation

The Saint-Georges study site, which is shown in Figure 3.12 is located on the right bank of the Saône river in Lyon, France, along a relatively straight reach of the river. It is 3.5 km upstream of the confluence of the Saône and Rhône rivers and about 20 m upstream of a footbridge. The river is trained at this location and there are vertical walls on both banks. The width and maximum depth during normal conditions at this site are 95 m and 10 m, respectively. The study site is 15 km downstream of the Couzon dam and 8 km upstream of the Pierre Bénite dams (CNR); the latter controls the water level and flow rate at the Saint-Georges site. A measure of discharge is available at the Couzon station, these values are calculated from a rating-curve that is a function of the water level at Couzon and at Pierre-Bénite. The discharge data from the Couzon dam can be combined with the water level from Saint-Georges to estimate the mean flow rate at Saint-Georges.

Figure 3.12: Aerial photograph of the Saint-Georges study site taken from Google Maps. The location of the side-looking ADCP is marked by an x and the direction of flow is indicated with an arrow.

The bathymetry and average flow field measured with a 600 kHz RD Instruments Workhorse RioGrande ADCP during six transects performed on February 18, 2006 are shown in Figure 3.13. These data correspond to relatively high flow conditions. From this figure, it can be seen that the flow is a maximum towards the centre of the river, and the flow field is nearly symmetrical about the centre. Based on our observations, the flow field is conserved at this site regardless of the mean flow speed.

A 300-kHz narrow beam Teledyne RD Instruments Workhorse H-ADCP has been installed on the right bank of this study site since February, 2006. The horizontal separation of the three transducers is 20°, as it is for all 300 kHz Workhorse H-ADCPs and the beam width of each transducer is 1°. The H-ADCP was positioned on the wall of the right river bank at an elevation of 160.00 m NGF (Nivellement Général de la France) system. The water level at this site typically fluctuates between 162 and 163 m NGF, meaning that the instrument is typically 2 or 3 m below the surface. The pitch of the instrument is -0.4° (it is angled downwards) and the roll is -0.1°, meaning that the downstream beam is angled slightly towards the bottom and the upstream beam is angled slightly towards the surface. The instrument is programmed to have a blank distance of 2 m and a bin size of 4 m. The ping repetition rate is set to the maximum possible ping rate, which is slightly greater than 2 Hz, and 180 pings are averaged per ensemble. This results in one

profile of velocity and intensity for each beam every 80 seconds.

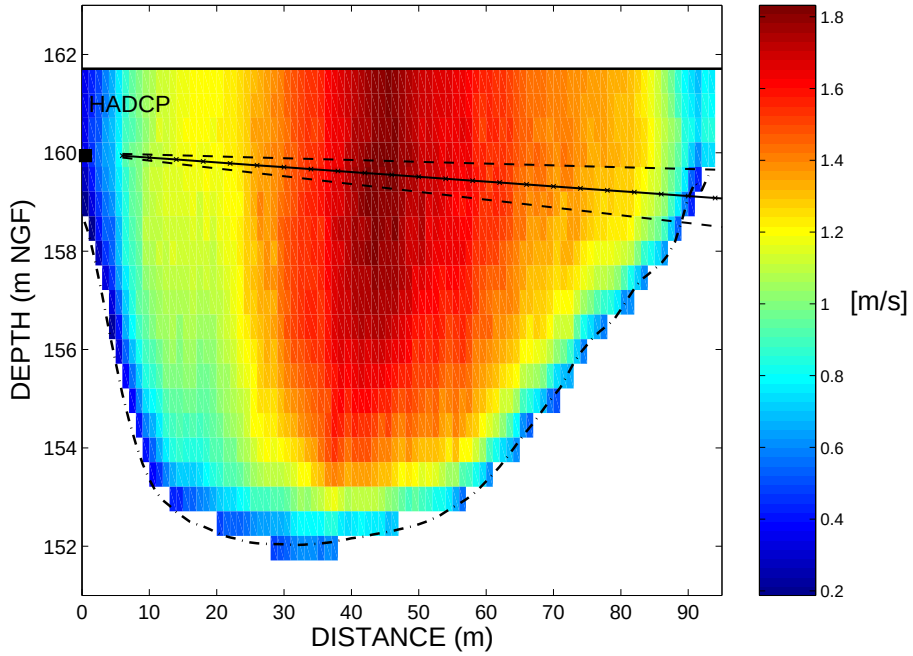

Figure 3.13: Upstream view of the Saint-Georges study site with velocity data obtained during moving-boat gauging with a 600 kHz ADCP attached to a motor boat. The dashed-dotted line is the river bathymetry. The H-ADCP is indicated as a square, the solid line represents the axis of the central transducer, the small xs represent the centre of each measurement cell and dashed lines represent the instrument's beam width (-3dB transmitted power).

A pneumatic water level sensor is installed next to the H-ADCP in order to provide an independent measure of water level. A SOLITAX sc optical turbidity meter constructed by Hach Lange is used to measure concentrations of suspended sediment at this site; it has been in place since October 14, 2009. This is the same turbidity meter as the one at Romans-sur-Isère, only it operates in "turbidity" mode as opposed to "total suspended solids" mode. It measures light scattering at 90° and records values in Nephelometric Turbidity Units (NTU). The turbidity meter has been calibrated with nine water samples that were collected between February and June, 2010. The relationship between the concentration of sediment measured in these samples and the turbidity at the time of sampling is shown in Figure 3.14. The least-squares linear regression forced through the origin is also shown. The equation of the line yields concentration/turbidity = 0.85. Although more data points at concentrations less than 40 mg/L are required, the high end of the concentration values have been fairly well sampled since most water samples were collected during small floods. In terms of extreme values at this site, the concentrations at this site can exceed 100 mg/L

a couple of times per year during the floods which can occur in the fall and winter months. The maximum observed concentration at this site of which we are aware was 146 mg/L (*Le Coz et al.*, 2007). As mentioned in the introduction to this chapter, concentrations are less than 10 mg/L the majority of the time. Therefore, if the turbidity meter is to be used as an accurate proxy for concentration, more low concentration samples should be collected in order to complete the data set shown in Figure 3.14.

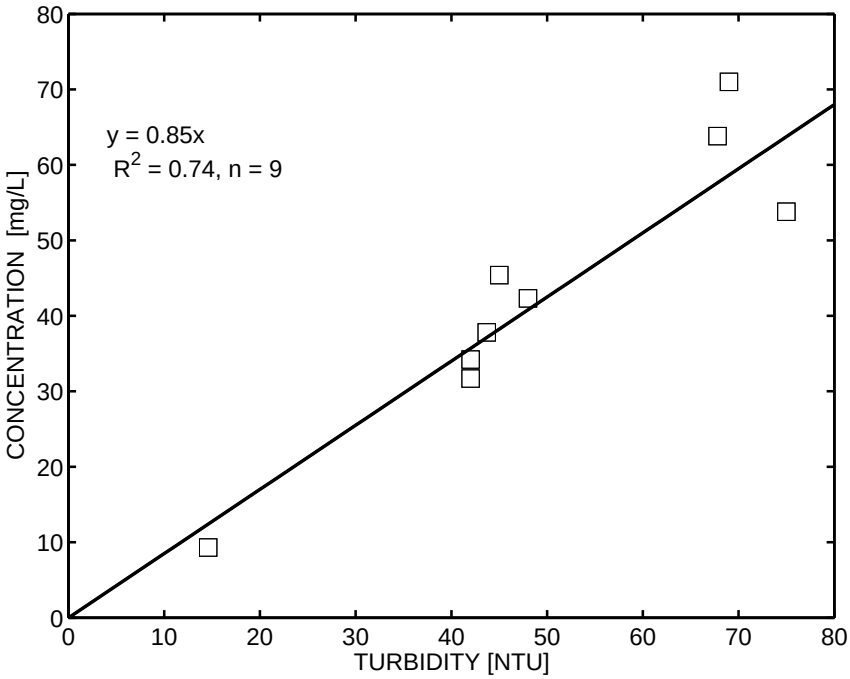

Figure 3.14: Calibration curve for the turbidity meter at Saint-Georges. The linear relationship between concentration and turbidity is forced through the origin.

3.2.2 Grain size distributions of the suspended sediment

The homogeneity of the concentration of suspended sediment at Saint-Georges was tested prior to the start of this thesis (*Le Coz et al.*, 2007). It was found that concentrations of the wash load were homogeneous throughout the cross section. The grain size distributions of these samples were not measured. However, during this thesis, grain size analysis was performed on ten samples that were collected on the Saône river on various days. These samples were collected either at the Saint-Georges study site, or 2 km upstream at the Koenig bridge, which is ∼200 m from our laboratory. The data set includes two samples collected in 2009 (March 26, 2009 and December 8, 2009), six samples collected during small floods on the Saône in 2010, and two samples from

floods in January, 2011. All samples had concentrations exceeding 20 mg/L and should therefore be sufficiently concentrated for reliable laser grain sizer measurements. (N.B. We do not have concentration data for the sample collected March 26 2009, but we think that it was fairly dilute.) The probability density distributions of volume and number size measured for these samples are shown in Figure 3.15. They are plotted on a logarithmic scale of grain size due to the multi modal and irregular grain size distributions.

Table 3.7 is a summary of the relevant information output from the laser grain sizer for each sample. It can be seen that the concentration detected by the grain sizer for all samples except that of December 2009 are orders of magnitude higher than the actual concentrations. This is a result of the high algal content of the samples. Much to our surprise, algae were even seen in the samples that were collected during the winter floods. Clearly, the samples should have been pre-treated to eliminate the organic matter, but since they were not, the resulting grain size measurements are unreliable. This is reassuring in a way because the results that are shown in Figure 3.15 suggest that the laser grain sizer "measured" particles with grain sizes greater than 1 mm. Since ultrasonic waves were used to break up flocs prior to grain size analysis, these results are clearly not representative of the sediment in suspension, but represent scattering from the organic matter.

We turn our attenuation to the results for the samples which we believe did not contain algae, those of March and December, 2009. The volume size distribution for the March 2009 sample, which was analysed in Fraunhofer mode, is bimodal with a peak at clay sized particles, and one at silt-sized particles. The median diameter is 10.7 μm. The volume size distribution for the December 2009 sample, which was analysed in Mie mode, was slightly bimodal and the median diameter was 28 μm. The difference in the values of d_{50} for these two samples may be due to the differences in the two theories. From these two samples we see that the suspended sediments at the Saint-Georges study site were mainly silts. In addition, from visual analysis of the samples we know that there were sand size particles in some of the samples and thus the small peaks in the volume size distributions around 100 μm seem realistic.

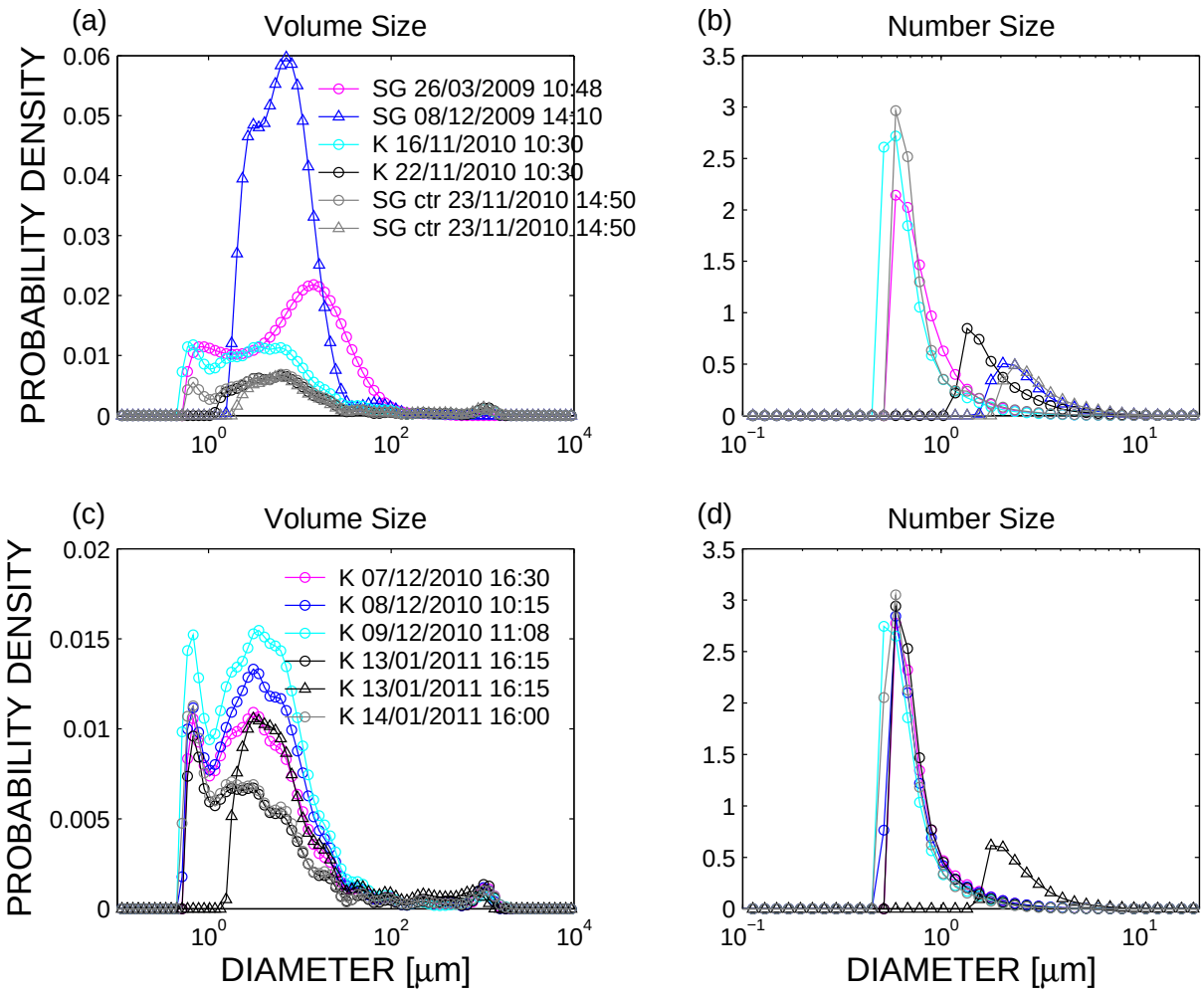

Figure 3.15: Grain size distributions measured for water samples collected from the Saône at the Saint-Georges study site (SG) and at the Koenig bridge (K) using the theories of Fraunhofer (circles) and Mie (triangles). Unless otherwise indicated, samples collected at Saint-Georges were taken from the right bank, and those collected at Pont Koenig were taken in the centre of the river.

Table 3.7: Relevant information for the samples collected on the Saône river and analysed using the laser grain sizer. This includes the sizing method (Fraunhofer or Mie), the concentration measured by filtration, and the sizer concentration (percent total volume and mass, assuming a particle density of 2650 kg/m^3). The residual error, or percent difference between the modelled and observed light scattering, is also listed.

Sample	Method	Sample Conc (mg/L)	Laser Obscuration (%)	Sizer Conc (% volume)	Sizer Conc (mg/L)	Residual Error (%)	Notes
SG 26/03/2009 10:48	Fr	-	-	-	-	-	-
SG R bank 08/12/2009 14:10	Mie	-	2.8	0.0030	80	1.6	-
Pont K. 16/11/2010 10:30	Fr	145	16.4	0.0663	1757	2.1	lots of algae
Pont K. 22/11/2010 10:30	Fr	33	8.0	0.0724	1919	3.3	a bit of algae, visible sand
SG ctr 23/11/2010 14:50	Fr	43	9.2	0.0686	1818	2.7	-
SG ctr 23/11/2010 14:50	Mie	43	8.6	0.0853	2260	3.5	-
Pont K. 07/12/2010 16:30	Fr	85	13.5	0.0646	1712	2.6	few floaters/algae, some clumping, some sand
Pont K. 08/12/2010 10:15	Fr	-	14.8	0.0595	1577	2.6	some algae
Pont K. 09/12/2010 11:08	Fr	96	18.3	0.0609	1614	1.7	lots of floaters and algae
Pont K. 13/01/2011 16:15	Fr	-	10.8	0.0742	1966	3.7	-
Pont K. 13/01/2011 16:15	Mie	-	10.0	0.0572	1516	1.7	-
Pont K. 14/01/2011 16:00	Fr	-	9.2	0.0568	1505	2.9	some floaters

3.2.3 Complementary data

Although the turbidity meter at Saint-Georges was installed in October 2009, we have little simultaneous optical and acoustical data. The computer responsible for data acquisition crashed regularly and there was a problem with corrosion of the central transducer of the H-ADCP. This influenced its measurements of both velocity and intensity. Although the central transducer is not imperative for streamflow measurements, the instrument was removed for repair on September 23, 2010.

In terms of validation of the velocity measurements at this study site, about twenty gauging campaigns have been performed during various flow conditions. The majority of these measurements were made in 2006; they are summarized in *Le Coz et al.* (2008). The procedure of ADCP gauging will be detailed in Section 5.1. Theoretically, we could also use the discharge data from Couzon (upstream of Saint-Georges) and the wetted area at Saint-Georges to obtain values of the cross-sectional averaged flow speed.

3.3 Montélimar

Moving downstream along the Rhône valley we come to the Montélimar study site. The site is on the left bank of the Rhône canal, 500 m before the Châteauneuf dam (see Figure 3.16). For a variety of reasons we believe this to be the ideal site for reliable H-ADCP measurements. To begin with, there should be no passage of either motor boats or barges in front of the instrument since the canal to the lock system diverges $\sim$ 50 m upstream of the site. The geometry of the section is also ideal(see bathymetry data collected during ADCP gauging in Figure 3.17), the canal is about 13 m deep and 170 m wide.

The site is equipped with a 300 kHz H-ADCP which was installed in October, 2007 at an elevation of 71.55 m NGF; this typically corresponds to a submergence of 5 m. The pitch of the instrument is -0.3° (it is angled downwards) and its roll is 0.2°. For the data presented in this thesis, the instrument was programmed with a blank distance of 1.00 m, a bin size of 4.00 m, 33 bins, and 4 pings averaged per ensemble. Each ensemble lasted approximately 1 minute. Unlike all other H-ADCPs used in this thesis, this instrument was operated in wide bandwidth mode. In this mode, the instrument applies a frequency filter of 25% of its central frequency to the return signal, as opposed to the 6.25% filter in narrow bandwidth mode. Operation in wide bandwidth mode results in (1) lower signal to noise ratios of the backscattered intensity (*Clay*

and Medwin, 1977), (2) lower velocity variance and (3) lower profiling range (*RD Instruments*, 2008, p. 162) compared to operation in narrow bandwidth mode. The explanation for the first point is that the Dopppler-shifted signal that we are trying to detect should be centered around the central frequency of the transducer, while the background noise has a broad spectrum. Thus, using a broader bandwidth filter results in a smaller total signal-to-noise ratio than with a narrow bandwidth filter (*Clay and Medwin*, 1977, p.123). The lower signal-to-noise ratio means that for a given concentration, an instrument operating in broad bandwidth mode cannot profile as far as one operating in narrow bandwidth mode. As for the lower velocity variance, the broader bandwidth permits higher temporal resolution and thus higher sampling rates since the ambiguity velocity is lower. The decreased time between two consecutive signals improves their correlation, resulting in lower variance in the measured velocity values (*Clay and Medwin*, 1977). This means that less pings need to be averaged to reduce the noise in the velocity data.

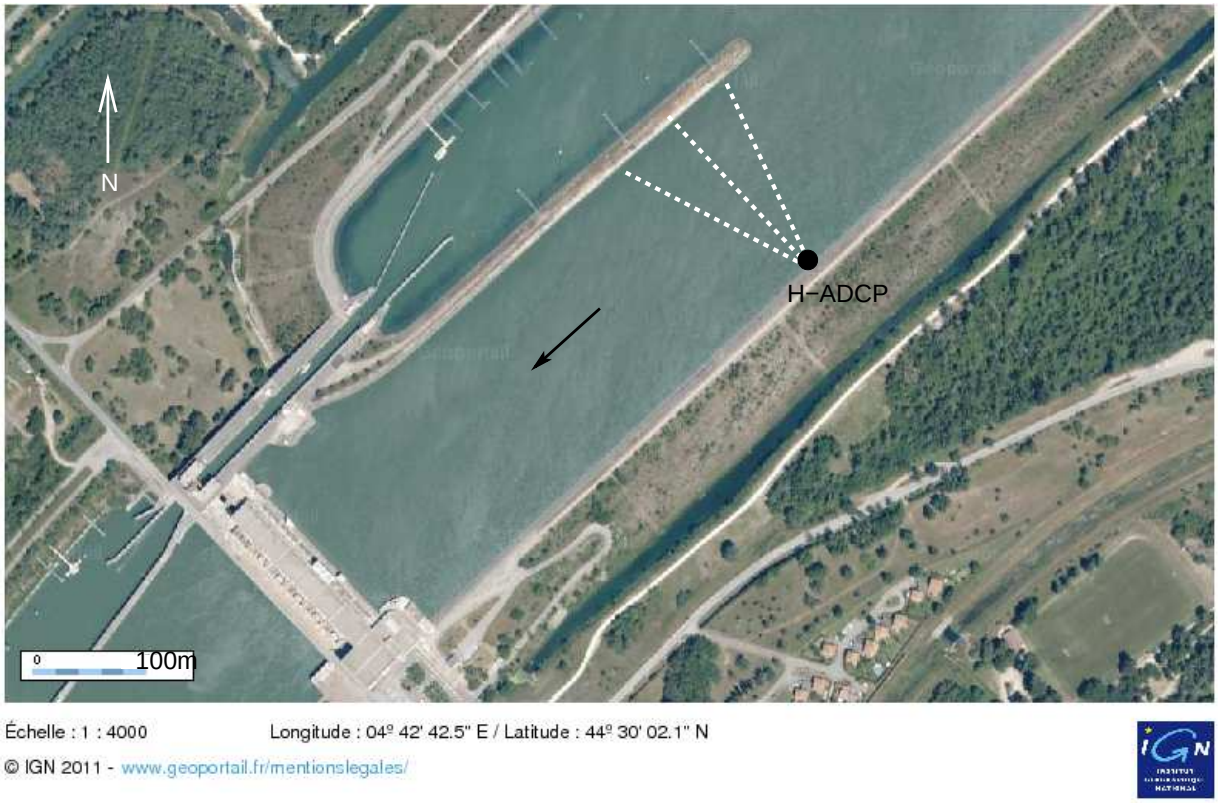

Figure 3.16: Aerial photograph of the Montélimar study site on the Rhône canal. The image is taken from Géoportail.

In terms of other instrumentation at Montélimar, a pneumatic gauge provides the water level

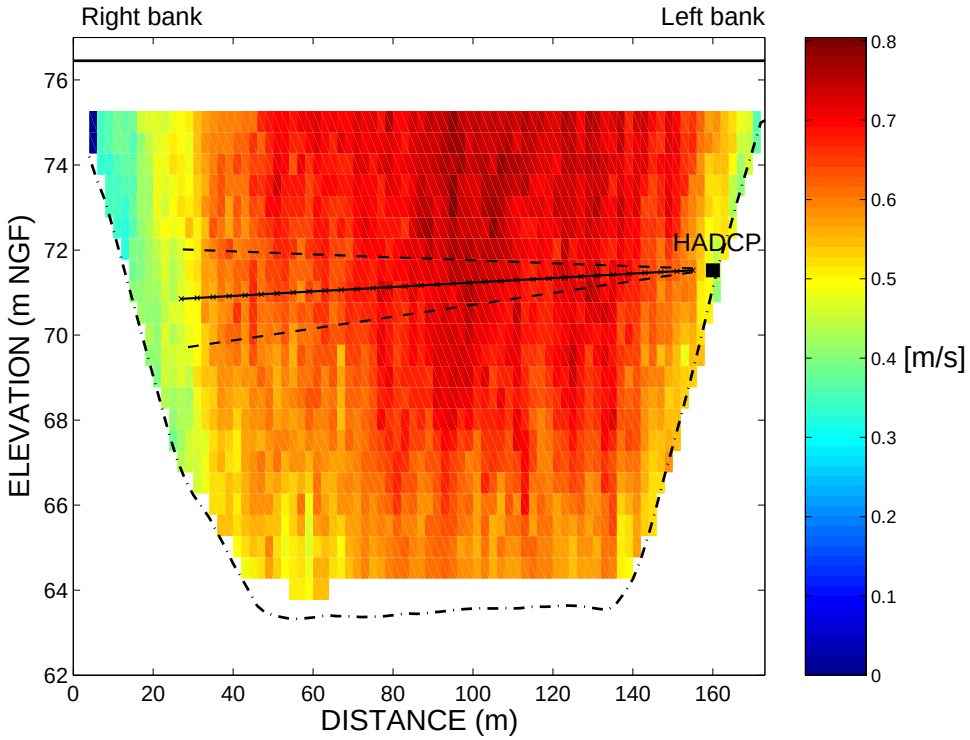

Figure 3.17: Upstream view of the velocity field at the Montélimar study site. The velocity data were obtained during moving-boat gauging with a 600 kHz ADCP and the magnitude of the velocity perpendicular to the ADCP crossing is shown. The dashed-dotted line is the river bathymetry. The horizontal ADCP is indicated as a square, the solid line represents the axis of the central transducer and dashed lines represent its beam width (-3dB transmitted power).

near the H-ADCP. These results are believed to be unreliable (*X. Martin, CNR, Personal communication, August, 2011*) and therefore the water level from the upstream end of the Châteauneuf dam is used in its place. It should essentially be equal to the water level at the H-ADCP. Discharge data from the Châteauneuf dam are available. A handful of gauging campaigns have been performed by CNR at Montélimar, but due to the proximity of the site to the dam, safety regulations prohibit frequent measurements.

Unfortunately we have no measurements of suspended sediment at this study site. However, we know that the suspended sediment should be predominantly controlled by the load brought downstream by the Isère river. Another controlling factor of the suspended sediment at Montélimar is the Châteauneuf dam which will have a tendency to retain fine sediments (dam in-filling). We have acoustic evidence that there may be regular resuspension of sediment from the bottom during dam operations, however we lack ground truth measurements to confirm this hypothesis.

3.4 Tricastin

Fifteen kilometers downstream of Montélimar is the Tricastin study site. This site, which belongs to EDF, is on the Donzère-Mondragon canal. It has been equipped with a 300 kHz Workhorse H-ADCP since June, 2006. The instrument is installed on the right bank at an elevation of 55.6 m NGF (IGN69). The water level at this site typically fluctuates between 57.9 and 58.6 m NGF (IGN69), meaning that the instrument is between 2 and 3 m deep. the pitch and roll are non-negligible. The pitch is -1.7° (instrument faces downwards) and the roll is 0.7° (downstream beam faces the surface, upstream beam faces the bottom). The H-ADCP settings are a blank distance of 2.5 m and a bin size of 2.0 m. The number of pings averaged per ensemble is 50 and the time between ensembles is 2 minutes. An external gauge measures the water level at this study site.

Only one velocity gauging campaign has been performed by Cemagref, but EDF has done a few dozen since the instrument's installation. The H-ADCP velocity data can also be compared to values calculated using the discharge from the Bollène dam (CNR) which is on the same canal, 8 km downstream. We do not have any concentration or grain size information at this study site, but daily measurements of concentration are available at Arles, which is 90 km downstream on the Rhône. The measurement station at Arles is the Station Observatoire du Rhône en Arles (SORA). It is run by Institut de Radioprotection et de Sûreté Nucléaire (IRSN), COM, CEFREM and CEREGE. The water samples collected at this location are time-weighted averaged: small amounts of water are collected in the same bottle throughout the day, so that the final sample represents the average concentration that day. During normal periods, there is one sample per day, but during floods, there are often hourly samples.

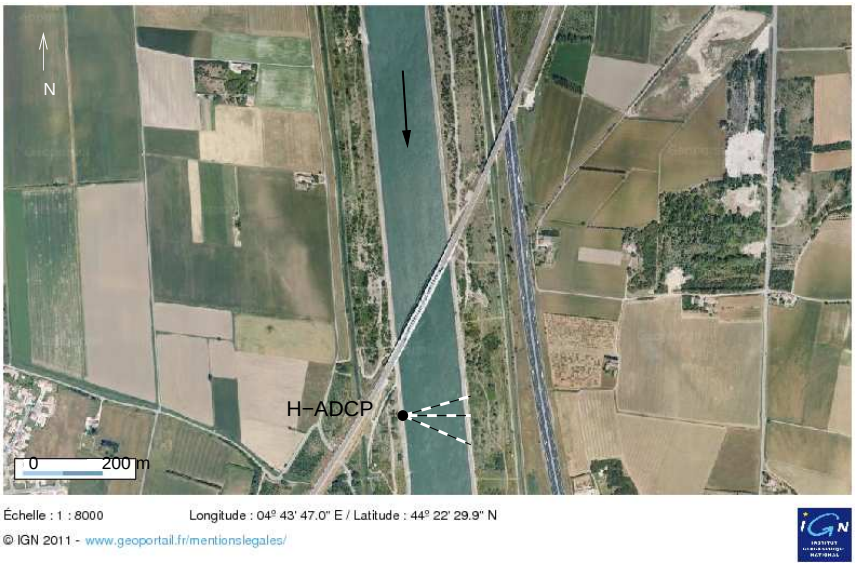

Figure 3.18: Aerial photograph of the Tricastin study site on the Donzère-Mondragon canal. The image is taken from Géoportail.

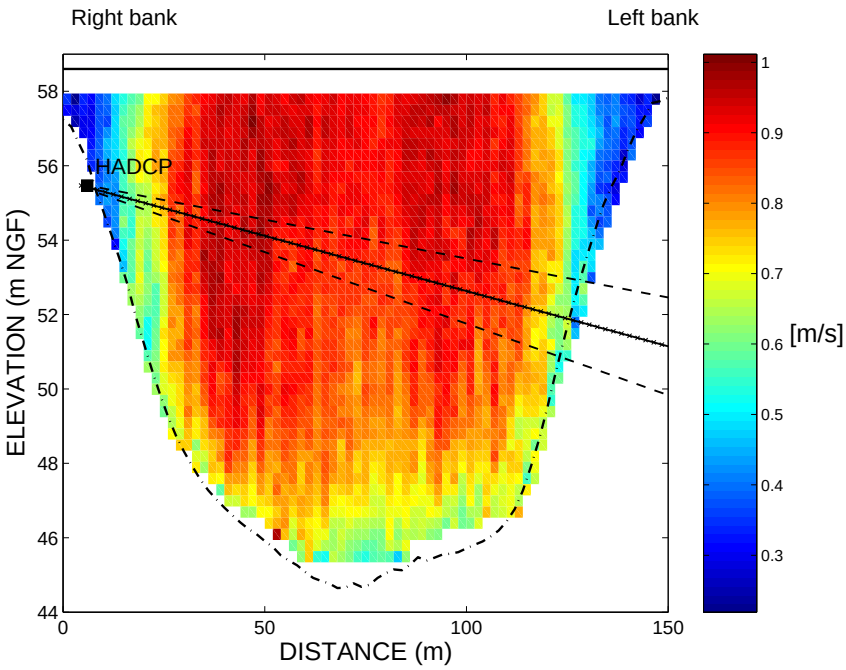

Figure 3.19: Upstream view of the velocity field at the Tricastin study site. The velocity data were obtained during moving-boat gauging with a 600 kHz ADCP, the values are the velocity magnitude perpendicular to the transect. The dashed-dotted line is the river bathymetry. The horizontal ADCP is indicated as a square, the solid line represents the axis of the central transducer and dashed lines represent its beam width (-3dB transmitted power).

3.5 Conclusion

The Romans-sur-Isère study site was presented in the first section of this chapter. Details of the hydrological conditions were provided, as were the concentrations and grain size distributions of the suspended sediment. The next three sections presented the Saint-Georges, Montélimar and Tricastin study sites in less detail. Table 3.8 summarizes the positioning and general specifications of the H-ADCPs used at these sites.

Table 3.8: A summary of the positioning and instrument specifications for the H-ADCPs used at Saint-Georges, Montélimar and Tricastin. The position is given in meters Nivellement Général de la France, and the average depth is given in meters. Positive pitch indicates upward inclination, positive roll indicates beam 1 facing upwards and beam 2 facing downwards. The beam width (β_0) and nominal maximum profiling range of each instrument are based on information from the instrument specification sheets. The distance to the far field of each instrument, r_n is also listed.

Site	Frequency (kHz)	Position (m NGF)	depth (m)	pitch (°)	roll (°)	max range (m)	β_0 (°)	r_n (m)
Saint-Georges	300	160	2.5	-0.4	-0.1	250	1	12.8
Montélimar	300	71.55	5	-0.3	0.2	250	1	12.8
Tricastin	300	55.6	2.6	-1.7	0.7	250	1	12.8

Of the four sites, the highest concentration values were observed at Romans-sur-Isère (> 10 g/L). This is because it is on the Isère river and is close to the mountains that supply the sediment. Concentrations on the order of 1 g/L occur during floods on the Rhône river downstream of the confluence with the Isère, while concentrations on the Saône at Saint-Georges rarely exceed 100 mg/L. The flow forcing conditions differ at the various study sites, but they are all controlled to some extent by dam operations. The bathymetry of the various study sites also differs noticeably. Romans-sur-Isère is a shallow study site compared to the other three and Montélimar and Tricastin are trapezoidal. The range of flow forcing conditions, boat traffic, geometry, instrument positioning and configuration observed in this study provide the grounds for a thorough investigation of the applicability of horizontal ADCPs to quantitatively measure sediment transport in medium-sized rivers.

CHAPTER 4

INFLUENCE OF THE H-ADCP POSITIONING ON THE PROFILES OF VELOCITY AND INTENSITY

This chapter focuses on an investigation of the proper positioning of horizontal acoustic Doppler current profilers in medium-sized rivers where depth can be limited. In order to have accurate measurements of flow velocity and suspended sediment concentrations, the instrument should be positioned horizontally (zero pitch and roll) so that all three transducers measure intensity and velocity at the same height above the bottom. The line of sight of each transducer must also be clear of obstructions which can bias the data. In terms of guidelines for the ideal deployment depth of the instruments, on page 12 of the *WorkHorse H-ADCP Operation Manual* (*RD Instruments*, 2008) it is stated that the ideal deployment depth is approximately 10 m submergence. Due to the limited depth of our river sites, we have sites where the submergence can be as little as one meter that were approved by the manufacturer. Referring once again to page 12 of the *WorkHorse H-ADCP Operation Manual*, there is a very misleading sentence about the deployment of H-ADCPs. The manual states that "The system is resilient to striking the **surface** at a grazing angle" (the word surface is in bold font in the manual). In our experience and in the experience of others (*A. E. Hay, personal communication, April, 2010*), this statement is false: striking the surface at a grazing angle can have an impact on the measurements of both velocity and intensity.

The goal of this chapter is to discuss the negative impact of scattering from obstructions on the measurements made using H-ADCPs. The majority of the chapter focuses on the impact of

scattering from the water-air interface. Results are predominantly presented from the Romans-sur-Isère study site, but measurements are also presented from the Montélimar study site for contrast since the geometry at this site is ideal. We felt that such an investigation was necessary since the literature and instrument manufacturer are somewhat vague on the subject, providing only suggestions for limiting aspect ratios. The first section of this chapter deals with scattering from obstacles such as boats and bridge pillars. The second section presents the measurements made at Romans-sur-Isère that lead to this study. The model for scattering from the surface is introduced in Section 4.3 and the results of the modelling are given in Section 4.4. Observations and model results from Montélimar and Saint-Georges are presented in Section 4.5 and the conclusions are presented in Section 4.6.

4.1 The impact of scattering from obstacles

Obstacles such as bridge pillars or large rocks in shallow rivers can block the line of sight of the a horizontal ADCP, often leading to misinterpretation of the data. In this study, obstacles on the river bottom limited the maximum profiling range of the H-ADCP at the St. Alban study site (Rhône river, EDF) and a pillar of a pedestrian bridge interfered with the measurements of the downstream beam of the H-ADCP at the Saint-Georges study site. Since the measurements at Saint Alban were of such poor quality, the site is no longer used and therefore it was not introduced in Chapter 3. An example of fifteen minutes of data from the downstream beam of the 300 kHz H-ADCP at Saint-Alban is shown in Figure 4.1. The peaks in the intensity profiles at distances greater than 50 m correspond to scattering from stumps of old bridge pillars. Figure 4.2 is 15 minutes of data from the downstream beam of the H-ADCP at Saint-Georges. The large peak that is centred around 90 m in Figure 4.2 corresponds to scattering from the left bank of the river. The smaller peak that is centred around 70 m corresponds to scattering from the bridge pillar just downstream of the instrument.

We refer to unmoving obstacles such as bridge pillars and the river bed as fixed targets. Fixed targets are easy to identify in the backscattered intensity profiles since they correspond to a peak in intensity at a set distance. If the fixed target occupies an entire measurement cell, then the range-corrected intensity of that cell ($I_{\text{dB}} + 20\log_{10} r + 2\alpha r$) should always be the same. If the obstacle does not occupy the entire volume of the measurement cell, then the scattering from the water will also have an influence on the backscattered intensity of the problematic cell, but the target itself should always scatter with the same intensity at the same distance.

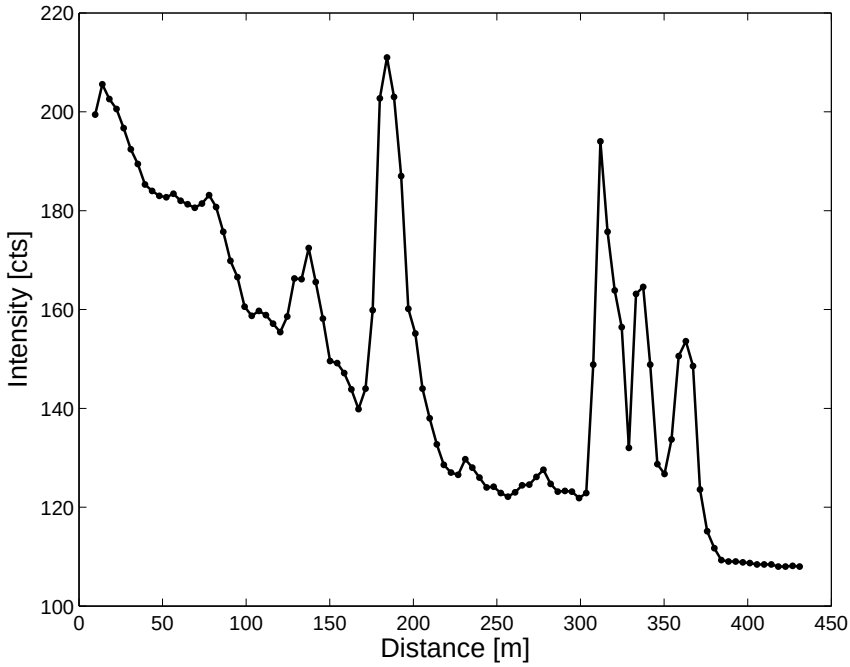

Figure 4.1: Fifteen minutes of intensity data from the downstream beam of the 300 kHz H-ADCP at the Saint-Alban study site. The peaks in intensity beyond 10 m are due to scattering from old bridge pillars.

Moving obstacles such as boats or the bubbles created in their wake can also interfere with our ability to accurately measure suspended sediment concentrations and velocity. During the hours of navigation on the Saône river, there can be upwards of three or four boats passing the St. Georges study site per hour in the summer months. The passage of boats is noticeable in the intensity data from each beam. If the ensemble times are short enough, one can see the passage of the boat from upstream to downstream by looking at the echo intensity data of the appropriate transducers. A trained user of horizontal ADCP data should be able to recognize the passage of boats in the echo intensity data.

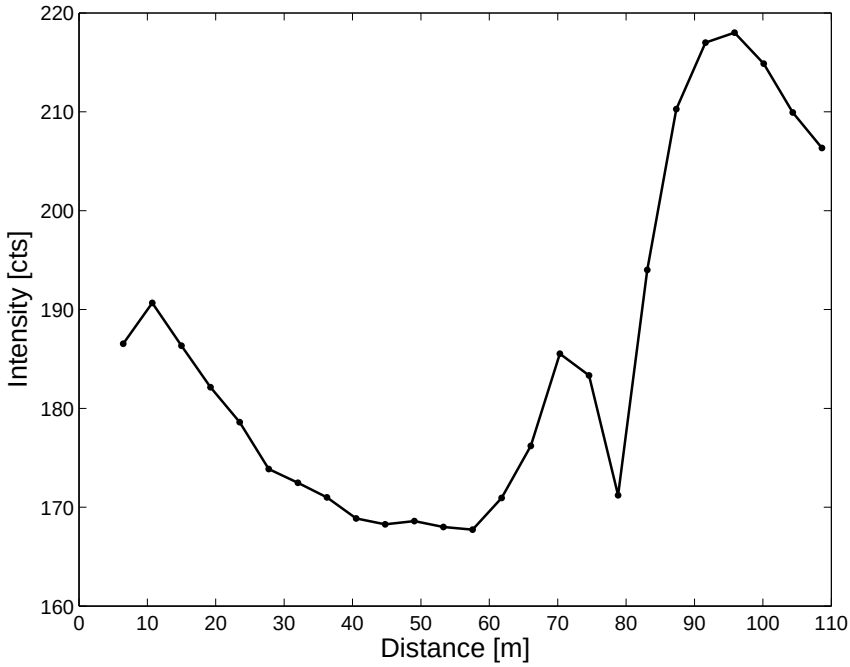

Figure 4.2: Example of fifteen minutes of data from the downstream beam of the 300 kHz H-ADCP at Saint-Georges. The peaks in intensity beyond 10 m are due to scattering from a bridge pillar and from the wall of the left bank of the river.

As an example of intensity data detected during a period of high boat traffic, Figure 4.3(a) is a time series of approximately 2.5 hours of backscattered intensity data collected with the central transducer of the H-ADCP at Saint-Georges on June 11, 2006. The zones of high intensity (red splotches) in Figure 4.3(a) correspond to the passage of boats. Figure 4.3(b) is the average intensity profile for fifteen minutes of data that appear to be unaffected by the passage of boats and Figure 4.3(c) is the equivalent plot for fifteen minutes of data that were affected by boat traffic.

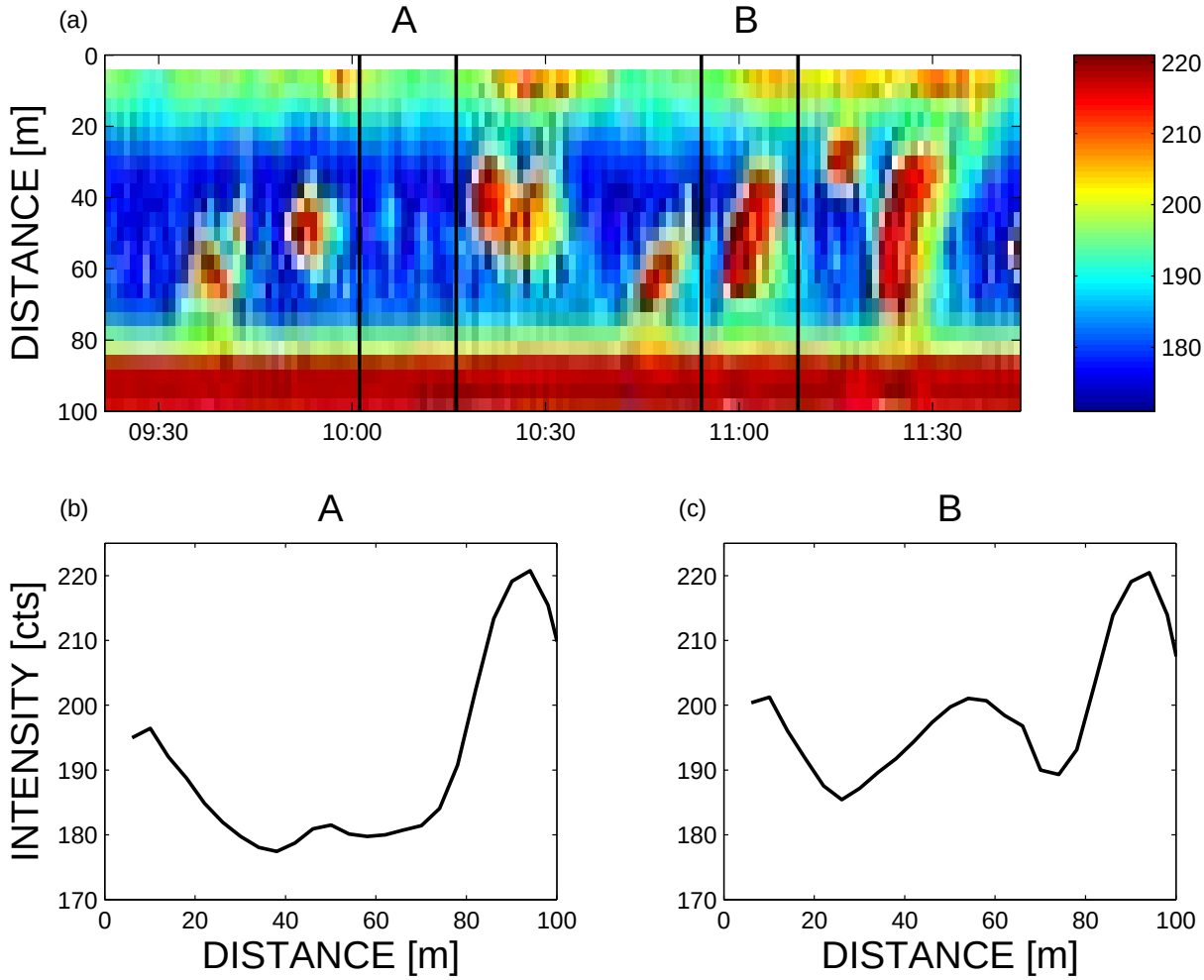

Figure 4.3: Echo intensity in counts measured with the central transducer of the H-ADCP at Saint-Georges on June 11, 2006 during a period of heavy boat traffic. (a) the raw intensity data; (b) the average profile in time period **A** - this corresponds to data seemingly unaffected by boat traffic; (c) the average profile in time period **B** - this corresponds to the passage of a boat.

4.2 Observations at Romans-sur-Isère

At the Romans-sur-Isère study site, there should be neither fixed targets nor frequent passage of boats in the line of sight of the instruments. Nonetheless, the intensity profiles that were recorded by the 300 and 600 kHz H-ADCPs were frequently inexplicable based on the concentrations of suspended sediment that were measured in water samples. The intensity profiles were irregular and the possibility of inhomogeneity of concentration or grain size across the river could not account for the magnitude of the fluctuations along the profile.

From the instrument configuration that was shown in Figure 3.3, it can be seen that the main

beam of both the 300 kHz and 600 kHz instruments intercept the surface 50 m and 60 m from the right bank, respectively. As a result, we did not expect to have valid measurements across the entire profile, but the data were perturbed at distances much nearer to the instruments than expected when concentrations were low ($\lesssim$ 0.03 kg/m^3 or equivalently, 30 mg/L). The velocity profiles were also perturbed at the same distances.

In order to test the validity of the H-ADCP velocity measurements, they were compared to velocities measured by vertically-oriented ADCPs deployed during repeated moving-boat transects under a variety of flow conditions. The ADCP data are used as the reference values since they provide an unbiased measure of velocity (*Oberg and Mueller*, 2007). An RD Instruments Workhorse RioGrande ADCP was secured to a bow swing mount attached to a motorboat. It was operated in RDI broadband mode 1. The frequency of the ADCP was either 600 kHz or 1.2 MHz, depending on the day. The acquisition bin size ranged from 30 cm to 40 cm and the results were 5-ping averaged. All data were referenced to ADCP bottom tracking. For each series of measurements, a minimum of six transects were performed. Transects typically began and ended two meters from each bank, and every effort was made to maintain a constant speed and straight path.

A vertical profile of the water column was obtained every 2 s which, depending on the boat speed, corresponded to profile widths of 5 - 30 cm. The straight-line distance from the departure point was recorded for each measured vertical profile. After ensuring that the flow conditions remained stable during the six transects, they were averaged. Averaging of ADCP data is required to yield accurate measurements of flow speed. The values from each (irregularly spaced) measurement cell of each transect were transposed onto a regular grid using inverse distance weighting and the transposed transects were averaged. The ADCP data from one transect performed on January 1, 2009 are shown in Figure 4.4a and the average of six transects is shown in Figure 4.4b. The cross-sectional averaged velocity measured by the ADCP was 0.66 m/s. The black dot-dashed lines in both subplots of Figure 4.4 indicate the river bottom according to ADCP bottom tracking.

In order to compare H-ADCP and ADCP measurements, H-ADCP data obtained during the time period corresponding to the ADCP transects (typically 15 minutes) were first isolated. The ADCP data were then projected onto the vertical plane that is centred on the axis of the H-ADCP. This was done using the heading of the H-ADCP and the directional data for each vertical velocity profile from the ADCP. The x and y coordinates of the centre of each H-ADCP measurement

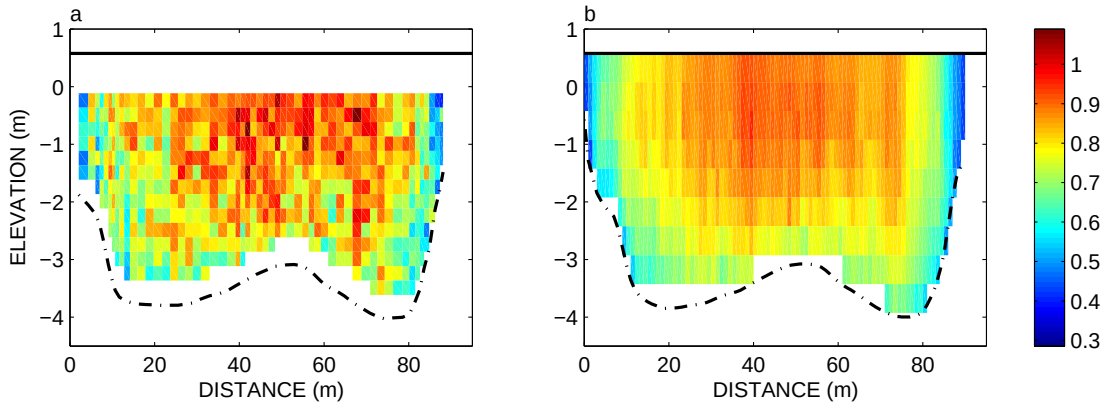

Figure 4.4: Velocity magnitude measured during ADCP gauging January 9, 2009 at Romans. Data obtained during one transect are shown on the left, while the average of six transects is shown on the right with velocities extrapolated to fill the water column.

cell were determined. In the same manner that the grid-averaged profiles of Figures 4.4b were obtained, the comparison ADCP data were determined using inverse distance weighted averaging at the positions of the H-ADCP cell centres. The end product is one ADCP value for comparison to the value in each H-ADCP measurement cell.

During this thesis, three gauging campaigns were performed at Romans-sur-Isère, but over a dozen gauging campaigns were performed prior to the thesis (*Pierrefeu*, 2008) (see Appendix B for relevant figure). Figure 4.5 is a comparison of the velocity profile measured by ADCP gauging on March 5, 2009 to the velocity profiles measured with the 300 and 600 kHz H-ADCPs at Romans-sur-Isère. It can be seen from this figure that there is substantial discrepancy between the ADCP and H-ADCP measurements.

In general, it was found that during periods of low velocity and concentration (mean velocities $\lesssim$ 1 m/s and concentrations on the order of 0.01 kg/m^3), the 300 and 600 kHz H-ADCPs underestimated velocity compared to measurements from ADCP gauging. The 300 kHz instrument underestimated the downstream velocity, v_x, in the far half of the river, while the 600 kHz instrument underestimated v_x across most of the river. To illustrate this, fifteen minutes of data collected by the two instruments during extended periods of (1) relatively low velocity and concentration (maximum velocity of 0.3 m/s and concentration of 0.012 kg/m^3) and (2) relatively high velocity and concentration (maximum velocity of 1.3 m/s and concentration of 0.045 kg/m^3) are shown side by side in Figure 4.6. The water level for the low velocity and low concentration

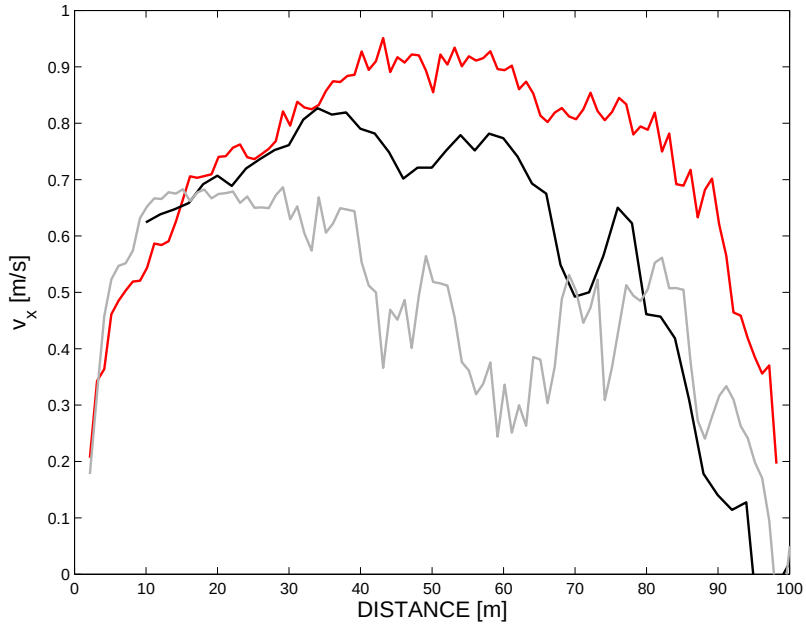

Figure 4.5: Comparaison between ADCP (red) and H-ADCP velocity data measured by the 300 kHz (black) and 600 kHz (gray) H-ADCPs at Romans-sur-Isère on March 5, 2009. The data are averaged over 15 minutes.

data was 0.09 m on the staff gauge, while it was 0.20 m for the high concentration and high velocity data. Velocity measurements are shown in the top two panels and intensity measurements are shown in the bottom two panels. The echo intensities have been converted from counts to decibels using Equation 6.1 and they have been corrected for losses due to spreading and attenuation by pure water in order to highlight their irregularities. In the remainder of this chapter, unless otherwise specified, "range-corrected intensity" will refer to the intensity in decibels corrected for spherical spreading and attenuation due to water.

If the instrument's line of sight was unobstructed and if grain size and concentration were homogeneous throughout the measurement volume, then we would expect to see velocity profiles having only positive values (i.e. downstream flow) with minima towards the edges and maxima towards the middle. We would also expect to see constant values of the range corrected intensity for all ranges less than 90 m, which is the distance at which the beams intercept the opposing river bank. This is more or less the case for the data collected when the concentration of suspended sediment was 0.045 kg/m^3 (see Figure 4.6(b,d)). However, when the concentration of suspended sediment was 0.012 kg/m^3, the velocity and intensity profiles were irregular for both instruments (see Figure 4.6(a,c)).

The low concentration data shown in Figure 4.6(a,c) are representative of a large portion of

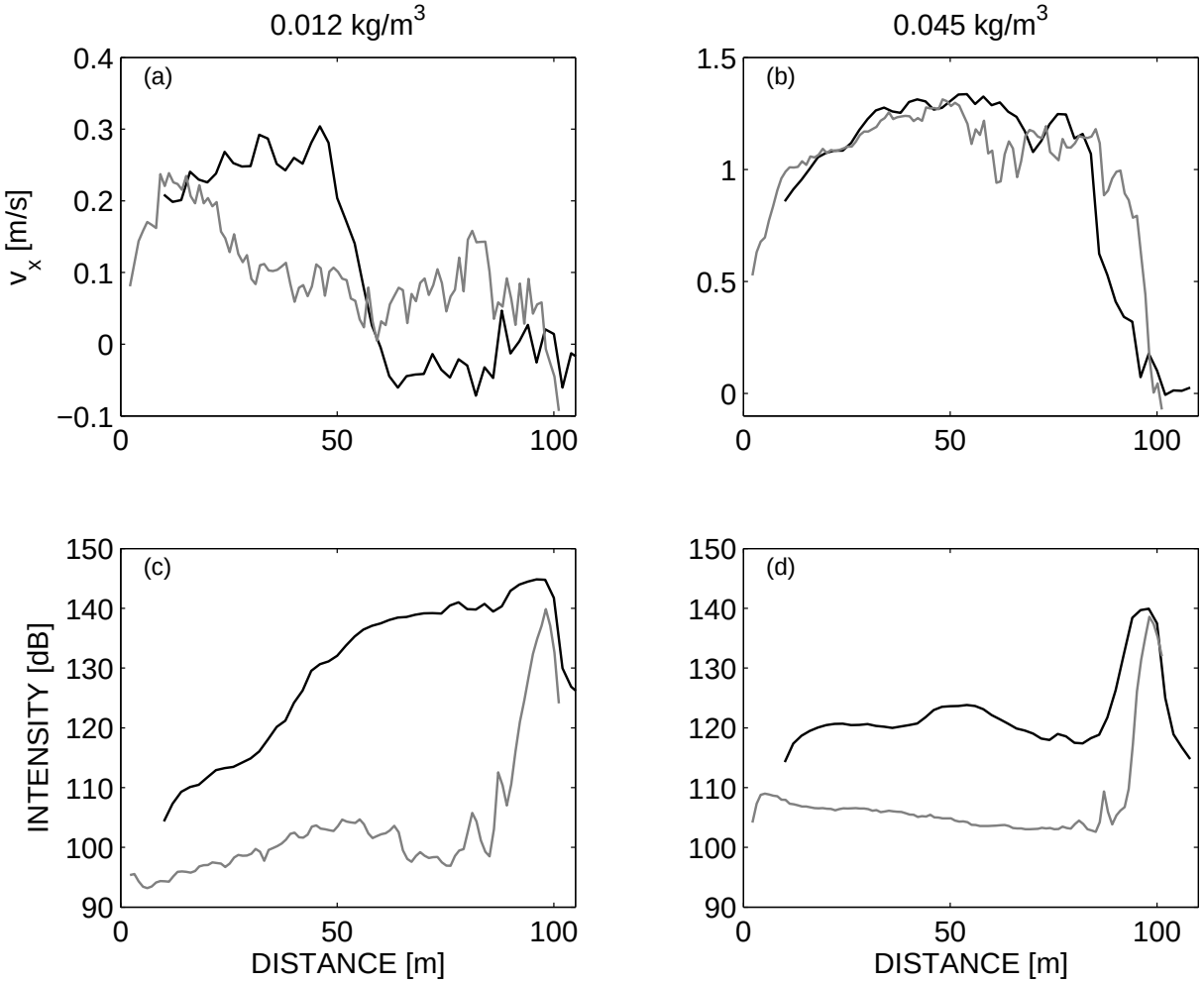

Figure 4.6: [(a,b)] Average streamwise velocity, v_x, measured by the 300 kHz (black) and 600 kHz (gray) H-ADCPs (a) November 25, 2009 between 18:15 and 18:30 (UTC+1) and (b) May 4, 2010 between 23:15 and 23:30 (UTC+1); [(c,d)] the corresponding range-corrected intensities measured by the central beam of each H-ADCP. Concentrations from the optical turbidity meter were 0.012 kg/m^3 for the data shown in panels (a,c) and 0.045 kg/m^3 for the data shown in panels (b,d) and the water levels were 0.09 m and 0.20 m, respectively. The distance from the right bank is plotted on the x axis.

the data collected when the concentration of suspended sediment was less than 0.020 kg/m^3 and the discharge was less than 100 - 200 m^3/s (mean velocities between 0.30 m/s and 1 m/s). This phenomenon of near-zero velocities and high intensities came and went in a continuous manner, despite constant values of discharge and concentration.

We suspect that when suspended sediment concentrations are low, the response of scattering from the air-water interface may over-power that from the suspended sediment and subsequently bias the results. Although the water at the air-water interface should move at the same speed

as the sub-surface water, capillary waves created by macro turbulence or wind-generated waves reflected from the river banks move in a variety of directions. If scattering from the air-water interface were to be detected by the transducers, we would expect to see high intensities and very low and irregular velocities. This is essentially what we observe. Consequently, in the remainder of this chapter we explore the influence of scattering from the air-water interface on the intensity profiles that are recorded by the 300 and 600 kHz H-ADCPs at Romans-sur-Isère through modelling. We also present observations and model results for the 300 kHz H-ADCP at the Montélimar study site for contrast, since this instrument is sufficiently deep (5 m), that scattering from the air-water interface should not pose a problem.

4.3 Modelling scattering from the air-water interface

In order to model the effect of scattering from the air-water interface on the backscattered intensity profiles, we model the surface as a Lambertian scatterer [1]. The intensity that is observed for scattering from a Lambertian surface is proportional to the cosine of the angle θ between the observer's line of sight and the surface normal. The incident power intercepted by the surface dA is $I_{\mathrm{i}} \cos\theta_{\mathrm{i}}$ dA, where I_{i} is the incident intensity and θ_{i} is the incident angle of the sound (see Figure 4.7 for geometry). The intensity that is scattered from a Lambertian surface is expressed as

$$I_s = \mu\, I_i \cos\theta \cos\theta_{\mathrm{i}}\, \mathrm{dA} \tag{4.1}$$

where μ is a proportionality constant known as the Lambert parameter.

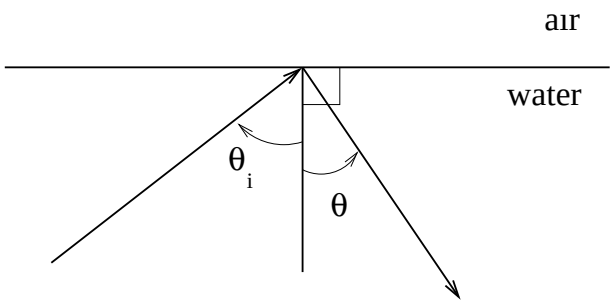

Figure 4.7: The relevant geometry for scattering from the air-water interface.

[1] N.B. We have simplified the analysis by using a continuous wave approach. This means that we have not accounted for the pulsed nature of the acoustic signal.

In oceanographic studies the seafloor is commonly treated as a Lambertian scatterer (see *Ainslie et al.* (2011), *Ellis* (2011), *LePage* (2011) or *Olson et al.* (2011) for a number of recent examples). The air-sea interface can also be treated as a Lambertian scatterer if the length scale of the surface roughness is on the same order as the incident wavelength (e.g. *Davis et al.*, 2002). Such is the case for our study if we consider the surface roughness to be created by capillary waves: the wavelength of the central frequencies of the 300 and 600 kHz H-ADCPs are 4.9 mm and 2.4 mm, respectively, while the root-mean-square amplitude of capillary waves will likely range from O(0.1 mm) - O(1 cm). Thus, there will likely be capillary waves from which the sound can be scattered.

Since the H-ADCPs are monostatic, we are only concerned with the case of backscatter, this is the special case for which $\theta = \theta_{\mathrm{i}}$. The backscattered intensity, I_{bs}, can be expressed as

$$I_{bs} = \mu \cos^2(\theta)\, I_i \,\mathrm{dA}\,. \tag{4.2}$$

The intensity that is incident on the surface is calculated for a given water level and angle of inclination of the instruments using Equation 2.11 to calculate the directivity patterns of the transducers for the beam widths listed in Tables 3.1 and 3.8. The geometry of the situation is shown in Figure 4.8, which is a side view of the central transducer of an H-ADCP tilted upwards and fixed at a depth of z_0 below the surface. For the ideal case where the instrument faces directly across-stream, this is an upstream view. The positive z direction is towards the surface, the x-axis extends outwards from the face of the transducer (it should be parallel to the cross-channel direction), and the y-axis is parallel to the face of the transducer and points upstream. The vector $\vec{R_0}$ is coincident with the axis of the transducer and $\vec{R}$ is the vector between the origin of the transducer and a point on the surface. The angle between the two vectors is β. Since we are only considering the case of backscatter, θ is the incident angle on the surface and its complement γ is the grazing angle. The vector $\vec{r}$ is the x and y component of $\vec{R}$, so that $\vec{R} = \vec{r} + z_0\hat{k}$. The vector $\vec{r}$ just happens to be parallel to the x-axis in this figure, but this is not always the case.

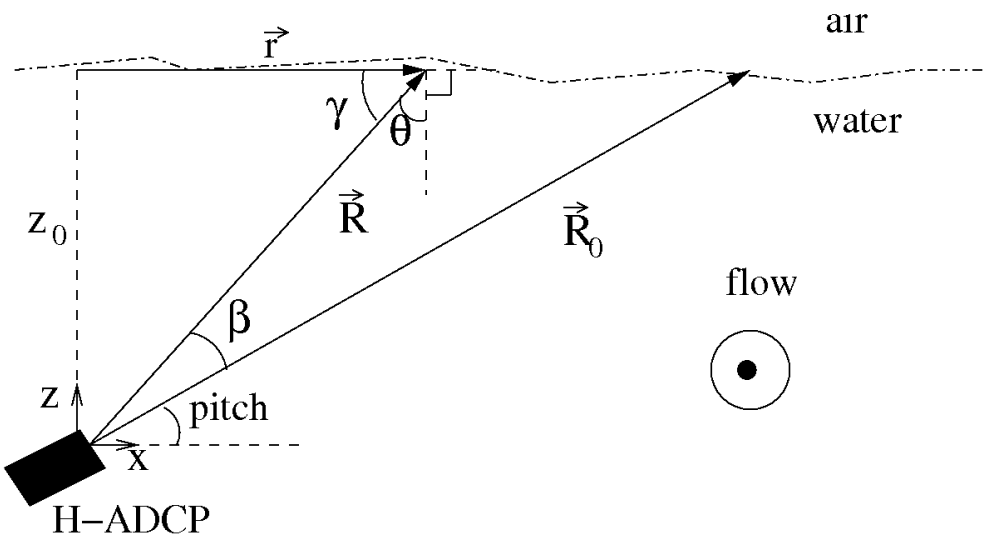

Figure 4.8: The relevant geometry in the vertical plane for a transducer installed at a depth z_0, angled upwards. The vector $\vec{R_0}$ is co-incident with the axis of the transducer. The vector $\vec{R}$ is between the transducer and the point of insonification of the surface; it is not necessarily in line with the x axis.

Figure 4.9 is a top view of the same system. The black dot depicts the point at which the axis of the transducer intercepts the surface, this corresponds to $y = 0$ and $x = x_0$, so that $\vec{r_0} = x_0\hat{\imath}$. The black square depicts the point of interception of the vector $\vec{R}$ with the surface, r is the distance along the surface between the location of the centre of the transducer and the point of insonification and the angle between this point and the x-axis is ϕ. For the geometry depicted in Figures 4.8 and 4.9 we have:

$$\begin{aligned} \vec{R_0} &= x_0\hat{\imath} + z_0\hat{k} \\ \vec{r} &= x\hat{\imath} + y\hat{\jmath} = r_j \cos\phi_k\hat{\imath} + r_j \sin\phi_k\hat{\jmath} = x_{jk}\hat{\imath} + y_{jk}\hat{\jmath} \\ \vec{R} &= x\hat{\imath} + y\hat{\jmath} + z\hat{k} = x\hat{\imath} + y\hat{\jmath} + z_0\hat{k}. \end{aligned} \tag{4.3}$$

where j is the index of the radial coordinate, and k is the index of the angular coordinate, not to be confused with the unit vectors $\hat{\jmath}$ and $\hat{k}$. In order to calculate the angle β between the axis of the transducer and the point of insonification on the surface for a vector $\vec{R}$, we use the trigonometric identity

$$\vec{R} \cdot \vec{R_0} = \|\vec{R}\|\|\vec{R_0}\| \cos\beta \tag{4.4}$$

which yields the following for the cosine of the angle between the two vectors at distance r_j and azimuth ϕ_k:

$$\cos\beta_{jk} = \frac{x x_0 + {z_0}^2}{\left[\left({x_{jk}}^2 + {y_{jk}}^2 + {z_0}^2\right)\left({x_0}^2 + {z_0}^2\right)\right]^{1/2}} \tag{4.5}$$

where

$$\begin{aligned} x_{jk} &= r_j \cos\phi_k \\ y_{jk} &= r_j \sin\phi_k. \end{aligned}$$

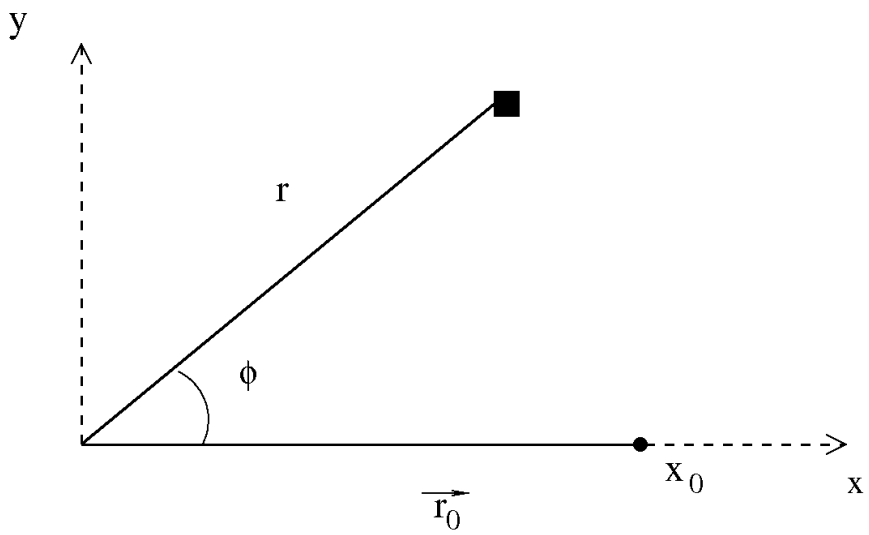

Figure 4.9: Top view of the geometry of Figure 4.8. The black dot at x_0 is the point of interception of the axis of the transducer with the surface and the square is the point of interception of the vector $\vec{R}$ with the surface.

Using Equation 2.8, we define the intensity that is incident on the surface, I_i, as

$$I_\mathrm{i} = \frac{|p_\mathrm{i}|^2}{\rho c} \tag{4.6}$$

where p_i is the incident pressure and ρ and c are the density and sound speed of water. In the same way, we define the intensity of the wave at distance r_* as

$$I_* = \frac{|p_*|^2}{\rho c}. \tag{4.7}$$

In order to obtain an expression for the intensity incident on the surface at a distance within the far field of the instrument, we combine Equations 4.6, 4.7 and 2.10 (N.B. The distance from the transducer to the point of insonification was represented as r in Equation 2.10 whereas it is now represented as $\|\vec{R}\|$). This yields

$$I_{\mathrm{i}} = \frac{I_* {r_*}^2 D^2 e^{-2\alpha\|\vec{R}\|}}{\|\vec{R}\|^2} \tag{4.8}$$

with

$$\|\vec{R}\| = \left(r^2 + {z_0}^2\right)^{1/2}. \tag{4.9}$$

Taking the reference distance r_* to be 1 m, the intensity that is incident on the surface relative to the intensity I_* can be written as:

$$\frac{I_{\mathrm{i}}}{I_*} = \frac{D^2 e^{-2\alpha\|\vec{R}\|}}{\|\vec{R}\|^2}. \tag{4.10}$$

In Figure 4.10 we have plotted I_{i}/I_* as a function of r and ϕ for the central transducer of the 300 kHz instrument at Romans-sur-Isère. These values were computed using the mean water level recorded throughout our study period: 0.16 m on the staff gauge; this corresponds to an instrument depth of 2.32 m below the surface. The pitch of the instrument is 1.8° towards the surface and the value of α used in this calculation was 0.0033 m^{-1}. This is the standard value for pure water at 10°C; it is calculated as $\alpha = 3.52 \times 10^{-8} F^2$ where F is the frequency in kilohertz (e.g. *Hay*, 1983, Equation 9). The instrument is plotted as a black square in Figure 4.10 and the point of interception of the axis of the transducer with the surface is shown with an x. It can be seen that the distance from the instrument at which the surface has the greatest influence is about 10 m before this point. This is primarily due to intensity loss from spherical spreading.

Lambert's law is used to calculate the intensity of the sound scattered from the air-water interface by combining Equations 4.2 and 4.10. Spherical spreading and attenuation are accounted for on both the outgoing and return paths. Since the backscattered sound that is interpreted as coming from the distance $\|R_0\|$ along the instrument's axis actually corresponds to the sound coming from all points that are a distance $\|R_0\|$ away, there will be some contribution from scattering from the surface to the intensity values recorded at all ranges greater than or equal to the depth of the instrument. Therefore, in order to determine the impact of the surface at a given range $\|R_0\|$, we must sum the contributions from all points having the same path length. The

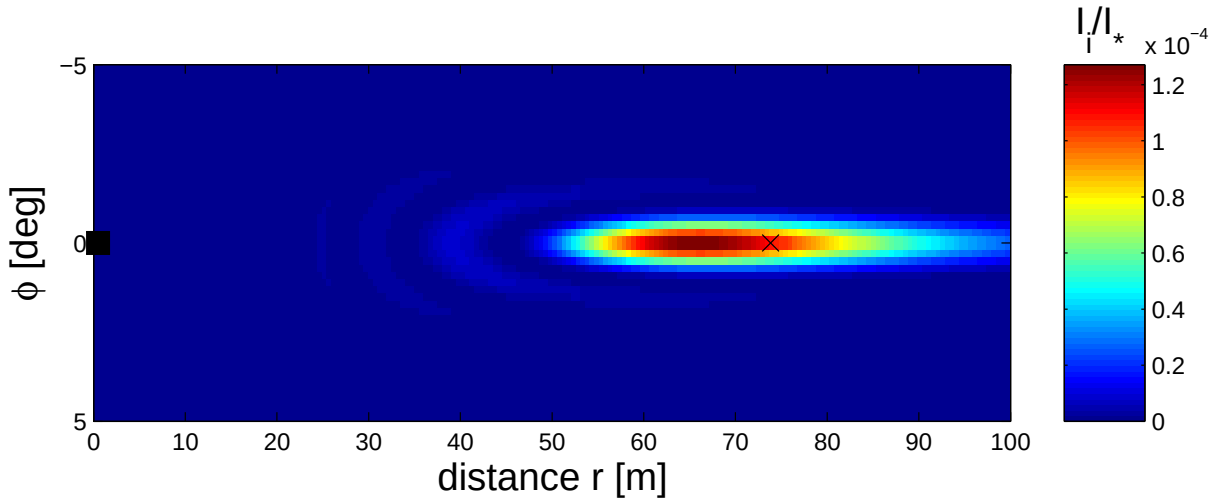

Figure 4.10: The theoretical intensity incident on the air-water interface for the central transducer of the 300 kHz H-ADCP at Romans-sur-Isère, relative to I_*. The location of the H-ADCP is shown as a black square and the point of interception of the axis of the transducer with the surface is shown as a black x. The attenuation α is 0.0033 m^{-1} in this calculation.

intensity that would be detected for scattering from the air-water interface at the radial distance r_j can be expressed as

$$I_{\text{detected}\,j} = \frac{\mu \cos^2(\theta_j)\, I_*\, e^{-4\alpha R_j}}{{R_j}^4} \sum_{k=-\phi}^{\phi} {D_{j,k}}^4\, r_j dr d\phi, \tag{4.11}$$

where $D_{j,k}$ is the directivity calculated at range r_j and angle ϕ_k. Note that the angle of incidence on the surface, θ, is only a function of r_j. Also, due to the small angle of inclination of the instruments, the range r along the surface is essentially equal to the range along the axis of the transducer which was also represented as r in Chapter 2.

Figure 4.11 is a plot of the intensity that would be detected by the central transducer of the 300 kHz H-ADCP at Romans-sur-Isère for scattering from the air-water interface at all ranges in its far field. These values are computed using the incident intensity pattern shown in Figure 4.10 combined with Equation 4.11, using $\mu = 1$, as an example. The dependence of I_{detected}/I_* on range r is plotted on both a linear and logarithmic scale. The wiggles that are seen at ranges less than 50 m correspond to the interception of the various side lobes with the surface.

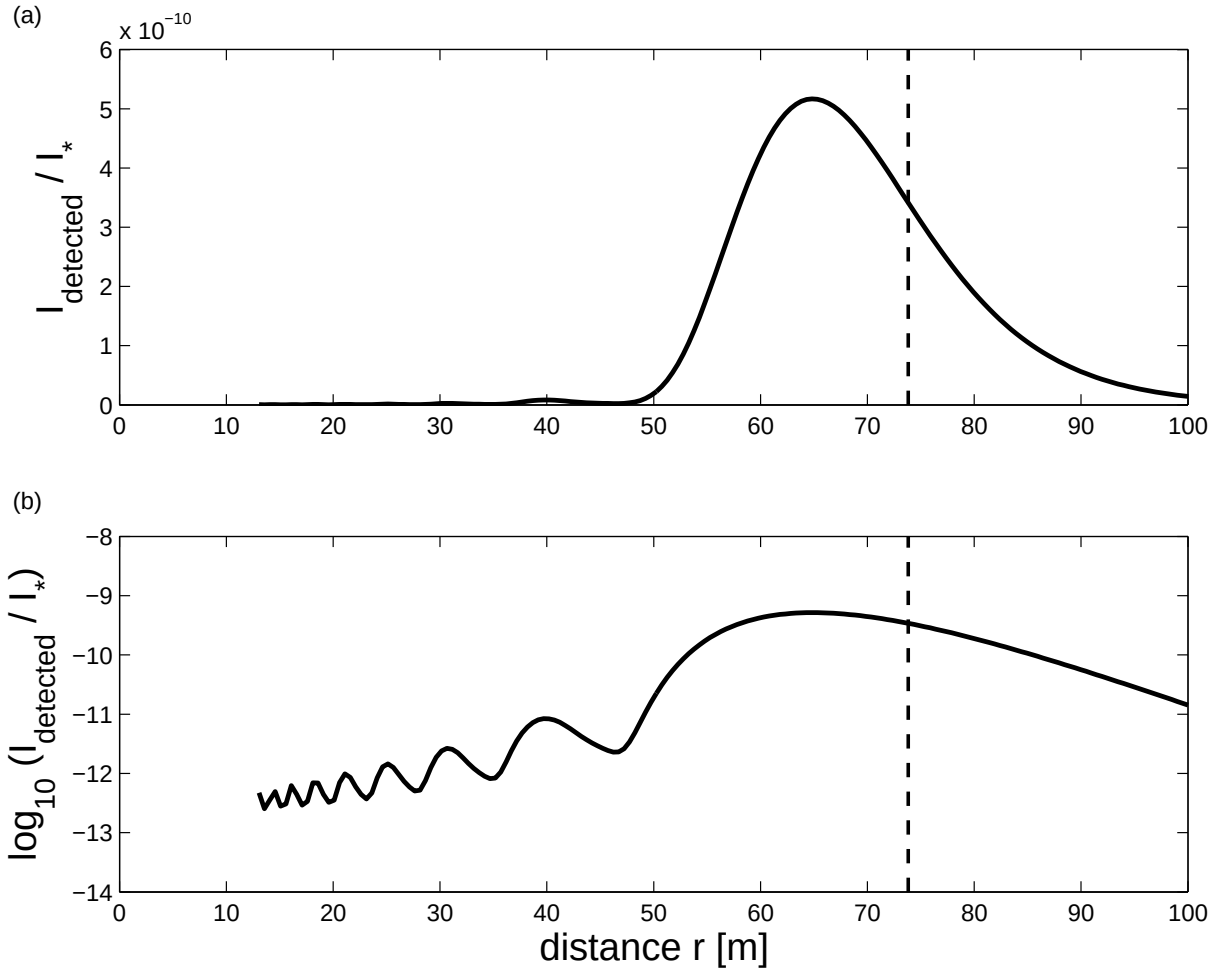

Figure 4.11: The theoretical intensity detected by the 300 kHz H-ADCP for scattering from the air-water interface, normalized by I_*. The point of interception of the axis of the transducer with the surface is shown as a dashed line. The Lambert parameter for this calculation is $\mu = 1$ and α = 0.0033m^{-1}.

4.4 Comparison of model results to data at Romans-sur-Isère

Using the procedure outlined in Section 4.3, we calculate the theoretical intensity profiles that would be measured by the central transducer of the 300 and 600 kHz instruments at Romans-sur-Isère for scattering from the air-water interface. Values are computed for a water level of 0.09 and 0.21 m on the staff gauge in order to show the effect of a varying water level. The theoretical intensity profiles are corrected for spreading and attenuation due to water so that the expression for the range-corrected theoretical intensity detected by the transducer (in decibels) at range r is

$$SL + 10\log_{10}(I_{\text{detected}}/I_*) + 20\log_{10} r + 2\alpha_w r, \tag{4.12}$$

where SL is the source level. The sediment attenuation is neglected because it is an order of magnitude less than the attenuation due to water for both instruments when the temperature is 10°C and the particle concentration is 0.010 kg/m^3.

The source levels for both instruments were taken to be 216 dB. This is the value given for a RD Instruments 300 kHz Workhorse Navigator DVL on their frequently asked questions website (`http://www.rdinstruments.com/nav_faq.aspx#two`, October, 2011). We were unable to find values for the Lambert parameter μ for the water-air interface in the literature. Since the objective of this modelling was to understand the form of the intensity profiles and not the absolute values, the Lambert parameter was taken to be the commonly used value for the ocean floor, 0.002 (e.g. *Ainslie et al.*, 2011; *Ellis*, 2011).

The theoretical profiles of range-corrected intensity for scattering from the surface for the two water levels (0.09 m and 0.21 m) are depicted as solid lines in Figure 4.12(a) for the 300 kHz H-ADCP and Figure 4.12(b) for the 600 kHz instrument. The wiggles that are seen in the theoretical profiles at ranges less than 50 m for the 300 kHz instrument and ranges less than 20 m for the 600 kHz instrument correspond to the interception of the various side lobes with the surface. These theoretical profiles are compared to two examples of data for the same water levels. The concentration from turbidity was 12 mg/L when the water level was 0.09 m and 22 mg/L when the water level was 0.21 m. To contrast the theoretical scattering from the surface, horizontal lines are depicted to represent what would be expected for scattering from a homogeneous suspension of particles.

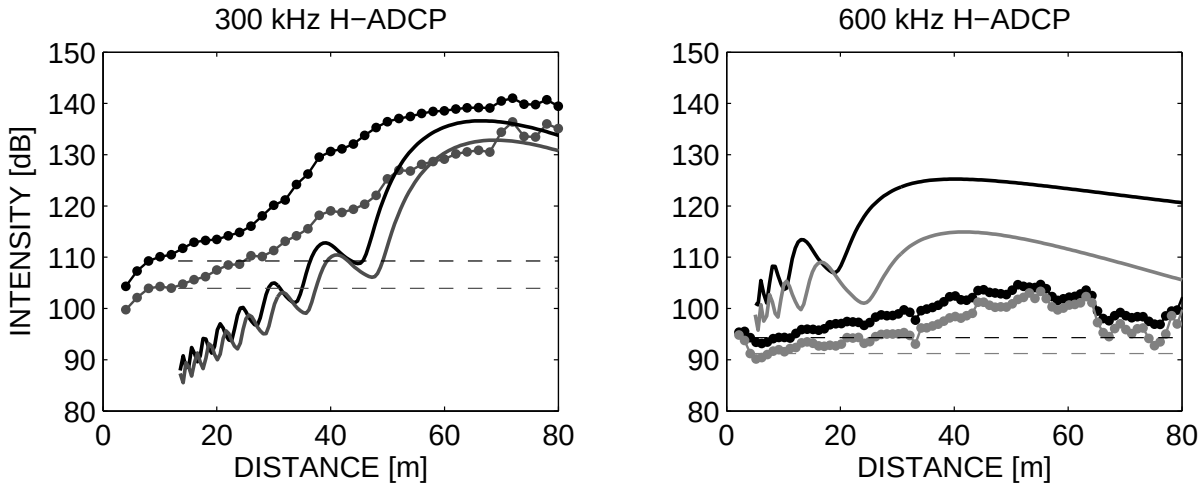

Figure 4.12: Theoretical profiles of the range-corrected intensity for scattering from the air-water interface in the far field of the transducers (solid lines) compared to measurements (dotted solid lines) for (a) the 300 and (b) the 600 kHz H-ADCPs for water levels of 0.09 m (black) and 0.21 m (gray) on the staff gauge. The concentrations from turbidity for the two data sets were 12 mg/L and 22 mg/L, respectively. Data are averaged over 15 minutes and the same time periods are used for both instruments. The dashed lines depict what would be expected for scattering from a homogeneous suspension of particles.

Comparison of the theoretical and experimental intensity profiles in Figure 4.12 reveals that the intensity profiles that were observed during periods of low flow and low suspended sediment concentration have a similar form to the theoretical profiles for scattering for the air-water interface. Even though a continuous wave approach was taken in this analysis, these results are sufficient to demonstrate that scattering from the surface was the reason for the velocity underestimation by the H-ADCPs when suspended sediment concentrations were low. In an attempt to avoid scattering from the surface, the positionings of the 300 and 600 kHz H-ADCPs were altered in December, 2010. The old and new positioning of both instruments are shown in Figure 4.13, which is an upstream view of the geometry of the central transducer of the 300 and 600 kHz H-ADCPs. The depth, pitch and roll before and after repositioning are summarized in Table 4.1.

Table 4.1: The positioning of the 300 and 600 kHz horizontal ADCPs at Romans-sur-Isère before and after December 14, 2010. Depth is given with respect to the zero on the staff gauge, positive values of pitch indicate upward inclination and positive roll indicates beam 1 facing upwards and beam 2 facing downwards.

Instrument	Before			After		
	depth (m)	pitch (°)	roll (°)	depth (m)	pitch (°)	roll (m)
300 kHz	-2.16	1.8	0.1	-2.16	0.7	-0.1
600 kHz	-0.36	0.1	-0.4	-1.5	-0.5	-2.5

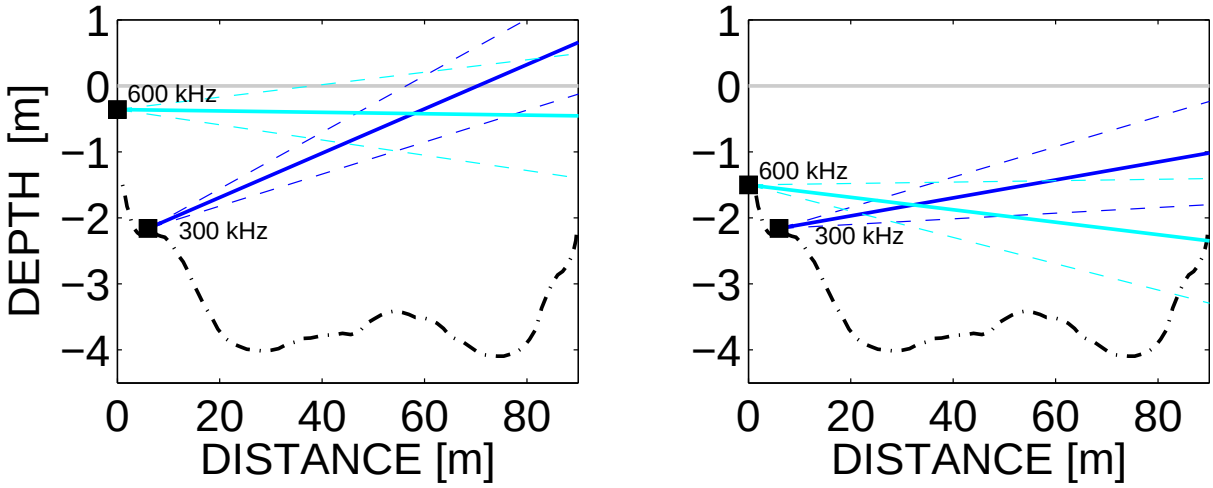

Figure 4.13: Positioning of the 300 and 600 kHz H-ADCPs at the Romans-sur-Isère study site before and after their repositioning on December 14, 2010. The zero level corresponds to the surface of the water. The dashed lines show the half-power angle of the main beam.

Figure 4.14 is a plot of the theoretical predictions of range-corrected intensity for scattering from the air-water interface for the two instruments before and after repositioning. The calculation is done for the mean water level, 0.16 m on the staff gauge. The theoretical decrease in the overall level of scattering shows that the impact of the surface on the backscattered intensity profiles should be less for the new position of both instruments. The range-dependence of the scattering from the surface for the 300 kHz instrument should also be less pronounced. As for our observations, improvement in the intensity data from the 300 kHz instrument was seen, though there now appears to be a problem with scattering from the bottom. The re-positioning of the 600 kHz instrument did not improve the velocity measurements since it now has a non-negligible roll. The roll of the instrument went from being -0.4° to -2.5°.

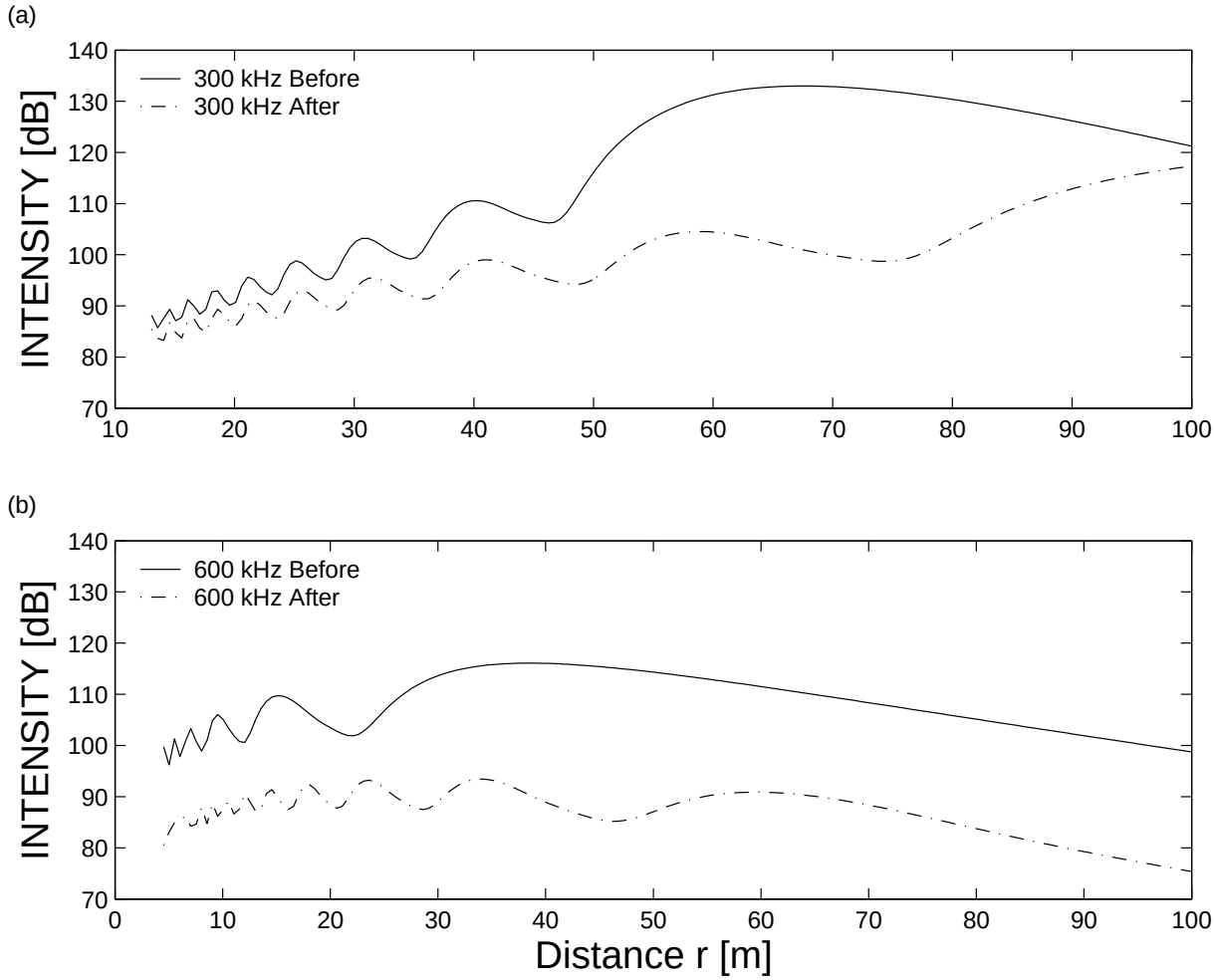

Figure 4.14: Theoretical profiles of the range-corrected intensity for scattering from the air-water interface in the far field of the central transducer of (a) the 300 kHz H-ADCP and (b) the 600 kHz H-ADCP at Romans in the old (solid line) and new (dashed-dotted line) positioning. These values were computed for a water level of 0.16 m, SL of 216 dB and μ of 0.002.

The accuracy of the velocity measurements made with horizontal ADCPs relies on the assumption that each transducer sees the same streamlines. Since the downstream beam of the 600 kHz transducer is currently angled downwards and the upstream beam is angled upwards, this assumption is no longer valid. Furthermore, the upstream beam intercepts the surface and the downstream beam intercepts the bottom at distances closer to the instrument than the range at which the surface was previously intercepted. As a consequence, measurements of velocity from the 600 kHz H-ADCP cannot be used, even when concentrations are high. The velocity profiles from the 600 kHz instrument tend to always have the same caved-in form that is seen in Figure 4.15(b), even during high flow conditions. Nevertheless, the intensity data make for an

interesting case study since we have simultaneous measurements of scattering from the bottom, water column and surface with the same instrument.

The low flow data that were previously presented in Figure 4.6 (a,c) are reproduced in Figure 4.15(a,c) and further low-flow data collected mid-January after the repositioning of the instruments are shown in Figure 4.15(b,d). The intensity data from all three beams of the 600 kHz instrument are shown in order to illustrate the effect of the change in the roll. In Figure 4.15(c,d), it can be seen that when the roll is -0.4°, all three transducers detect very similar signals, while their measurements are noticeably different when the roll is -2.5°. In the instrument's current position, the data from the upstream beam are very noisy and the form of the profile evolves with time as it would for scattering from the air-water interface. (Please note that the time evolution of the signal is not discernible from Figure 4.15.) The forms of the range-corrected profiles from the central and downstream beams now change negligibly with time. A second observation is that the range-corrected intensity for the central and downstream beams appear to decrease with range. We suspect that this is the result of scattering from the bottom which may be more pronounced closer to the instrument.

The only improvement in the low flow measurements appears to be the intensity profiles of the 300 kHz H-ADCP, which are now independent of time. However, the two contiguous bumps that can be seen between 30 and 45 m from the right bank in Figure 4.15(d) are now a permanent feature of the range-corrected intensity profiles. We believe this to be the result of scattering from the bottom which would explain the underestimation of velocity in the centre of the river that can be seen in Figure 4.15(b).

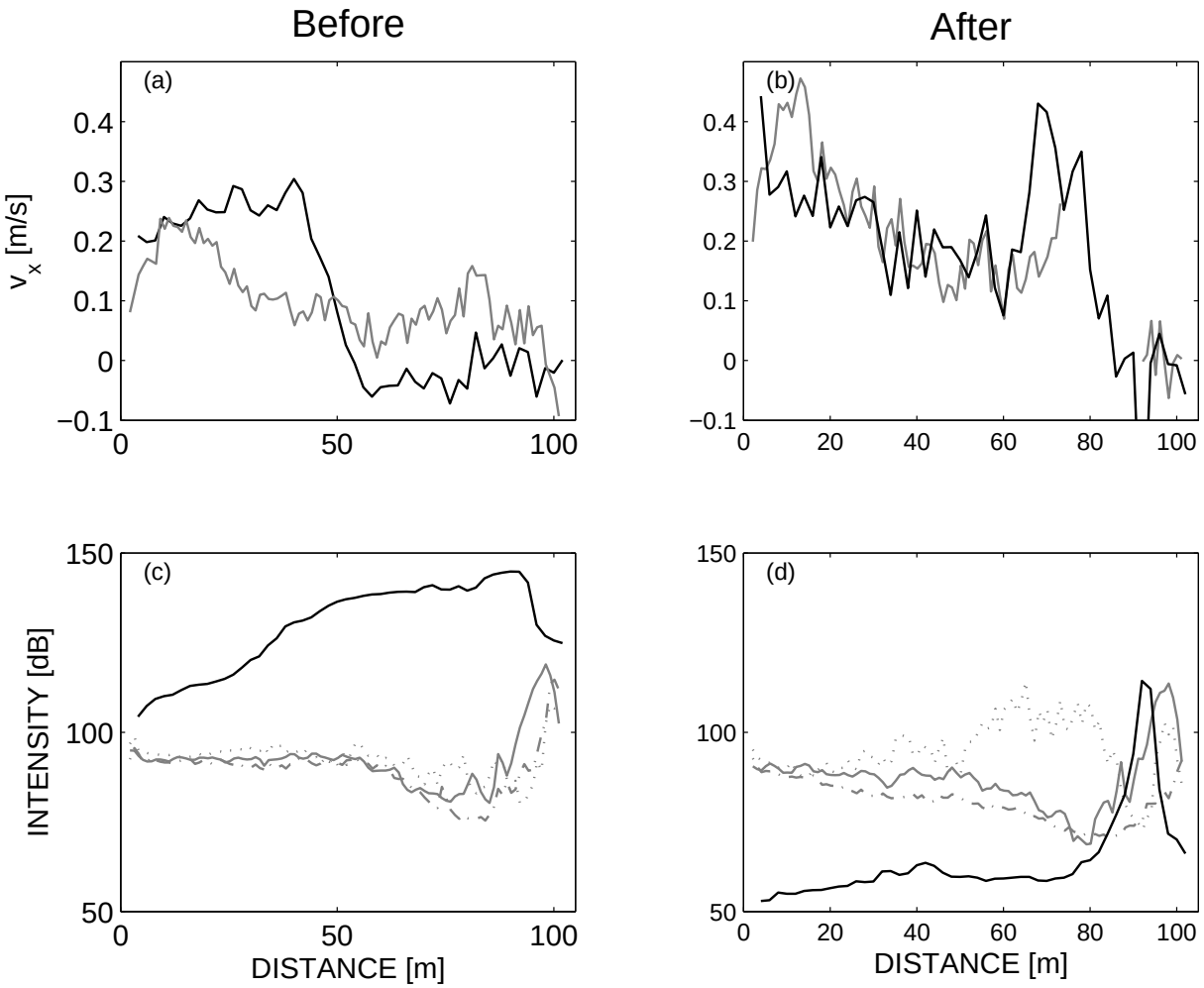

Figure 4.15: Along-stream velocity profiles (top panels) and range-corrected intensity profiles (bottom panels) measured with the 300 kHz (black) and 600 kHz (gray) instruments at Romans-sur-Isère. The data in panels (a) and (c) were collected before the instrument repositioning and the data in panels (b) and (d) were collected afterwards. Data are averaged over 15 minutes and the same time periods are used for both instruments. Solid lines indicate data from the central beam, dotted from the upstream beam, and dashed-dotted from the downstream beam.

4.5 Comparison to data from Montélimar and Saint-Georges

In order to contrast the data from Romans-sur-Isère, which is clearly a problematic study site, we present data from Montélimar. This study site is ideal for measurements since the H-ADCP is more than 6 m from the bottom and it is typically submerged by 5 m. The minimum submergence observed throughout the study period was 4.5 meters. Figure 4.16 shows three examples of range-corrected intensity profiles measured at Montélimar during periods of high, medium and

low flow speeds. As in the rest of this chapter, our use of the expression "range corrected" implies that $20\log_{10} r$ and $2\alpha_{w,\mathrm{dB}}\, r$ have been added to the intensity in decibels at each range r. The mean velocities across the corresponding H-ADCP velocity profiles for the data shown in Figure 4.16 were 1.11 m/s, 0.55 m/s, and 0.22 m/s. We do not have concentration measurements at this site, but the observations are consistent with what we would expect for concentrations sufficiently low that there is no attenuation: the higher the flow speed, the higher the range-corrected backscattered intensities, which implies either higher concentrations and/or larger particles in suspension.

The same y-axis as in Figures 4.15(c,d) has been used to facilitate comparison between the Romans-sur-Isère and Montélimar data. It can be seen that while the range-corrected intensity profiles observed at Romans-sur-Isère could fluctuate by tens of decibels before interception with the opposing river bank, the fluctuations across more than 100 m at Montélimar are between one and two decibels. Apart from the two points in the near field of the instrument, and the last one to three points of the profile, which are presumably affected by scattering from the right bank, the profiles are essentially horizontal lines. This is what we would expect for scattering from a suspension of particles with homogeneous concentration and grain size.

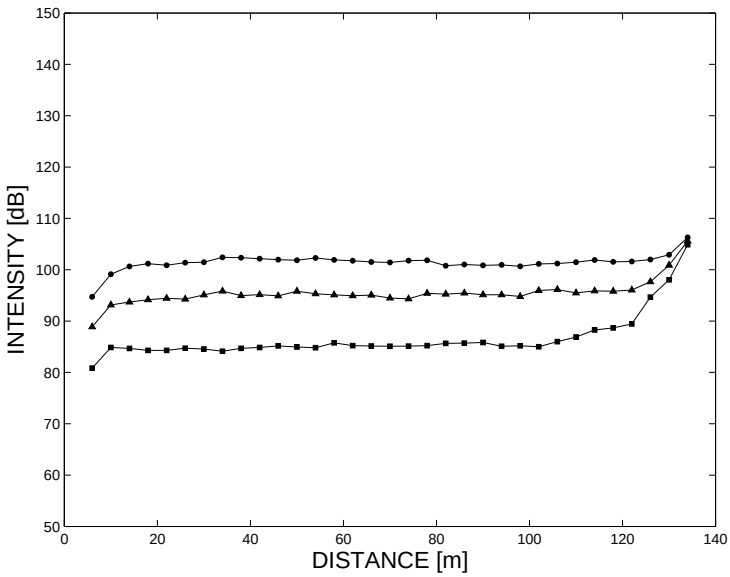

Figure 4.16: Three 15-minute averaged profiles of range-corrected intensity measured with the 300 kHz H-ADCP at Montélimar. The mean water velocity measured by the H-ADCP was 1.11 m/s (circles), 0.55 m/s (triangles) and 0.22 m/s (squares). The y-axis scale is the same as in Figure 4.15(c,d) to facilitate comparison.

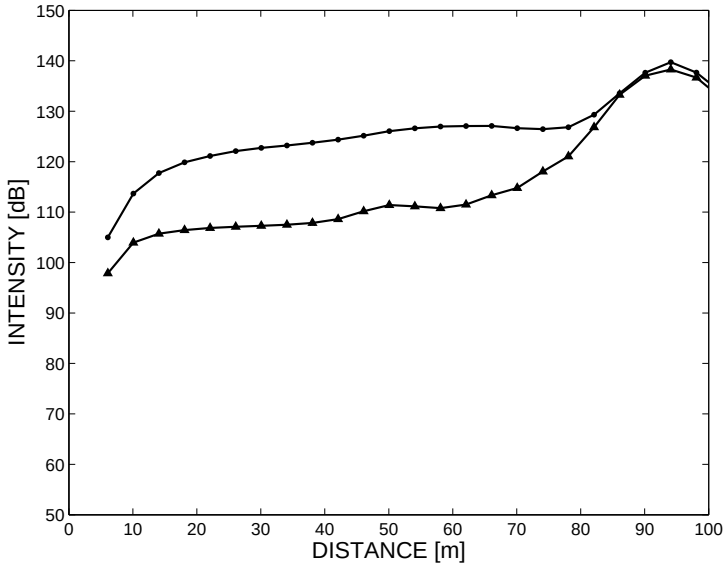

Figure 4.17: Two 15-minute averaged profiles of range-corrected intensity measured by the central transducer of the H-ADCP at Saint-Georges. The mean velocity for the two profiles were ∼1.3 m/s (circles) and ∼0.3 m/s (triangles).

As a second example, Figure 4.17 depicts two examples of the intensity data measured by the central transducer of the H-ADCP at Saint-Georges, for which the mean flow speeds were 1 m/s and 0.2 m/s. Within the region of the far field of the H-ADCP and before interception with the left bank, i.e. between 15 and 80 m from the instrument, the range-corrected intensity at Saint-Georges appears to be more or less a slowly increasing function of range. When the velocity (and presumably suspended sediment concentration) are low (see triangles), the range-corrected intensity increases by 10 dB within the first 80 m from the instrument, whereas it increases by only 5 dB for the high velocity data. These range corrected intensity profiles are less horizontal than what was seen at Montélimar, but more so than what was seen at Romans-sur-Isère. Also, unlike at Romans-sur-Isère the form of the profile at Saint-Georges is fairly constant, only the amplitude of the curve seems to change. Based on the positioning of this instrument, we believe there to be scattering from the river bed. This seems a plausible explanation since the distance between the H-ADCP and the bottom decreases with increasing range, which would explain why the effect is more pronounced on the far side of the river. We have not attempted to model scattering from the bottom since it was not one of the goals of this thesis.

4.6 Conclusions

This chapter presented observations of the different forms of the range-corrected intensity profiles that were recorded at the different study sites. At the Montélimar study site, where the instrument is installed 5 m from the surface and bottom, the range-corrected intensity appeared to be independent of range for a variety of flow speeds. This is what we would expect for a cross section having a homogeneous distribution of suspended sediment. The properties of the suspended sediment at the Saint-Georges study site should also be constant throughout the measurement volume of the H-ADCP. The form of the range-corrected intensity profiles at Saint-Georges remained the same despite changes in the scattering level with changing flow speed. Nonetheless, the range-corrected intensity increased slightly with range. This trend was strongest when the flow speeds were the lowest. Since the distance between the axis of the transducer and the bottom decreases with distance from the instrument, we suspect that there is increased scattering from the bottom at distances approaching the left bank.

In studying the velocity and backscattered intensity profiles that were recorded by the 300 and 600 kHz H-ADCPs at Romans-sur-Isère, we found that the measurements were perturbed at distances closer to the instrument than what was anticipated based on simple geometry. These perturbations came and went in a continuous manner when the mean flow speed was less than $\sim$1 m/s. Since the 300 kHz H-ADCP was angled towards the surface and the 600 kHz instrument was not very deep, this led to a study of the effect of scattering from the air-water interface on the backscattered intensity profiles. By simply treating the surface as a Lambertian scatterer, we were able to reasonably model the form of the range-corrected backscattered intensity profiles that were observed during periods of low flow (low velocities and low concentrations) by the two instruments.

The positioning of both instruments was modified in December, 2010. The 300 kHz instrument was tilted away from the surface and the 600 kHz instrument was installed deeper, but with a non-negligible roll. The 300 kHz intensity profiles are no longer influenced by the surface, but scattering from the bottom now poses a problem and the velocities continue to be underestimated when concentrations are weak. The measurements made with the 600 kHz H-ADCP at Romans-sur-Isère were altered with its repositioning, but they were not improved. The instrument is now positioned with one beam facing downwards, one more or less horizontal and one upwards. This means that each beam measures the velocity at a different height above the bottom. The velocity measurements are therefore invalid, no matter the concentration of suspended sediment.

Nevertheless, the intensity data from this instrument make for an interesting case study. We conclude that the Romans-sur-Isère study site is too shallow to expect reliable measurements across the entire cross section during all flow conditions.

Our ability to reasonably model the effect of scattering from the air-water interface suggests that this technique could be used to determine the ideal depth and inclination for future H-ADCP installations when limited depth is expected to cause problems. Also, we suggest a criterion for data invalidation: if the concentration and size of suspended sediment are expected to be homogeneous across the insonified area, yet the acoustic intensities increase with range, these data should be discarded. In future applications at sites where depth is limited to less than 10 m, the modelling of scattering from the bottom and surface could cut down on costs of hiring divers to test different positions. This is especially interesting if the instrument is installed on a day when concentrations are sufficiently high that scattering from the bottom or surface are not noticeable, since simple in-situ positioning tests will not detect this problem. Such was the case at Romans-sur-Isère.

CHAPTER 5

VELOCITY DATA ANALYSIS

A number of researchers in fluvial hydraulics have published work on the use of horizontal acoustic Doppler current profilers for velocity measurements (e.g. *Huang*, 2006; *Nihei and Kimizu*, 2008; *Hoitink et al.*, 2009; *Buschman et al.*, 2009; *Sassi et al.*, 2011) and sediment load measurements (e.g *Wood*, 2010). Nonetheless, few published works include an evaluation of the validity of the velocity measurements, and those that do (e.g. *Nihei and Kimizu*, 2008; *Hoitink et al.*, 2009; *Sassi et al.*, 2011) often neglect to mention pertinent information on the concentration of suspended sediment and/or the backscattered intensity at the time of measurement. This gap in the research was one of the main motivations for this thesis.

Prior to the start of this thesis, J. Le Coz and G. Pierrefeu compared the velocity profiles obtained with the horizontal ADCPs used in this study to measurements made with a vertically-oriented ADCP attached to a moving boat, as mentioned in Chapter 4, Section 4.2. In *Le Coz et al.* (2008), results were presented from the Saint-Georges study site: measurements of along-stream velocity made with the 300 kHz H-ADCP at Saint-Georges were compared to results from 17 ADCP gauging campaigns. They found that the velocity measurements obtained with the H-ADCP were acceptable (within 5% of the reference values) when the cross sectional averaged velocity exceeded 0.4 m/s (equivalent to discharge > 300 m^3/s), but below this value the H-ADCP significantly underestimated velocity. They found that the measurement campaign with the lowest discharge, for which the concentration of suspended sediment was only 10 mg/L, corresponded to the worst underestimation of velocity by the H-ADCP (50%) [1]. In their perspectives for future work, *Le Coz et al.* (2008) mention the need for an investigation of the connection between backscattered intensity and velocity underestimation, since the backscattered intensity

[1] It should be noted that, due to the various dam operations, water levels at all study sites tend to be the most variable when discharge is high. High discharge values are therefore not necessarily co-incident with high water levels, and vice versa.

is typically weak when the concentration of suspended sediment is low.

Pierrefeu (2008) also found that velocity underestimation by the H-ADCPs correlated with flow rate: the slower the flow, the more the velocity was underestimated. He found that the velocity at which measurements switched from being acceptable to being unacceptable was site-specific. Furthermore, *Pierrefeu* (2008) showed that there was a trend between velocity underestimation by the H-ADCPs at Romans-sur-Isère and the intensity of the backscattered signal. When the velocities measured by the ADCP were low and the intensity of the backscattered signal was low (presumably due to low concentrations), the H-ADCPs tended to underestimate velocity. However, when the flow speed was high, the H-ADCPs tended to output the correct velocity regardless of whether the backscattered signal was high or low. Pierrefeu conjectured that it may be necessary to establish a specific index velocity relationship for each measurement cell as a function of backscattered intensity, but concluded that further investigation was required. As such, the goal of this chapter is to assess the validity of (1) the form of the across-stream profiles of velocity measured with the H-ADCPs and (2) their absolute values, exploring the role played by the concentration of suspended sediment, the intensity of the backscattered signal and the distance from the instrument on these results.

In terms of the layout of this chapter, the first section deals with the validity of the form of the horizontal velocity profiles. Velocity data from ADCP gauging are used for the comparison. Using the average velocity field obtained from multiple transects during ADCP gauging, we extract the horizontal profile of along-stream velocity that corresponds to the depths and distances of the measurement cells of the horizontal-ADCP in question. When simultaneous ADCP and H-ADCP measurements exist, we can compare the form and values of the two profiles directly. When simultaneous or quasi-simultaneous ADCP and H-ADCP data do not exist, we can evaluate the accuracy of the form of the H-ADCP profiles by examining normalized profiles. Recalling Chapter 4, Section 4.2, it is the examination of the form of the velocity profiles at Romans that tipped us off to the positioning problem of the 300 and 600 kHz H-ADCPs. As such, we shall not focus on the results of Romans, but present results from the Saint-Georges and Montélimar study sites.

The second section focuses on the applicability of an index-velocity method in order to obtain discharge from H-ADCP velocity measurements. Using data acquired in measurement cells that are unaffected by boats, the river bed, bridge piers or the surface, we investigate whether it is possible to establish a relationship between the H-ADCP velocity and the discharge velocity.

Recalling Equation 3.1, the discharge velocity, V_q, is simply the discharge divided by the wetted area; it is equivalent to the cross-sectional averaged velocity. We examine the difference between the velocity measured by the horizontal ADCP at a given distance from the H-ADCP and the discharge velocity as a function of discharge velocity, backscattered intensity, and concentration of suspended sediment.

5.1 Validation of the form of the velocity profiles

In order to test the validity of the H-ADCP results, they were compared to results from ADCP gauging. In a laboratory setting, ADCPs have been found to yield velocity measurements within 0.3 cm/s of the actual value (see tow-tank tests of *Oberg*, 2002). River discharge values calculated using ADCP data have been found to be within 5% of values from current meters (*Morlock*, 1996), while the mean deviation from reference values has been shown to be 4–5% during ADCP intercomparison tests in large river sections such as the ones studied in this thesis (*Le Coz et al.*, 2009).

The gauguing procedure was outlined in Chapter 4, Section 4.2. For each ADCP gauging campaign, six consecutive transects were averaged. It was ensured that flow conditions remained stable during this period. This typically corresponded to 10 to 20 minutes of acquisition and processing time, which is sufficient to average out the effects of random instrument noise and turbulent fluctuations of the flow (*Oberg and Mueller*, 2007). The H-ADCP data were averaged over fifteen minutes.

Comparisons between the velocities measured during river gauging and those measured by the horizontal ADCP at Saint-Georges have been presented in *Le Coz et al.* (2008) and *Moore et al.* (2009). In both articles, the data were presented in terms of profiles of the relative difference between the two measures of velocity. In this chapter the data are presented in a slightly different manner. The profiles of velocity from the ADCP and H-ADCP are normalized by the maximum value observed in each of their profiles and the comparison is done between the normalized velocity profiles. This normalization is done so that we can compare the form of the H-ADCP velocity profiles to the expected form of the profile on days for which there are no gauging data. At a given site, the form of the velocity profiles should be similar, in the geometric sense of the word, with changing velocity and discharge if the site is far from any hydroelectric plants or confluences that might alter the flow field. A second assumption is that the fluctuations in water level remain small enough that the velocity at the height of each H-ADCP measurement cell is

always the same proportion of the mean velocity. Since ADCPs provide an unbiased measure of velocity (*Oberg and Mueller*, 2007), any discrepancy between the normalized ADCP and H-ADCP velocity profiles should indicate a problem with the H-ADCP measurements.

Gauging campaigns at Saint-Georges have been performed during a variety of flow conditions. We have measurements made when the discharge velocity was as little as 16 cm/s and as high as 2.1 m/s. Only the results from five gauging campaigns are summarized here, but further results can be found in *Le Coz et al.* (2008) and *Moore et al.* (2009). A summary of the relevant information from the five campaigns, including measurement dates and mean velocities, is provided in Table 5.1 and the data are shown as solid lines in Figure 5.1. Horizontal ADCP data collected on the same day as the ADCP measurements are shown for comparison in Figure 5.1. Simultaneous data from the two instruments are not shown since the presence of the motor boat used for gauging can affect the H-ADCP results. The H-ADCP data that are shown in Figure 5.1 are the average of fifteen minutes of data.

Table 5.1: Summary of the ADCP gauging campaigns at the Saint-Georges study site that are analyzed in this chapter. The mean velocity values correspond to the mean velocity measured by the ADCP along the axis of the H-ADCP.

Date (yyyy-mm-dd)	ADCP (kHz)	Mean velocity (m/s)	Discharge (m^3/s)	Colour
2006-02-15	1200	0.18	115	magenta
2006-02-16	1200	0.33	246	cyan
2006-05-03	600	0.40	262	green
2006-02-18	600	1.35	902	blue
2006-03-17	600	2.27	1787	black

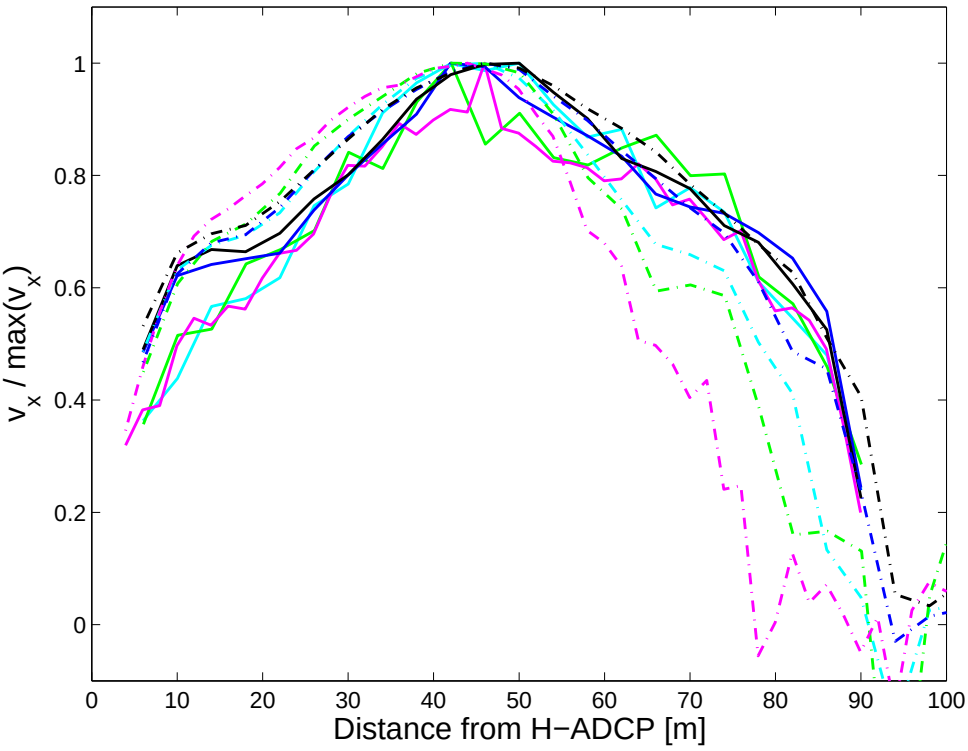

Figure 5.1: Saint-Georges: horizontal profiles of along-stream velocity normalized by the maximum value of each profile. The H-ADCP data (dashed-dotted lines) are averaged over 15 min and the ADCP data (solid lines) are averaged over six transects (∼15 min). Each color corresponds to a different day. The dates and discharges from the ADCP data are: magenta for 2006-02-15 (115 m^3/s), cyan for 2006-02-16 (246 m^3/s), blue for 2006-02-18 (902 m^3/s), green for 2006-05-03 (262 m^3/s) and black for 2006-03-17 (1787 m^3/s).

From Figure 5.1 we see that the form of the velocity profiles measured with the ADCP is conserved for the range of discharge values observed (115 m^3/s - 1787 m^3/s). We also see that there is nearly perfect agreement between the ADCP and H-ADCP data for the measurement campaign that corresponded to the highest velocities (see the data in black) and there is good agreement when the mean velocity from the ADCP was 1.35 m/s (data in blue). However, the normalized H-ADCP profiles shown in magenta, green and cyan differ notably from the ADCP data. For these three profiles, the maximum velocities measured with the H-ADCP were less than 0.70 m/s (N.B. The velocity values are not discernible from the figure). Based on these data and the data that were presented in *Le Coz et al.* (2008) and *Moore et al.* (2009), we find that whenever the cross-sectional averaged velocity measured with ADCP gauging was less than 0.40 m/s, the H-ADCP measurements were biased to lower values. The negative velocity bias increased with increasing distance from the instrument. This can be seen from the apparent

positive bias in the velocity values measured by H-ADCP in the first part of the section and the negative bias in the far half of the section, as seen in Figure 5.1. These results clearly indicate that even the measurements in the cell corresponding to the maximum H-ADCP velocity were underestimated.

Considering the apparent flow structure similarity in the ADCP data, we interpret the discrepancy between the ADCP and H-ADCP normalized velocity profiles as underestimation of velocity by the H-ADCP. The H-ADCP increasingly underestimates velocity as the mean velocity of the flow decreases. Velocity underestimation is first seen in the cells furthest from the instrument. As the flow speed decreases it occurs at cells nearer to the instrument. Since the backscattered intensity from the water is typically weak when the flow is low (low concentrations) and since the echo intensity decreases with range from the instrument, we suspect that the cause of the velocity underestimation is a combination of an insufficient signal-to-noise ratio and increased scattering from the river bottom with increased range (see discussion in Chapter 4 surrounding Figure 4.17). Since the river bottom should be stationary at this site, the signal scattered from the bottom would have a Doppler shift of zero which would bias the mean velocity measurements towards lower values.

To test the conjecture that ambient scattering from the surface or bottom may bias velocity measurements when concentrations of suspended sediment are low, we examine velocity data collected at Montélimar. In Chapter 4 we concluded that neither the surface nor the bottom posed a visible problem for the backscattered intensity measurements at Montélimar. We therefore use it as our reference site, but remind the reader that the H-ADCP at Montélimar operates in broad bandwidth mode, while all the other instruments operate in narrow bandwidth mode (see Section 3.3). Since Montélimar was not a major focus of this study until late in the thesis, there are no days for which there are both ADCP and H-ADCP data. However, this highlights the interest of normalizing the velocity profiles by their maximum velocity: we can investigate the role of flow speed on the form of the velocity profiles without requiring simultaneous ADCP and H-ADCP measurements.

In Figure 5.2 we present ADCP data from five gauging campaigns at Montélimar for which the mean velocity measured by the ADCP ranged from 0.2 m/s to 1.2 m/s. The date of the various measurement campaigns, the discharge and the mean velocity measured by the ADCP along the H-ADCP profile are summarized in Table 5.2. Four examples of 15 minutes of H-ADCP data are shown as dashed-dotted lines in Figure 5.2. The gray scale of these lines gets lighter as velocity

increases: going from black to light gray the maximum velocities of the H-ADCP profiles are 0.19 m/s, 0.31 m/s, 0.70 m/s and 1.36 m/s, respectively.

Table 5.2: Summary of the ADCP gauging campaigns at the Montélimar study site analyzed in this chapter. The mean velocity values correspond to the mean velocity measured by the ADCP along the axis of the H-ADCP.

Date (yyyy-mm-dd)	ADCP (kHz)	Mean velocity (m/s)	Discharge (m^3/s)	Colour
2007-11-06	1200	0.19	332	cyan
2009-09-30	1200	0.20	354	green
2009-09-07	1200	0.42	746	blue
2007-10-04	600	0.49	847	yellow
2007-12-11	600	1.22	1961	magenta

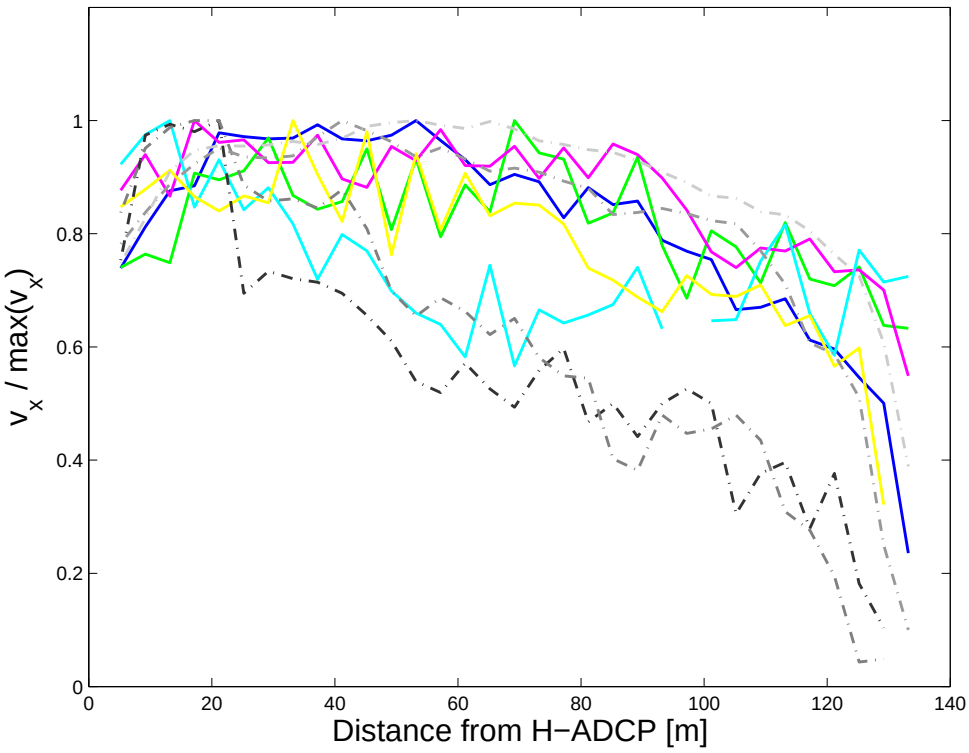

Figure 5.2: Montélimar: examples of the horizontal profiles of along-stream velocity averaged over 15 minutes and normalized by the maximum velocity of each profile. The H-ADCP data are shown as dashed-dotted lines and the ADCP data are shown as solid lines. The ADCP data are summarized in Table 5.2, the maximum value of each H-ADCP velocity profile is 0.19 m/s, 0.31 m/s, 0.70 m/s and 1.35 m/s, going from black to light gray. There are no co-incident ADCP and H-ADCP data at this site.

In Figure 5.2 it can be seen that all ADCP profiles have the same form except the data collected

on November 6, 2007, for which the velocities appear to be relatively weak in the centre of the river. This may indicate that there are multiple flow structures at Montélimar due to differing dam operations. This point could be elucidated with further low velocity data or by obtaining the possible operational configurations of the Châteauneuf dam. However, we will assume for the meantime that the data shown in cyan in Figure 5.2 are anomalous. Looking at the other four ADCP profiles we see that, unlike at Saint-Georges, the velocity profile is not symmetrical about the centre of the river. This is no doubt the result of standard dam operations downstream, which clearly lead to higher velocity on the left bank of the river than on the right bank. From Figure 5.2 we see that the H-ADCP profiles have the same form as the ADCP profiles when velocities are high, but when velocities are low, the normalized profiles fall off beyond 22 m from the instrument. We interpret this as underestimation of velocity by the H-ADCP. Velocity underestimation at ranges greater than $\sim$20 m is observed whenever the maximum H-ADCP velocity is less than 40 cm/s.

Although the onset of velocity underestimation at Saint-Georges occurred at higher velocity values (the velocity was underestimated when $\max(V_h) \lesssim 0.7$ m/s), the velocity underestimation at Montélimar appears to be much more pronounced, with velocities falling off at distances much closer to the instrument for similar flow speeds. This may be linked to the decreased signal-to-noise ratio at Montélimar compared to Saint-Georges due to its different mode of operation. Since scattering from either the surface or the bottom does not appear to have a noticeable impact on the measurements at Montélimar, we suspect that the instrument validates measurements with too low a signal-to-noise ratio and, to put it simply, amplifies noise when concentrations of suspended sediment are weak. This points to the need for an investigation of the dependence of the velocity underestimation on the intensity of the backscattered signal and concentration during periods of low flow.

5.2 Validation of the velocity measurements

The index velocity method is a way of determining the mean-channel velocity from the water velocity measured in only a portion of the river (*Rantz*, 1982, Ch. 12). In our case the "index velocity", V_i, is the velocity measured in one H-ADCP cell. In order to establish an index-velocity relationship one needs a reference value of the mean-channel velocity. This can be obtained by performing transects with a vertically-oriented ADCP attached to a motor boat (e.g. *Ruhl and Simpson*, 2005). Alternatively, if one has a record of the water level at the site of

interest and the relationship between water level and wetted area is known, then the discharge at a nearby gauging station can be used to calculate the discharge velocity, V_q at the site using Equation 3.1, since the discharge is conserved. A relationship is established between the index velocity and discharge velocity using all available data. If the velocity at height h above the bottom, $V_i(h)$, is always the same proportion of the cross-sectional averaged velocity, then V_q/V_i should be a constant. In this work, we refer to this constant as the index. Since it is imperative to ensure that a maximum number of flow conditions are included in the data from which the index velocity relationship is established, we use discharge measurements from nearby gauging stations to calculate the discharge velocity.

Results are presented from the Montélimar and Romans-sur-Isère study sites, since the distances between these sites and their nearest measure of discharge is much smaller than it is for Saint-Georges or Tricastin. This eliminates the complications of propagation delay. For Romans we use the measure of the total discharge that is output from the Pizançon dam 2 km upstream, and for Montélimar we use the measure of discharge that is output from the Châteauneuf dam, 500 m downstream of the instrument. In both cases we neglect the propagation delay. Since there are no confluences between the locations of the discharge measurements and those of the H-ADCPs, these data are representative of the discharge passing each site. The relationship between water level and wetted area at a given study site is obtained using the bathymetry data from one ADCP boat crossing plus the corresponding record of water level. The water level at Romans-sur-Isère is measured directly at the study site, but for Montélimar we use the water level from the power plant 500 m downstream, since the pressure gauge at the H-ADCP is unreliable (*Personal com., X. Martin, August 2011*).

For the two study sites, we examine the relative difference between the velocity measured by the H-ADCP, V_h, and the discharge velocity V_q, as a function of discharge velocity, backscattered intensity and concentration of suspended sediment. This is done for a number of different measurement cells for each instrument. If the measurements made with the H-ADCP were unbiased, we would expect $(V_h - V_q)/V_q$ to be independent of all of these factors. That is to say, we expect to find a unique index velocity relationship for each measurement cell. One might argue the precarious nature of an index velocity relationship at Montélimar since variable dam operations at the Châteauneuf generation station might alter the flow field, however, if this were the case we should see periods with coherent biases in the H-ADCP data, and we did not.

5.2.1 300 kHz H-ADCP data at Romans-sur-Isère

In Figures 5.3 to 5.7 we present data collected with the 300 kHz H-ADCP at Romans-sur-Isère between November, 2009 and July, 2010 for measurement cells 3, 6, 9, 12 and 15, which correspond to distances of 8 m, 14 m, 20 m, 26 m, and 32 m from the instrument. All of these measurement cells should be unaffected by scattering from the air-water interface (cf. Section 4.2). The data are averaged over 15 minutes and data collected when the turbidity meter indicated concentrations greater than 200 mg/L are shown as green dots. This was done in order to highlight the difference between the measurements made during periods of low and high suspended sediment concentrations, since it will be seen that the concentration of suspended sediment plays an important role in the validity of the velocity measurements. The variable that is plotted on the y-axis of Figures 5.3 to 5.7 is the difference between what is observed and what would be predicted by a simple index velocity relationship established with the high intensity data, we call this the index-velocity error. The index-velocity error is defined as

$$\frac{V_h - V_q}{V_q} - \frac{V_h|_{\text{high intensity}} - V_q}{V_q}. \tag{5.1}$$

It is given as percentage of the actual discharge velocity. The value at which $(V_h - V_q)/V_q$ plateaus as a function of echo intensity, $(V_h|_{\text{high intensity}} - V_q)/V_q$ is traced as a solid line in each subplot at y equals zero. As such, a positive index-velocity error indicates that the discharge would be overestimated with the use of a simple index-velocity relationship, and a negative value indicates that the discharge would be underestimated. This manner of plotting the data was decided upon since the value of the index, V_q/V_h, should evolve with distance from the instrument: it should be highest in the centre of the river where velocity values are a maximum, and lowest on the edges, where velocity values are lowest. Overlayed on the data points are box plots of the same data grouped into slightly arbitrary classes of velocity, intensity, or concentration, respectively. Unlike a standard box plot, the whiskers indicate the 2.5 and 97.5 percentile values for each class so that 95% of the data lie within the whiskers.

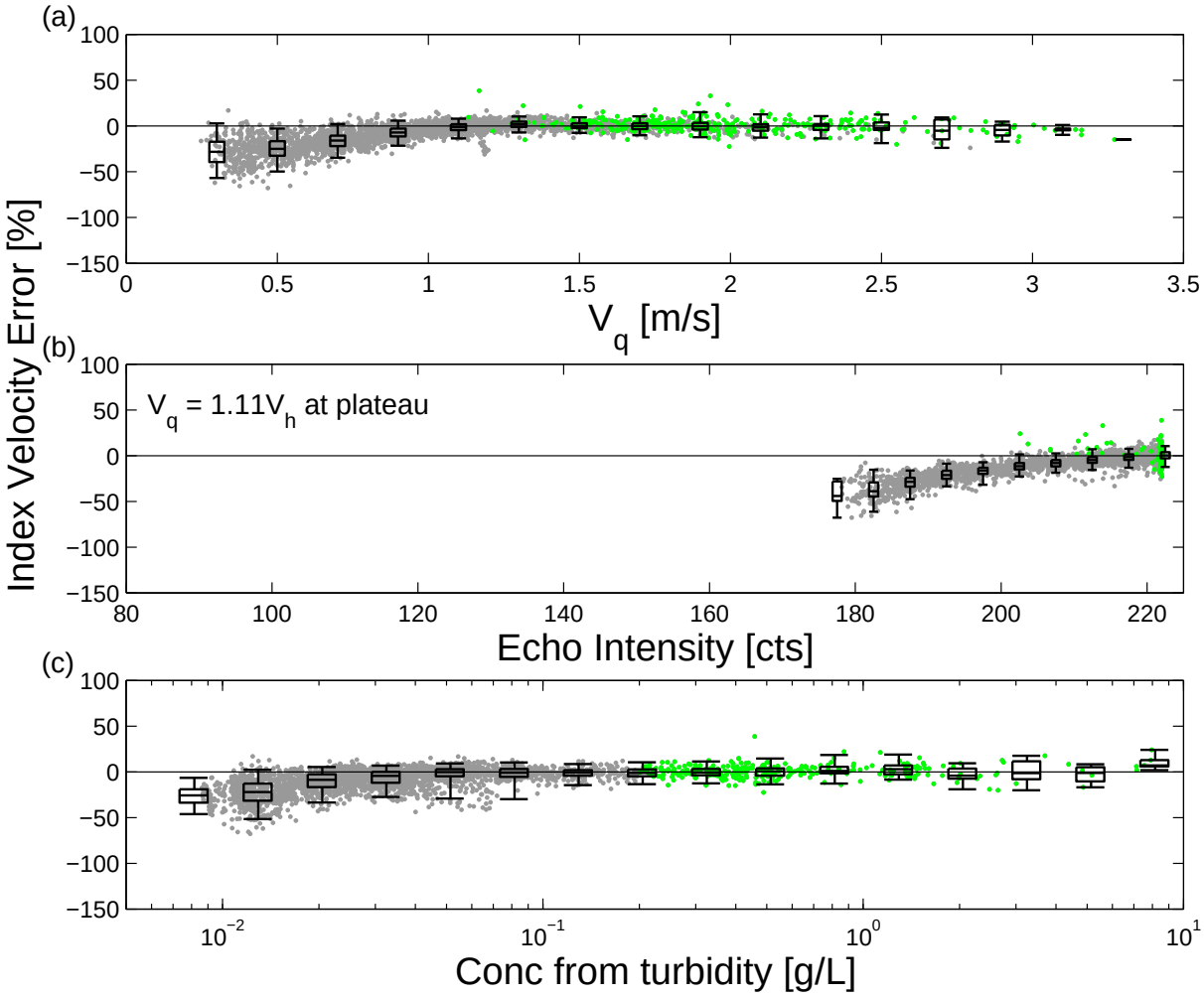

Figure 5.3: The percent error in the discharge velocity that would be calculated using a unique index-velocity relationship for the 300 kHz H-ADCP at Romans-sur-Isère using data collected between November, 2009 and July, 2010 in measurement **cell 3 (8 m from the H-ADCP)**. The data are plotted as a function of (a) actual discharge velocity; (b) echo intensity; (c) concentration from the optical turbidity meter.

In Figure 5.3, the high intensity index-velocity relationship is $V_q = 1.11V_h$. Starting with Figure 5.3(a) we see that when the concentration of suspended sediment is greater than 200 mg/L (green dots), the discharge velocity is high, as expected. We also see that when the discharge velocity is high, there is good agreement between the H-ADCP velocity and the discharge velocity, i.e. the index-velocity error is near zero. In contrast, when the concentration is less than 200 mg/L (gray dots), the H-ADCP increasingly underestimates velocity with decreasing values of V_q when V_q is less than 1 m/s. The underestimation by the H-ADCP also increases with decreasing echo intensity (see Figure 5.3(b)) and decreasing concentration (see Figure 5.3(c)). Velocity

values are increasingly underestimated as the echo intensity decreases below about 210 counts, but above this values, V_q/V_h tends towards 1.11 and the spread of the data is minimal. Since the dispersion in the data is less in Figure 5.3(b) than in Figure 5.3(a,c) (look at height of the whiskers), we can see that the velocity underestimation depends more strongly on echo intensity than on concentration or discharge velocity.

Looking at the data collected 14 m from the H-ADCP at Romans (Figure 5.4), we see similar results: the H-ADCP underestimates velocities when $V_q < 1$ m/s and the velocity underestimation and spread in the data worsen as the velocity decreases. As for the relationship between index velocity error and intensity, the value of V_q/V_h is stable at 1.02 when the echo intensity exceeds 205 counts, but when concentrations are low (gray points), there is velocity underestimation for echo intensities below this value, and the bias worsens with decreasing intensity. In contrast, when the concentration is high but the echo intensity is low, there is no velocity underestimation, even for much lower intensities than those that are observed when concentrations are low. We were expecting to see a dependence on echo intensity alone, since the signal-to-noise ratio should typically give an indication of the quality of the data. However, the problem appears to be a question of the provenance of the signal that is amplified. When concentrations are low, the signal is dominated by scattering from the surface and/or bottom, whereas when concentrations are high, although the signal may be weak due to attenuation, it is dominated by scattering from the sediment. Therefore, the signal that is amplified during periods of high concentration is representative of the motion of the suspended sediment and the water, while it is mainly noise when the concentration is low.

Figures 5.5, 5.6, and 5.7 reveal similar trends for cells 9, 12, and 15, which are 20 m, 26 m, and 32 m from the instrument, respectively. The velocity is increasingly underestimated with decreasing echo intensity when both the flow speed and the concentration of suspended sediment are low, but when echo intensities are low but velocities and concentrations are high, there appears to be a unique index velocity relationship for each measurement cell. The high echo intensity values of V_q/V_h for the three distances are 0.98, 0.88, and 0.85. These values are consistent with what we would expect: as we approach the centre of the river, the velocity measured at that distance is a larger proportion of the mean velocity.

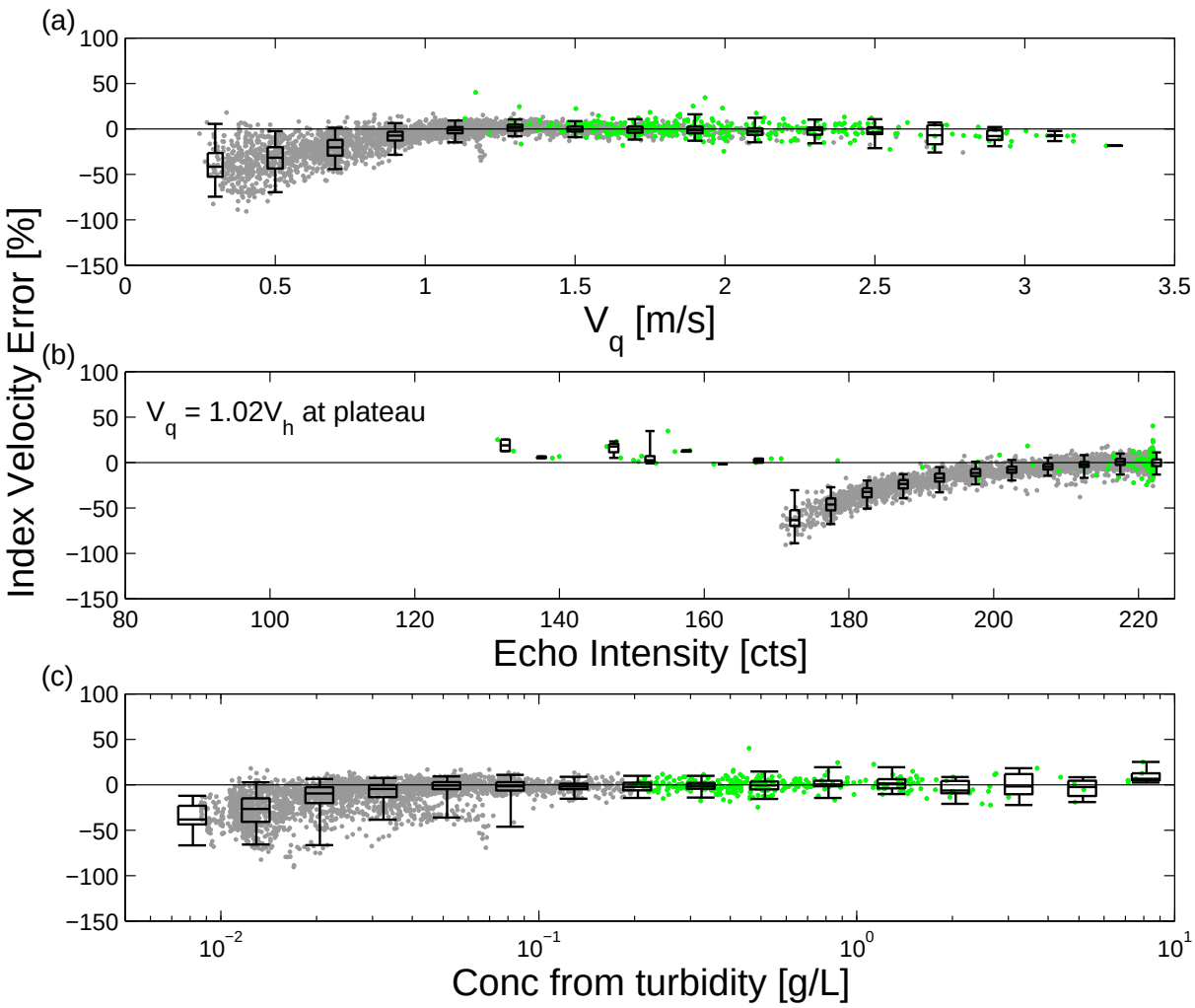

Figure 5.4: The percent error in the discharge velocity that would be calculated using a unique index-velocity relationship for the 300 kHz H-ADCP at Romans-sur-Isère using data collected between November, 2009 and July, 2010 in measurement **cell 6 (14 m from the H-ADCP)**. The data are plotted as a function of (a) actual discharge velocity; (b) echo intensity; (c) concentration from the optical turbidity meter.

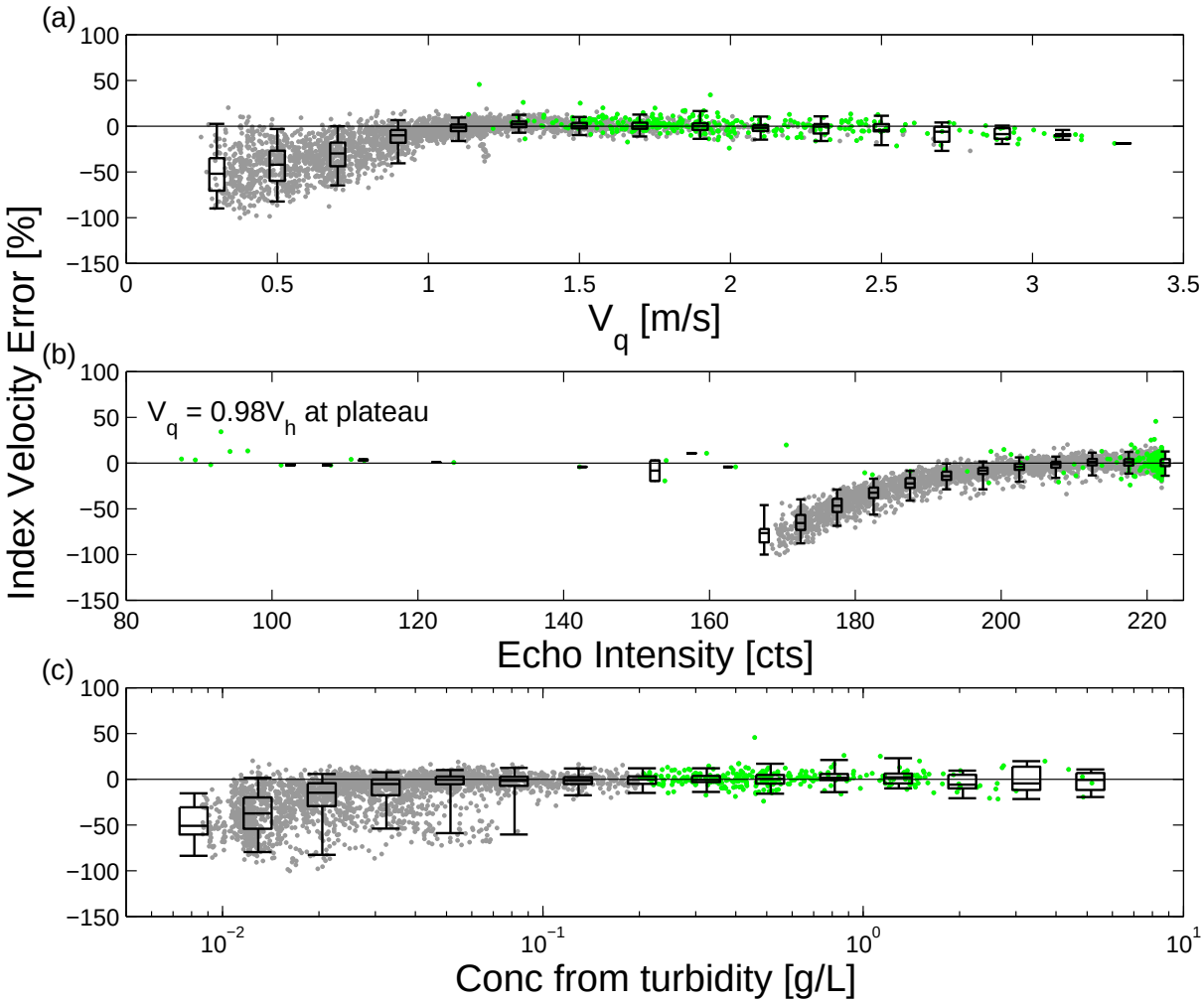

Figure 5.5: The percent error in the discharge velocity that would be calculated using a unique index-velocity relationship for the 300 kHz H-ADCP at Romans-sur-Isère using data collected between November, 2009 and July, 2010 in measurement **cell 9 (20 m from the H-ADCP)**. The data are plotted as a function of (a) actual discharge velocity; (b) echo intensity; (c) concentration from the optical turbidity meter.

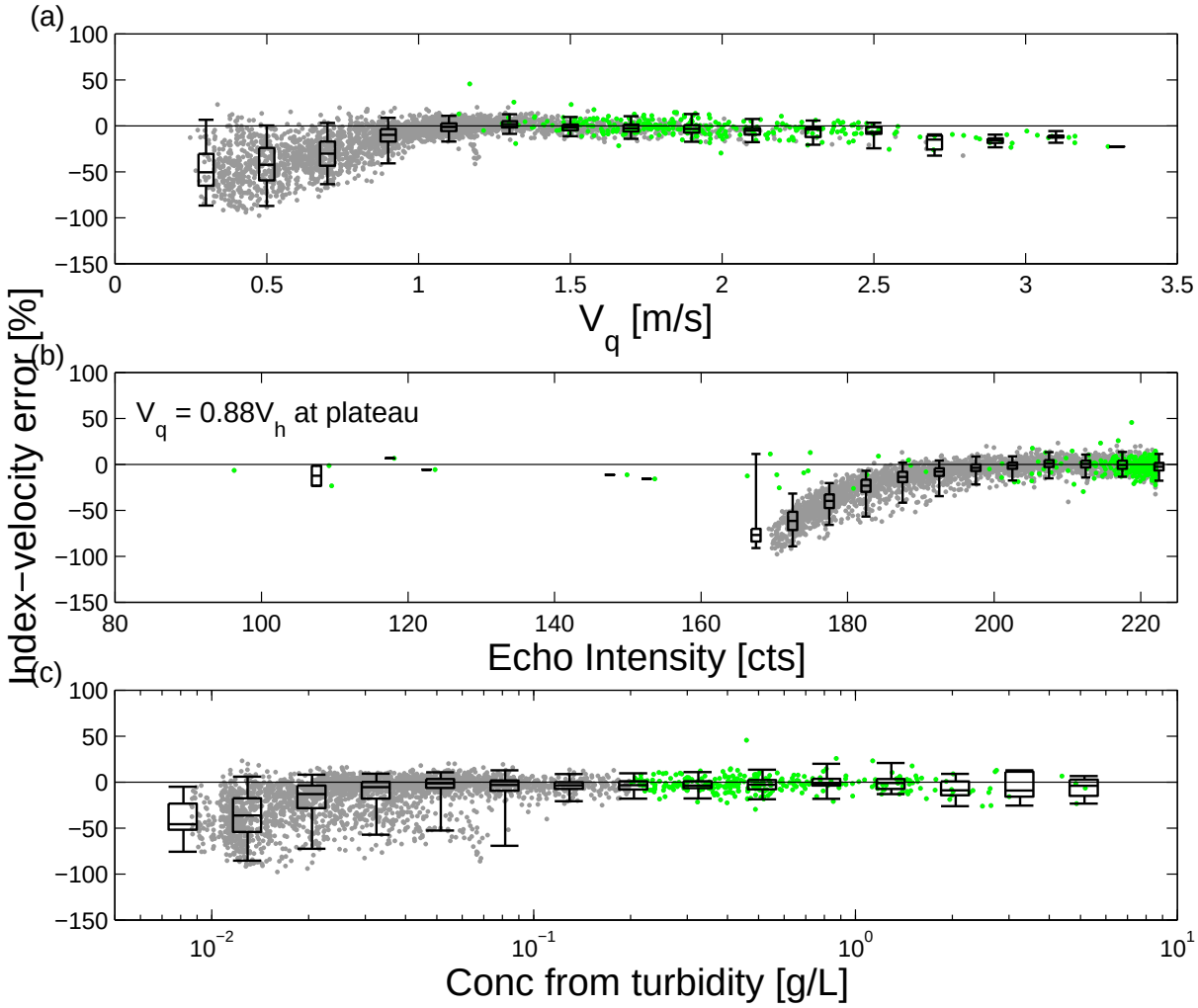

Figure 5.6: The percent error in the discharge velocity that would be calculated using a unique index-velocity relationship for the 300 kHz H-ADCP at Romans-sur-Isère using data collected between November, 2009 and July, 2010 in measurement **cell 12 (26 m from the H-ADCP)**. The data are plotted as a function of (a) actual discharge velocity; (b) echo intensity; (c) concentration from the optical turbidity meter.

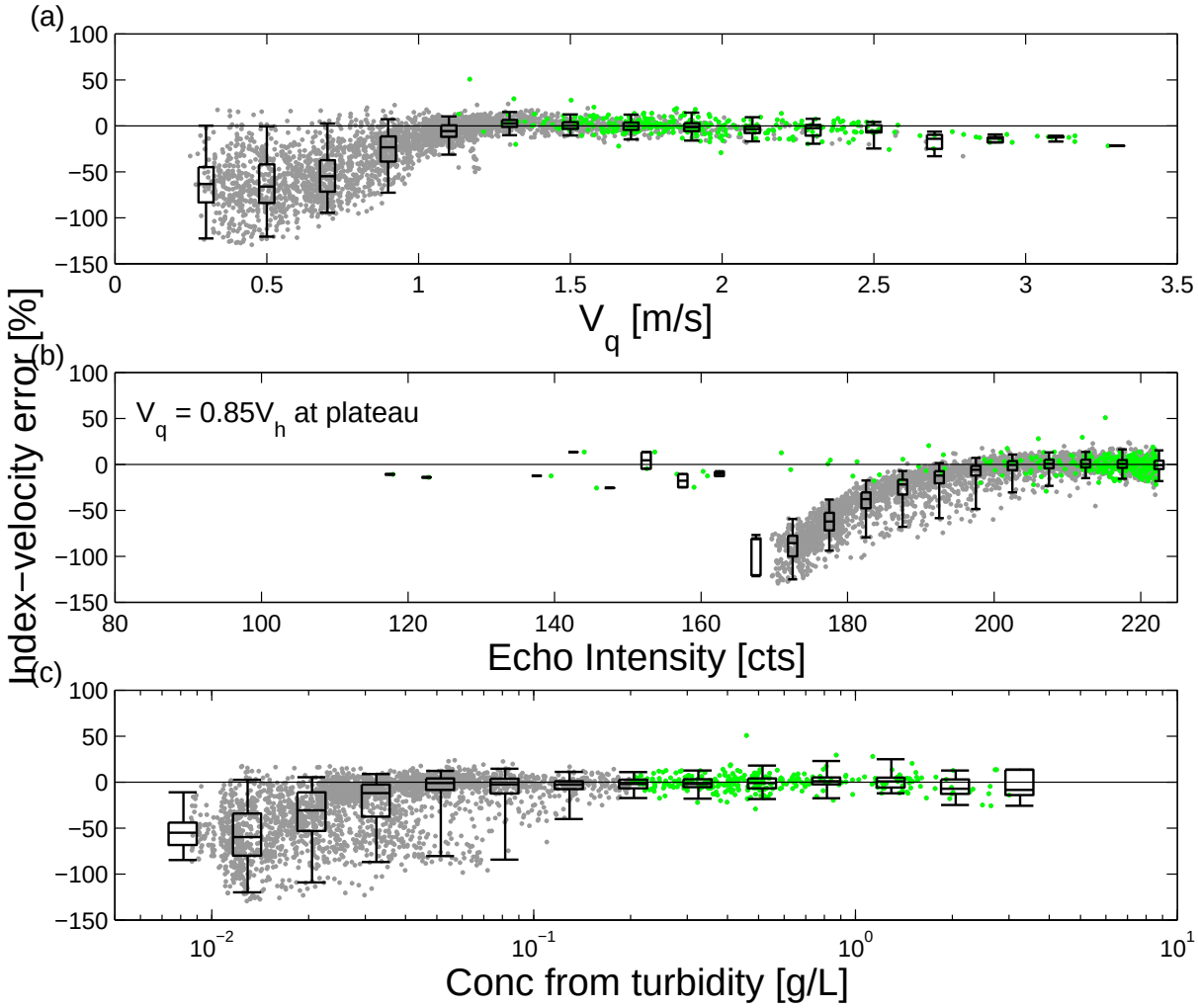

Figure 5.7: The percent error in the discharge velocity that would be calculated using a unique index-velocity relationship for the 300 kHz H-ADCP at Romans-sur-Isère using data collected between November, 2009 and July, 2010 in measurement **cell 15 (34 m from the H-ADCP)**. The data are plotted as a function of (a) actual discharge velocity; (b) echo intensity; (c) concentration from the optical turbidity meter.

5.2.2 600 and 1200 kHz H-ADCP data at Romans-sur-Isère

We have seen that the validity of the velocity measurements made with the 300 kHz H-ADCP at Romans-sur-Isère is not only controlled by the value of the echo intensity, but also by the concentration of suspended sediment. Since we have multiple H-ADCPs at this site, we can compare the ability of the three H-ADCPs to measure accurate velocities. In Figures 5.8 and 5.9 we have plotted the data collected in the cell located 14 m from the right bank for the 600 and 1200 kHz instruments, respectively, for comparison with Figure 5.3. It should be kept in mind that this is more or less equivalent to 14 m from the 600 and 1200 kHz instruments, whereas it is only 8 m from the 300 kHz H-ADCP. Also, the scale on the y-axis for the 1200 kHz plot differs from the others.

It can be seen that the high intensity value of V_q/V_h is slightly different for the various instruments, though the measurements are made at approximately the same along-stream distance. It is 1.11 for the 300 kHz instrument, 1.05 for the 600 kHz instrument and 1.09 for the 1200 kHz instrument. These values, which were estimated by eye, are not substantially different considering that the cell size and measurement depth of the various instruments are not the same.

Looking first at the 600 kHz data, it can be seen that the 600 kHz H-ADCP predicts biased velocities when concentrations are low and the echo intensity is below $\sim$170 counts. However, above this value, the unique index-velocity relationship works quite well and the spread in the data is only $\pm$ 10%. The range of intensity values over which the simple index-velocity relationship can be applied is much greater than it is for the 300 kHz instrument (170 counts - 220 counts as opposed to 210 - 225 counts). As far as the 1200 kHz data are concerned, there is much less velocity underestimation, even at echo intensities near the instrument's noise level (40 counts). Nonetheless, the spread in the data does increase with decreasing echo intensity and there is a slight tendency to underestimate velocity when the intensity is around 40 - 55 counts and the concentration is low. Based on these results, we conclude that the 1200 kHz H-ADCP makes much more accurate velocity measurements than the 300 and 600 kHz H-ADCPs. The velocity underestimation by the 600 kHz H-ADCP could be as pronounced as that of the 300 kHz instrument; however, the range of intensity values over which it provides reasonable estimates of velocity is much larger.

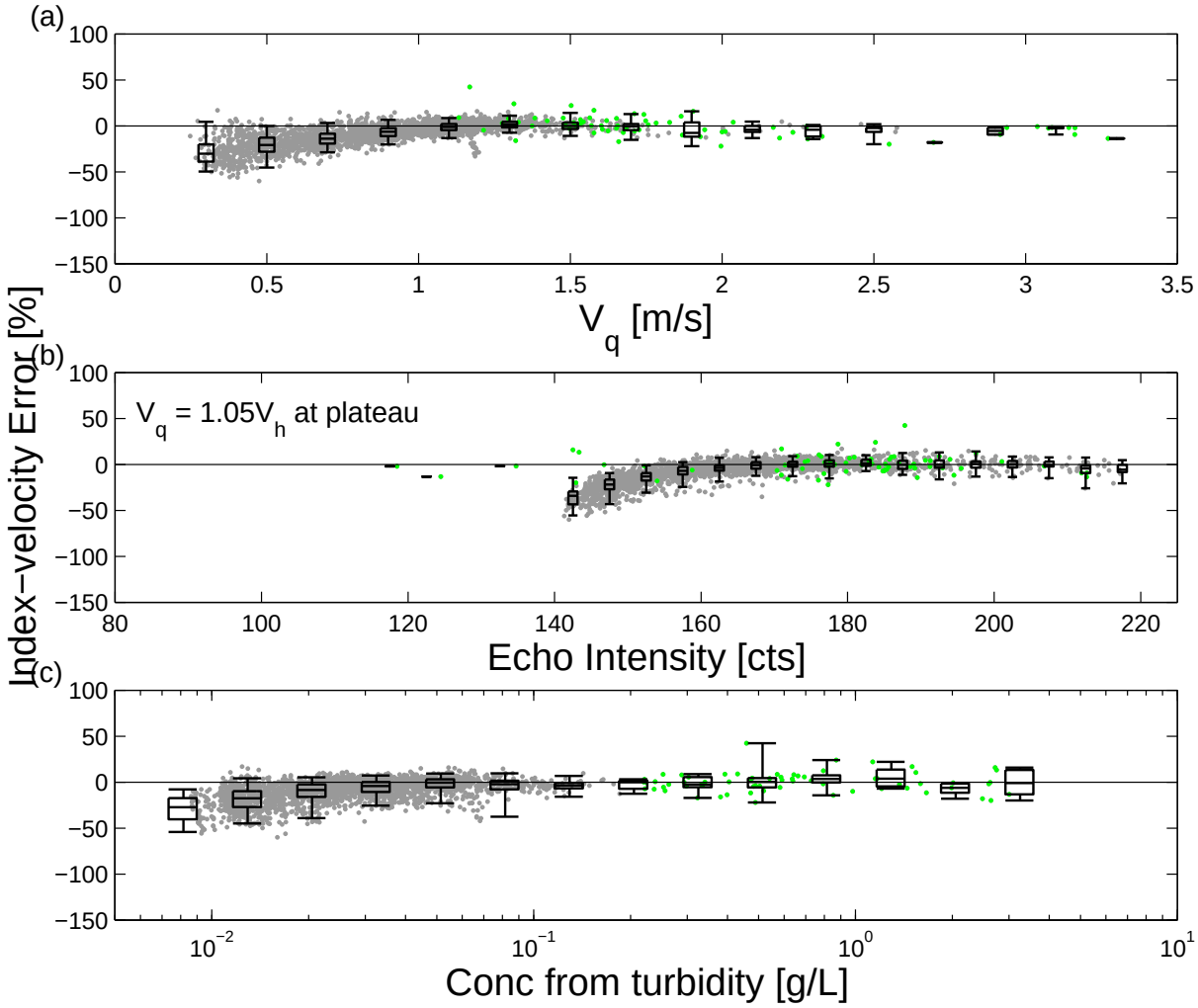

Figure 5.8: The percent error in the discharge velocity that would be calculated using a unique index-velocity relationship for the **600 kHz H-ADCP** at Romans-sur-Isère using data collected between November, 2009 and July, 2010 in **measurement cell 13 (14 m from the wall)**. The data are plotted as a function of (a) actual discharge velocity; (b) echo intensity; (c) concentration from the optical turbidity meter.

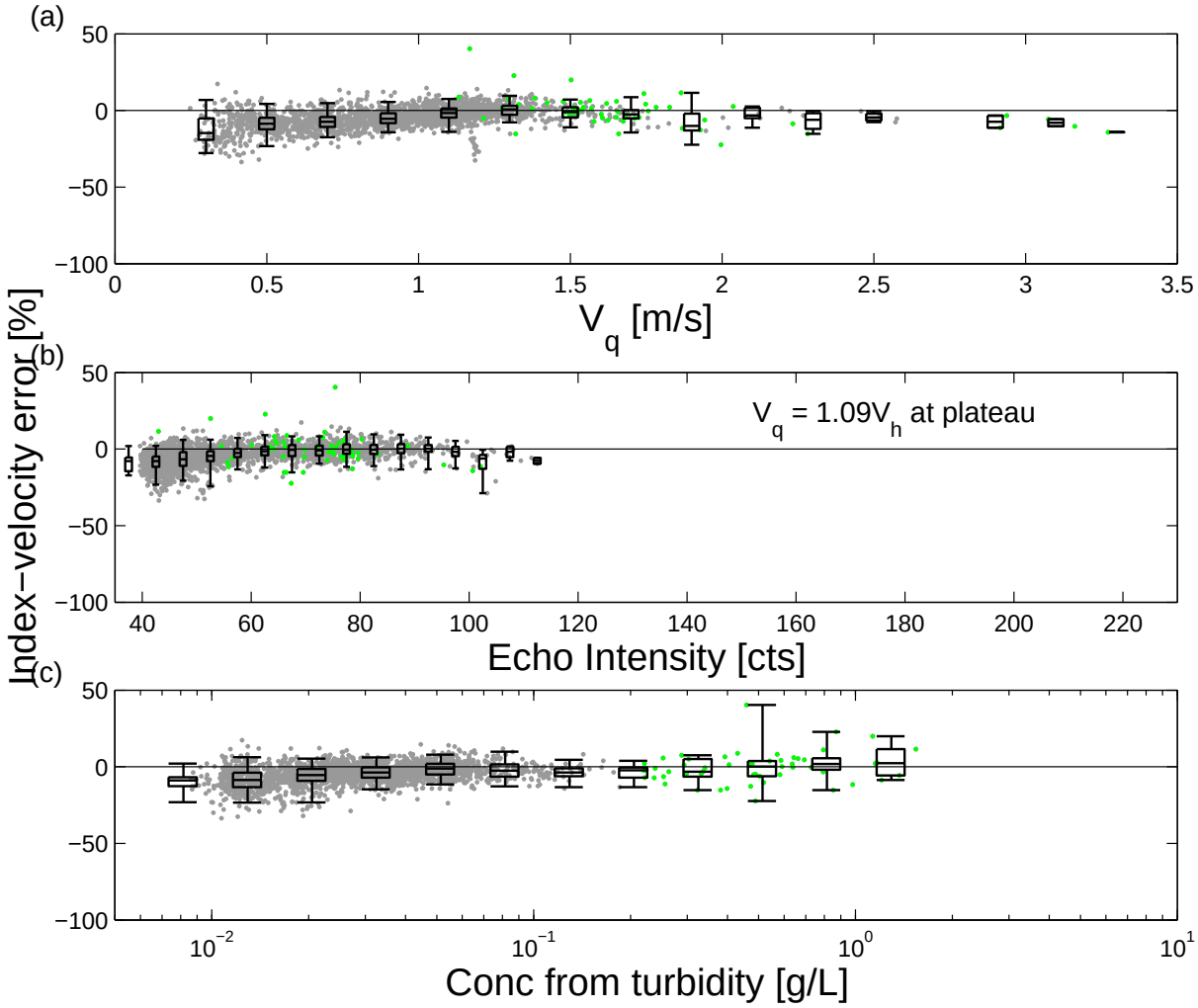

Figure 5.9: The percent error in the discharge velocity that would be calculated using a unique index-velocity relationship for the **1200 kHz H-ADCP** at Romans-sur-Isère using data collected between November, 2009 and July, 2010 in measurement **cell 27 (14 m from the right bank)**. The data are plotted as a function of (a) actual discharge velocity; (b) echo intensity; (c) concentration from the optical turbidity meter.

5.2.3 Results at Montélimar

Before presenting the velocity data from Montélimar, we remind the reader that the bin size used at this site is 4 m, while it is 2 m for the 300 kHz H-ADCP at Romans. This difference, combined with its operation in broad bandwidth mode mean that there should be reduced random noise at Montélimar compared to Romans-sur-Isère (`http://www.rdinstruments.com/tips/tips\_archive/optimizesetup\_1203.aspx`). This means that the spread in the value of $(V_h - V_q)/V_q$ should be reduced, which would result in smaller whiskers on the box plots. Since the H-ADCP at Montélimar appears to be unhindered by either the surface or the bottom across most of the profile (recall discussion surrounding Figure 4.16), we present measurements at much larger ranges than at Romans-sur-Isère.

In Figures 5.10 - 5.13, we present data from measurement cells 3, 10, 18, and 24, which are 13.2 m, 41.2 m, 73.2 m and 101.2 m from the instrument, respectively. These data were collected between January, 2010 and December, 2010. As with the data from Romans, the relationships between the index velocity error and (a) discharge velocity, (b) intensity and (c) concentration are shown in individual subplots with all data corresponding to concentrations exceeding 200 mg/L shown as green dots. Since we do not have a turbidity meter at the Montélimar study site, the concentration of suspended sediment can only be estimated when there is attenuation due to the sediment using the inversion method that will be described in Section 6.1.2. When this is the case, the difference between the observed attenuation and the attenuation due to pure water is divided by an attenuation factor of 0.03 m^2/kg in order to get an estimate of concentration [1]. The concentration estimates in the following section give the reader an idea of the concentrations that were observed. However, since the attenuation method only applies to concentration on the order of 100 mg/L and higher, the reader may be under the false impression that low concentrations are much rarer at Montélimar than at Romans-sur-Isère, this is not the case.

Comparing Figures 5.10 - 5.13 to the corresponding Figures for Romans-sur-Isère, we notice that the range of velocity values observed at Montélimar is less than what was observed at Romans-sur-Isère: the maximum velocity is $\sim$1.2 m/s at Montélimar as opposed to $\sim$3.3 m/s at Romans. This is partly because the hydroelectric-generation station just downstream of the H-ADCP regulates the flow at Montélimar, limiting high velocities during floods, but it is mainly due to the diversion of a minimum discharge to the Old Rhône which occurs upstream of Montélimar. During floods excess water is also diverted. A second major difference between the

[1] This value corresponds to the experimental attenuation factor that was observed in the data from the 300 kHz H-ADCP at Romans-sur-Isère during the flood of May 31 - June 1, 2010 (Table 4 of *Moore et al.*, 2011).

Romans-sur-Isère and Montélimar data is the range of intensity values that are detected, the backscattered intensity ranges from 40 counts to 215 counts at Montélimar as opposed to 120 - 225 counts at Romans. The major contributing factor to this difference is the fact that the Montélimar instrument operates in broad bandwidth mode, as opposed to narrow bandwidth mode and the noise levels for the two modes of operation differ.

Looking at the data measured in the cell that is 13.2 m from the instrument (Figure 5.10), the high echo intensity value of V_q/V_h is 0.85 and there appears to be little velocity underestimation at this distance. However, as both the discharge velocity and the echo intensity decrease, there is greater spread in the value of the index-velocity error. Secondly, a number of green points in Figure 5.10(a) at discharge velocities between 0.5 m/s and 1 m/s demonstrate that high concentrations are less well correlated with high discharge velocities at Montélimar than at Romans-sur-Isère. This is likely due to the fact that flow speeds are regulated by the downstream dam, whereas the sediment load is primarily controlled by the sediment brought to the Rhône river by the Isère river. This means that velocities and concentrations are not always well correlated. Lastly, it can be seen that the spread in the Montélimar data (variance) at high echo intensities is less than it is at Romans-sur-Isère. The 95% confidence interval is $\pm$ 5% about the mean value at Montélimar, as opposed to $\pm$ 10 - 15% at Romans.

The data from the cell centred 41.2 m from the H-ADCP at Montélimar are shown in Figure 5.11. They have similar tendencies to the data at Romans-sur-Isère. As the discharge velocity decreases below 1 m/s, the spread in the index-velocity error increases and the H-ADCP increasingly underestimates velocity. When the concentration of suspended sediment is low (i.e. no significant attenuation is observed), the H-ADCP increasingly underestimates velocity as the echo intensity decreases. The intensity value below which the H-ADCP underestimates velocity is much lower at Montélimar than at Romans-sur-Isère: $\sim$120 counts, as opposed to $\sim$200 counts. Similar results of velocity underestimation when concentrations and echo intensities are low are seen in the data collected at 73.2 m (Figure 5.12) and 101.2 m from the instrument (Figure 5.13). The trend in the high-intensity value of V_q/V_h with range from the instrument is consistent with what we would expect. The values are 0.85, 0.80, 0.82, 0.88, with increasing range from the instrument; this is consistent with the along-stream velocity being highest towards the centre of the river, and lowest on the edges.

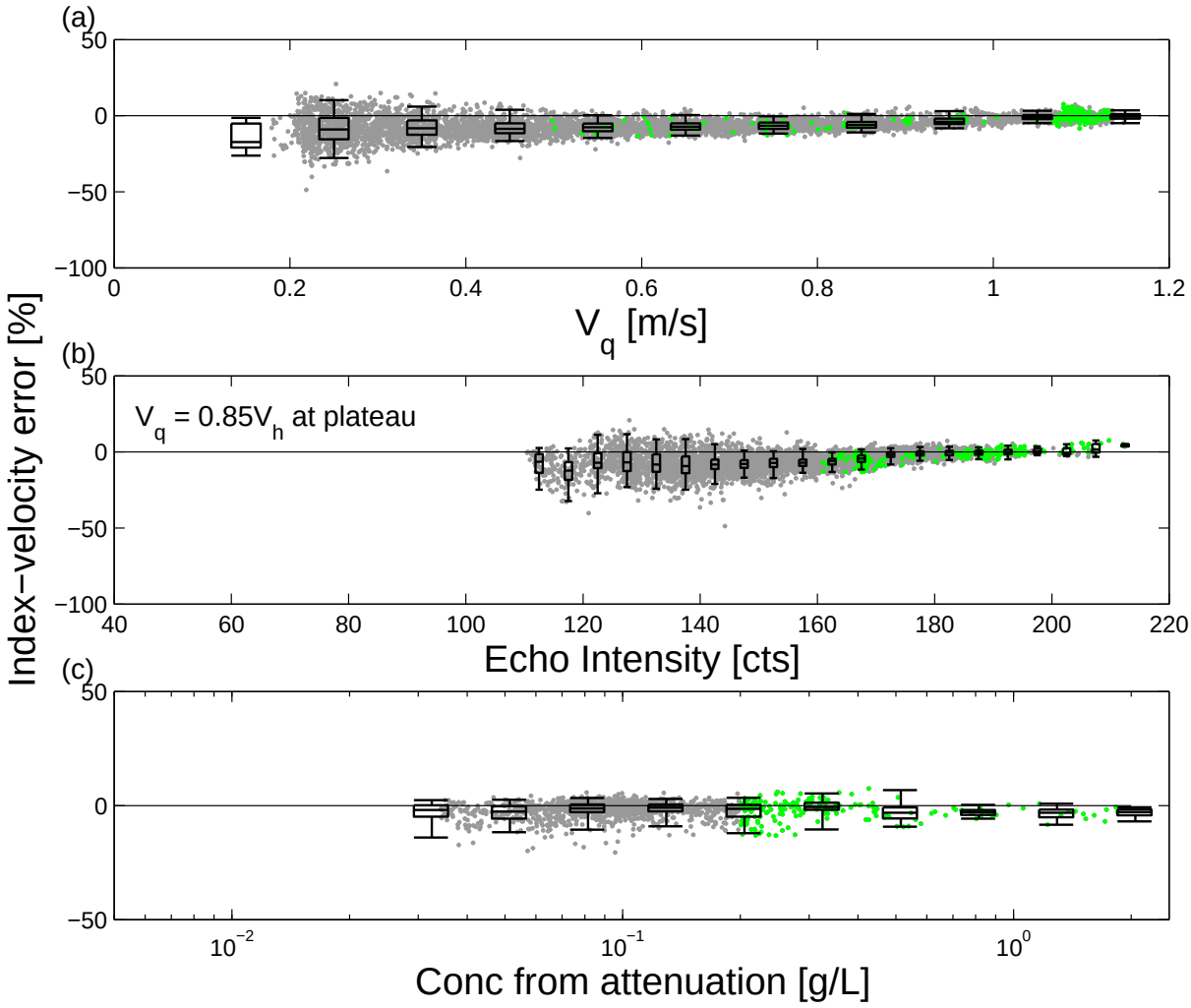

Figure 5.10: The percent error in the discharge velocity that would be calculated using a unique index-velocity relationship for the 300 kHz H-ADCP at Montélimar using data collected between January, 2010 and December, 2010 in **cell 3 (3.2 m from the H-ADCP)**. The data are plotted as a function of (a) actual discharge velocity; (b) echo intensity; (c) concentration from the optical turbidity meter.

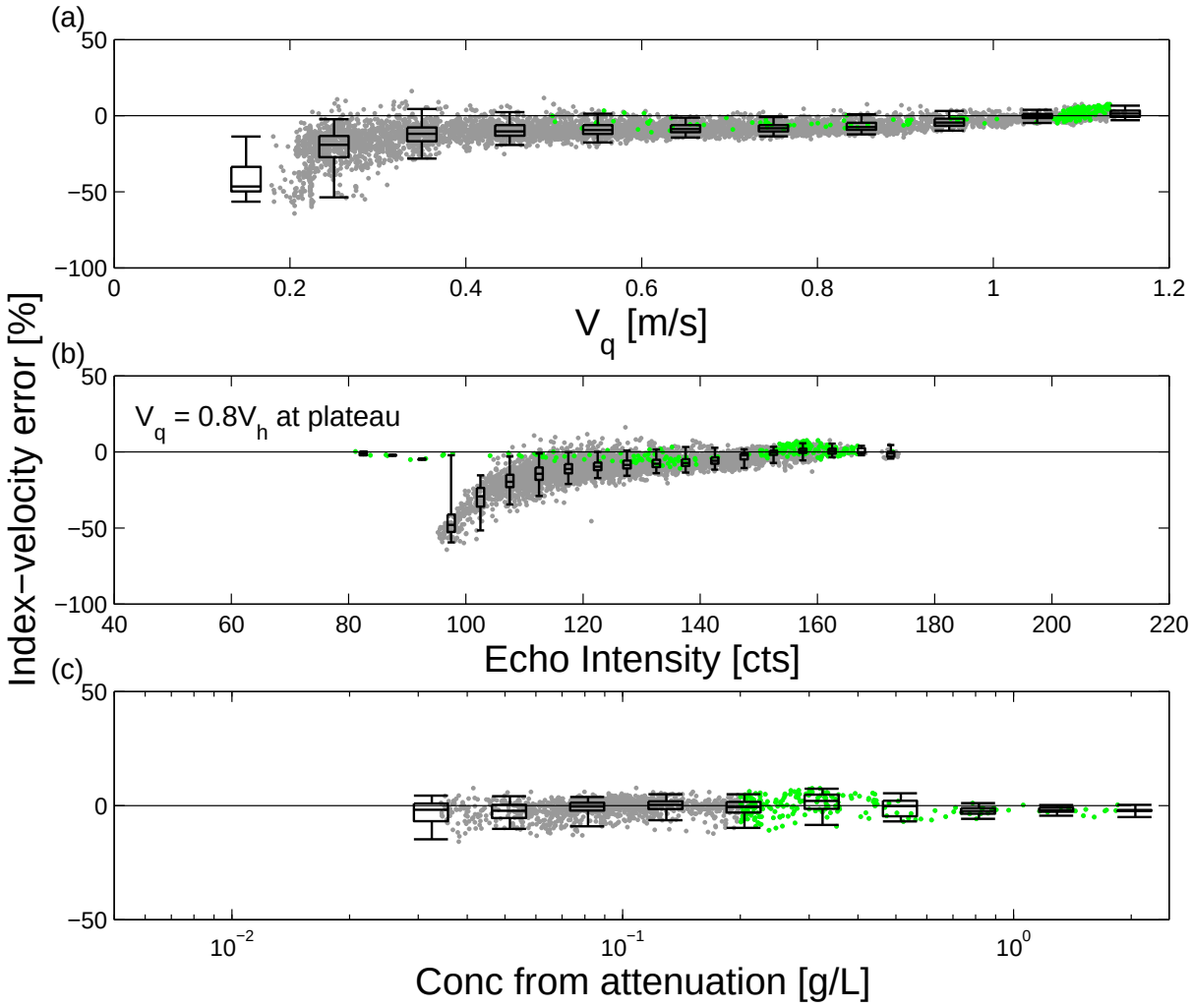

Figure 5.11: The percent error in the discharge velocity that would be calculated using a unique index-velocity relationship for the 300 kHz H-ADCP at Montélimar using data collected between January, 2010 and December, 2010 in **cell 10 (41.2 m from the H-ADCP)**. The data are plotted as a function of (a) actual discharge velocity; (b) echo intensity; (c) concentration from the optical turbidity meter.

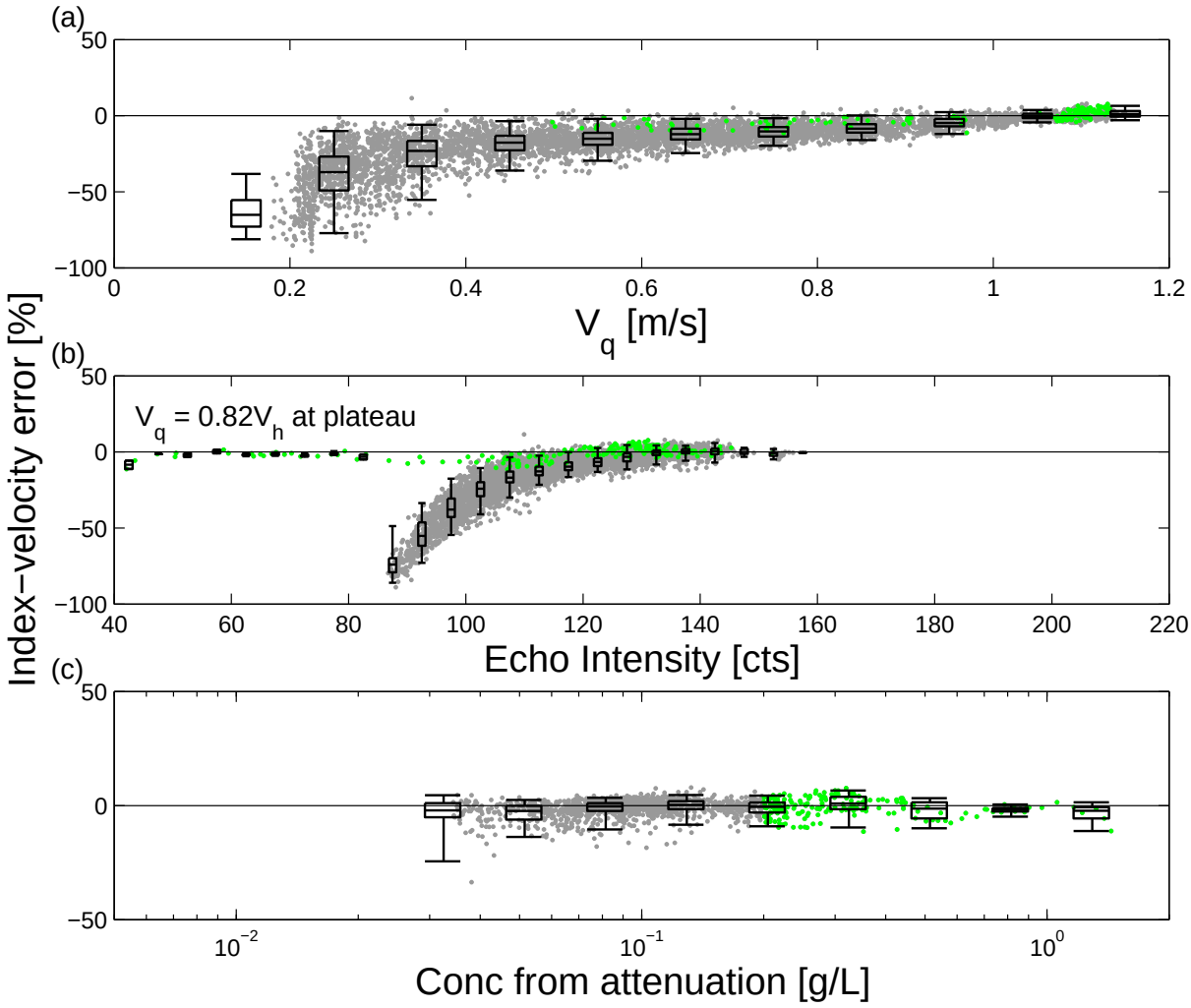

Figure 5.12: The percent error in the discharge velocity that would be calculated using a unique index-velocity relationship for the 300 kHz H-ADCP at Montélimar using data collected between January, 2010 and December, 2010 in **cell 18 (73.2 m from the H-ADCP)**. The data are plotted as a function of (a) actual discharge velocity; (b) echo intensity; (c) concentration from the optical turbidity meter.

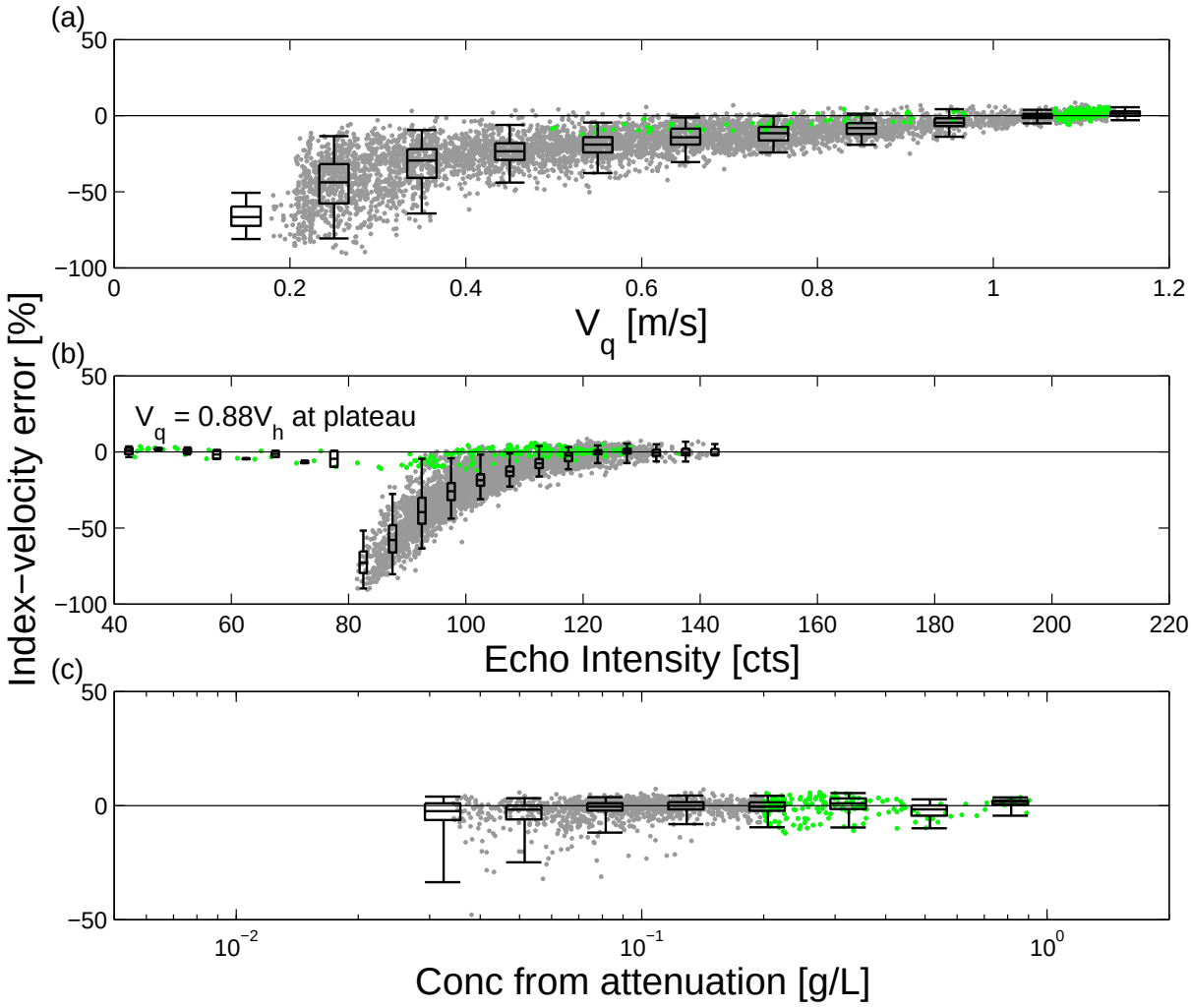

Figure 5.13: The percent error in the discharge velocity that would be calculated using a unique index-velocity relationship for the 300 kHz H-ADCP at Montélimar using data collected between January, 2010 and December, 2010 in **cell 24** (**101.2 m** from the H-ADCP). The data are plotted as a function of (a) actual discharge velocity; (b) echo intensity; (c) concentration from the optical turbidity meter.

In order to compare the data obtained at Montélimar to the 300 kHz data obtained at Romans-sur-Isère, Figure 5.14 is a plot of the fitted curves of the index-velocity error as a function of echo intensity for the low concentration data of all measurement cells previously presented in this section. The distance at which the measurements were made are listed in the legend and the different colours represent the different sites. Negative values of the index-velocity error indicate underestimation of velocity by the H-ADCP.

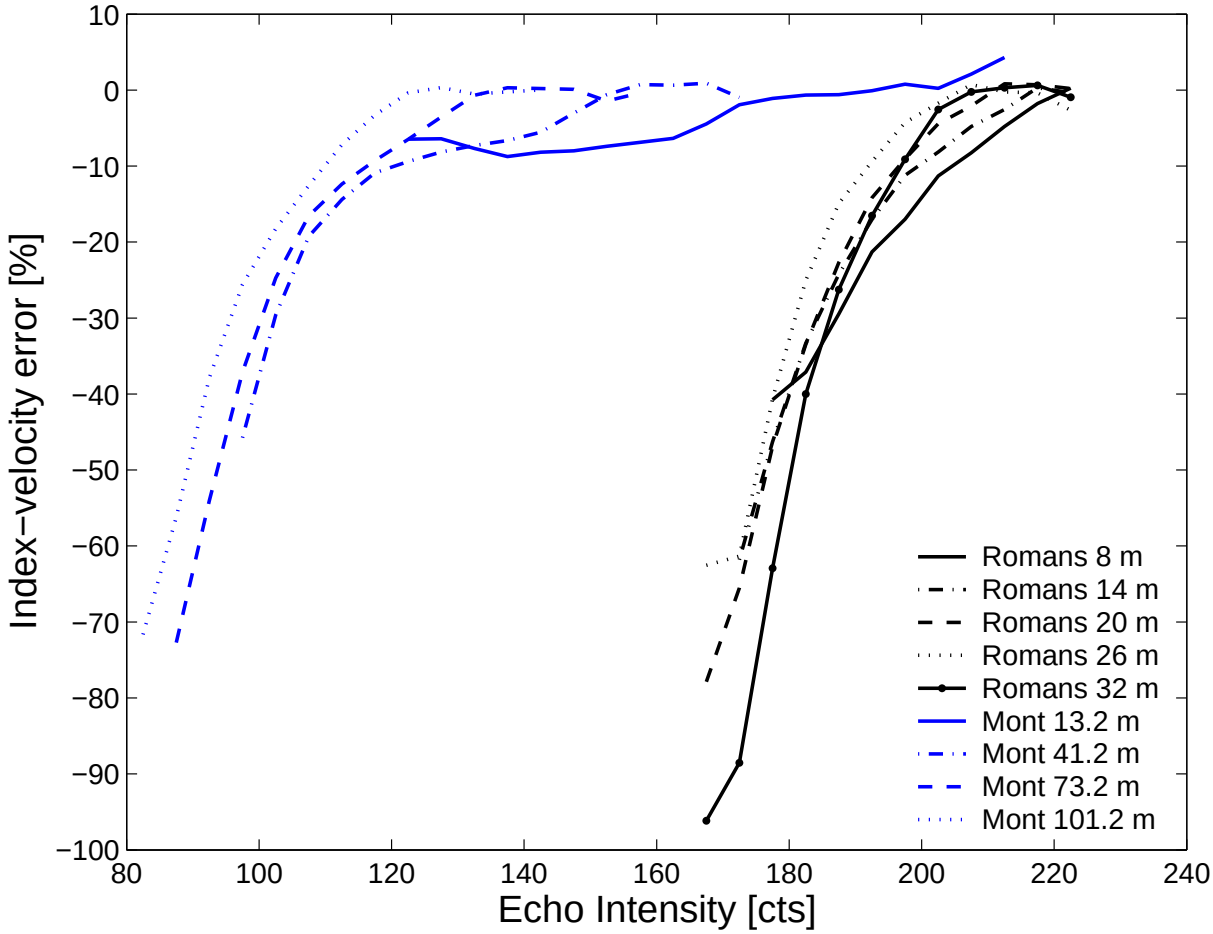

Figure 5.14: Index velocity error measured at Montélimar (blue) and Romans-sur-Isère (black) as a function of the backscattered intensity. These curves are only representative of the low concentration data.

Looking at Figure 5.14, it could be argued that the intensity below which the horizontal ADCPs underestimate velocity is a function of range from the instruments. Since the intensity data were not corrected for range, this is to be expected because the backscattered intensity detected for scattering from a given concentration of particles decreases with range. Therefore, since the underestimation is related to the amount of sediment in the water, the onset of underestimation

occurs at lower intensity values further from the instrument.

The velocity underestimation that is observed at both study sites when concentrations and backscattered intensities are low suggests that these instruments accept data with too low a signal-to-noise ratio during low flow conditions. Nevertheless, each of the curves shown in Figure 5.14 is a distinct, intensity-dependent index velocity relationship for that measurement cell that can be used to obtain a measure of discharge from the H-ADCP data. One could apply these relationships to the data from each cell to obtain a presumably accurate discharge velocity, assuming that we have encountered all possible situations.

In order to obtain the discharge velocity from the velocity measured in any one of these cells, the steps to follow are the following:

1. Look at the intensity profile to determine if there is attenuation caused by suspended sediment.

2. If there is sediment attenuation, multiply V_h by the index (the plateau value from previously presented figures), to get the discharge velocity. Even if the intensity values are low, the velocity measurements are likely accurate.

3. If there is no sediment attenuation, this means that low intensity values are due to a lack of suspended sediment. In this case, use the curves shown in Figure 5.14 to determine the discharge velocity, i.e. use an intensity-dependent index velocity relationship.

5.3 Conclusions

In the first section of this chapter we presented comparisons between horizontal profiles of along-stream velocity measured during ADCP gauging to the measurements obtained with the horizontal ADCPs at the Saint-Georges and Montélimar study sites. The profiles of along-stream velocity were normalized by the maximum value of each profile in order to highlight differences in the forms of the expected and observed profiles. It was found that velocities measured with the H-ADCP at Saint-Georges were typically accurate when the maximum velocity of the profile was greater than $\sim$70 cm/s, but below this value velocities were underestimated. This underestimation worsened with range from the instrument and with decreasing flow speeds. Similarly, when the maximum velocity measured by the H-ADCP at Montélimar was less than 40 cm/s, the velocity was underestimated. The underestimation was more drastic than at Romans.

In the second section of this chapter we used discharge data measured 2 km upstream of Romans-sur-Isère and 500 m downstream of Montélimar to establish index velocity relationships for measurements made in a number of different measurement cells using six full months of data at Romans-sur-Isère and nearly a year of data at Montélimar. The relative difference between the velocity measured by the horizontal ADCPs and the discharge velocity was examined as a function of discharge velocity, echo intensity, and concentration. It was seen that when concentrations and echo intensities were low, the H-ADCP underestimated velocity. This was true of the instruments at the two sites, which operated in narrow bandwidth and broad bandwidth modes, respectively. This velocity underestimation worsened with decreasing echo intensity. However, when concentrations (and typically velocities) were high, the H-ADCPs measured what we believe to be the correct velocity, even when the echo intensities were near the instrument's noise level. The echo intensity at which H-ADCP velocities went from being acceptable to unacceptable was a function of range.

Since Montélimar has an ideal geometry for horizontal ADCP measurements, the observation of underestimation at this site demonstrates that velocity measurements are not accurate when concentrations and backscattered intensities are low. When the signal is low due to insufficient suspended sediment, velocities are underestimated, whereas velocity values are correct when the signal is low due to attenuation. This is not a surprise, since we know that velocity measurements based on backscattering do not work in clear-water conditions. Nevertheless, the velocity underestimation needs to be addressed by the manufacturer, and taken into account by the user. As was shown in this chapter, this can be done by establishing an intensity-dependent index-velocity relationship when concentrations are less than 100 mg/L.

CHAPTER 6

INVERSION METHODS AND THEIR APPLICATION TO SUSPENDED SEDIMENT SURVEYS

6.1 Theory

Acoustic Doppler current profilers are composed of piezoelectric transducers which measure the backscattered signal as a voltage. The intensity is internally converted to the logarithmic unit of Received Signal Strength Indicator (RSSI) counts (*RD Instruments*, 2008), which is the information available to the user. The intensity in counts, E, can be converted to the intensity in decibels, I_{dB}, if the noise level in counts, E_{noise} is known. Values of E_{noise} can be obtained from the low-intensity floor when the signal is sufficiently attenuated either due to (1) a long profiling range or (2) significant sediment attenuation. Herein, the conversion from counts to decibels is done using the following equation from *Gostiaux and van Haren* (2010):

$$I_{\text{dB}} = 10 \log_{10} \left(10^{k_c E/10} - 10^{k_c E_{\text{noise}}/10} \right) , \tag{6.1}$$

where $I_{\text{dB}} = 10 \log_{10} \left(\langle {p_s}^2 \rangle / {p_{\text{ref}}}^2 \right)$ and k_c is the conversion factor to go from counts to decibels. For RD Instruments ADCPs, the reference pressure, p_{ref}, is 1 μPa. According to the WinRiver II User's Guide, the counts to decibels conversion factor depends on the temperature of the electronics, T_{e} (°C) as

$$k_c = \frac{127.3}{T_{\text{e}} + 273} \text{ dB/count} \tag{6.2}$$

(*RD Instruments*, 2009, p. 57), but the value of k_c is typically taken to be the value at 20°C,

0.43 dB/count, since it changes little with temperature (0.466 at 0° versus 0.420 at 30°). Nonetheless, in our calculations it is calculated at each time step using the temperature data.

Equation 6.1 is a correction to the commonly used formulation of *Deines* (1999). It is important to use this formulation when the signal to noise ratio, $(k_c E - k_c E_{\text{noise}})$ is less than 10. Otherwise $I_{\text{dB}} = k_c E$. The latter is the formulation most typically used (see for example *Lohrmann* (2001)).

Returning now to Equation 2.15, it can be rearranged as follows (*Thorne and Hanes*, 2002):

$$\left\langle {p_s}^2 \right\rangle = {p_*}^2 {r_*}^2 \left(\frac{3\tau c}{16}\right) \left(\frac{0.96}{k a_t}\right)^2 \frac{\left\langle {f_\infty}^2 a^2 \right\rangle}{\rho_s \left\langle a^3 \right\rangle} M \frac{e^{-4\alpha r}}{r^2} \,, \tag{6.3}$$

where τ is the acoustic pulse duration, c is the speed of sound in water and we recall that angular brackets represent the average over the number size distribution of the particles. Dividing Equation 6.3 by the square of the reference pressure, ${p_{\text{ref}}}^2$ and taking ten times the common logarithm of both sides, we get

$$I_{\text{dB}} \;=\; 10 \log_{10} \left(\frac{{p_*}^2 {r_*}^2}{{p_{\text{ref}}}^2}\right) + 10 \log_{10} \left(\frac{3\tau c}{16} \left(\frac{0.96}{k a_t}\right)^2 \frac{\left\langle {f_\infty}^2 a^2 \right\rangle}{\rho_s \left\langle a^3 \right\rangle} \frac{M e^{-4\alpha r}}{r^2}\right) . \tag{6.4}$$

The first term on the right hand side of Equation 6.4 is the term commonly referred to as the source level (*Clay and Medwin*, 1977) when r_* = 1 m.

6.1.1 Inversion of the backscattered intensity to concentration

If the composition, density, and size distributions of the particles are uniform throughout the measurement volume and if there is no multiple scattering, then Equation 6.4 can be written as

$$I_{\text{dB}} \;=\; C + 10 \log_{10} (M) - 20 \log_{10}(r) - 2\alpha_{\text{dB}}\, r \tag{6.5}$$

where C is a constant and α_{dB} is the total attenuation in decibels. If the sediment attenuation is negligible or if it can be calculated from intensity profiles (the technique to do so will be discussed in the following section), then Equation 6.5 can be used to establish a direct relationship between the backscattered intensity and the suspended sediment concentration. This is often done by end-users of ADCPs. The first example of such an application was that of *Thevenot et al.* (1992). Using water samples collected at a known distance from a 2.4 MHz broadband ADCP, they established a linear relationship between log base ten of the suspended sediment

concentration and the relative backscattering strength of the particles for both field and laboratory measurements. The relative backscattering strength of the particles, which *Thevenot et al.* (1992) refer to as BL for backscattering level, is simply the intensity detected by the transducer corrected for losses due to spherical spreading and attenuation:

$$BL = I_{\text{dB}} + 20\log_{10}(r) + 2\alpha_{\text{dB}}r. \tag{6.6}$$

It is expressed in units of decibels. Combining Equations 6.5 and 6.6, we see that

$$BL = C + 10\log_{10}(M) \tag{6.7}$$

or equivalently

$$M = 10^{(BL-C)/10}. \tag{6.8}$$

Thevenot et al. (1992) found that the relationship between concentration and backscattered intensity that was observed in the field differed slightly from that observed in the laboratory and both relationships differed from the theoretical relationship presented above. They found

$$M = 10^{(0.97+0.077\,BL)} \tag{6.9}$$

for the laboratory experiments and

$$M = 10^{(1.43+0.042\,BL)} \tag{6.10}$$

for the field experiments. The data on which these calibrations were based are depicted in Figure 6.1, which is a reproduction of Figure 37 of *Thevenot et al.* (1992). We note that neither the distance at which the acoustic measurements were made, nor the distance at which the water samples were collected appear to be reported in *Thevenot et al.* (1992).

Once a log-linear relationship has been established between concentration and range-corrected backscattered intensity for a given suspension of particles, this relationship can be used to invert the acoustic data to suspended sediment concentration provided that the size and physical properties of the particles remain unchanged in time and along the profile. This method has been applied in a number of studies, including those of *Gartner* (2004), *Topping et al.* (2007) and *Wood* (2010). The disadvantage of this method is that the calculation of BL depends on the

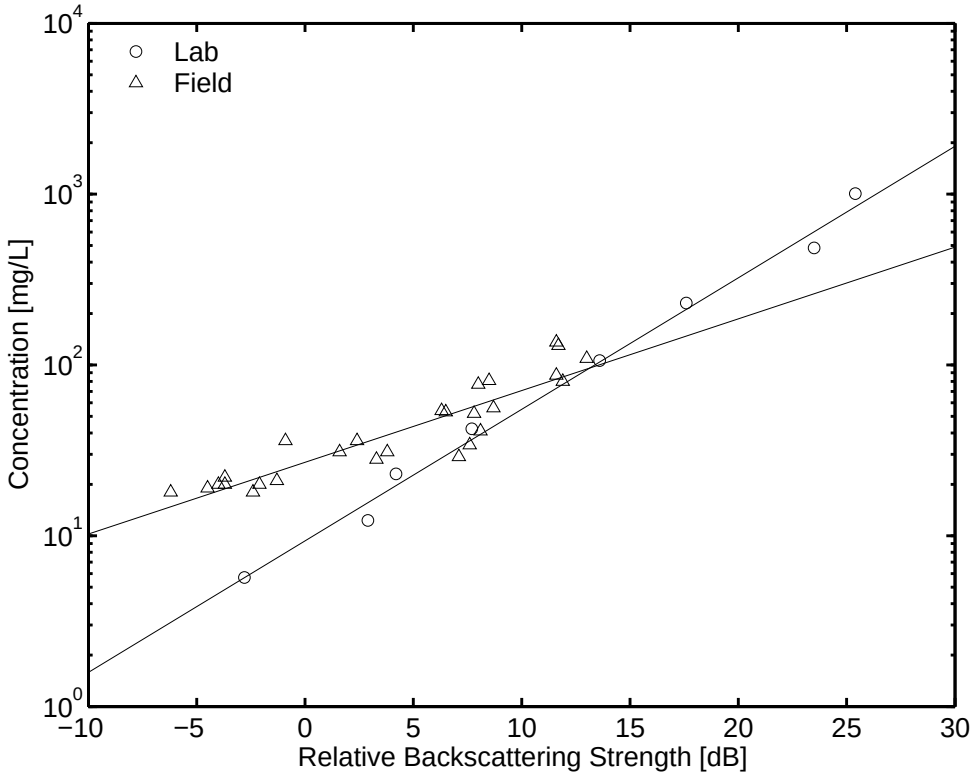

Figure 6.1: Reproduction of figure 37 of *Thevenot et al.* (1992). Calibration curves for a 2.4 MHz broadband ADCP for measurements made in the laboratory (circles) and in the field (triangles). (We do not know the distances at which the acoustic measurements were made, or the water samples were collected.)

attenuation α_{dB}, which depends on the concentration M, our unknown, when the sediment attenuation is non-negligible. This poses a problem if the concentration varies with distance from the transducer. However, we remind the reader that with a side-looking ADCP in a well-mixed river, the concentration should be homogeneous throughout the measurement volume since all measurement cells are at essentially the same height above the bed. This means that the attenuation can be calculated from the intensity profiles. The steps to do so are outlined in the following section.

6.1.2 A novel inversion of the acoustic attenuation to concentration

If the concentration of suspended sediment varies with range from the instrument, then the attenuation must be calculated between neighbouring measurement cells. When the concentration of suspended sediment does not vary with range from the instrument, the average attenuation is calculated using the full intensity profile (Note, only measurement cells within the river are used).

The method that is presented below is for the case where concentration is constant throughout the measurement volume.

The first step in calculating the sediment attenuation is to add the correction for spherical spreading, $20\log_{10}(r)$, and the correction for absorption by the water, $2\alpha_w r$, to the intensity in decibels at each range r. The attenuation due to water is calculated using Equation 2.20. This results in what *Wright et al.* (2010) refer to as the "fluid-corrected backscatter", FCB where

$$FCB = I_{\text{dB}} + 20\log_{10}(r) + 2\alpha_w r. \tag{6.11}$$

If the attenuation due to the sediment is negligible and if the concentration of scatterers M is independent of range then in the absence of obstacles the fluid-corrected intensity profile should be a horizontal line. On the other hand, if there is sufficient sediment to cause attenuation of the intensity, either due to viscous absorption or scattering by the sediments, then FCB will decrease linearly with range. The sediment attenuation can be calculated as -1/2 the slope of the fluid corrected intensity profile:

$$\alpha_{s\,\text{dB}} = -\frac{1}{2}\frac{d\,(FCB)}{dr}. \tag{6.12}$$

For demonstration purposes, Figure 6.2 is an example of the uncorrected and fluid corrected intensity profiles for data measured with the downstream beam of the 1200 kHz H-ADCP at Romans-sur-Isère for a concentration of 2.3 g/L. Notes on the figure show how the sediment attenuation is calculated from the slope of FCB versus range. The sediment attenuation in linear units is equal to the attenuation in decibels divided by $(20/\ln 10)$.

Next, in order to convert the acoustic attenuation to concentration of suspended sediment, we can do one of two things. The first possibility is to establish a linear relationship between concentration and attenuation using filtration data for water samples or concentration values from a calibrated turbidity meter, as was done in the backscattered intensity inversion. The slope of the linear fit gives the experimental value of the ensemble-averaged attenuation constant, $\langle\zeta_{\text{,exp}}\rangle$, so that

$$M = \frac{\alpha_s}{\langle\zeta_{\text{,exp}}\rangle}. \tag{6.13}$$

The second method consists in assuming a particular grain size distribution and calculating the concentration by rearranging Equation 2.21 as

$$M = \frac{\alpha_s}{\langle \zeta_v \rangle + \langle \zeta_s \rangle}. \tag{6.14}$$

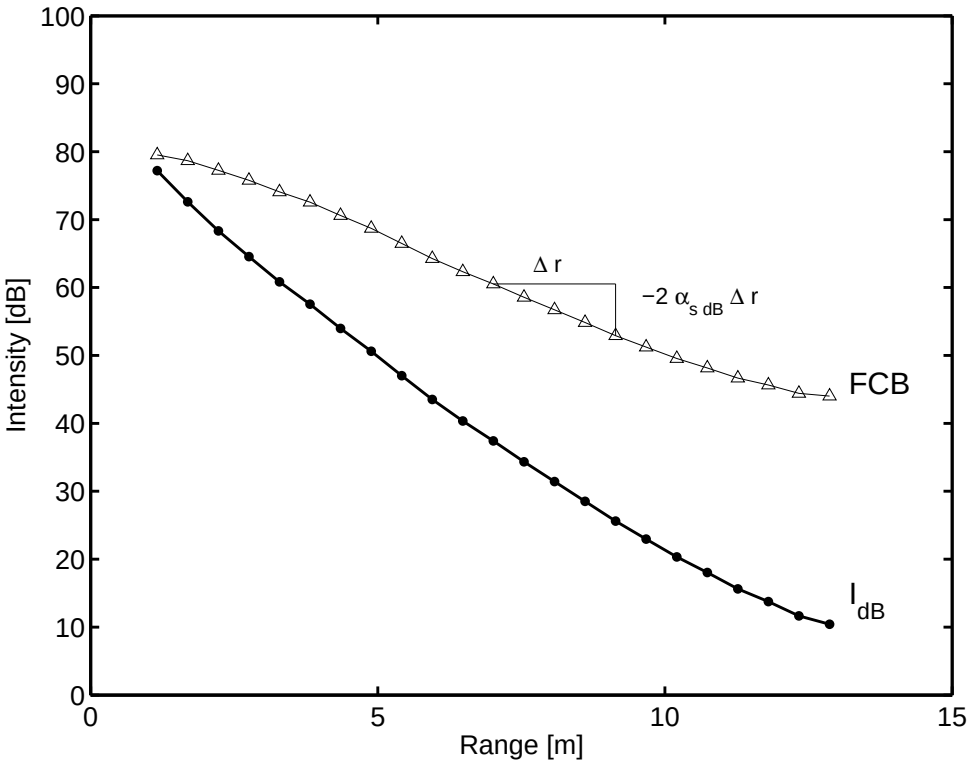

Figure 6.2: An example of the raw and range-corrected intensity profiles for data collected with the downstream beam of the 1200 kHz H-ADCP at Romans-sur-Isère. I_{dB} is the intensity in decibels and FCB is the intensity corrected for attenuation due to the water. The concentration from optical turbidity was 2.3 g/L.

As an example of method (1), data from a high concentration event which occurred June 30, 2010 at Romans-sur-Isère are shown in Figure 6.3 for the three H-ADCPs. The data that were used for this calibration were collected between 8:00 and midnight and the concentration data are from the calibrated optical turbidity meter. The time series of concentration of suspended sediment at the right bank is shown in the small subplot that is over-layed on the calibration curves. It can be seen from Figure 6.3 that there are very clear linear relationships between sediment attenuation and suspended sediment concentration for all three instruments. A second observation is that the attenuation increases more or less linearly with increasing frequency. This implies that the attenuation is due primarily to viscous absorption, since it would increase as frequency to the power of four if the attenuation were due to scattering.

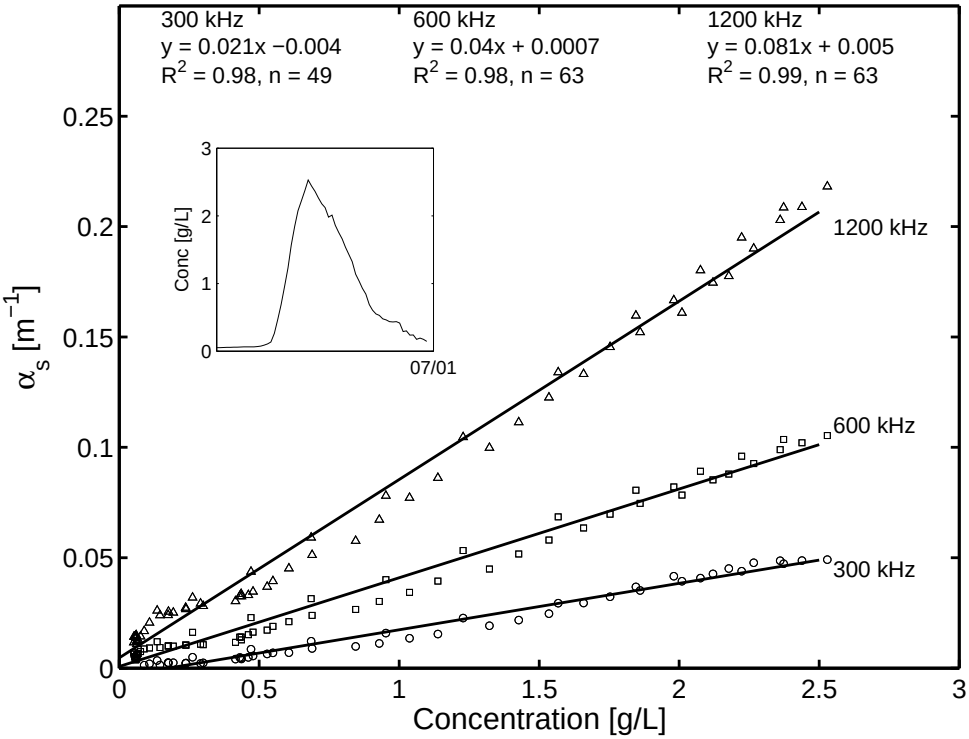

Figure 6.3: The relationship between sediment attenuation and concentration of suspended sediment for the three H-ADCPs at Romans-sur-Isère on June 30, 2010 (circles for 300 kHz, squares for 600 kHz and triangles for 1200 kHz data). Concentration values are from the calibrated optical turbidity meter. The least-squares linear regressions for each instrument are given, as are their equations, and correlation coefficients.

Linear regressions are fit to the data in Figure 6.3, using the least-squares method; the slope of these lines gives the experimental value of the ensemble-averaged attenuation constant, $\langle \zeta_{,\mathrm{exp}} \rangle$. An advantage to this method of establishing a relationship between sediment attenuation and concentration is that it requires no assumptions about the shape of the particles, since it is based purely on experimental observations. The disadvantage is that it requires simultaneous measurements from either an optical turbidity meter or water samples and the resulting calibration curve may be event-specific. If one does not have concentration data then method (2) can be used to invert the attenuation data to concentration by assuming a theoretical value of the attenuation constant. The disadvantage to this method is that the inversion is based on theoretical calculations and the theory for viscous absorption was developed for spherical particles. Also, the empirical formula used to calculate the scattering attenuation is based on measurements of attenuation from suspensions of sand-sized particles, which likely do not have the same shape as silts. Both inversion methods will be tested in Section 6.3.

6.1.3 Measuring grain size with multi-frequency attenuation data

For suspensions of particles that have size distributions with a single dominant mode, multi-frequency acoustic backscatter data can be used to determine the mean acoustic size of particles in suspension. This was first done by *Sheng* (1991) in his PhD thesis. His method was later adapted by *Crawford and Hay* (1993) and modified versions of their formulation have been used since then. Using multi-frequency data, *Crawford and Hay* (1993) take the effective acoustic size to be the particle radius that minimizes the difference between the ratios of the detected voltage to the theoretical scattering at two frequencies; that is they find the radius that minimizes $\mathrm{Obs}_i/\mathrm{Th}_i - \mathrm{Obs}_j/\mathrm{Th}_j$ where **Obs** refers to observations, **Th** refers to theory and i and j are different frequencies. They used measurements at three frequencies and the mean size was taken to be the particle radius that minimized the difference between the ratios for two of the three frequency pairs. As demonstrated in Figure 1 of *Thorne and Hardcastle* (1997), three frequencies are typically required when inverting backscattered intensity measurements at MHz frequencies because there are inflection points in the ratios of the form factor at sizes typical of sand grains for the frequencies commonly used in oceanography (1 - 5 MHz).

Herein, we take a similar approach to that of *Crawford and Hay* (1993), but use attenuation data instead of backscattered intensity. Grain size is obtained by minimizing the difference between concentration estimates from data at two frequencies. If $\zeta_i(a)$ is the theoretical attenuation constant for particles of radius a at frequency i, then $\alpha_{s\,i}/\zeta_i(a)$ is the concentration of particles of radius a that would produce the observed attenuation. Since the multi-frequency measurements are quasi-simultaneous, the concentrations observed by the two instruments are the same. Therefore, the effective particle size should be the radius that minimizes

$$\epsilon_{i,j} = \frac{\alpha_{s\,i}}{\zeta_i(a)} - \frac{\alpha_{s\,j}}{\zeta_j(a)}, \tag{6.15}$$

where $\alpha_{s\,i}$ is the measured sediment attenuation at frequency i and $\zeta_i = \zeta_v + \zeta_s$ is the theoretical total sediment attenuation constant at frequency i.

In practice, minimizing $\epsilon_{i,j}$ is similar to finding the size that minimizes $\alpha_{s\,i}/\alpha_{s\,j} - \zeta_i/\zeta_j$. The ratios of the theoretical attenuation constants can be calculated from the curves shown in Figures 2.4 or 2.5, depending on whether or not one has prior knowledge about the grain size distributions. Plots of the theoretical ratios for the three frequency combinations are shown in Figure 6.4. The values shown in Figure 6.4(a) are computed for the single size case (Figure 2.4) while those shown in Figure 6.4(b) are computed for the case of lognormal size distributions.

It can be seen that in both cases $\epsilon_{i,j}$ will be a multivalued function of grain size. This means that with only one frequency pair there can be multiple estimates of size for a given data set, as was the case with the backscatter method of *Crawford and Hay* (1993). Consequently, three combinations of frequency are required in order to deduce grain size without ambiguity. The particle radius is taken to be the size that minimizes the sum of the absolute value of all three values of $\epsilon_{i,j}$.

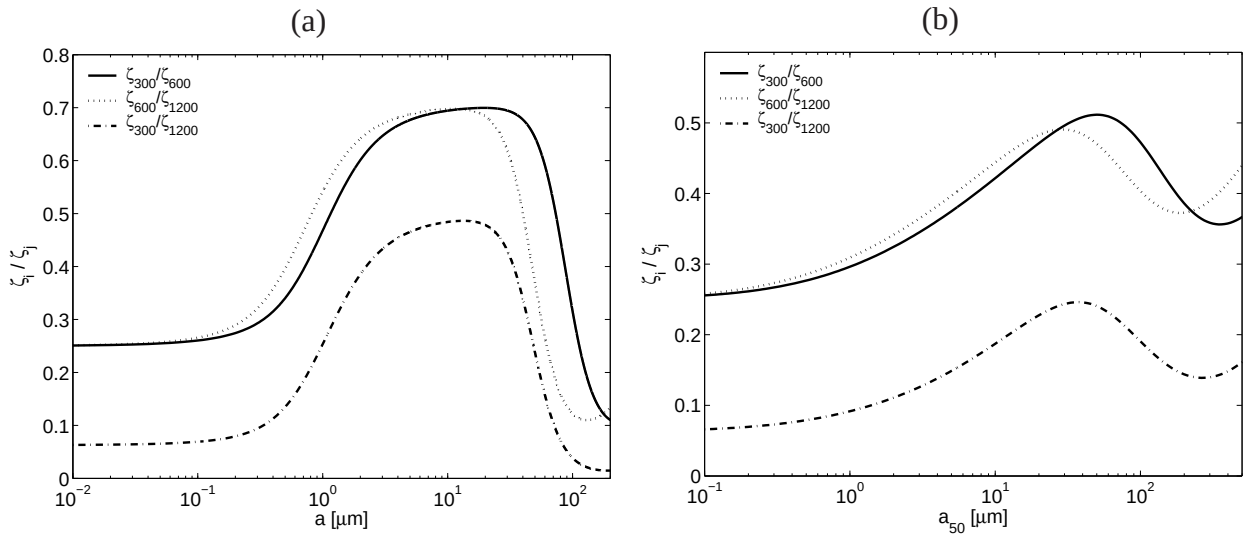

Figure 6.4: The ratios of the theoretical attenuation constants at two frequencies as a function of grain size: 300 kHz to 600 kHz (solid line), 600 kHz to 1200 kHz (dotted line), 300 kHz to 1200 kHz (dash-dotted line). Subplot (a) is for the single size case (see Figure 2.4) and subplot (b) uses the values presented in Figure 2.5, which are smoothed over lognormal grain size distributions.

Figure 6.5 is an example of the application of the size inversion using data collected at Romans-sur-Isère using the two methods: (1) assumption of a single size and (2) assumption of a lognormal volume size distribution with $\mu = \ln a_{50}$ and σ = 1. In both cases, the three values of $\epsilon_{i,j}$ are plotted versus particle radius. The data were collected at Romans-sur-Isère on June 30, 2010 between 13:45 and 14:00 during the rise of a high concentration event which lasted over 12 hours. The concentration from the turbidity meter at the time of measurement was 2.09 g/L. Figure 6.5(a) is a plot of the values of $\epsilon_{i,j}$ as a function of grain radius for the single size case. The sum of the absolute values of $\epsilon_{i,j}$ is depicted in red. Figure 6.5(b) is a plot of the values of $\epsilon_{i,j}$ as a function of median radius, considering lognormal distributions; the sum of the absolute values of $\epsilon_{i,j}$ is depicted in red. It can be seen that the particle radius that is predicted using the single size scenario is 0.9 μm, whereas the estimated median radius is 18 μm, when accounting for grain size distributions. The twenty-fold difference between these values highlights the important role

of the assumed grain size distribution in the determination of size. The median radius measured by laser grain sizer in water samples collected at other times in the year is typically 5 μm. This value lies somewhere between the two theoretical estimates. There are multiple explanations for this discrepancy. Firstly, the theory used for the inversion is based on the assumption of spherical particles. Secondly, the form of the grain size distribution is only roughly modelled by a lognormal distribution and any discrepancy between the actual shape of the distribution and our assumption will induce error. It is clear from this example that if the size distribution of the particles in suspension is unknown or poorly quantified, then the grain size results obtained from the attenuation data may be vastly different from reality.

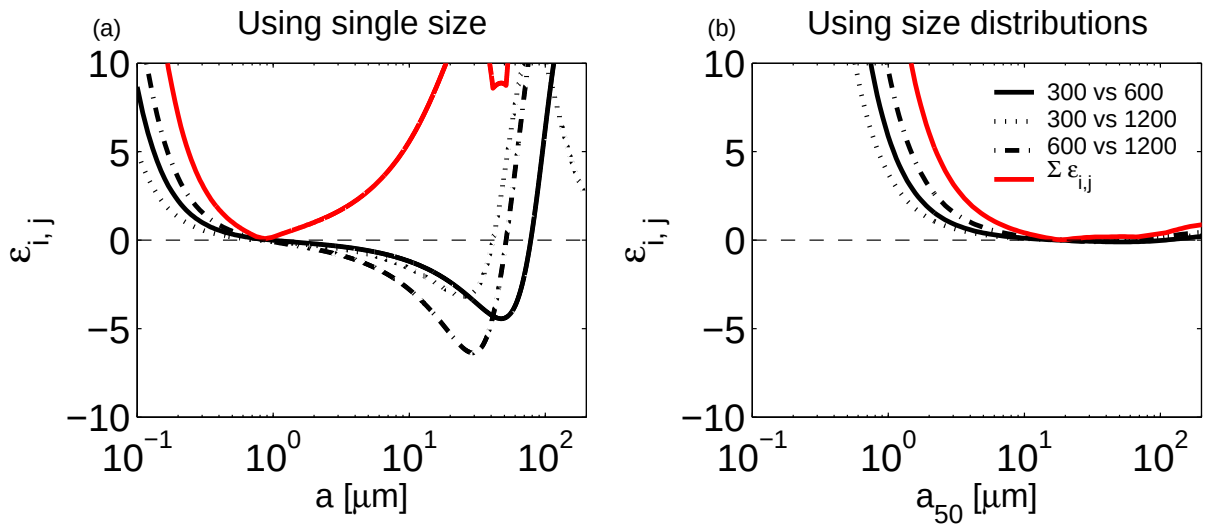

Figure 6.5: The values of $\epsilon_{i,j}$ (black) and $\Sigma\,\epsilon_{i,j}$ (red) versus grain size calculated for data collected at Romans between 13:45 and 14:00 June 30, 2010: (a) using theoretical values based on a single grain size, plotted against grain radius; (b) using theoretical values for lognormal size distributions, plotted against the median radius. The comparisons are between the 300 and 600 kHz (solid line), 600 and 1200 kHz (dotted line) and 300 and 1200 kHz (dot-dashed line) data. The concentration according to the turbidity meter was 2 g/L.

This technique for determining grain size from multi-frequency attenuation data is innovative and unique to this thesis. Although *Topping et al.* (2007) presented multi-frequency attenuation measurements, they only provided one estimate of size for their entire data set, using multiple months of concentration and attenuation data to determine the grain size that best corresponded to Urick's theory for a single grain size at a single frequency (Equation 2.25). Our approach differs notably from their's because we focus on quasi-instantaneous measurements and combine the data from the three frequencies to get a better estimate of size. Indeed, we admit that caution

must be used when quoting specific grain sizes due to the significant role played by the grain size distributions, but the advantage of our method is that by using quasi instantaneous data at three frequencies we can study the time variation of grain size during high concentration events such as floods or dam flushing. This method should also be sufficiently robust to monitor changes in grain size from event to event. Examples of application of this method will be shown in Chapter 7.

6.2 Application of the backscattered intensity inversion

In order to establish the calibration curve for the backscattered intensity method, water samples are typically collected at a known distance from the acoustic instrument. Data from a calibrated turbidity meter can also be used. The intensity data must be corrected for losses due to both spherical spreading and total attenuation. The attenuation due to water, α_w, is calculated with the use of Equation 2.20 and the record of temperature from each H-ADCP. When applicable, the sediment attenuation, α_s, is calculated from the slope of the fluid-corrected intensity profile as explained in Section 6.1.2. These data are then used to calculate the BL values (see Equation 6.6) at all distances from the transducer. If there are no obstacles blocking the line of sight of the ADCP and if concentration, size, and physical properties of the suspended sediment are homogeneous throughout the measurement volume, then the relationship between BL and concentration should be independent of range.

In the following subsections we examine the relationship between the backscattering level, BL, and the concentration of suspended sediment at the Saint-Georges, Romans-sur-Isère, Montélimar and Tricastin study sites. The results are presented going from North to South. As presented in Section 3.2, approximately six months of concurrent acoustical and optical data are available at Saint-Georges. For Romans-sur-Isère, only the data from the 1200 kHz instrument shall be presented in order to avoid the questions that plague the 300 kHz and 600 kHz data, regarding their proper positioning. Unfortunately, very few or no measurements of concentration are available at the Montélimar and Tricastin study sites but we have a record of the daily-integrated values of concentration collected approximately 100 km downstream on the Rhône river at Arles. Due to the temporal averaging of these concentration measurements and the propagation time between study sites ($\sim$ 30 hours at 1 m/s), they cannot be used to explain fluctuations of intensity on hourly time-scales, but they are useful for multi-day events.

6.2.1 Saône river at Saint-Georges

Figure 6.6 is a plot of six months of acoustical and optical data observed at the Saint-Georges study site. Periods with missing data in Figure 6.6 are due to technical problems with either the optical or the acoustical instruments. This is a typical record of the events that are observed at this site, where concentrations are always less than 200 mg/L, even during floods. The intensity values that are depicted are the three-beam average intensity recorded in bin 3 by the 300 kHz H-ADCP. This corresponds to the first cell in the far field of the instrument which is 14 m from the central transducer. From Figure 6.6 it can be seen that when concentrations are low, the acoustic data are noisy. We also see that for periods for which we have simultaneous acoustic and optical data, relatively high turbidity values correspond to high backscattered intensities. It can also be seen that the intensity is saturated when the concentration exceeds $\sim$ 40 mg/L, as the intensity plateaus at 218 counts. These observations imply that the range of concentration values over which we will be able to establish a working relationship between concentration and intensity is limited.

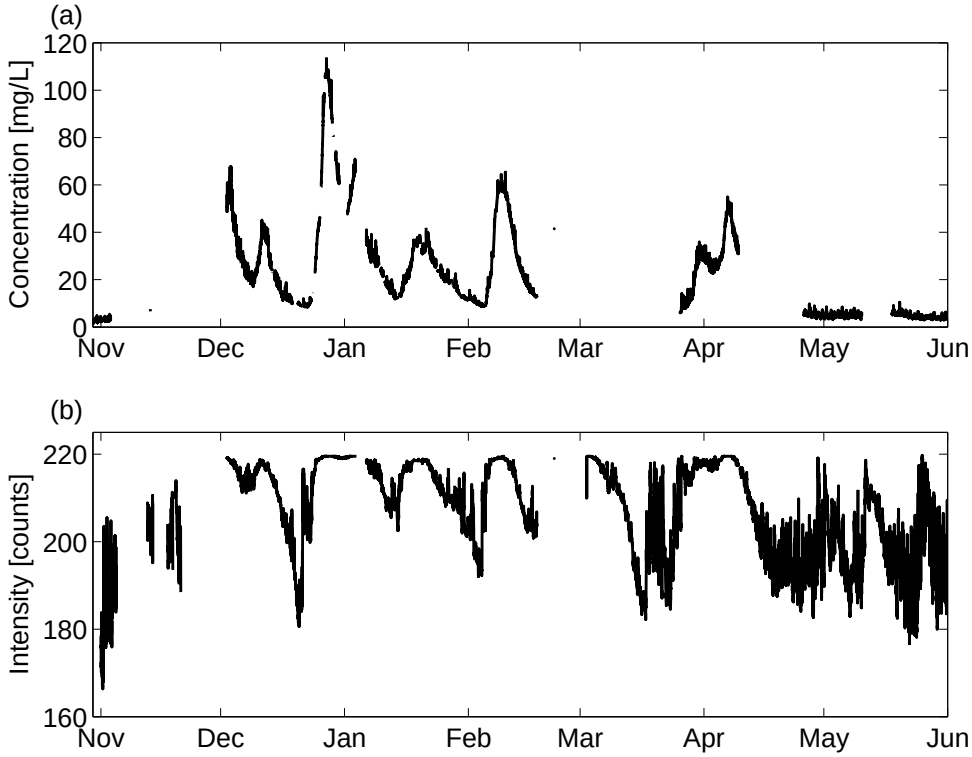

Figure 6.6: Time series of (a) concentration data from the optical turbidity meter at Saint-Georges and (b) the backscattered intensity recorded at the cell located 14 m from the 300 kHz H-ADCP. The intensity data (in counts) are the average intensity recorded by the three beams.

Figure 6.7 is a log-linear plot of concentration versus BL for the data depicted in Figure 6.6. The thick gray line represents the least-squares fit linear relationship to the data and the thin gray lines represent $\pm$ 50% of the concentration values predicted by this line. The slope of the log-linear regression is 0.049; this is very close to 0.042, the value found by *Thevenot et al.* (1992) for field measurements with a 2.4 MHz broadband ADCP. For comparison, the data recorded in the sixth measurement cell of the same instrument are shown in Figure 6.8. These data are collected 26 m from the H-ADCP. The slope and y-intercept of the least-squares linear regression for the data collected at 26 m from the instrument are the same as those for the data collected at 14 m. A larger range of concentration values are observable at this distance (see difference in maximum y values) because the signal decreases with range from the instrument, pushing the concentration at which the signal saturates to higher values. Nonetheless, the manner in which the range-corrected intensity values plateau around 60 mg/L tends to suggest signal saturation. In both Figures 6.7 and 6.8, one's eye may be drawn to the lack of data for concentration values

between 6 mg/L and 8 mg/L. Concentration values in this range have been observed, but there are no simultaneous measurements of acoustic scattering due to technical problems.

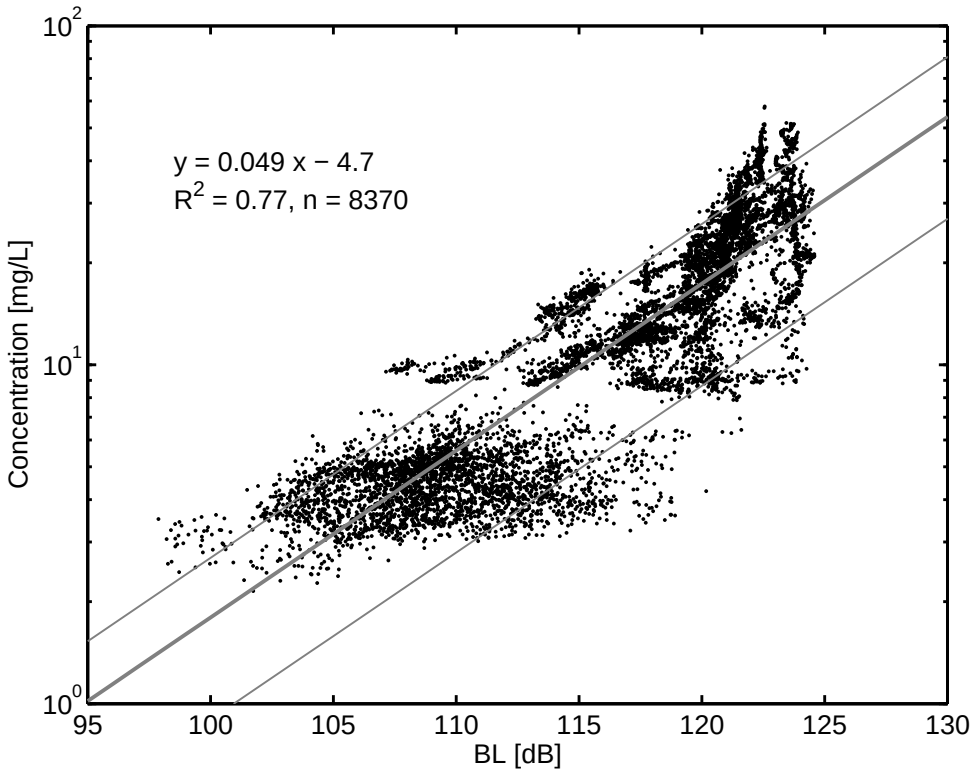

Figure 6.7: Concentration of suspended sediment versus the backscattering level BL measured at 14 m from the H-ADCP at Saint-Georges. The thick gray line is the least-squares linear regression to the data, the thin gray lines represent $\pm$ 50% of the concentration values predicted by the linear regression, R^2 is the correlation coefficient and n is the number of data points used for the fit.

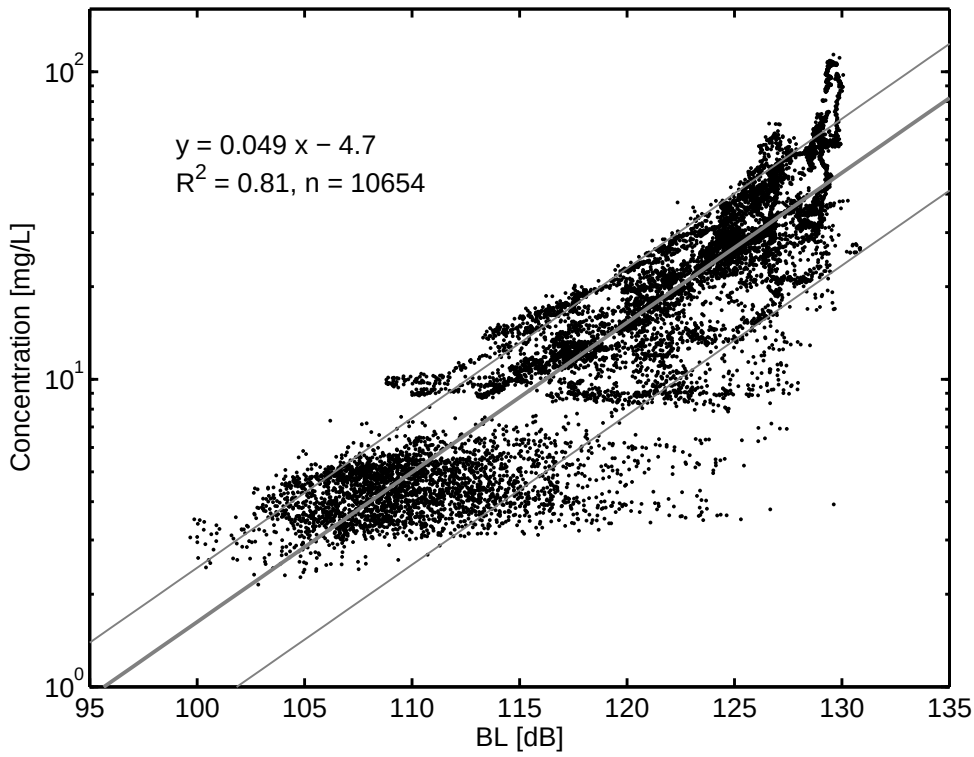

Figure 6.8: Concentration of suspended sediment versus the backscattering level BL measured at 26 m from the H-ADCP at Saint-Georges. The thick gray line is the least-squares linear regression to the data, the thin gray lines represent $\pm$ 50% of the concentration values predicted by the linear regression, R^2 is the correlation coefficient and n is the number of data points used for the fit.

Since it is hard to discern trends from the scatter plots of Figures 6.7 and 6.8, these data are also plotted as box and whisker plots in Figures 6.9 and 6.10. This is done by grouping the data into bins of $\log_{10}$(concentration) that are 0.1 units wide. The lower quartile, median and upper quartile of the sample are calculated for each bin, along with the 2.5% and 97.5% quantiles. As with a typical box and whisker plot, the box for each concentration class represents the zone in which 50% of the data are confined, but unlike a typical box and whisker plot, the extremes represent the 2.5 and 97.5 % quantiles. The box plots of Figures 6.9 and 6.10 show that at least half of the data lie within $\pm$ 50 % of the linear fit when concentrations are low ($<$ 35 mg/L at 14 m and $<$ 50 mg/L at 26 m), but as concentrations increase, the data diverge from this linear relationship and the range-corrected intensities plateau, suggesting signal saturation. Use of the regression model for concentrations greater than 50 mg/L would therefore result in underestimation of the suspended sediment concentration on average. A similar result was found by *Wood* (2010) for the calibration of a 3 MHz side-looking Sontek acoustic Doppler velocity meter in the Clearwater River. She found that when the actual concentration exceeded 100 mg/L,

the concentration obtained from the acoustic backscatter data using a single calibration curve was less than the actual value that was measured in water samples. Since the Workhorse H-ADCP that is used at Saint-Georges was operated in high-gain mode (which is the default setting), the configuration could be switched to low-gain mode if the purpose of the installation was to monitor suspended sediment concentrations. The reduction of the gain would prevent the signal from saturating at such low concentrations.

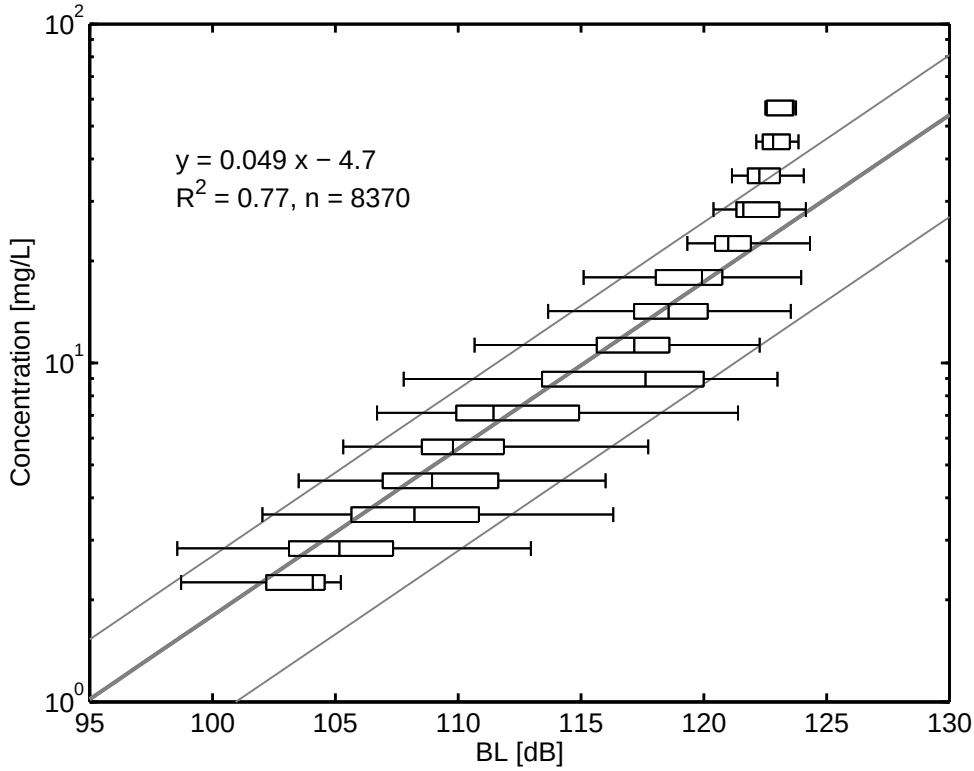

Figure 6.9: Box and whisker plots of the data presented in Figure 6.7: concentration of suspended sediment versus the backscattering level BL measured 14 m from the H-ADCP at Saint-Georges. The thick gray line is the least-squares linear regression to the data, the thin gray lines represent $\pm$ 50% of the concentration values predicted by the linear regression, R^2 is the correlation coefficient and n is the number of data points used for the fit.

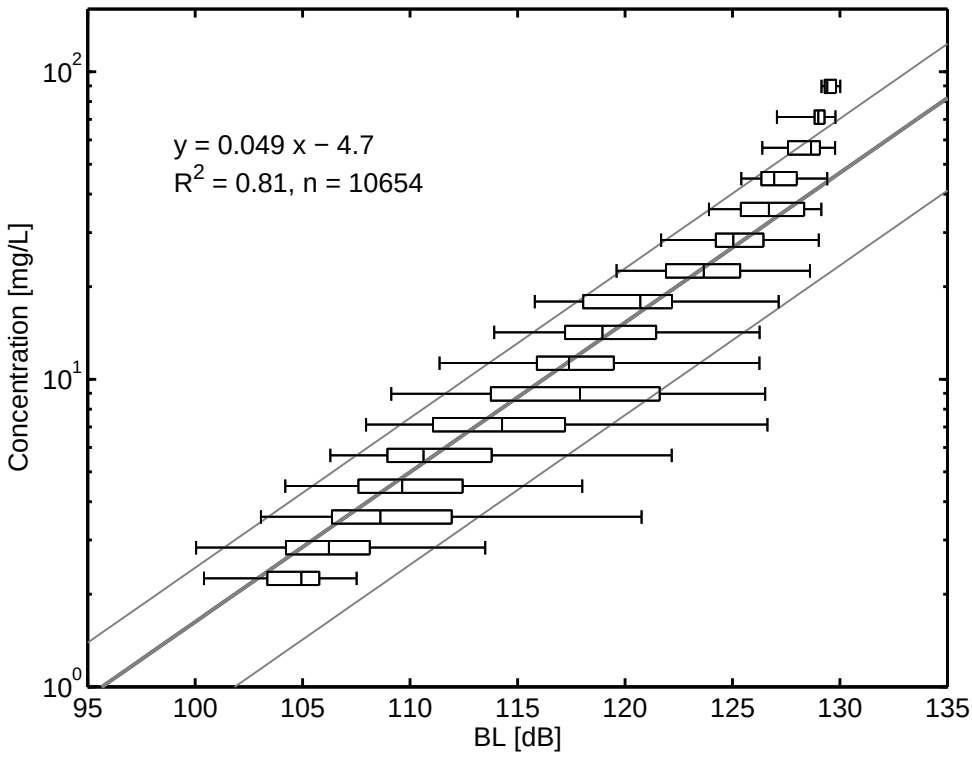

Figure 6.10: Box and whisker plots of the data presented in Figure 6.7: concentration of suspended sediment versus the backscattering level BL measured 26 m from the H-ADCP at Saint-Georges. The thick gray line is the least-squares linear regression to the data, the thin gray lines represent $\pm$ 50% of the concentration values predicted by the linear regression, R^2 is the correlation coefficient and n is the number of data points used for the fit.

The intensity data that were presented in this section are the average intensity recorded by all three beams, since this was the data that we had available. For days on which we have the raw data, we observe that the intensity profiles that are recorded by the downstream and across-stream beams of the H-ADCP at Saint-Georges are very noisy and the backscattering level does not appear to be range independent, as it should be. Consequently, the three-beam averaged intensity profiles are also noisy and we were not able to establish a satisfactory calibration curve between concentration and backscattering level at ranges greater than 30 m from the instrument.

In summary, we were able to establish a log-linear relationship between concentration and range-corrected intensity for the data collected within 30 m of the 300-kHz H-ADCP at Saint-Georges. The data are highly scattered, but acceptably unbiased when concentrations are below about 30 - 50 mg/L, depending on the distance at which the measurements are made. The measurable range of concentration is very limited, but it could be increased if the gain of the instrument was reduced in order to avoid saturation.

6.2.2 *Isère river at Romans-sur-Isère*

In this section we establish a linear relationship between the logarithm of the concentration and the backscattering level that is measured in the far field of the 1200 kHz H-ADCP at Romans-sur-Isère. Concentrations are calculated from the turbidity time series at Romans-sur-Isère using only periods during which the measurements are reliable. Instead of trying to find one unique relationship for months worth of data, data are presented from a number of different events. This includes ten days of low concentrations (10 - 25 mg/L) observed between Nov. 20 and Nov. 30, 2009, a spring flood which occurred between May 30 and June 3, 2010 (maximum concentration of $\sim$ 8 g/L) and a man-made event caused by dam operations $\sim$ 200 km upstream which occurred June 30 2010 (maximum concentration of $\sim$ 2.5 g/L). Apart from the November 2009 data, all of the turbidity data used in this comparison are plotted in Figure 6.11a.

The different colours used in Figure 6.11 represent data collected during November (blue), on the rise of the spring flood (magenta), the fall of the flood (cyan), the start of the increase in concentration June 16 (green) and the dam-driven event June 30 (yellow). Everything else is shown in black. Figure 6.11b is the log-linear plot of concentration versus the backscattering level, BL. The thick gray line is the least-squares linear regression to all the data and the thin gray lines represent $\pm$ 50% of the concentration values predicted by the linear regression.

The slope of the least-squares linear regression fit to all data is 0.059. This is within the range of values seen by *Thevenot et al.* (1992). Although we have fit one line to all the data, it is clear from this plot that the data are grouped in terms of events. The group of points corresponding to concentrations of 10 - 25 mg/L corresponds to the data collected during November. Like at the Saint-Georges study site, intensities fluctuate significantly when concentrations are low. The green dots which are seen at concentrations between 400 and 600 mg/L and intensities of 95 - 110 dB correspond to a peak in backscattered intensity that was observed between 04:00 and 06:00 (UTC+1) June 17 when the turbidity began to increase abruptly. We suspect that the divergence of these points from the main trend indicates temporarily coarser grain sizes, since larger particles have a tendency to be resuspended on the rise of floods. The 1200 kHz H-ADCP may be more sensitive than the turbidity meter to the potential variation in grain size.

The data collected on the rise and fall of the spring flood lie on opposite sides of the overall linear regression to the Romans-sur-Isère data. By fitting linear regressions to these two subsets, we see that the y value at x = 0 for the data on the rise of the flood is -4.0 while that on the fall of the flood is -2.2. From Equations 6.4 and 6.5, we know that the absolute value of the y-intercept

is the constant C and, for a given instrument, the only term which can vary in the expression for C is $\left\langle {f_\infty}^2 a^2 \right\rangle / \rho_s \left\langle a^3 \right\rangle$. This term is often referred to as the scattering function. When $ka < 1$, as is the case for our measurements, f_∞ is proportional to a^2. This means that for spheres of a unique size, the absolute value of the y-intercept should increase as a^3. As such, the observation of a larger absolute value of C on the rise of the flood than on the fall of the flood supports the hypothesis that larger grains are in suspension on the rise of the flood.

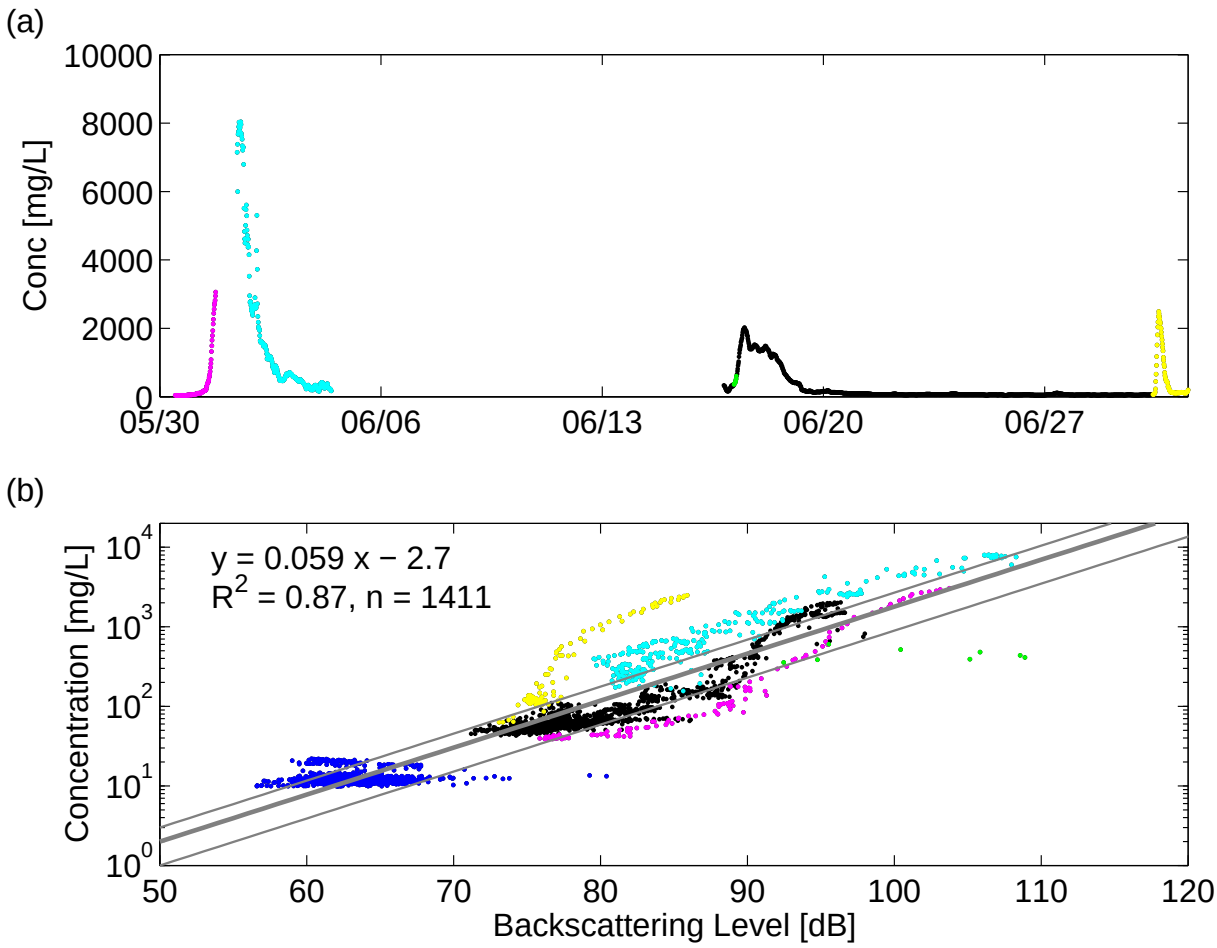

Figure 6.11: Romans-sur-Isère: (a) Concentration from turbidity and (b) acoustic calibration data for the 1200 kHz H-ADCP using intensities recorded 3 m from the instrument. The data depicted in panel (b) include all the data shown in panel (a) plus data from ten days of low concentration data from November 2009. The thick gray line is the least-squares linear regression to the data, the thin gray lines are $\pm$ 50 % these y values, R^2 is the correlation coefficient and n is the number of data points used for the fit.

The purpose of grouping the data in terms of events was to show that the relationship between concentration and backscattering level changes significantly from one event to another. This is due to the slight changes in grain size that may be observed between and within events.

In Table 3 of *Moore et al.* (2011), we presented theoretical values of the scattering function, $\left\langle {f_\infty}^2 a^2 \right\rangle / \rho_s \left\langle a^3 \right\rangle$, for three distinct grain size distributions that were observed at Romans-sur-Isère. Although the differences between the probability density distributions of grain size appeared negligible, the presence of larger particles in some of the samples led to substantial differences in the theoretical scattering function [1]. For an acoustic wave with a frequency of 1228.8 kHz, the three values of $\left\langle {f_\infty}^2 a^2 \right\rangle / \rho_s \left\langle a^3 \right\rangle$ were 9.4×10^{-4} m^2/kg, 4.4×10^{-3} m^2/kg and 6.1×10^{-3} m^2/kg. The first two values were computed for samples collected on the fall of the spring flood, while the third value corresponded to a sample collected mid-May during a small high concentration event (max concentration of $\sim$ 120 mg/L). We see that the theoretical scattering function can change by almost an order of magnitude as a result of the slight differences in grain size that occur at Romans-sur-Isère. Both the theory and our observations suggest that using the calibration model fit with data from one event to invert the backscattered intensity to concentration during another event with different grain sizes, can lead to an over or under prediction of concentrations by almost an order of magnitude.

Since the calibration curve is so sensitive to slight changes in grain size, caution must be taken when using this method to predict sediment transport. Nevertheless, single calibration curves can and have been used by other researchers to estimate daily suspended sediment loads (e.g. *Wood*, 2010) from side-looking ADCP intensity data. Using calibration curves based on less than twenty samples collected at different times throughout a year, Wood used the backscattered intensity of a 3.0 MHz and 1.5 MHz H-ADCP to obtain time series of the daily load of suspended sediment at two study sites. These results were found to be in reasonable agreement with transport curves. Therefore, depending on the desired accuracy and the time scale on which one is interested in studying sediment transport, the backscattered intensity inversion method may be acceptable. However, if an order of magnitude error is not acceptable, then an event-specific intensity inversion method must be used.

6.2.3 Rhône Canal at Montélimar

As stated earlier in this chapter, we have insufficient measurements of concentration at the Montélimar study site in order to perform the acoustic calibration properly, however we can use the daily-averaged values of concentration downstream at Arles. We have measurements of backscattered intensity at Montélimar and concentration at Arles for a good part of 2010. As with Saint-Georges, the intensity values are the three-beam averaged intensity. Figure 6.12 is a plot of the

[1] N.B. The distributions that are plotted in *Moore et al.* (2011) are not probability distributions.

concentration at Arles versus the daily-averaged backscattering level, BL, recorded 14 m from the 300 kHz H-ADCP at Montélimar. We have not accounted for propagation time between the two sites since the purpose of this subsection is merely to determine whether or not such an inversion method is feasible.

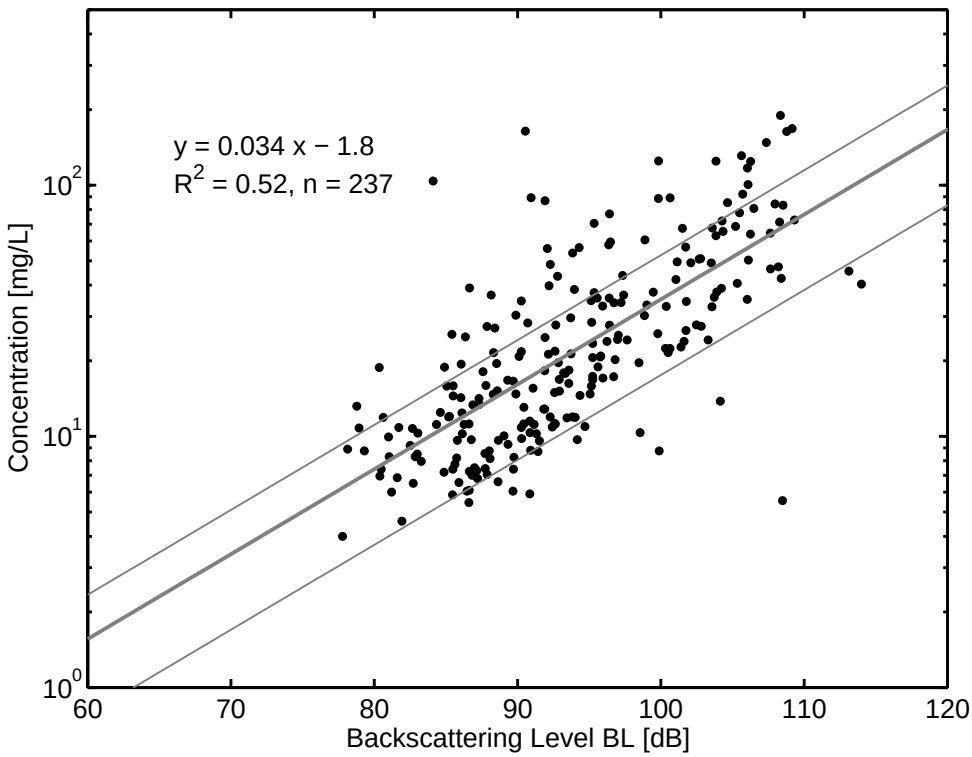

Figure 6.12: Daily-averaged values of suspended sediment concentration at Arles versus the daily-averaged backscattering level BL measured at 14 m from the H-ADCP at Montélimar for all available data in 2010. The thick gray line is the least-squares linear regression to the data, the thin gray lines are $\pm$ 50% the y-values predicted by this line, R^2 is the correlation coefficient and n is the number of data points used for the fit.

Although the maximum concentration in 2010 for which we have acoustic measurements is only 200 mg/L, it can be seen from Figure 6.12 that the backscattering level is a continuously increasing function of concentration. Signal saturation is not a problem at Montélimar as it is for the 300 and 600 kHz H-ADCPs at Romans and the 300 kHz H-ADCP at St-Georges. This is likely because the H-ADCP at Montélimar operates in wide bandwidth mode, unlike the 300 kHz instruments elsewhere, as was previously discussed in Section 3.3. When an instrument operates in wide bandwidth mode, the signal to noise ratio (backscattered intensity) is less than when it operates in narrow bandwidth mode (*Clay and Medwin*, 1977, p. 122).

The results at Montélimar are very promising. Since the backscattering level is independent

of range at this study site (see Figure 4.16), as it should be for a homogeneous distribution of sediment and an unobstructed line of sight, the data from all measurement cells resemble the data that were presented in Figure 6.12. The range-independence of the relationship combined with the large range of detectable concentrations implies that the backscattered intensity inversion method could be applied to data at this site. However, it is clear that a proper calibration can only be obtained using water samples collected at Montélimar.

6.2.4 Rhône Canal at Tricastin

In this section we present a comparison between the data collected by the 300 kHz H-ADCP at Tricastin and the concentration at Arles in order to examine the feasibility of using the backscattered intensity inversion method at this study site. As with Montélimar, the intensities are the three-beam average. Figure 6.13 is a plot of the daily-averaged concentration at Arles versus the daily-averaged backscattering level using data recorded 14 m from the H-ADCP for all data recorded in 2008.

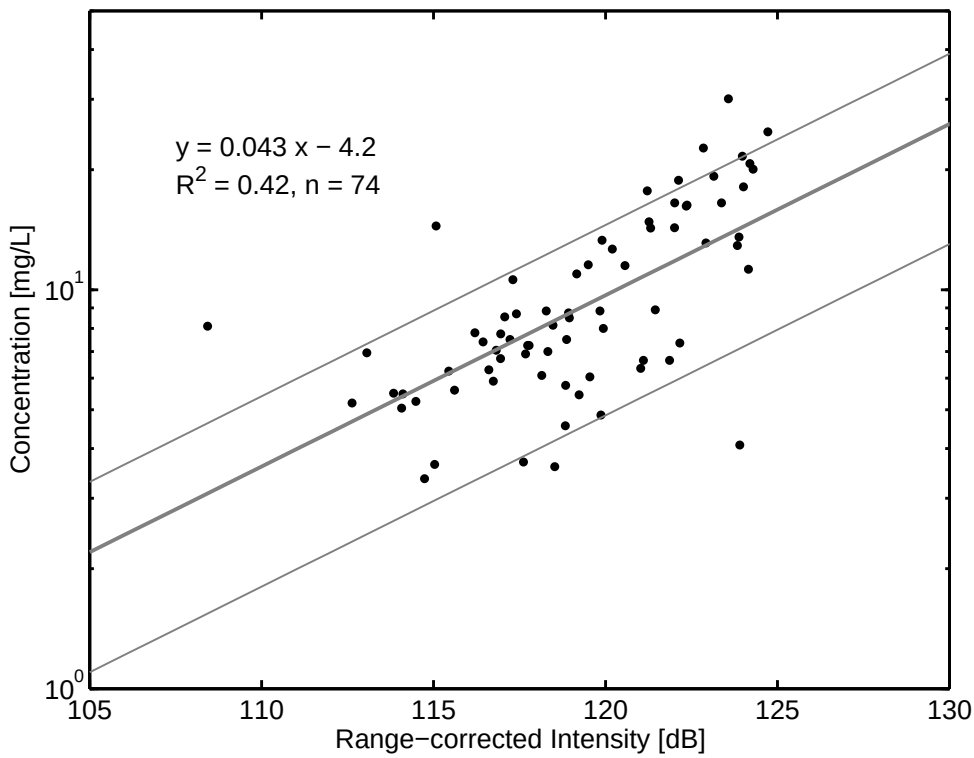

Figure 6.13: Daily-averaged values of suspended sediment concentration at Arles versus the backscattering level measured at 14 m from the H-ADCP at Tricastin for 2008. The thick gray line is the least-squares linear regression to the data, the thin gray lines are $\pm$ 50% the y-values predicted by this line, R^2 is the correlation coefficient and n is the number of data points used for the fit.

As with Montélimar, we find that the concentration is a continuously increasing function of BL, although the maximum concentration at which we have acoustic measurements is only 40 mg/L. Since this H-ADCP operates in narrow bandwidth mode, we expect that at concentrations higher than 40 mg/L, the signal will saturate, as it does for the 300 kHz instruments at Saint-Georges and Romans. By further examination of data not shown here, we saw that the backscattering level at Tricastin was independent of range for all distances within 50 m of the H-ADCP. This implies that the data from any of the cells within the first 50 m could possibly be used to do an inversion based on the backscattering level. As with Montélimar, in-situ measurements with a higher temporal resolution are required in order to perform a proper calibration.

6.3 Application of the attenuation inversion

6.3.1 Saône River at Saint-Georges

As can be seen from the turbidity data that were presented in Figure 6.6, the maximum concentration that was observed at Saint-Georges during the study period was 120 mg/L. Since this value is fairly low, we did not expect to see attenuation due to the suspended sediment, and nor did we. Historical records at this site show that concentrations are rarely much higher: records from a flood that occurred in February 2006 show that the maximum concentration was 146 mg/L (*Le Coz et al.*, 2007), while the maximum concentration of 1995 recorded at a station 28 km upstream was 124 mg/L (*Astrade*, 2005). As a consequence, the high concentration method of converting sediment attenuation to suspended sediment concentration cannot be used at this study site.

6.3.2 Isère river at Romans-sur-Isère

Concentrations at the Romans-sur-Isère study site are on the order of 10 mg/L most of the year, but during the spring snow melt they are on the order of 1 g/L. They are also high during the annual dam maneuvers which occur during the summer months 70 km upstream at the St Egrève dam and on the Longefan retention basin on the Arc river which is a tributary to the Isère, $\sim$ 130 km upstream. During the spring and summer of 2010 we captured a number of natural and man-made events with the three H-ADCPs and therefore have significant attenuation data at this site.

To begin with, results are presented from the spring flood which occurred between May 31 and June 2, 2010. Figure 6.14 is a plot of the concentration measured by the optical turbidity

meter versus the sediment attenuation observed at the three frequencies for this event. Linear regressions are fit to the data using the least-squares method; the inverse of the slope of these lines is the experimental value of the attenuation constant, $\langle \zeta_{\mathrm{exp}} \rangle$. Water samples were collected every four hours on the fall of the flood. The concentration values measured in these samples were about 20% less than the actual concentration. This is what we would expect from the data presented in Figure 3.6 which show that use of the linear relationship between concentration and turbidity will have a tendency to over-estimate the actual concentration at values greater than $\sim$200 mg/L.

Another thing to note about Figure 6.14 is that the value of the y-intercept of the linear regressions increases with increasing frequency. Theoretically, it should be zero, since zero suspended sediment should lead to zero sediment attenuation. The non-zero y-intercepts may indicate that either the attenuation due to pure water was underestimated, or there was some other source of attenuation that was unrelated to the suspended sediment, such as bubbles. However, they more likely represent normal experimental error.

Since we have grain size measurements for samples collected on the fall of this flood (one every 4 hours starting at noon June 1), we can compare the theoretical values of the attenuation constants computed for the measured grain size distributions to the experimental results. From the inverse of the slope of the linear regressions in Figure 6.14, the experimental attenuation constant is 0.032 m^2/kg for the 300 kHz instrument, 0.059 m^2/kg for the 600 kHz instrument and 0.115 m^2/kg for the 1200 kHz instrument. The 300 kHz value is in good agreement with the theoretical values for this event (0.032 - 0.035) m^2/kg. The 600 value is about two thirds what is predicted by theory: 0.087 - 0.090 m^2/kg, while the 1200 kHz value is about half the theoretical values, 0.211 - 0.214 m^2/kg.

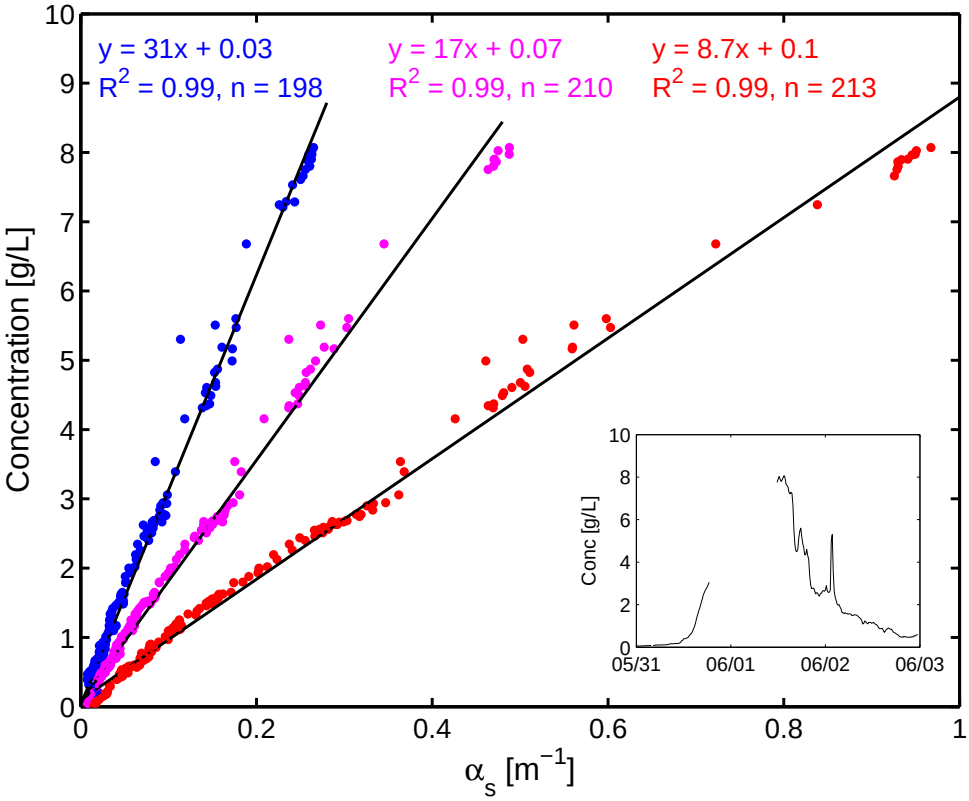

Figure 6.14: Relationship between concentration from optical turbidity and sediment attenuation measured with the 300 kHz (blue), 600 kHz (magenta) and 1200 kHz (red) H-ADCPs between May 31 and June 3, 2010 at Romans-sur-Isère. The least-squares linear regressions to the data are shown, R^2 is the correlation coefficient and n is the number of data points used for the fit.

Four days of data from what appears to be a second natural flood are shown in Figure 6.15. This event occurred between June 16 and June 20, 2010 and the maximum concentration was 2 g/L. In Figure 6.15, one's eye may be drawn to the handful of outliers in the 1200 kHz data. These points correspond to a peak in attenuation that occurred at the start of the flood. Since sediment deposits are often eroded on the leading edge of floods when velocities increase quickly, we speculate that the 1200 kHz instrument is detecting a change in grain size to which the other instruments are less sensitive. Unfortunately we did not collect any water samples during this event, but we know from Figure 2.4 that the 1200 kHz instrument should detect attenuation due to scattering from particles with radii between 30 and 100μm (large silts and fine sands), while the 300 and 600 kHz instruments should not. Thus, it is likely that the peak in 1200 kHz attenuation data on the rise of the flood indicates the presence of larger particles.

As for the 300 kHz instrument, considerable differences were seen between the attenuation

data that were calculated from the three beams. There were also large fluctuations in the attenuation value when the concentration was less than 500 mg/L, as can be seen in Figure 6.15. As such, we have limited confidence in the 300 kHz attenuation data at low concentrations. The slope of the linear regression to the 300 kHz data is twice that for the May 31 event, though it yields an experimental attenuation constant of 0.018 m^2/kg, which is within the limits of the theoretical values computed for all grain size distributions measured at Romans throughout the year. The slopes of the linear regressions in Figure 6.15 decrease with increasing frequency, as in Figure 6.14, but there is more scatter in the data at concentrations less than 500 mg/L. The slopes of the 600 and 1200 kHz data are similar to those for the previous flood. They are half the theoretical values computed for the grain size distributions that were presented in Table 3.5.

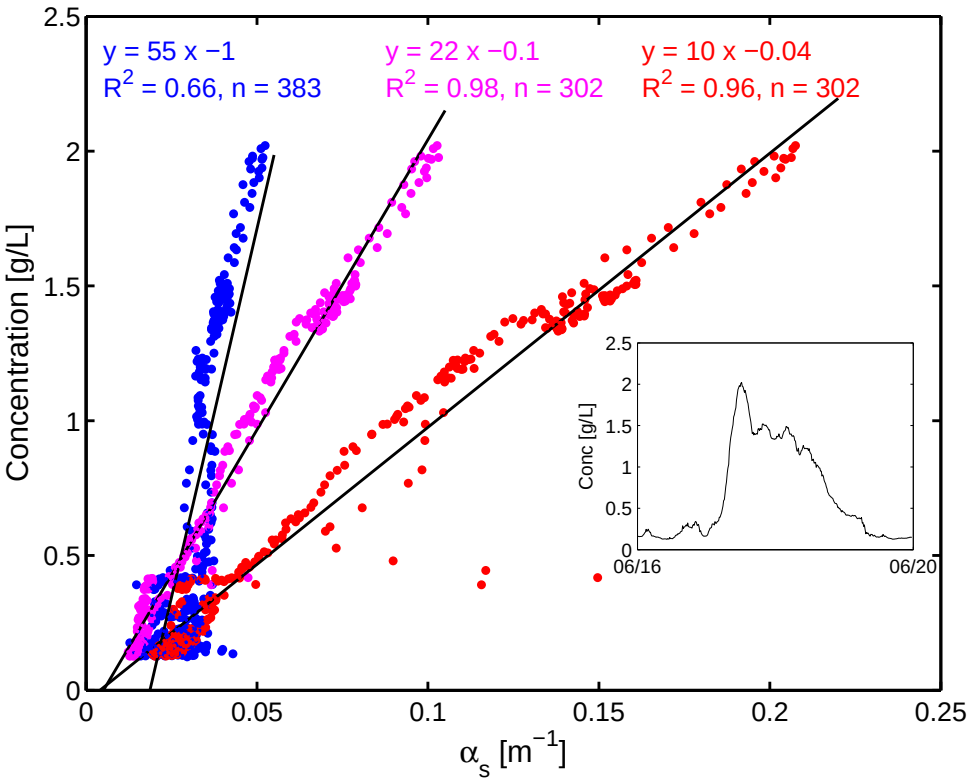

Figure 6.15: Relationship between concentration from optical turbidity and sediment attenuation measured with the 300 kHz (blue), 600 kHz (magenta) and 1200 kHz (red) H-ADCPs between June 16 and 20, 2010 at Romans-sur-Isère. The least-squares linear regressions to the data are shown, R^2 is the correlation coefficient and n is the number of data points used for the fit.

Lastly, results are presented from a man-made event which occurred June 30 2010. This event was characterised by a quick rise in concentration from 60 mg/L to 2.5 g/L over a period of 3 hours, followed by a descent that lasted 8 hours. The results are shown in Figure 6.16. As

with the second flood, we have no water samples for this event. The experimental attenuation constants for the data presented in Figure 6.16 are 0.020 m^2/kg, 0.040 m^2/kg and 0.077 m^2/kg for the 300, 600, and 1200 kHz data, respectively. Again, the value for the 300 kHz attenuation data is in agreement with the theoretical values for spherical particles, while the values for the 600 and 1200 kHz data are smaller than the theoretical values by about a factor of two.

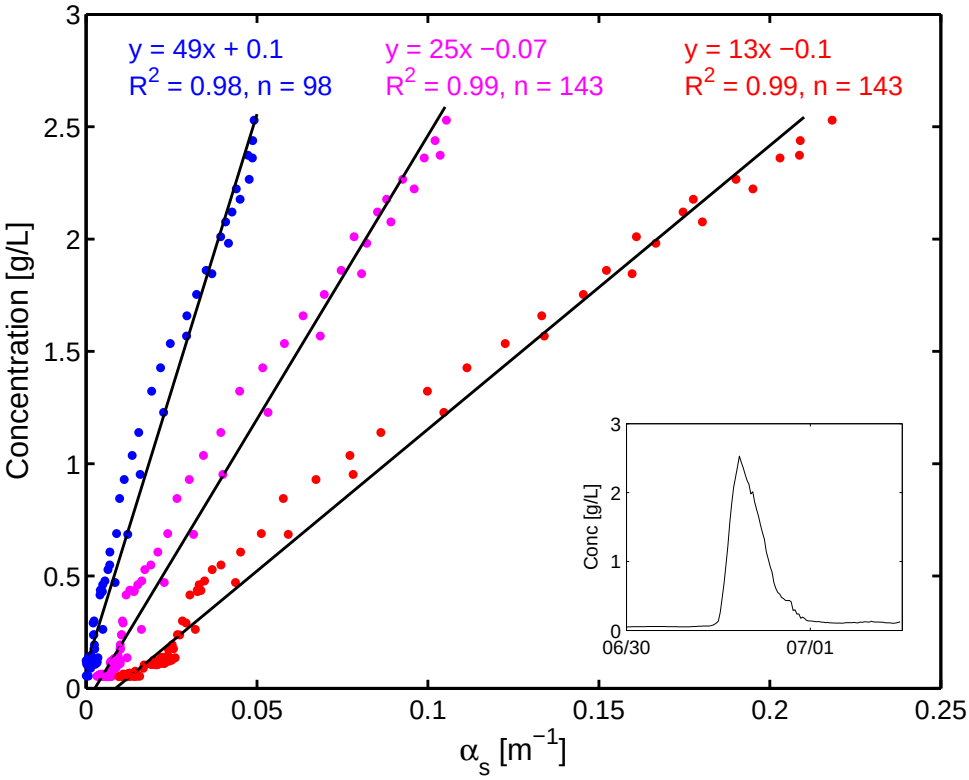

Figure 6.16: Relationship between concentration from optical turbidity and sediment attenuation measured with the 300 kHz (blue), 600 kHz (magenta) and 1200 kHz (red) H-ADCPs between June 30 and July 1, 2010 at Romans-sur-Isère. The least-squares linear regressions to the data are shown, R^2 is the correlation coefficient and n is the number of data points used for the fit.

The discrepancy between theoretical and experiment values is likely because the theoretical values assume two things: (1) all particles are spherical and (2) the results from laser grain size analysis are correct. The particles are clearly not spherical and, as has been previously discussed, there is uncertainty in the grain size measurements. Part of the discrepancy between theoretical and experimental values could also be explained by the possibility of flocculated particles at the study site. Although the scattering and attenuation characteristics of flocculated particles are not known, the presence of flocs in rivers has been confirmed by *Droppo and Ongley* (1994). The possibility of flocs could be explored in future studies with the use of an in-situ laser grain sizer

such as the LISST.

The results of Figures 6.14 - 6.16 show that the calibration curve for the attenuation method can change from event to event by up to 60% for the 300 kHz data, and by 20 - 30% for the 600 kHz and 1200 kHz data. Since the differences between the observed and theoretical values at 600 kHz and 1200 kHz are upwards of 100%, this supports the use of a single calibration curve based on observations at this study site. However, in the absence of turbidity measurements or water samples to fit an experimental relationship, we should be able to predict concentration from the attenuation data within a factor of two using the grain size distributions of the primary particles that were measured in the laboratory.

6.3.3 Rhône Canal at Montélimar and Tricastin

As previously mentioned, the nearest station at which we have concentration data for both Montélimar and Tricastin is Arles. Since attenuation values can change significantly in the course of a day, it is not prudent to use this information to calibrate a relationship between attenuation at Montélimar and Tricastin and concentration. We therefore use inversion method (2), by computing concentration values using Equation 6.14, with $\langle\zeta\rangle = \langle\zeta_v\rangle + \langle\zeta_s\rangle = 0.03$ m^2/kg and with $\langle\zeta\rangle$ =0.064 m^2/kg. The first value is a typical value for the grain sizes observed upstream at Romans-sur-Isère, while the second value is the maximum of the theoretical viscous attenuation at 300 kHz for spheres of a single size (see Figure 2.4). Since we expect the grain sizes at Montélimar to be similar to those at Romans, the first value gives what we expect to be reasonable results. The latter provides the minimum possible concentration for the event. Time series of the two concentration estimates from the Montélimar attenuation data are compared to the daily averaged concentration at Arles in Figure 6.17.

It can be seen from Figure 6.17 that the acoustic attenuation data at Montélimar can be used to capture high concentration events both in form and magnitude. As for the measurements at Tricastin, the concentration from the attenuation data is plotted against the concentration data at Arles in Figures 6.18 and 6.19. Figure 6.18 is a plot of all available data in 2008 and Figure 6.19 is a plot of the 2010 data.

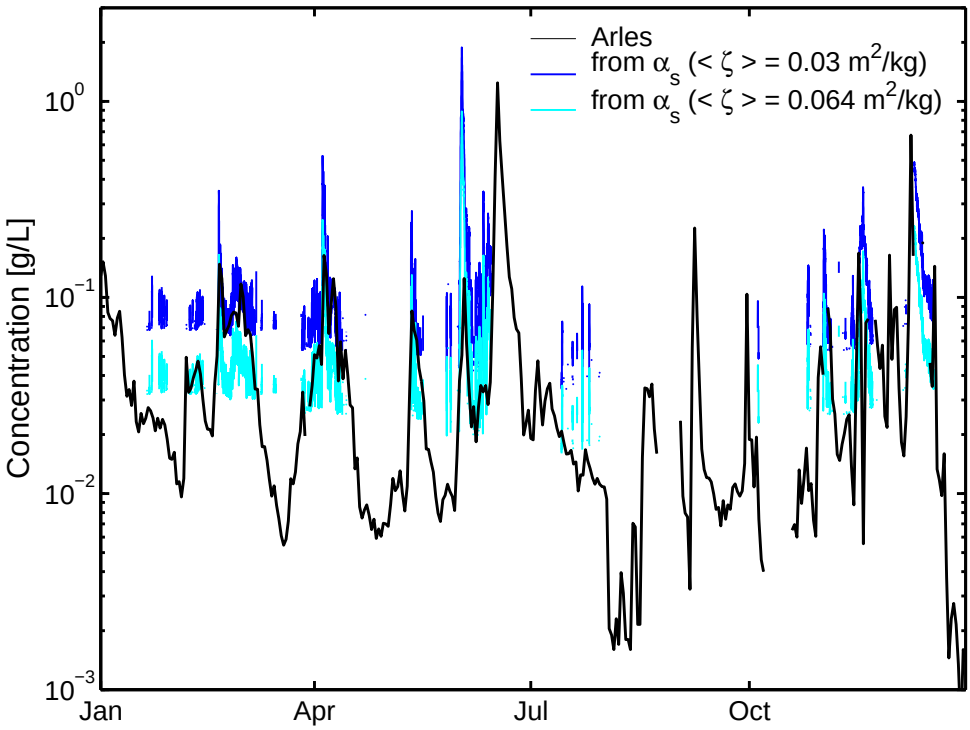

Figure 6.17: Time series of concentration measured by filtration at Arles (black) compared to values from the attenuation of the 300 kHz H-ADCP intensity at **Montélimar for 2010**. Data from Arles are daily averages, while the data from Montélimar are calculated from fifteen-minute averaged intensity profiles using $M = \alpha_s/\langle\zeta\rangle$ with $\langle\zeta\rangle$ = 0.03 m^2/kg (blue) and 0.064 m^2/kg (cyan), which is the maximum value for grains of a single size at 300 kHz.

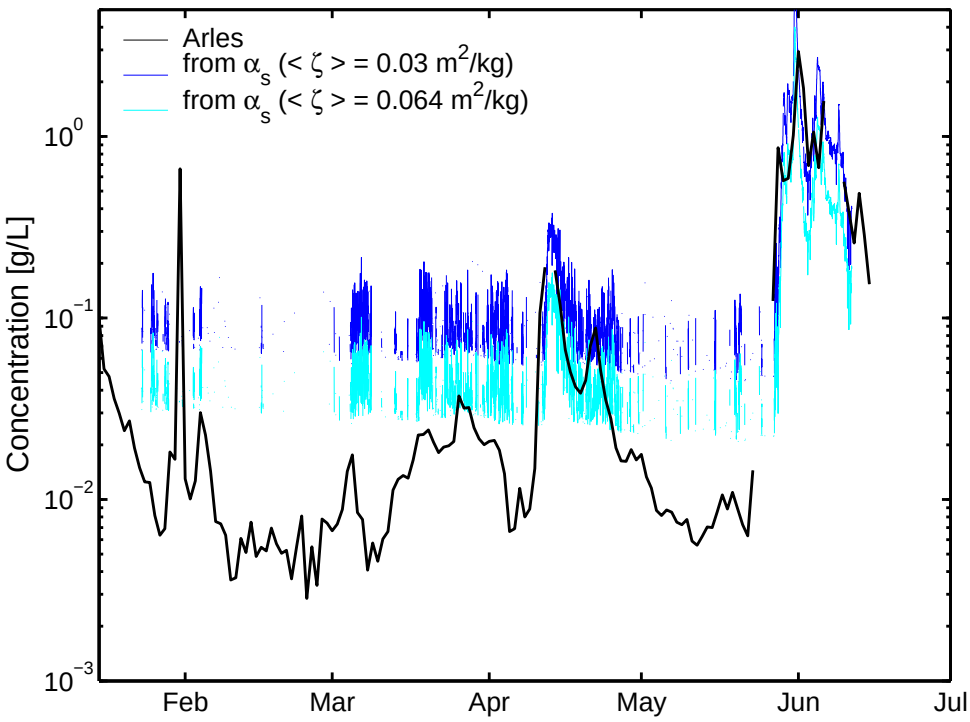

Figure 6.18: Time series of concentration measured by filtration at Arles and by the attenuation of the 300 kHz acoustic data at **Tricastin for 2008**. Data from Arles are daily averages, while the data from Tricastin are calculated from fifteen-minute averaged intensity profiles using $M = \alpha_s/\langle\zeta\rangle$ with $\langle\zeta\rangle$ = 0.03 m^2/kg (blue) and 0.064 m^2/kg (cyan), which is the maximum value for grains of a single size at 300 kHz.

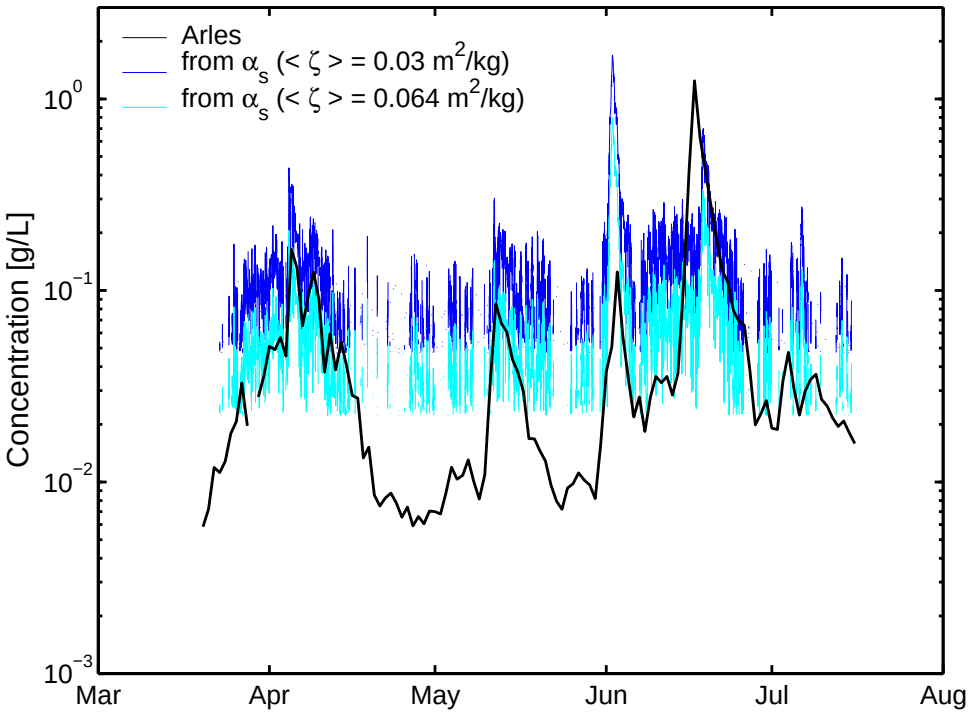

Figure 6.19: Time series of concentration measured by filtration at Arles and by the attenuation of the 300 kHz acoustic data at **Tricastin for 2010**. Data from Arles are daily averages, while the data from Tricastin are calculated from fifteen-minute averaged intensity profiles using $M = \alpha_s/\langle\zeta\rangle$ with $\langle\zeta\rangle$ = 0.03 m^2/kg (blue) and 0.064 m^2/kg (cyan), which is the maximum value for grains of a single size at 300 kHz.

Next we compare the concentration time series obtained from the attenuation data at Montélimar to the values obtained at Tricastin. Although the sites are only separated by 15 km, it must be kept in mind that between the two sites there is the Châteauneuf Dam, the confluence with the old Rhône, the branching of the river into the old Rhône and the Donzère canal and the Donzère-Mondragon Dam. A comparison of the two concentration time series is shown in Figure 6.20 for all concurrent data recorded in 2010, along with a zoom on two major events in the bottom two panels of the plot. It can be seen that there is very good agreement between the concentration data at the two study sites. Nevertheless, the Tricastin data are much noisier. This may be due to a variety of reasons including the relative shallowness of the instrument, its non-negligible roll (-1.7°), and the fact that it is in a navigation canal.

As for the downstream propagation of the suspended sediment, the observations are consistent with what we would expect. Firstly, the concentration values are less at Tricastin than at Montélimar. This is expected because the sediment will have a tendency to settle to the bottom and get trapped behind the various dams as it propagates downstream (*Bravard*, 1987). In addition, there are no other sources of suspended sediment between the two sites. Secondly, the propagation time of the peaks in concentration is between 2 and 4 hours. This is consistent with a mean flow speed of 1 - 2 m/s to cover the 15 km that separates them. This flow speed is consistent with the velocities that were observed at the Châteauneuf dam.

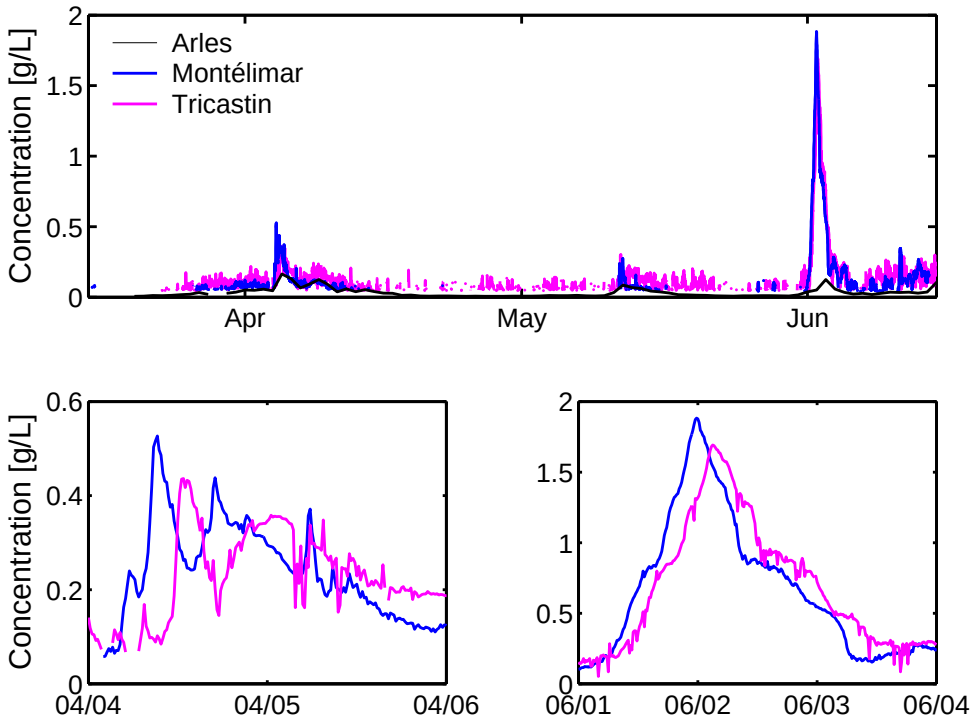

Figure 6.20: Time series of concentration measured by filtration at Arles (black) and by the attenuation of the 300 kHz acoustic data at Montélimar (blue) and Tricastin (magenta) for 2010. Data from Arles are daily averages, while the data from Montélimar and Tricastin are calculated from fifteen-minute averaged intensity profiles using $M = \alpha_s/\langle\zeta\rangle$ with $\langle\zeta\rangle$ = 0.03 m^2/kg.

6.4 Conclusion

In this chapter we presented the two methods that can be used to invert the backscattered intensity profiles from the H-ADCPs to suspended sediment concentrations. The first method is the inversion of the backscattered intensity. We presented calibration curves between the backscattering level and the concentration of suspended sediment at the four different study sites. The application of this method is limited to relatively low concentrations of suspended sediment. This is because the intensity values obtained when using the default settings of RD Instruments 300 and 600 kHz Workhorse H-ADCPs are saturated at relatively low concentrations ($<$ 60 mg/L) within the first 30 m from the instruments. We concluded that this method was very sensitive to the changes in grain size that can be observed between normal flow conditions (mainly silts) and floods (mainly silts with some sands).

The second method that was presented in this Chapter is the attenuation method. This method

is what we call the high-concentration inversion method, since it requires relatively high concentrations of suspended sediment in order to induce sediment attenuation. The hypothesis underlying this method is that the concentration and grain size are homogeneous across the profile, though the attenuation can also be calculated between neighbouring cells. The attenuation method could not be used with the data collected on the Saône river since the concentrations that were observed (<100 mg/L) were not high enough to induce attenuation of the 300 kHz signal. In contrast, the method was applied with outstanding success at the Romans-sur-Isère study site.

Co-incident measurements with the calibrated optical turbidity meter at Romans were used to establish experimental relationships between sediment attenuation and concentration of suspended sediment for a number of different events. We found distinct linear relationships between the two parameters, which is consistent with theory. The experimental values of the sediment attenuation constant were within a factor of two of the values predicted by theory for attenuation from spherical particles. The experimental values of the attenuation constant varied by 20 - 60% from event to event. This is greater than the typical inter-event variation of the calibration curve of a turbidity meter, but it is much better than the variation of the calibration curve for the backscattered intensity method. It was concluded that the attenuation inversion method is ideal for measuring suspended sediment concentrations when concentrations at our study sites are on the order of 100 mg/L or higher.

Chapter 7

Application of the Attenuation Inversion Method to Specific Hydrological Events

In this chapter we combine the measurements at the various study sites to analyse the data from a natural flood. In terms of the propagation of discharge, we have measurements at the various dams and hydrometric stations as well as the measurements of flow speed from the horizontal ADCPs. The index-velocity relationships that were presented in Chapter 5 are used to convert the H-ADCP velocity to the discharge velocity, which is then multiplied by the wetted area to get the discharge. As for measurements of the suspended sediment, we have data from a turbidity meter on the Isère at Beaumont-Monteux, the concentration measurements on the Rhône at Arles, and the acoustic data from the various H-ADCPs. The locations of the various sites were previously presented in Figure 3.2.

We use the attenuation inversion method that was presented in Section 6.1.2 to determine concentrations of suspended sediment, and the method presented in Section 6.1.3 to determine grain size from the attenuation measurements. The event that is analysed is the flood which occurred on the Isère river between May and June 2010. This event was selected for two reasons, the first being that it was the largest flood that occurred on the Isère river during this thesis. Secondly, the turbidity meter did not function during twelve hours on the rise of the flood; thus, the objective was to determine whether the acoustic data could fill the gap in the optical measurements of concentration.

7.1 Studying the Propagation of a Spring Flood

A spring flood on the Isère river was first detected at Romans-sur-Isère on May 31, 2010. In order to collect water samples throughout the event, we went to the study site to program the automatic sampler. We arrived at the site on the morning of June 1, 2010 and found that the turbidity meter had stopped working due to a programming error. It was restarted around noon. The automatic sampler was used to collect water samples every four hours on the fall of the flood. These samples were analysed for both concentration and grain size and the concentration data were found to be in satisfactory agreement with the turbidity data, as can be seen from Figure 7.1. Data were collected with the three H-ADCPs and the water level sensor throughout the flood.

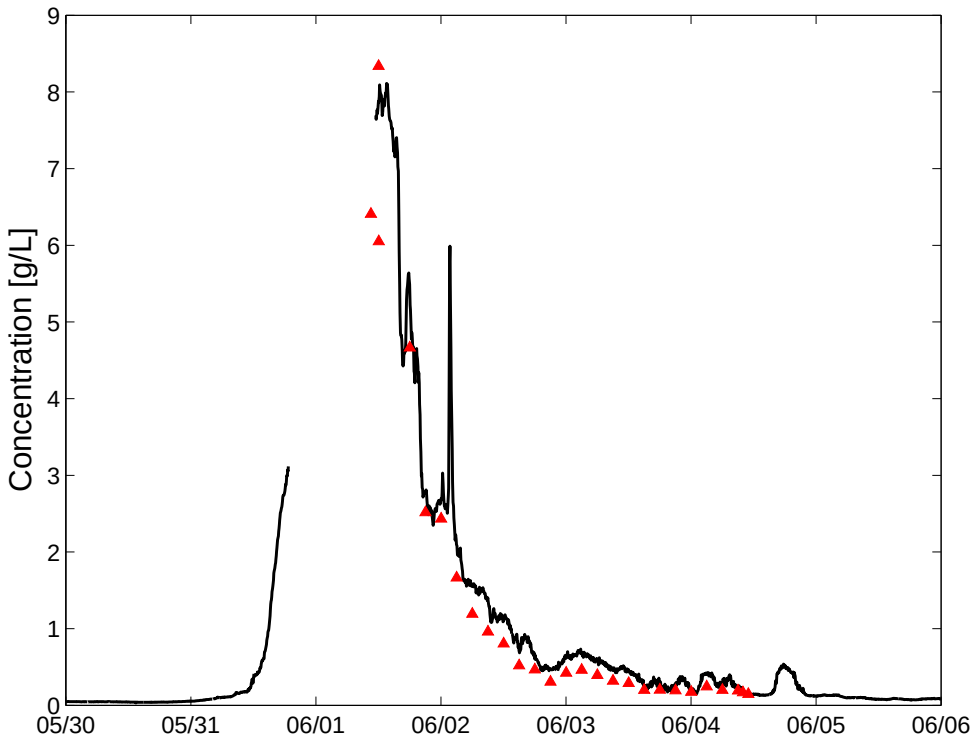

Figure 7.1: A time series of the concentration data at Romans-sur-Isère measured by the turbidity meter (black line) and by in-situ sampling (red triangles).

In the following analysis, we average the raw H-ADCP data over fifteen minutes in order to smooth fluctuations. In order to obtain the discharge velocity from the velocities measured by the H-ADCPs, we use the data collected in the cell that is centred 14 m from the right bank for each instrument since this is one of the few distances at which velocity measurements could be made by all three instruments. The velocity at 14 m is converted to the discharge velocity using the

index velocity relationships that were presented in Figures 5.3, 5.8 and 5.9. Since concentrations were high throughout the entire event, a unique relationship can be used to convert the velocity measured by the H-ADCPs to the discharge velocity, i.e. V_q/V_h is a constant. The index-velocity values for each H-ADCP are $V_q/V_h = 1.11$, 1.05 and 1.09 for the 300, 600 and 1200 kHz H-ADCPs, respectively. As previously discussed in Section 5.2.2, the difference between the ratios for the different instruments is not significant since the standard deviation about this value at high intensities is 5–6 % (Note: the spread between the whiskers in the box and whisker plots of Chapter 5 is four standard deviations).

To get the discharge, we multiply the discharge velocity from each H-ADCP by the average wetted area for the fifteen minutes corresponding to the H-ADCP data. We determine the wetted area from the water level and bathymetry data, as was previously discussed in Section 5.2. Based on the temporal fluctuations in the water level and the portion of the river near the edges for which we do not have bathymetry data, we estimate the uncertainty in our values of the wetted area to be about 4%. The concentration of suspended sediment is determined from the sediment attenuation that is detected by each H-ADCP. We use the method outlined in Section 6.1.2 to get the sediment attenuation from the fifteen-minute averaged intensity profiles. The calibration curve for this particular event (Figure 6.14) is used to invert attenuation to concentration. Based on the difference between the concentration values from the optical turbidity meter and the water samples that were depicted in Figure 7.1, we estimate the uncertainty in the concentration values from the attenuation inversion method to be about 10% for this particular event.

Figure 7.2(a) is a plot of the concentration values from the sediment attenuation at the three frequencies overlayed on the data from the optical turbidity meter. Figure 7.2(b) is the time series of the velocity measured by each H-ADCP at 14 m from the right bank. Periods of missing velocity data in subplot (b) indicate that the velocity could not be measured at that distance due to too high a sediment attenuation. Figure 7.2(c) is a time series of the sediment transport rate, or suspended sediment discharge, in kg/s assuming that the concentration of suspended sediment was vertically uniform. These values are calculated by multiplying the concentration in kg/m^3 by the discharge, which is the product of the wetted area and the discharge velocity. As previously mentioned, the discharge velocity is obtained from the previously established index-velocity relationships.

The turbidity data and the 600 kHz acoustic data are not discernible in Figure 7.2(a) because

they are nearly identical to the 1200 kHz data, which were the last to be plotted. It is not surprising that the concentration values from the three H-ADCPs are in good agreement with one another. This is because the co-incident optical and acoustical data for this event are the calibration data that were used to determine the experimental sediment attenuation constant. There are, however, slight differences between the values predicted by the 300 kHz instrument and the 600 and 1200 kHz instruments: the 300 kHz instrument predicts higher concentration values prior to the rise of the flood and slightly different values during the flood. The high concentration values that it predicts prior to the start of the flood are not realistic. The instrument's difficulty in measuring concentration when the sediment attenuation is low is not surprising given its poor positioning and the relatively low attenuation at this frequency. Regardless of this disadvantage, from Figure 7.2(b) it can be seen that the 300 kHz instrument was able to measure velocities at distances further across the river than its higher frequencies counterparts. This is partly due to its positioning 6 m from the wall, but also because the signal is not as strongly attenuated.

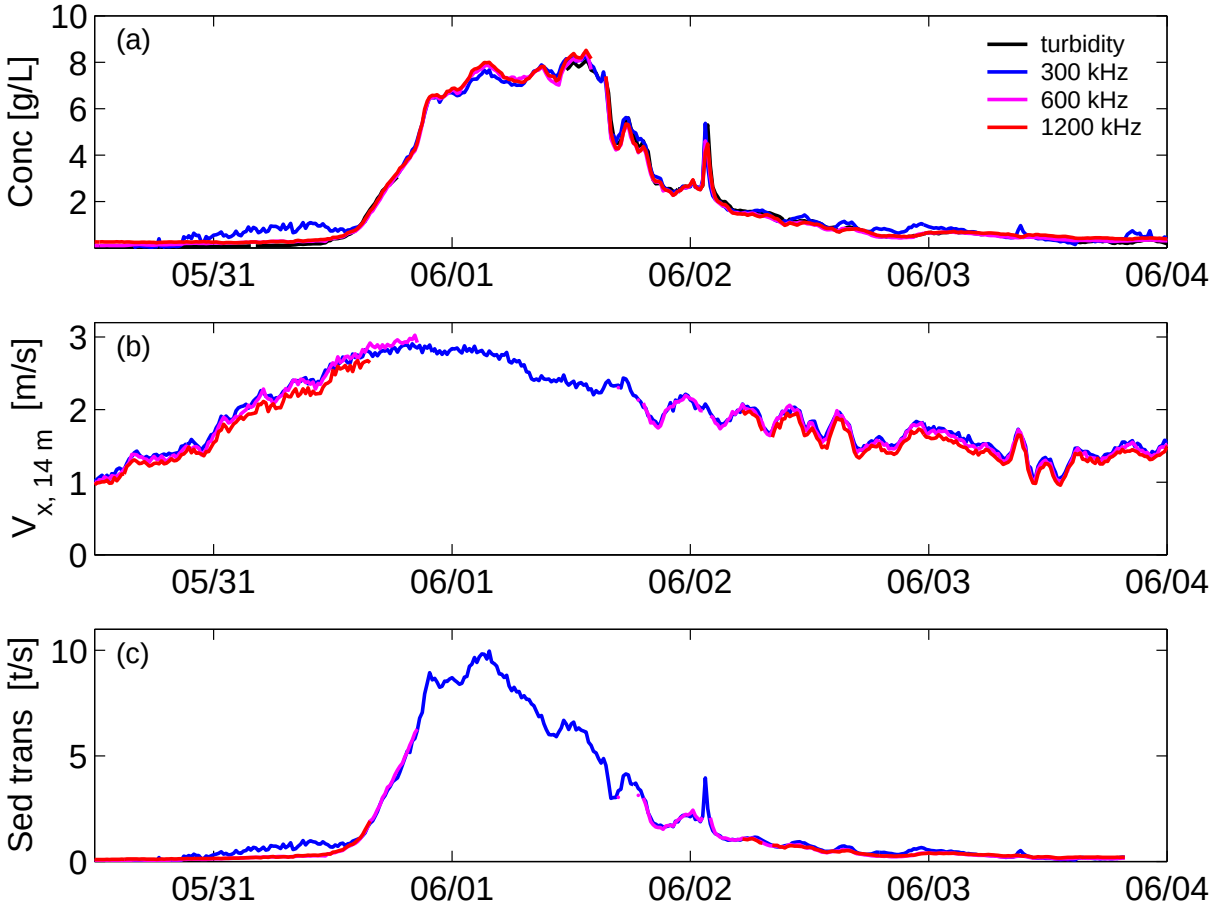

Figure 7.2: (a) Concentration of suspended sediment at Romans-sur-Isère measured with the turbidity meter (black) and the 300 kHz (blue), 600 kHz (magenta) and 1200 kHz (red) H-ADCPs. (b) Along-stream velocity measured at 14 m from the right bank with the three H-ADCPs and (c) the resulting sediment transport rates in tonnes per second.

In order to study the propagation of this event, we have hourly data from a turbidity meter belonging to EDF on the Isère river at the Beaumont-Monteux station, 15 km downstream of Romans. These values, which are averaged over one hour, are multiplied by the discharge at Beaumont-Monteux in order to get the sediment transport rate. Further downstream is the 300 kHz H-ADCP at Montélimar. We calculate the concentration from the sediment attenuation using the experimental attenuation constant at Romans for this event, $\langle\zeta_{exp}\rangle$=0.03 m^2/kg. To get the transport rate of suspended sediment we multiply the concentration by the discharge data from the Châteauneuf dam 500 m downstream. (Note: we could have also used the velocity values

from the H-ADCP itself). Lastly, we have measurements of concentration and discharge at Arles. The concentration values are integrated over one day, with the automatic sampler collecting small amounts of water every hour. The discharge values that we have are the daily maximum discharge. The multiplication of the daily integrated concentration and the daily maximum discharge gives an upper estimate of the average daily sediment transport rate, though it gives no information on the details of the sediment transport event. In all cases it has been assumed that the concentration was vertically uniform.

Figure 7.3 is a plot of the rate of suspended sediment transport in kg/s measured with the various techniques at the various sites for this event. Figure 7.4 is the same data with the sediment transport rates plotted on a logarithmic scale. Error bars are not depicted in this plot since it is already busy enough, however, we estimate the standard uncertainty on the sediment transport rate that was determined with the H-ADCP data to be $\pm$ 12 % for this event. The details of this calculation are given below.

The sediment transport rate from the H-ADCP data, Ψ_h is the product of the index-velocity constant, K, the index velocity V_h, the wetted area, A, and the mass concentration from the H-ADCP, M_h:

$$\Psi_h = K\, V_h\, A\, M_h. \tag{7.1}$$

The standard uncertainty, u_Ψ, in the sediment transport rate can be calculated using the following formula if we assume that the errors on the different parameters are mutually independent:

$$\left(\frac{u_\Psi}{\Psi}\right)^2 = \left(\frac{u_K}{K}\right)^2 + \left(\frac{u_{V_h}}{V_h}\right)^2 + \left(\frac{u_A}{A}\right)^2 + \left(\frac{u_{M_h}}{M_h}\right)^2 \tag{7.2}$$

From the error bars in Figures 5.3, 5.8 and 5.9 we see that u_K/K is $\sim$5%. For the three H-ADCPs, the statistical uncertainty for velocity measurements made with one ping is 66 mm/s. Since we average over 15 pings, the standard error is 66/$\sqrt{15}$, which is 17 mm/s. For a flow speed of 2 m/s, this corresponds to an uncertainty of 1%. We already mentioned that the uncertainty in the wetted area is 4% and the uncertainty in the concentration values for this event is 10%. Combining these values we obtain a standard uncertainty of 12% for the sediment transport rate.

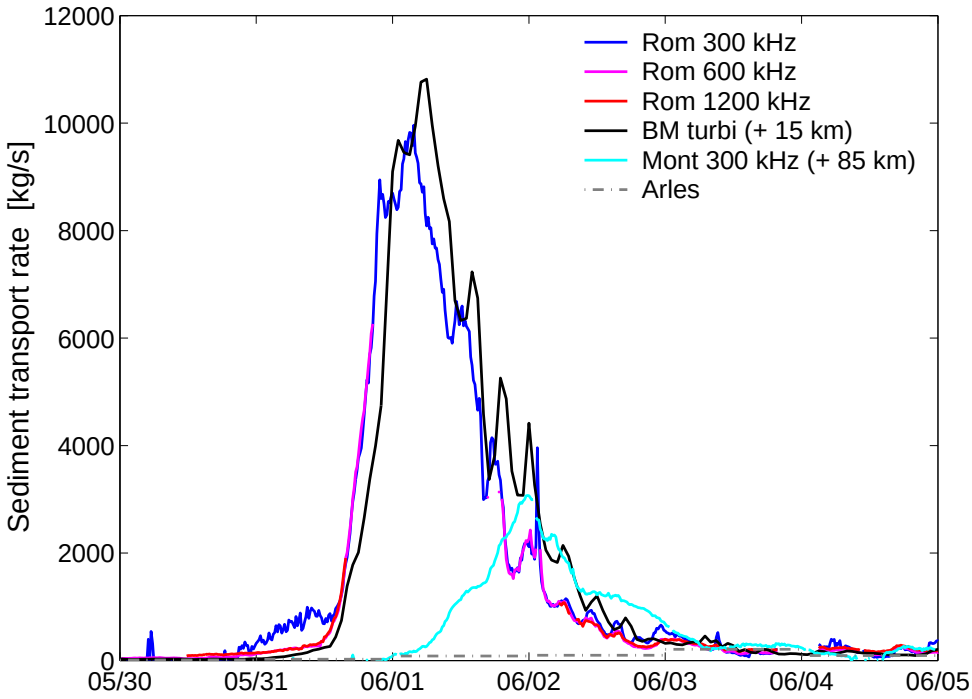

Figure 7.3: Sediment transport rates calculated using data from the various H-ADCPs at Romans-sur-Isère, the turbidity meter at Beaumont-Monteux combined with the discharge at the Beaumont-Monteux dam, the H-ADCP at Montélimar combined with the discharge at the Montélimar dam and water samples at Arles combined with values of the maximum daily discharge.

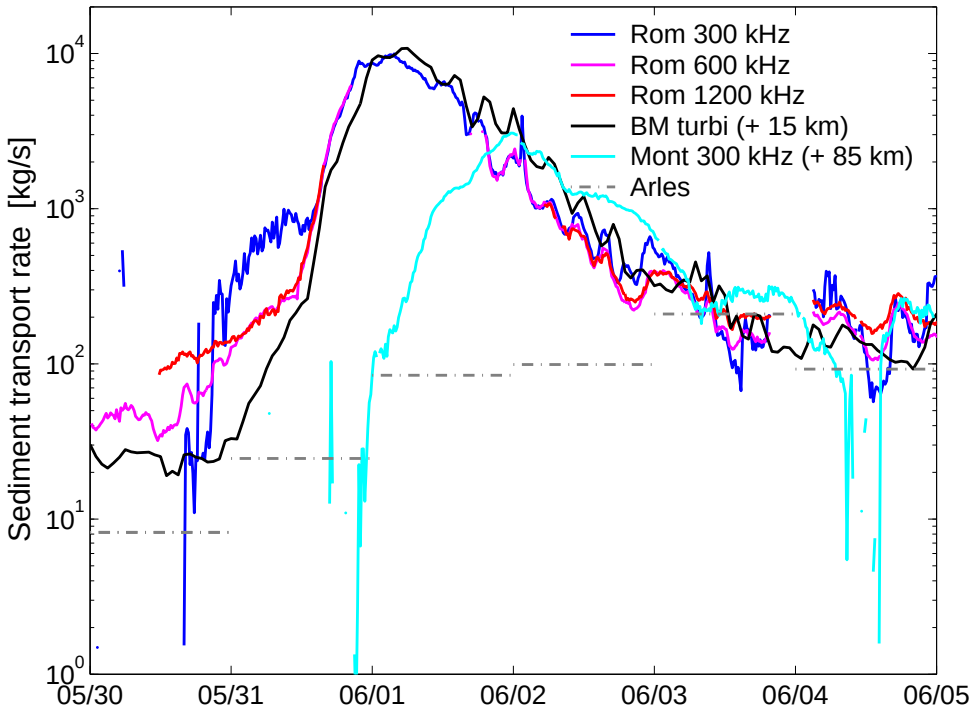

Figure 7.4: Sediment transport rates plotted on a logarithmic scale. Values are calculated using data from the H-ADCPs at Romans-sur-Isère, the turbidity meter at Beaumont-Monteux combined with the discharge at the Beaumont-Monteux dam, the H-ADCP at Montélimar combined with the discharge at the Montélimar dam and water samples at Arles combined with values of the maximum daily discharge.

It can be seen that the sediment transport rate that is measured at Beaumont-Monteux is slightly higher than that at Romans-sur-Isère, though it is not significantly different, given the uncertainty of the data. Nonetheless, multiple explanations exist for potentially higher sediment transport rates at Beaumont-Monteux than at Romans-sur-Isère. To begin with, further sediment may be eroded into suspension with propagation downstream. Secondly, the La Vanelle dam, which is in between Romans and Beaumont-Monteux, could have been opened wider than usual during this natural flood, which would likely result in erosion of the sediment that was previously deposited upstream of the La Vanelle dam.

It can be seen that the rate of sediment transport at Montélimar (on the Rhône canal) is significantly less than it is on the Isère river. This is what we would expect since the flood only occurred on the Isère river and not on the Rhône. As such, the water would have been heavily diluted at the confluence of the two rivers. There would also have been sedimentation behind the Beaumont-Monteux dam. The estimate of the sediment transport rate at Arles is an order of magnitude less than at Montélimar. We expected a decrease in suspended sediment since the sediment should have a tendency to deposit with propagation downstream, both along the river and behind the numerous dams.

7.2 Variations in suspended sediment grain size throughout the flood

In this section we use the theory that was outlined in Section 6.1.3 to compute the grain size of the suspended sediment for the flood that was presented in the previous section. For this analysis it is assumed that the particles had lognormal size distributions. By comparing the attenuation that is observed at the different frequencies to the theoretical attenuation constants for a range of median grain sizes, we obtain an estimate of the size of particles in suspension throughout the event. The median radius of the particles is taken to be the size that minimizes the sum of the absolute values of $\epsilon_{i,j}$ for all three frequency combinations (see Section 6.1.3 for further details).

Figure 7.5(a) is a plot of the attenuation data at the three frequencies for the flood, and Figure 7.5(b) is a plot of the median grain radius a_{50} determined from the acoustic measurements. It can be seen that apart from the apparent decrease in the median radius from 35 μm to 20 μm at the start of June 2, 2010, the median grain size changes minimally throughout the event. The time at which the observed change in grain size occurred corresponds to the time at which there was a peak in attenuation (see Figure 7.5(a)). Since the peak in the 300 and 600 kHz data occurred slightly earlier than the peak in the 1200 kHz data, the ratios of the attenuation at the different

frequencies are altered, which leads to the different estimation of a_{50}.

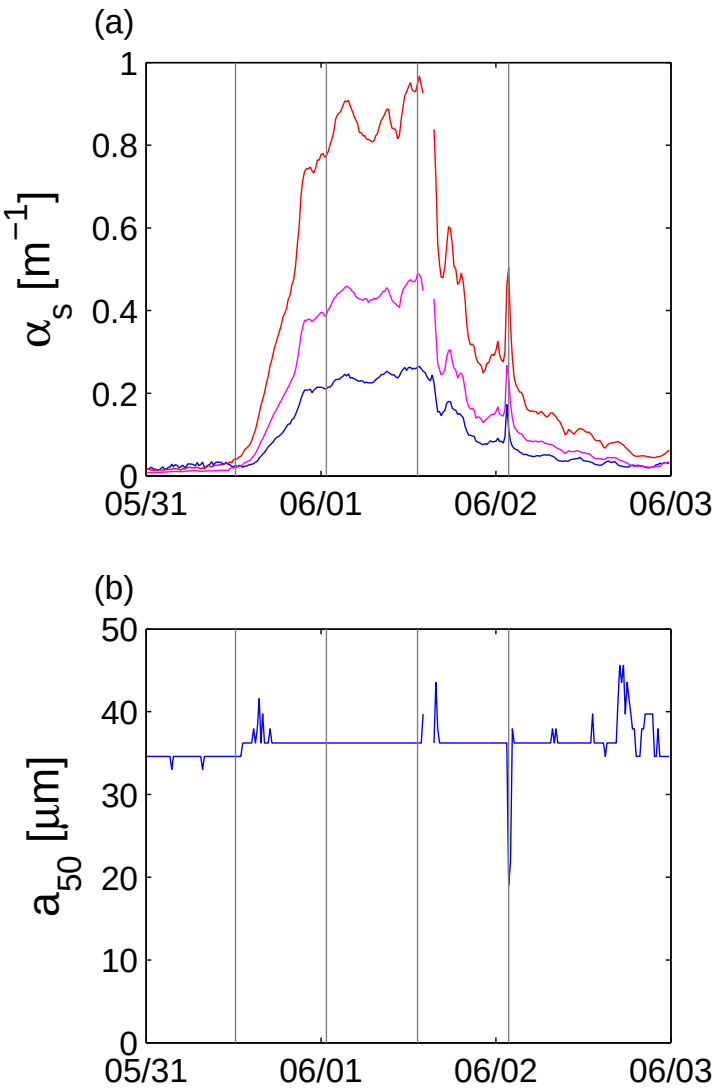

Figure 7.5: (a) Attenuation data measured with the 300 kHz (blue), 600 kHz (magenta) and 1200 kHz (red) H-ADCPs at Romans-sur-Isère. (b) The median grain radius obtained using the multi-frequency attenuation inversion method.

The vertical lines in Figure 7.5 represent the time for which detailed grain size determination plots are presented in Figure 7.6. This Figure depicts the value of $\epsilon_{i,j}$ as a function of median grain radius for the three frequency combinations for each of the four time steps. The sum of their absolute values is shown in red. The data in subplot (a) correspond to the very start of the flood, the data in subplot (b) and (c) correspond to high values of attenuation towards the middle of the flood, and the data in subplot (d) correspond to the narrow peak in attenuation that

was just discussed. We see that at 12:15 May 31, a particular grain size is hard to discern since the minimum value of $\Sigma\epsilon_{i,j}$ is not very pronounced. This is likely due to the small amount of attenuation at the start of the flood. At 00:45 June 1, the attenuation is high at all frequencies, and the sum of $\epsilon_{i,j}$ has a fairly distinct minimum. The same is true of the data from 13:15 June 1. At 01:45 June 2 we see that there are two possible grain size estimates, either 20 μm or 66 μm, but the minimum is at 20 μm.

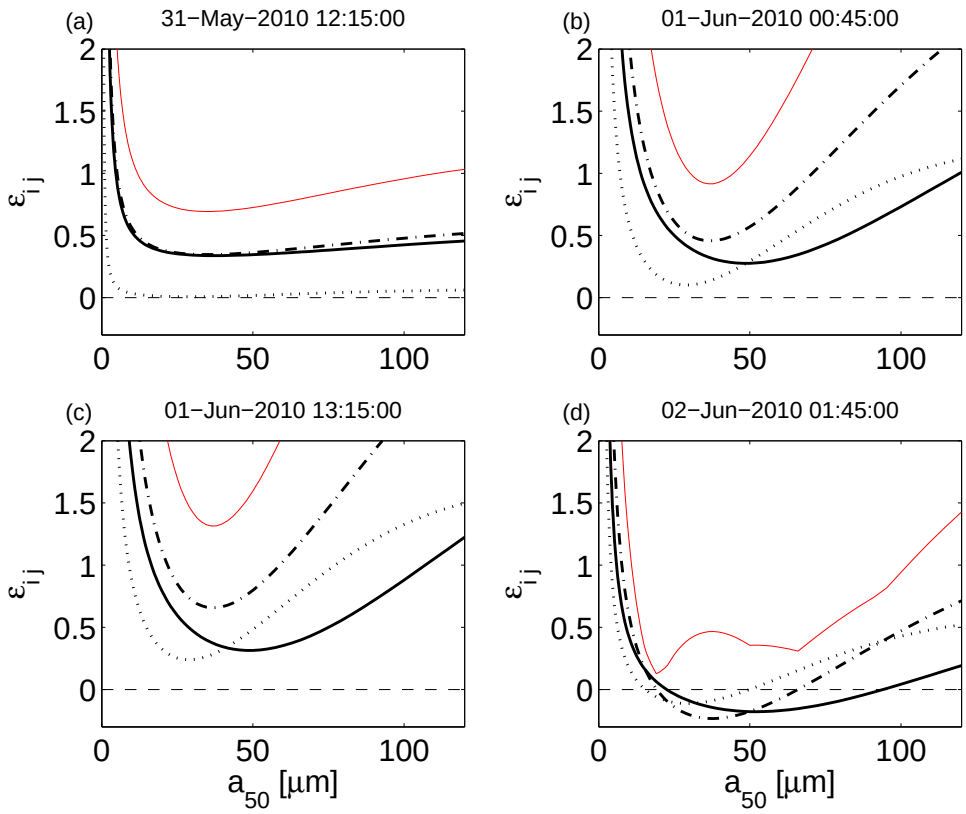

Figure 7.6: Four examples of the multi-frequency size estimation method based on the acoustic attenuation data. The parameter $\epsilon_{i,j}$ is the relative difference between the estimations of concentration with the data from two frequencies, assuming a particular median radius.. The solid line is the size from the 300 to 600 kHz comparison, the dotted line is from 600/1200, the dash-dotted line is from 300/1200 and the red line is the sum of the absolute value of the three curves.

Grain size analysis was performed on all of the samples collected on the fall of the flood (see Figure 7.1). The size distributions measured for these samples are shown in Appendix A. The median radius from the laser grain sizer was about 6 μm for all samples. This value is substantially different from the estimation from the multi-frequency attenuation data, 35 μm. As was seen in Chapter 2, Section 6.1.3, the size estimates are very dependent on the assumed form of the grain size distribution. Nevertheless, the results presented in this section show that

even with a good assumption of the form of the grain size distribution, it is not always easy to discern a particular grain size from the multi-frequency attenuation data. Therefore, we conclude that at this stage of the research multi-frequency attenuation data are not sufficient to provide quantitative estimates of grain size.

On the other hand, multi-frequency attenuation data appear to provide qualitative information of the variation in size of the suspended sediment throughout events. Take for example the multi-frequency data shown in Figure 6.15. These data were collected during a flood which occurred in June 2010. Although there is a fairly distinct linear relationship between sediment attenuation and concentration for the 300 and 600 kHz H-ADCPs, the same is not true of the 1200 kHz data. There are a handful of points that correspond to relatively high attenuation at 1200 kHz for relatively low concentrations. These values, which diverge from the otherwise straight line, occurred on the rise of the flood.

The observation of attenuation at 1200 kHz but not 300 and 600 kHz indicates that the 1200 kHz instrument detected attenuation from a size of particles to which the other two instruments were less sensitive. From Figure 2.4, it can be seen that the 1200 kHz instrument should be more sensitive to fine sand particles (radii ranging from 30-100 μm) than the other two instruments. Thus our observation suggest that larger particles were eroded into suspension on the leading edge of the flood. This is very plausible. However, when applying the multi-frequency size inversion method, we could not get a satisfactory estimate of grain size. The value tended towards infinity for this temporary peak in 1200 kHz attenuation.

Our results demonstrate that at the present time multi-frequency attenuation data can be used to monitor changes in grain size of suspended sediment qualitative but not quantitatively. Laboratory experiments with controlled grain size distributions are required in order to better understand how sound is attenuated by suspension of silts and clays. Better grain size analysis of the sediments is also required. For one, the samples should be pre-treated to assure that no organic matter is present. Also, complementary size analysis with an electro-resistance sizer, such as a Coulter Counter should also be performed.

CHAPTER 8

CONCLUSIONS

The aim of this thesis was to determine the capacities and limitations of using commercial horizontal ADCPs to measure sediment fluxes in rivers by proposing adequate inversion approaches and methods. Over the last five years these instruments have gained popularity for continuous measurements of flow speed in rivers. Their use for measuring concentrations of suspended sediment has also been explored. Despite this, the literature seems to lack sufficient information on the capacities and limitations of these instruments. Since preliminary studies showed that velocity measurements made using H-ADCPs were not accurate during low flow conditions, one aim of this study was to identify the source of measurement errors and quantify their accuracy as a function of hydrological and suspended sediment conditions. The second aim was to develop a method for determining fluxes of suspended sediment at the various study sites.

In this thesis we presented measurements made using RD Instruments horizontal-ADCPs at five different study sites in the Rhône river basin. These sites are run by Compagnie Nationale du Rhône (CNR), Electricité de France (EDF) and Cemagref Lyon, and the H-ADCPs from which the measurements were presented belong to either CNR, EDF, or Teledyne RDI. The areas of focus of this dissertation were four-fold. To begin with, the importance of proper positioning of the instruments was explored. Next we focused on the accuracy of the velocity measurements and the factors controlling this accuracy. Thirdly, we presented two methods for determining concentration of the suspended sediment, but concentrated primarily on a novel attenuation method. A novel method for monitoring changes in grain size of the suspended sediment throughout high concentration events was also developed. Finally, we applied the attenuation inversion method to determine sediment transport rates and variations in grain size for a particular event.

8.1 Positioning

In Chapter 4 we demonstrated that despite what is stated by the manufacturer, horizontal ADCPs are not resilient to scattering from the surface at a grazing angle. By applying oceanographic concepts to hydrological studies we modelled the air-water interface as a Lambertian scatterer. We showed that the irregularities that were observed in the 300 and 600 kHz velocity and intensity profiles at Romans-sur-Isère during periods of low concentration were likely due to scattering from the surface. This can overpower the scattering from the particles in the water column when the water is dilute. The H-ADCPs at Romans were repositioned, but we found that due to the limited depth and the problems with precisely positioning the instruments, it was not possible to profile across the 85-m width of the river. The simple modelling done in this thesis can be used as a tool in the future, since *in situ* tests to verify proper positioning are not sufficient if done on a day when concentrations are relatively high.

8.2 Measuring velocity

Data from three study sites were used to investigate the validity of the H-ADCP velocity profiles. The H-ADCP data from Saint-Georges and Montélimar were compared to results from moving-boat gauging with an ADCP. It was seen that the H-ADCPs underestimated velocity when the flow speeds were low and the underestimation worsened with distance from the instrument. We used discharge data from nearby gauging stations and the water level at the H-ADCPs to calculate the mean cross-sectional velocity (the discharge velocity) at Romans and Montélimar. Seven months of discharge velocity data were compared to the velocity measured by the three H-ADCPs at Romans-sur-Isère at a range of distances from the instruments. It was found that when the backscattered intensity was low due to insufficient sediment (at concentrations $\lesssim$ 70 mg/L), the 300 kHz H-ADCP underestimated the velocity. The velocity underestimation and spread in the data worsened with decreasing intensity. Alternatively, when the intensity was low due to sediment attenuation resulting from high concentrations (at concentrations $\gtrsim$ 100 mg/L), the velocities measured by the 300 kHz H-ADCP were generally within 10% of the values from ADCP gauging.

We concluded that one could apply an intensity-dependent index velocity type relationship to obtain the discharge velocity from the 300 kHz H-ADCP data if the signal was low due to low sediment concentrations. To decide whether the signal is low due to low or high sediment

concentrations, one must look at the intensity profiles. If a non-negligible sediment attenuation is calculated from the intensity profile, then use of a unique index-velocity relationship is more appropriate. The 600 and 1200 kHz instruments at Romans also underestimated velocity when concentrations were low, though to a lesser extent. The 1200 kHz instrument provided the most accurate velocity measurements of the three instruments. Since higher frequency signals are more significantly attenuated, the maximum range at which the 1200 kHz instrument can profile concentration and velocity is much less than that of the 300 kHz instrument. Thus, a decision must be made. If one is interested is accurate velocity measurements up to ranges of only 20 m, then a 1200 kHz instrument should be used. If, on the other hand, the goal is to profile further, but accuracy is less important, then a 300 kHz or 600 kHz H-ADCP should be used.

8.3 Measuring suspended sediment concentrations and grain size

Two methods were presented for determining the concentration of suspended sediment from the backscattered intensity data: direct use of the intensity data or use of the attenuation data. At the range of frequencies of the instruments used in this study, clay and silt-sized particles lead to significant attenuation of the acoustic signal when concentrations exceed $\sim$100 mg/L. The attenuation is linearly proportional to the concentration of suspended sediment. Since the sediment attenuation was less sensitive than the backscattered intensity to the changes in grain size that were observed, the majority of our study focused on the inversion of the attenuation data. Considering that the majority of sediment transport in rivers is done by extreme events such as floods and dam flushing, this method is particularly adapted to fluvial sediment transport studies.

Relationships between sediment attenuation and concentration from optical turbidity were established for the three instruments at Romans-sur-Isère for a number of different events. The experimental values of the sediment attenuation constants obtained from these calibrations were compared to theoretical values calculated for the size distributions of the primary particles that were measured in water samples at Romans-sur-Isère. There was very good agreement between theory and observations for the 300 kHz signal. For the 600 kHz instrument the experimental value was about two-thirds the theoretical value and for the 1200 kHz instrument it was half. Since the attenuation due to viscous absorption is not a simple function of grain size (see Figure 2.4), over or underestimation of particles of a given size can have different effects on the theoretical attenuation calculated for different frequencies. This may explain why the agreement between the data and the theoretical values calculated from the observed grain size distributions

is not the same at all frequencies. In addition, part of the disagreement between theory and observations may be related to the fact that what we measured in the laboratory were the grain size distributions of the primary particles in suspension, while flocs may be present in the river. In a future study the possibility of flocculation could be investigated with use of an in-situ laser grain sizer such as a LISST. Lastly, the theory is based on the assumption of spherical grains.

Although we had no physical measurements of concentration or grain size at Montélimar or Tricastin, attenuation data from these two sites were divided by the experimental sediment attenuation constant observed during a flood at Romans in order to estimate concentrations of suspended sediment during a series of small floods. The temporal separation of the peaks in concentration was consistent with the flow speeds that were observed, and the concentration of suspended sediment decreased with downstream propagation, as we would expect.

We presented a method for determining grain size from multi-frequency attenuation data and discussed the importance of having *a priori* knowledge of the form of the grain size distributions. The difference between the size of the particles obtained with the multi-frequency inversion can differ by a factor of 20 depending on whether one makes the simplistic assumption of single-sized particles, or the more realistic assumption of a lognormal distribution. The actual median grain size measured by laser grain sizing in water samples collected during the same event was somewhere between the two values. We presented attenuation data from a natural flood at Romans-sur-Isère during which only the 1200 kHz instrument measured a large peak in attenuation on the leading edge of the flood. Since this peak in attenuation was not detected by the other two instruments, we suspect that this was due to the presence of fine sands. We make this assertion because sands with radii ≤ 100 μm have been observed during floods at Romans-sur-Isère, and we know that the attenuation at 300 and 600 kHz is negligible for particles with radii ranging from 30-100 μm. Multi-frequency attenuation data can therefore be used to provide qualitative information on variations in the size of suspended sediments throughout an event.

8.4 Application of the method

In the last section of this thesis we combined the measurements of velocity and concentration (from attenuation) to determine the rate of suspended sediment transport for a large flood that occurred in the spring of 2010. Since concentrations were high, the velocity measurements were assumed to be accurate. For each instrument we used a unique index velocity relationship to determine the mean cross-sectional velocity; that, combined with the wetted area from bathymetry

and water level data gave the discharge. This was multiplied by the concentration from the attenuation to determine the rate of suspended sediment transport. The downstream propagation of the event was studied with the use of turbidity data 15 km downstream, the H-ADCP data from Montélimar and daily-averaged values of concentration and discharge from Arles. With the use of the size inversion method we determined a value for the median particle radius of the suspended sediment at Romans-sur-Isère throughout the event. We saw that size variation throughout this particular event was minimal.

8.5 Perspectives

In terms of perspectives for this work, the primary objective is the validation of the intensity-dependent index-velocity method at Romans and Montélimar. We would like to see if the discharge velocity can be calculated from the H-ADCP data with this method with acceptable accuracy. This will be done by examining data not used for the calibration of the relationship. If the method is successful, the next step will be to program the acquisition systems for the instruments such that these relationships are taken into account as the data are acquired. This would provide the hydropower producers to whom these instruments belong with accurate measurements of velocity in real-time.

Secondly, we would like to further investigate the suspended sediment conditions at Montélimar. We have acoustic data that suggests that there is re-suspension of the sediment behind the dam during dam maneuvers. We also have data that suggest that the concentrations and/or grain size are not homogeneous across the profile during these maneuvers, but lack the data to confirm this hypothesis. We would like to measure both the spatial and temporal variability of the grain size and concentration at Montélimar through water sampling campaigns. This would enable us to decide whether these instruments and the methods developed in this thesis can be used to detect changes in concentration or grain size across a profile.

Other perspectives include a comparison of RDI horizontal ADCPs to Sontek instruments, since the latter are used by a number of researchers at the USGS (e.g. *Topping et al.*, 2007; *Wright et al.*, 2010; *Wood*, 2010). In the publications that we have cited in this thesis, the problem of signal saturation is not addressed, nor is there any mention of inaccuracies in the velocity measurements. This could be because there are no problems, but is likely because the studies have not yet been undertaken.

The last immediate perspective of this work is the application of the attenuation inversion

method to data collected on the Isère and Rhône rivers during the spring of 2008. A large flood occurred between May and June, 2008 with concentrations at Romans-sur-Isère reaching 20 g/L. This event was of particular interest to the French hydro-meteorological community and our new method will provide those interested in studying this event with data at sites where none were previously available.

Further horizons for studies include an investigation of the influence of flocculated particles on acoustic scattering and attenuation. This calls for both laboratory and field studies. In future river studies it would be important to quantify whether or not flocs are present in the measurement volume. This could be done with the use of an in-situ laser grain sizer, such as a LISST.

The methods presented in this thesis for determining fluxes of suspended sediment from horizontal-ADCP data are very promising for the continued use of these instruments to survey rivers. We think that the attenuation inversion method could be used to detect large scale variations in suspended sediment across the measurement volume of an H-ADCP, since a change in concentration or grain size should induce a change in the slope of the intensity profile. This would be of particular interest for the study of confluences or turbidity currents in reservoirs.

This study also highlights the possibilities that exist for the use of instruments that operate at multiple frequencies. River surveying ADCPs that can operate at two different frequencies are now commercially available. This study suggests that the multi-frequency measurements that they provide could potentially be used to determine both concentration and variation in the grain size of suspended sediment, even during extreme flow conditions.

Appendix A

Laser Grain Sizer Results for Romans-sur-Isère Suspended Matter

The complete results of grain size analysis done with the laser grain sizer are presented in this section. The relevant information is listed in the tables, and the size distributions are shown as both volume and number size distributions. In all figures, volume fractions are shown on the left hand side, and number size distributions are shown on the right hand side. The samples analysed using the Fraunhofer method are depicted as circles, and those analysed using the Mie method are depicted as triangles. If the samples were collected by hand the symbols are open and if they were collected by the automatic sampler, they are filled.

Table A.1: Relevant information for the samples collected at Romans-sur-Isère between January, 2009 and June, 2010 and analysed using the laser grain sizer. This includes the sizing method (Fraunhofer or Mie theory),the concentration measured by filtration, the sizer concentration in percent volume and mass and the residual error. A star in the concentration column indicates that the sample may have been diluted for grain size analysis and the daggers in the sample column indicate that the sample from 01/06/2010 was analysed on three different days.

Sample	Method	Measured Conc (mg/L)	Laser Obscuration (%)	Sizer Conc (% volume)	Sizer Conc (mg/L)	Residual Error (%)	Notes
09/01/2009 10:20	Fr	8*	0.9	0.0014	37	0.4	-
09/01/2009 12:00	Fr	2*	0.9	0.0012	32	0.7	-
09/01/2009 14:25	Fr	4*	1.1	0.0018	48	0.4	-
16/01/2009 11:00	Fr	3*	0.6	0.0008	21	0.6	-
21/01/2009 13:41	Fr	5*	1.1	0.0017	45	0.5	-
21/01/2009 13:41	Fr	5*	1.2	0.0019	50	0.7	-
26/01/2009 11:30	Fr	15*	3.3	0.0028	74	0.5	-
30/01/2009 11:00	Fr	8*	1.7	0.0020	53	0.5	-
05/02/2009 13:15 (R1)	Fr	6*	1.0	0.0014	37	0.7	-
05/02/2009 13:15 (R2)	Fr	6*	1.0	0.0012	32	0.6	-
05/03/09 13:00	Fr	7*	-	-	-	-	-
05/03/09 15:00	Fr	4*	-	-	-	-	-
05/03/09 16:15	Fr	5*	-	-	-	-	-
11/05/2010 04:31	Fr	104*	4.9	0.0042	111	4.0	-
11/05/2010 08:31	Fr	91*	5.8	0.0052	138	3.9	-
11/05/2010 08:31	Fr	91*	5.3	0.0063	167	3.3	-
11/05/2010 12:31	Fr	54*	3.3	0.0034	90	4.8	-
01/06/2010 11:34	Fr	6407*	13.7	0.0142	376	0.3	-
01/06/2010 11:34	Mie	6407*	14.2	0.0193	511	1.1	-
01/06/2010 11:34 †	Fr	5838 (then diluted)	26.7	0.0283	750	0.6	-
01/06/2010 11:34††	Fr	5838 (then diluted)	20.5	0.0225	596	0.6	-
01/06/2010 12:02	Fr	8337*	28.3	0.0313	829	0.9	-
01/06/2010 12:04	Fr	3823 (6051.4 mg/L 2nd time)*	15.2	0.0158	419	2.0	-
01/06/2010 18:02	Fr	4664*	28.7	0.0288	763	1.1	-
01/06/2010 21:02	Fr	2516*	15.4	0.0147	390	2.2	-
02/06/2010 00:02	Fr	2433*	14.6	0.0147	390	2.2	-
02/06/2010 03:02	Fr	1665*	17.1	0.0172	456	2.0	-
02/06/2010 06:02	Fr	1191*	12.2	0.0119	315	2.3	-
02/06/2010 06:02	Mie	1191*	12.1	0.0161	427	2.4	-
02/06/2010 09:02	Fr	958*	15.6	0.0161	427	2.0	-
02/06/2010 12:02	Fr	804*	11.1	0.0114	302	2.4	-
02/06/2010 15:02	Fr	518*	8.8	0.0092	244	2.8	-
02/06/2010 18:02	Fr	466*	9.9	0.0106	281	2.8	-
02/06/2010 21:02	Fr	306*	8.7	0.0085	225	2.7	-
03/06/2010 00:02	Fr	423*	10.8	0.0112	297	2.9	-
03/06/2010 03:02	Fr	460*	11.2	0.0107	284	2.3	-
03/06/2010 06:02	Fr	3945*	9.9	0.0095	252	2.4	-
03/06/2010 09:02	Fr	318*	10.3	0.0105	278	2.7	-

Table A.2: Relevant information for the grain size analysis results of samples collected at Romans-sur-Isère in June, 2010 and analysed using the laser grain sizer. This includes the sizing method (Fraunhofer or Mie theory) and the measured concentration. The sizer concentration in percent volume and mass are given along with the residual error. A star in the concentration column indicates that the sample may have been diluted for grain size analysis.

Sample	Method	Measured Concentration (mg/L)	Laser Obscuration (%)	Sizer Concentration (% volume)	Sizer Concentration (mg/L)	Residual Error (%)	Notes
03/06/2010 12:02	Fr	289*	10.3	0.0098	260	2.3	-
03/06/2010 15:02	Fr	200*	8.2	0.008	212	2.7	-
03/06/2010 18:02	Fr	201*	8.7	0.0081	215	2.6	-
03/06/2010 21:02	Fr	192*	8.2	0.0078	207	2.9	-
04/06/2010 00:02	Fr	173*	7.0	0.0066	175	3.3	-
04/06/2010 03:02	Fr	244*	7.2	0.0069	183	3.3	-
04/06/2010 06:02	Fr	198*	7.0	0.0068	180	3.3	-
04/06:2010 09:02	Fr	191*	7.2	0.0077	204	3.5	-
04/06/2010 09:59	Fr	167*	8.1	0.0097	257	3.4	-
04/06/2010 11:01	Fr	145*	8.0	0.0083	220	3.3	-
08/06/2010 11:00	Fr	330*	7.5	0.0075	199	0.4	-
08/06/2010 14:00	Fr	270*	6.7	0.0065	172	0.4	-
08/06/2010 17:00	Fr	251*	6.6	0.0067	178	0.4	-
08/06/2010 20:00	Fr	232*	5.5	0.0058	154	0.4	-
08/06/2010 20:00	Mie	232*	5.5	0.0081	215	0.9	-
08/06/2010 23:00	Fr	218*	7.4	0.007	186	0.7	-
09/06/2010 02:00 (R1)	Fr	236*	6.4	0.0078	207	0.4	-
09/06/2010 02:00 (R2)	Fr	236*	10.9	0.0128	339	0.3	-
09/06/2010 05:00	Fr	312*	10.2	0.0101	268	0.4	-
09/06/2010 08:00	Fr	269*	7.5	0.007	186	0.4	-
09/06/2010 11:00	Fr	242*	8.0	0.0074	196	0.6	-
09/06/2010 14:00	Fr	239*	7.0	0.006	159	0.8	-
09/06/2010 17:00	Fr	247*	7.3	0.0069	183	0.5	-
09/06/2010 20:00	Fr	450*	9.8	0.0089	236	0.4	-
09/06/2010 20:00	Mie	450*	9.8	0.011	292	1.1	-
09/06/2010 23:00	Fr	728*	13.6	0.0127	337	0.5	-
10/06/2010 02:00	Fr	588	13.3	0.0132	350	0.4	-
10/06/2010 05:00	Fr	460	8.4	0.0077	204	0.3	-
10/06/2010 08:00	Fr	266	6.8	0.007	186	0.6	-
10/06/2010 11:00	Fr	254	6.4	0.0067	178	0.4	-
10/06/2010 14:00	Fr	239	5.7	0.006	159	0.5	-
10/06/2010 17:00	Fr	238	6.2	0.0068	180	0.4	-
10/06/2010 20:00	Fr	199	5.3	0.0058	154	0.4	-
10/06/2010 23:00	Fr	226	6.8	0.0076	201	0.7	-
11/06/2010 02:00 (Part 1)	Fr	323	6.8	0.0079	209	0.4	-
11/06/2010 02:00 (Part 1)	Mie	323	6.9	0.0099	262	0.9	-
11/06/2010 02:00 (Part 2)	Fr	323	6.6	0.0077	204	0.4	-
11/06/2010 05:00	Fr	479	9.1	0.0104	276	0.4	-
11/06/2010 08:00	Fr	364	8.5	0.0095	252	0.4	-

Table A.3: Relevant information for the grain size analysis results of samples collected at Romans-sur-Isère between June and October, 2010 and analysed using the laser grain sizer. This includes the sizing method (Fraunhofer or Mie theory), the measured concentration, the sizer concentration in percent volume and mass and the residual error. A star in the concentration column indicates that the sample may have been diluted for grain size analysis.

Sample	Method	Measured Concentration (mg/L)	Laser Obscuration (%)	Sizer Concentration (% volume)	Sizer Concentration (mg/L)	Residual Error (%)	Notes
23/06/2010 10:49	Fr	64	6.4	0.0362	959	2.7	-
24/06/2010 04:00	Fr	160	3.6	0.0046	122	0.5	-
25/06/2010 04:00	Fr	87	1.0	0.0014	37	0.7	contains one big particle
26/06/2010 04:00	Fr	80	1.4	0.002	53	0.5	-
27/06/2010 04:00	Fr	93*	5.8	0.007	186	1.3	-
28/06/2010 04:00	Fr	85*	5.9	.008	212	1.6	-
29/06/2010 04:00	Fr	82*	5.5	.0081	215	1.7	-
30/06/2010 04:00	Fr	79*	6.6	.0084	223	1.6	-
01/07/2010 04:00	Fr	146*	10.1	0.011	292	1.6	-
02/07/2010 04:00	Fr	98*	6.9	0.007	186	1.2	-
03/07/2010 04:00	Fr	194*	13.7	0.0124	329	0.7	-
04/07/2010 04:00	Fr	195*	10.6	0.0178	472	0.9	-
05/07/2010 04:00	Fr	206*	13.3	0.0143	379	1.2	-
06/07/2010 04:00	Fr	168*	11.7	0.014	371	1.1	-
07/07/2010 04:00	Fr	141*	9.9	0.0099	262	1.3	-
08/07/2010 04:00	Fr	126*	10.8	0.0109	289	1.1	-
09/07/2010 04:00	Fr	94*	8.7	0.0094	249	1.5	-
10/07/2010 04:00	Fr	77*	7.2	0.0075	199	1.1	-
11/07/2010 04:00	Fr	73*	6.9	0.0069	183	1.4	-
12/07/2010 04:00	Fr	doute	8.5	0.0085	225	1.4	-
13/07/2010 04:00	Fr	doute	12.5	0.0107	284	0.8	-
14/07/2010 04:00	Fr	84*	12.77	0.0647	1714.55	3.271	-
15/07/2010 04:00	Fr	118*	9.64	0.0095	251.75	0.853	-
16/07/2010 04:00	Fr	59*	6.01	0.0062	164.3	1.17	-
17/07/2010 04:00	Fr	57*	5.35	0.0057	151.05	1.195	-
22/07/2010 04:00	Fr	XXX	3.42	0.0053	140.45	1.533	-
27/07/2010 04:00	Fr	XXX	4.3	0.0091	241.15	1.605	-
04/08/2010 04:00	Fr	XXX	3.8	0.0061	161.65	1.222	-
13/08/2010 04:00	Fr	XXX	6.59	0.0214	567.1	0.771	-
28/09/10 04:00	Fr	21	4.06	0.0159	421.35	0.679	contains algae
02/10/10 04:00	Fr	13	4.08	0.0946	2506.9	3.815	contains algae
10/10/10 04:00	Fr	25	7.22	0.0847	2244.55	2.544	contains algae
10/10/10 04:00	Mie	25	6.5	0.0891	2361.15	3.341	contains algae
12/10/10 04:00	Fr	22	6.59	0.0823	2180.95	3.154	contains algae
24/10/10 04:00	Fr	12	4.28	0.0706	18709	8.039	a bit of algae
30/10/10 04:00	Fr	18	2.28	0.0023	60.95	5.24	algae and clumping

Table A.4: Relevant information for the grain size analysis results of samples collected at Romans-sur-Isère between October, 2010 and January, 2011 and analysed using the laser grain sizer. This includes the sizing method (Fraunhofer or Mie theory), the measured concentration, the sizer concentration in percent volume and mass and the residual error. A star in the concentration column indicates that the sample may have been diluted for grain size analysis.

Sample	Method	Measured Concentration (mg/L)	Laser Obscuration (%)	Sizer Concentration (% volume)	Sizer Concentration (mg/L)	Residual Error (%)	Notes
10/12/2010 12:15	Fr	64	6.58	0.0054	143.1	2.904	many biological floating particles
10/12/2010 13:10	Fr	85	10.34	0.0124	328.6	0.479	some big floaters
10/12/2010 17:10	Fr	63	7.99	0.0069	182.85	2.262	no observable floaters
11/12/2010 01:10 (Part 1)	Fr	57	9.66	0.0435	1152.75	2.891	appears to contain only sediment
11/12/2010 01:10 (Part 2)	Fr	57	4.59	0.003	79.5	2.554	appears to contain only sediment
11/12/2010 01:10 (Part 2)	Mie	57	4.6	0.0041	108.65	2.494	appears to contain only sediment
11/12/2010 05:10	Fr	62.4	7.11	0.0043	113.95	1.77	only sediment
11/12/2010 17:10	Fr	57.9	6.71	0.012	318.0	0.532	only sediment
12/12/2010 05:10 (Part 1)	Fr	-	7.85	0.0562	1489.3	2.987	-
12/12/2010 05:10 (Part 2)	Fr	-	2.89	0.003	79.5	3.535	-
12/12/2010 05:10 (Part 2)	Fr	-	2.9	0.004	106.0	4.108	-
12/12/2010 21:10	Fr	-	3.37	0.0029	76.85	3.938	-
13/12/2010 05:10	Fr	-	4.39	0.2751	7290.15	4.922	-
13/12/2010 13:10	Fr	-	2.99	0.1159	3071.35	3.864	-
15/12/2010 04:00	Fr	-	4.18	0.1113	2949.45	3.817	lots of algae, used ultrasound
25/12/2010 04:00	Fr	-	4.51	0.0845	2239.25	3.524	-
17/01/2011 15:00	Fr	4.8	1.09	0.0007	18.55	15.411	-

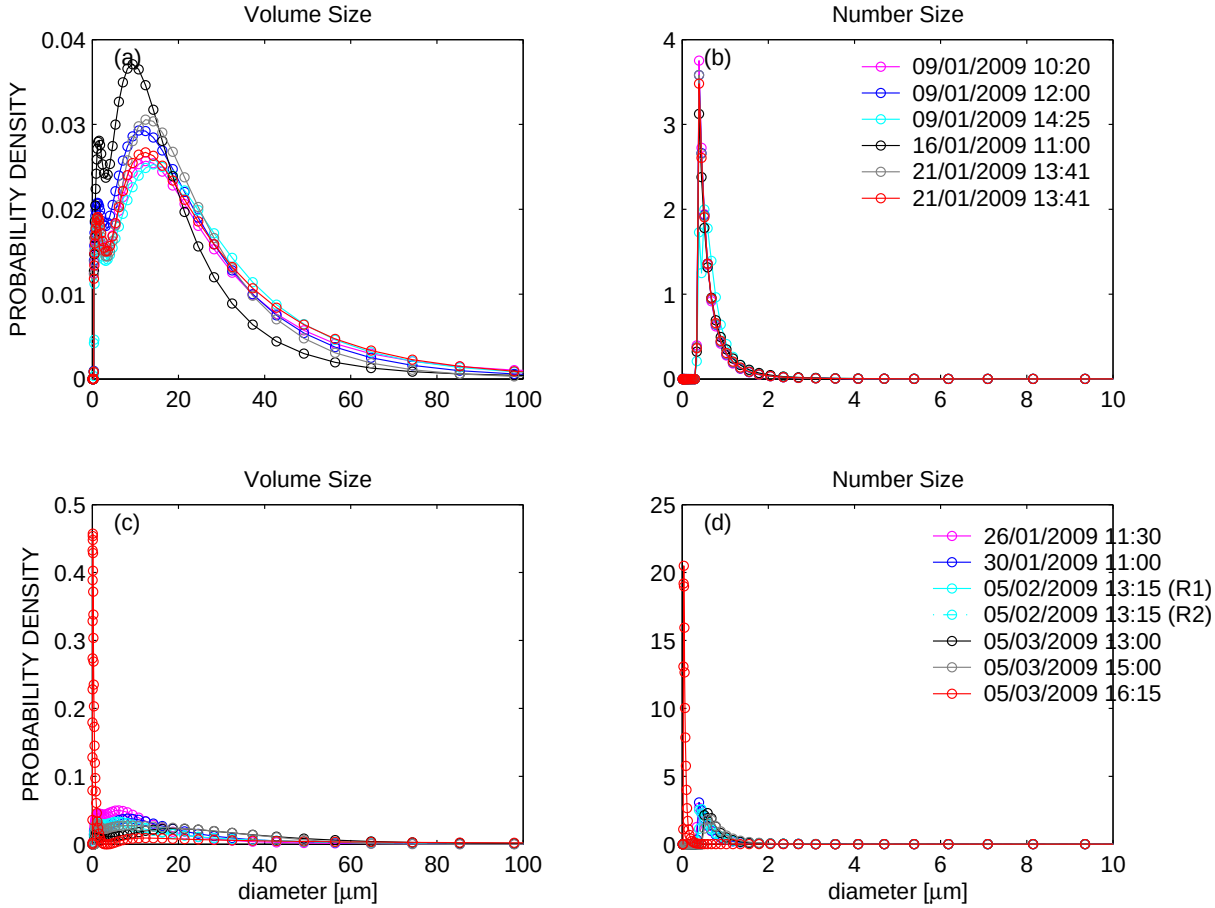

Figure A.1: Grain size distributions measured using a laser sizer for water samples collected at Romans-sur-Isère between January and March, 2009.

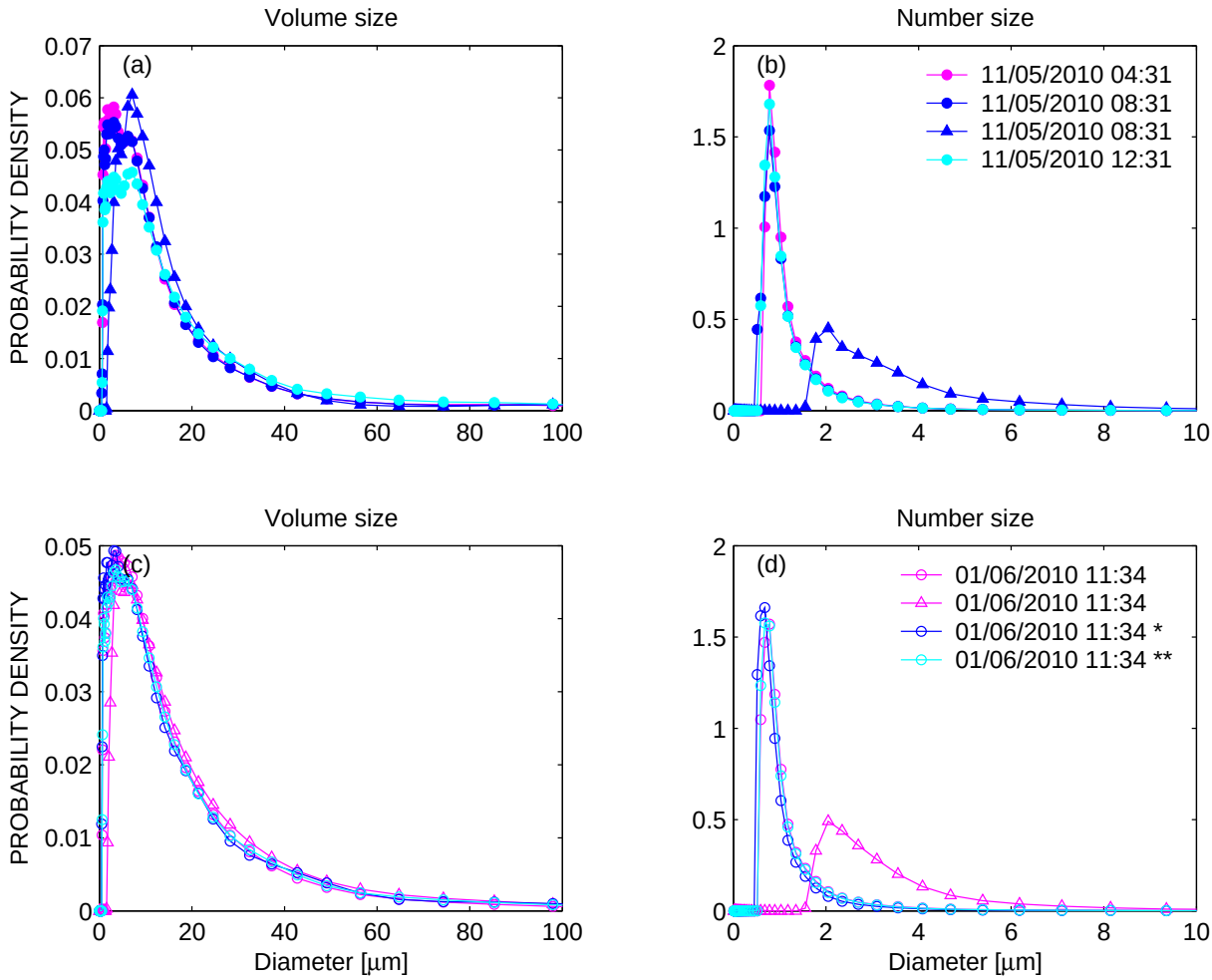

Figure A.2: Grain size distributions measured using a laser sizer for water samples collected at Romans-sur-Isère during May and June, 2010. Samples analysed using the Fraunhofer theory are shown as circles, while those analysed using the Mie theory are shown as triangles. Empty symbols represent samples collected by hand, and filled symbols represented samples collected by the automatic sampler.

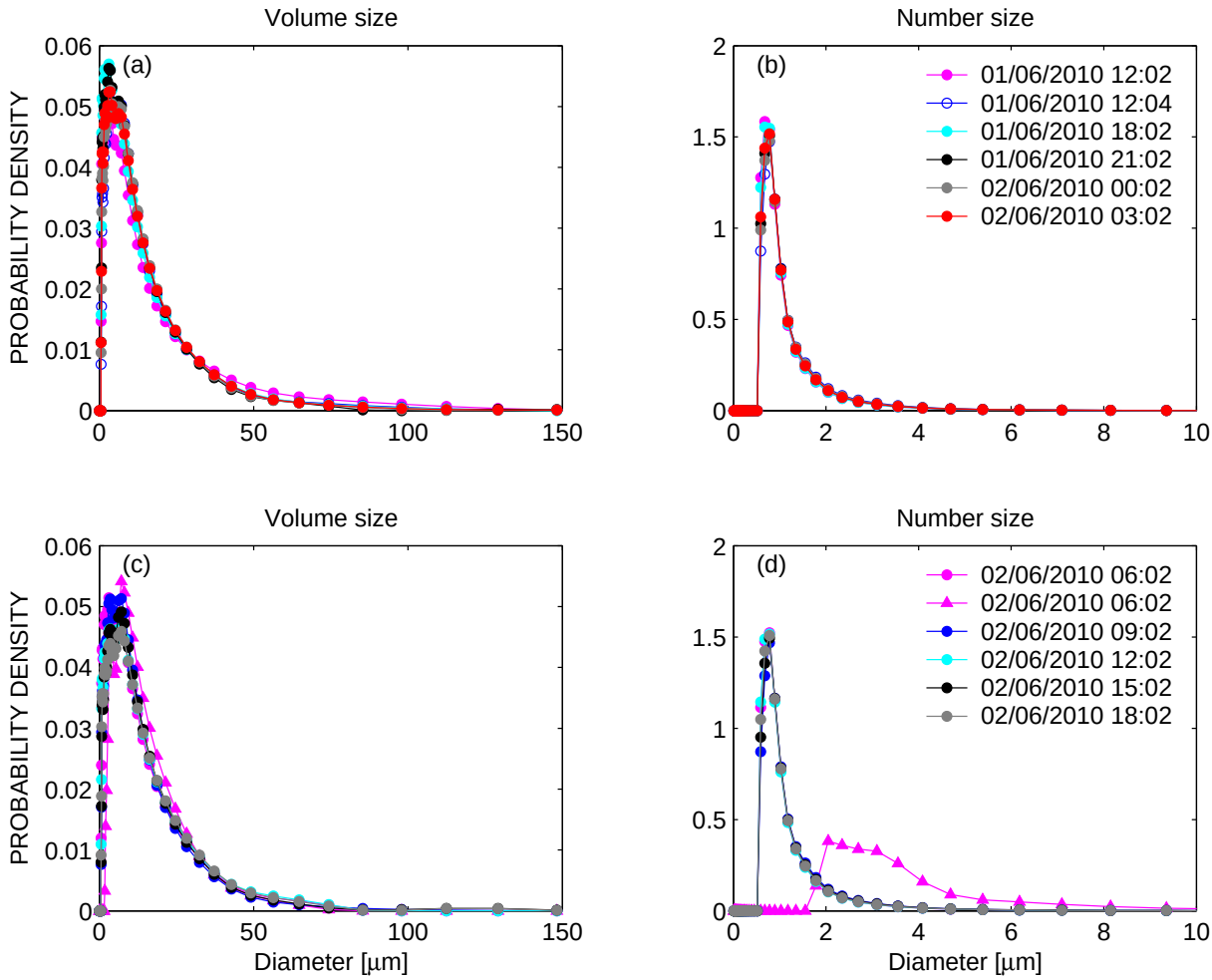

Figure A.3: Grain size distributions measured using a laser sizer for water samples collected at Romans-sur-Isère during June, 2010. Samples analysed using the Fraunhofer theory are shown as circles, while those analysed using the Mie theory are shown as triangles. Empty symbols represent samples collected by hand, and filled symbols represented samples collected by the automatic sampler.

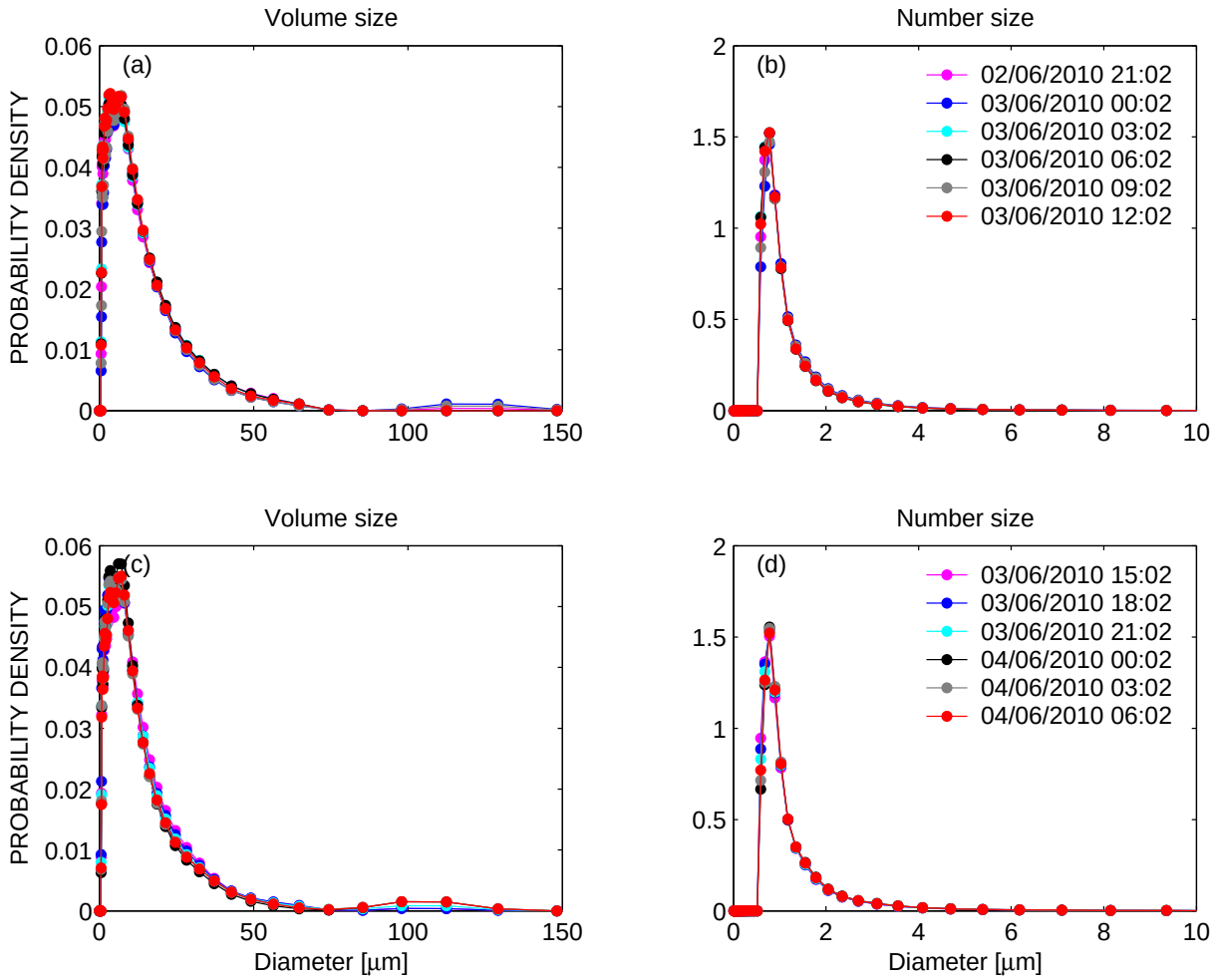

Figure A.4: Grain size distributions measured using a laser sizer for water samples collected at Romans-sur-Isère during June, 2010. Samples analysed using the Fraunhofer theory are shown as circles, while those analysed using the Mie theory are shown as triangles. Empty symbols represent samples collected by hand, and filled symbols represented samples collected by the automatic sampler.

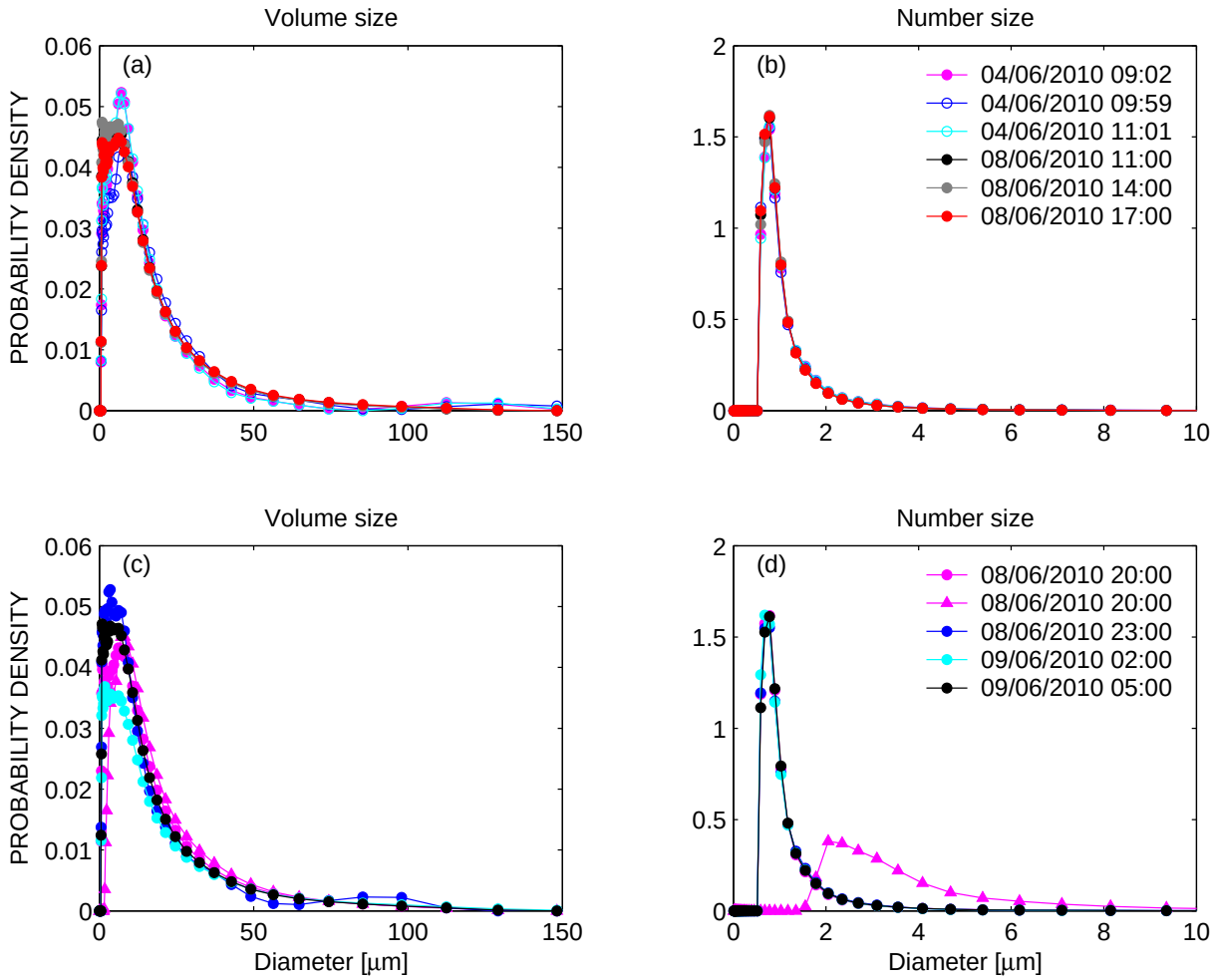

Figure A.5: Grain size distributions measured using a laser sizer for water samples collected at Romans-sur-Isère during June, 2010. Samples analysed using the Fraunhofer theory are shown as circles, while those analysed using the Mie theory are shown as triangles. Empty symbols represent samples collected by hand, and filled symbols represented samples collected by the automatic sampler.

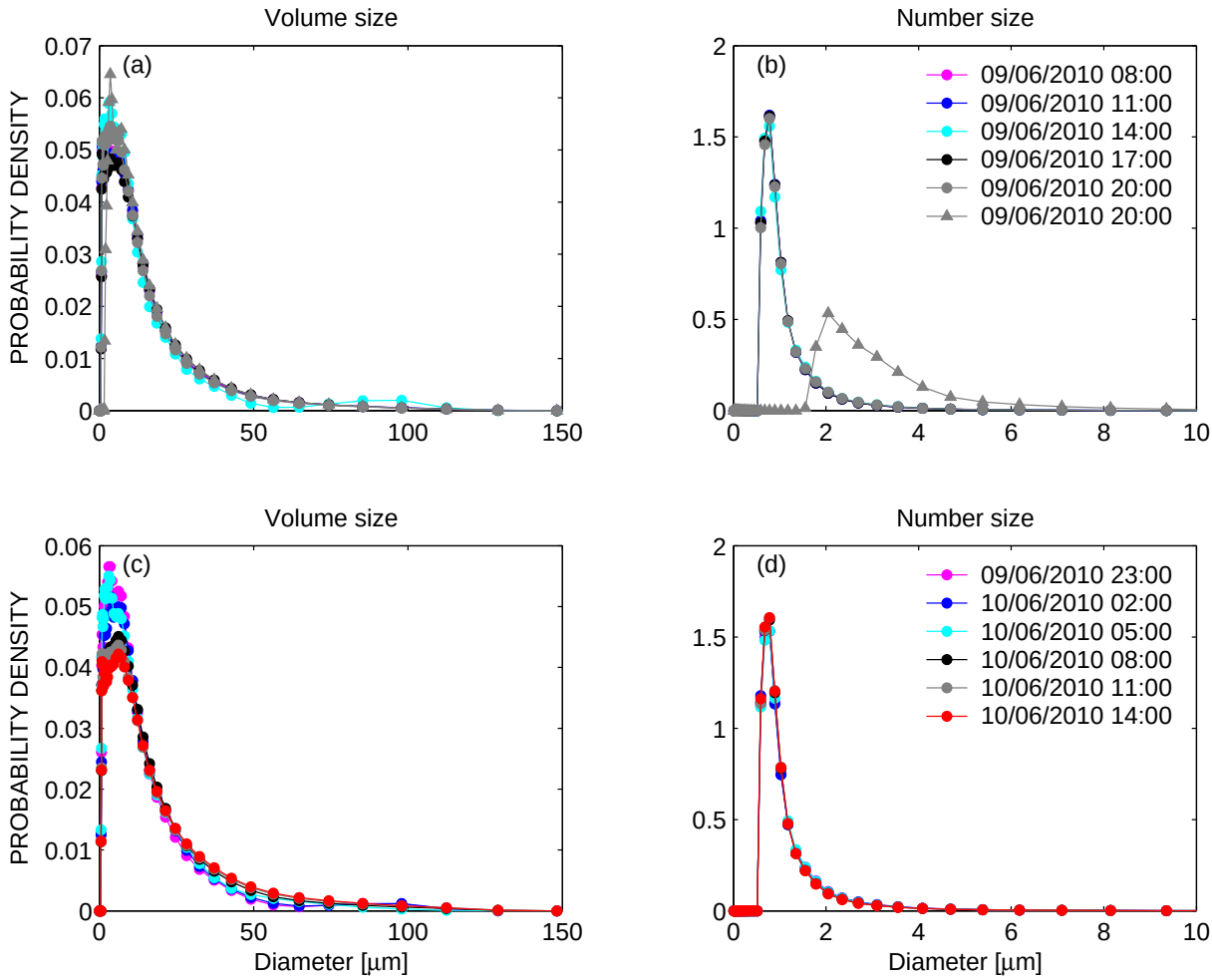

Figure A.6: Grain size distributions measured using a laser sizer for water samples collected at Romans-sur-Isère during June, 2010. Samples analysed using the Fraunhofer theory are shown as circles, while those analysed using the Mie theory are shown as triangles. Empty symbols represent samples collected by hand, and filled symbols represented samples collected by the automatic sampler.

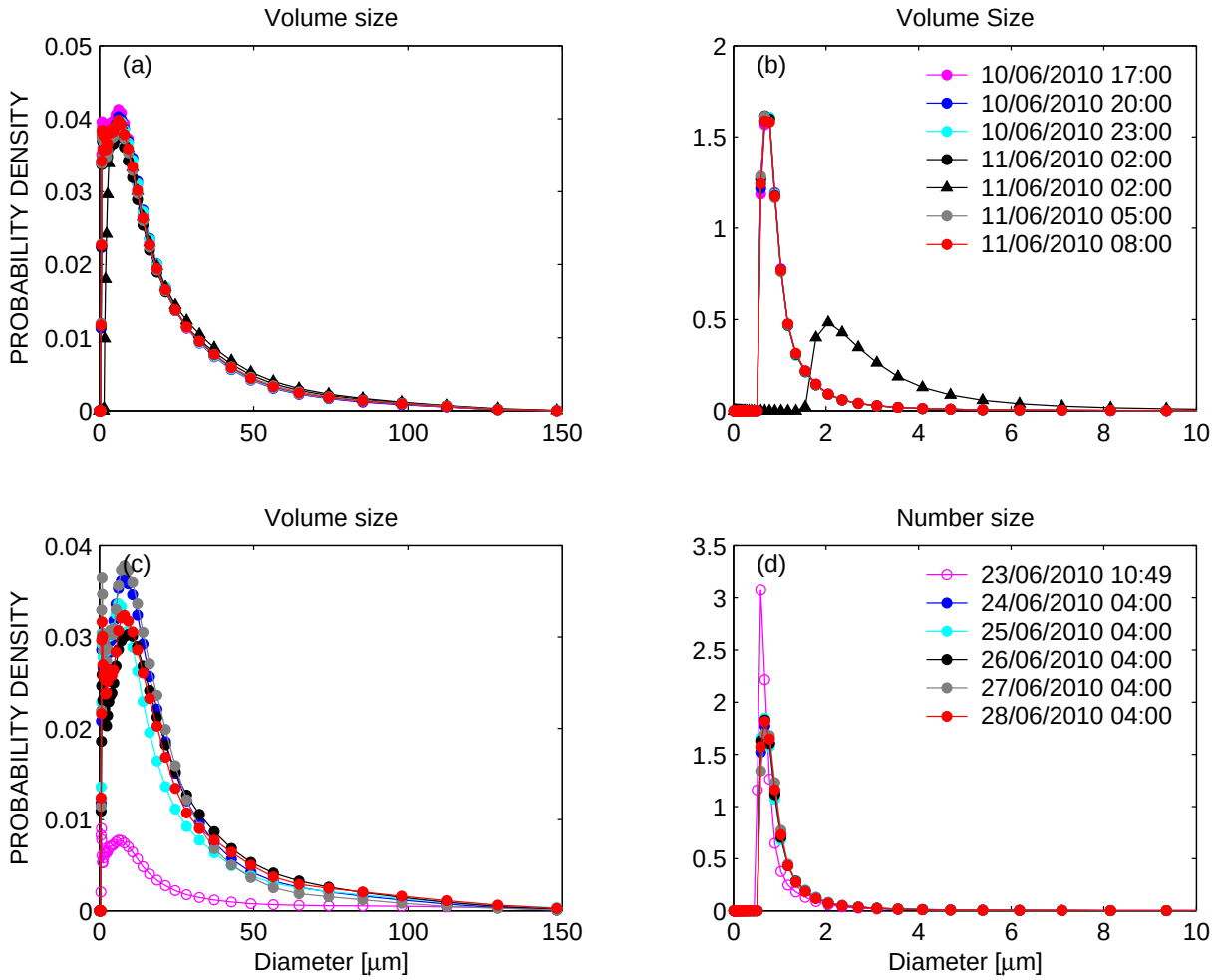

Figure A.7: Grain size distributions measured using a laser sizer for water samples collected at Romans-sur-Isère during June, 2010. Samples analysed using the Fraunhofer theory are shown as circles, while those analysed using the Mie theory are shown as triangles. Empty symbols represent samples collected by hand, and filled symbols represented samples collected by the automatic sampler.

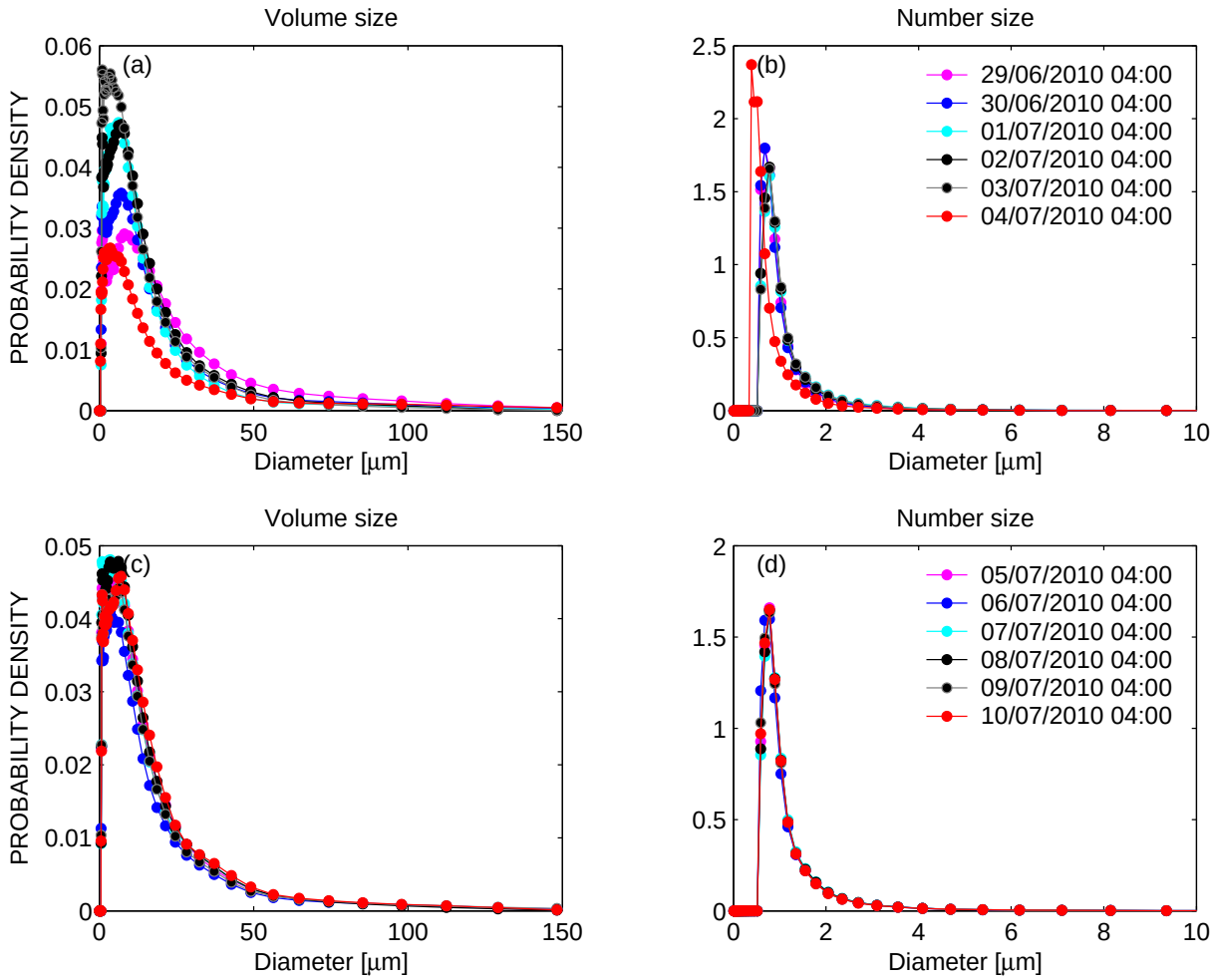

Figure A.8: Grain size distributions measured using a laser sizer for water samples collected at Romans-sur-Isère during June and July, 2010. Samples analysed using the Fraunhofer theory are shown as circles, while those analysed using the Mie theory are shown as triangles. Empty symbols represent samples collected by hand, and filled symbols represented samples collected by the automatic sampler.

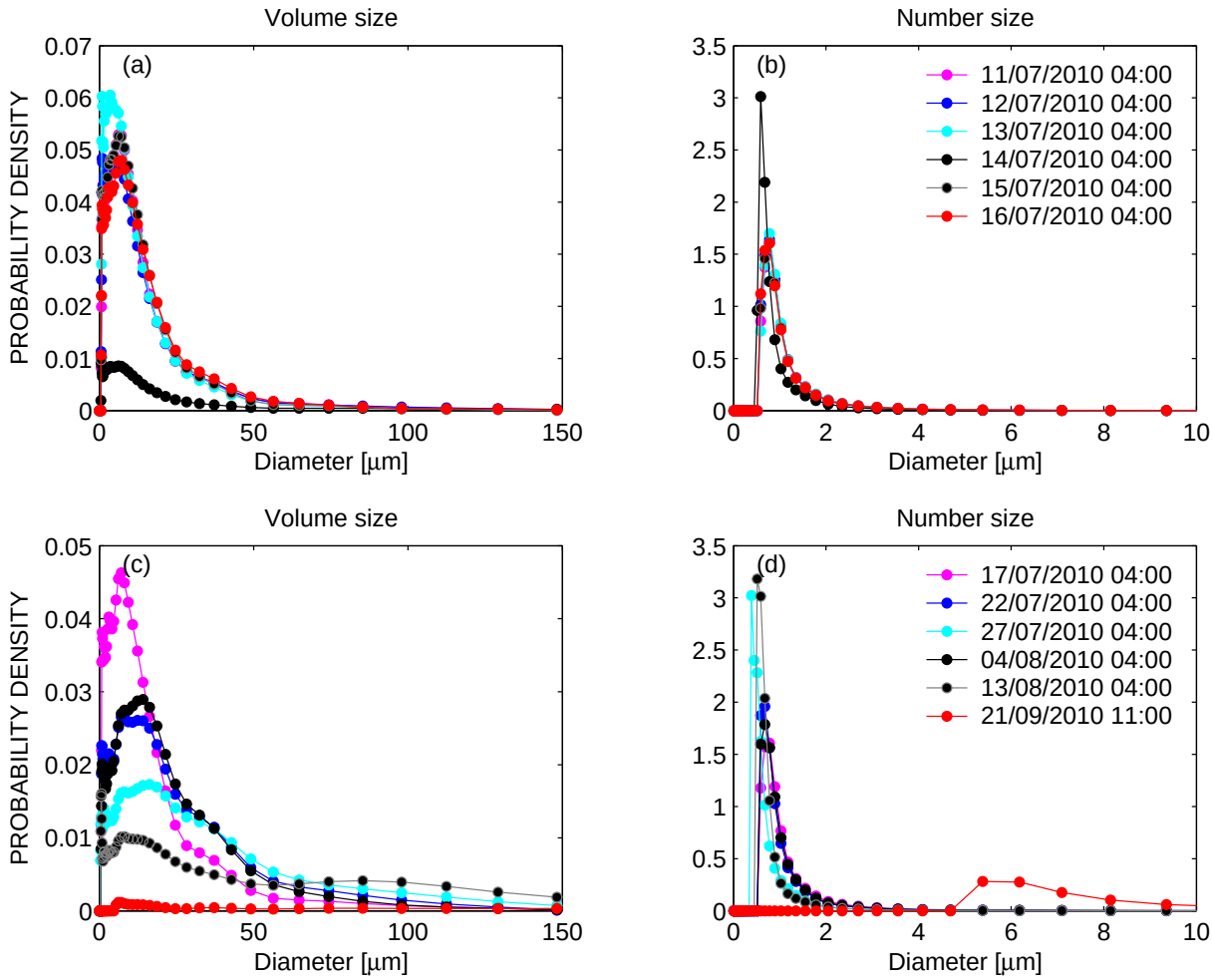

Figure A.9: Grain size distributions measured using a laser sizer for water samples collected at Romans-sur-Isère between July and September, 2010. Samples analysed using the Fraunhofer theory are shown as circles, while those analysed using the Mie theory are shown as triangles. Empty symbols represent samples collected by hand, and filled symbols represented samples collected by the automatic sampler.

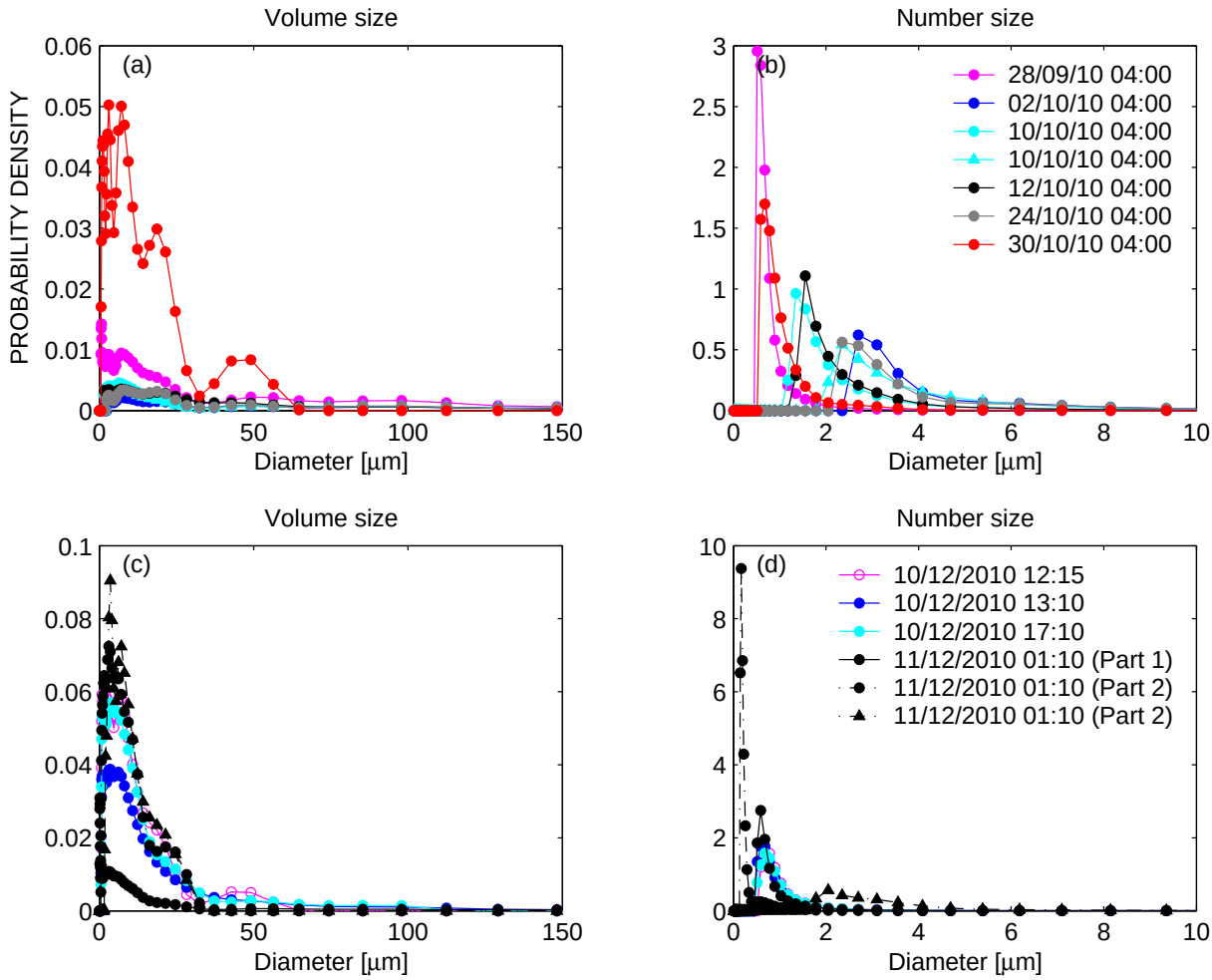

Figure A.10: Grain size distributions measured using a laser sizer for water samples collected at Romans-sur-Isère between September and December, 2010. Samples analysed using the Fraunhofer theory are shown as circles, while those analysed using the Mie theory are shown as triangles. Empty symbols represent samples collected by hand, and filled symbols represented samples collected by the automatic sampler.

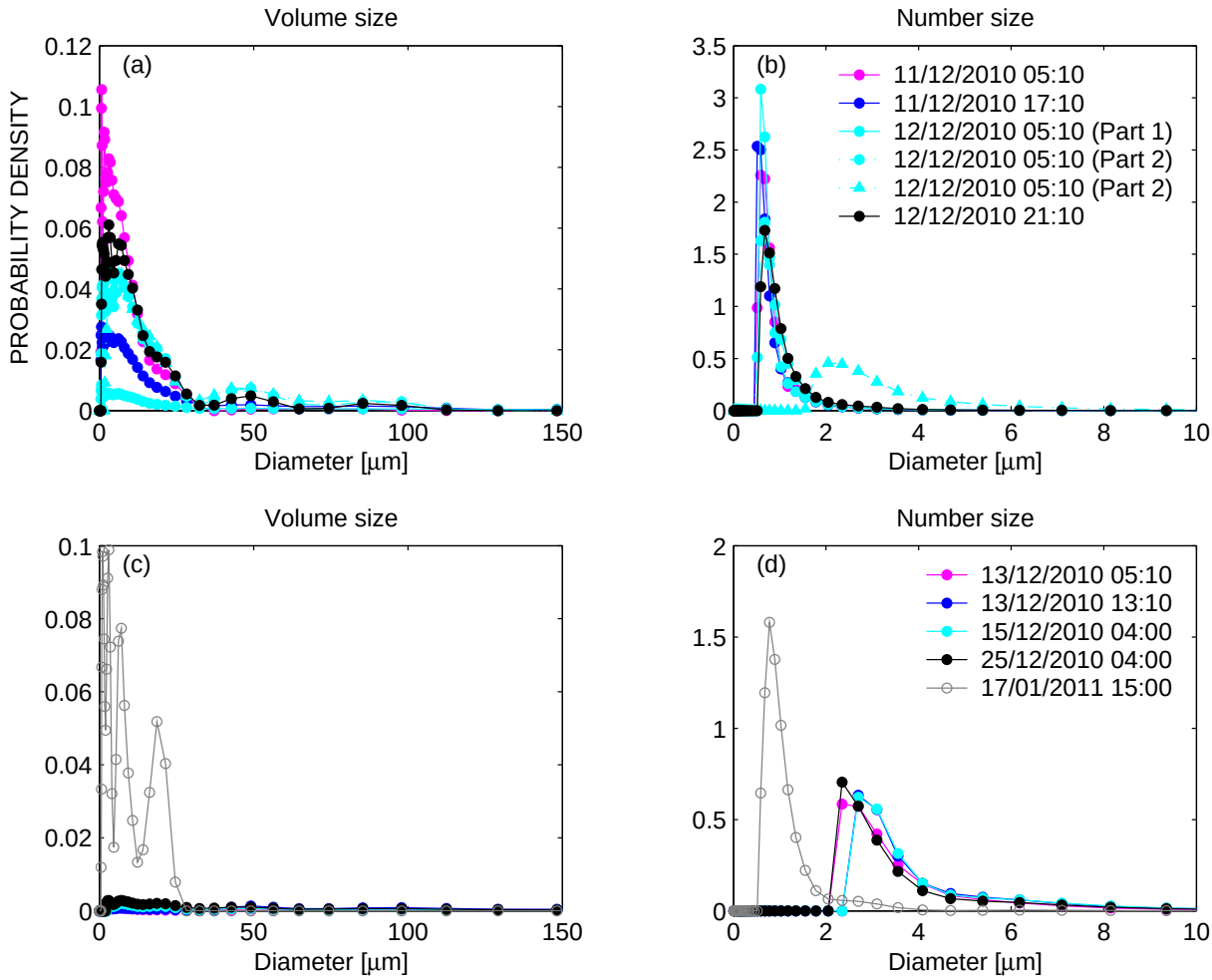

Figure A.11: Grain size distributions measured using a laser sizer for water samples collected at Romans-sur-Isère during December, 2010 and January, 2011. Samples analysed using the Fraunhofer theory are shown as circles, while those analysed using the Mie theory are shown as triangles. Empty symbols represent samples collected by hand, and filled symbols represented samples collected by the automatic sampler.

Appendix B

ADCP velocity data collected at Romans-sur-Isère prior to the thesis

The following figure is taken from *Pierrefeu* (2008)'s presentation at the *Journée utilisateurs Technitrade*. It summarizes the results from ADCP gauging at Romans-sur-Isère by grouping the velocity profiles by discharge. It can be seen from this figure that all velocity profiles have essentially the same form, regardless of the range of discharge values within which the measurements were made.

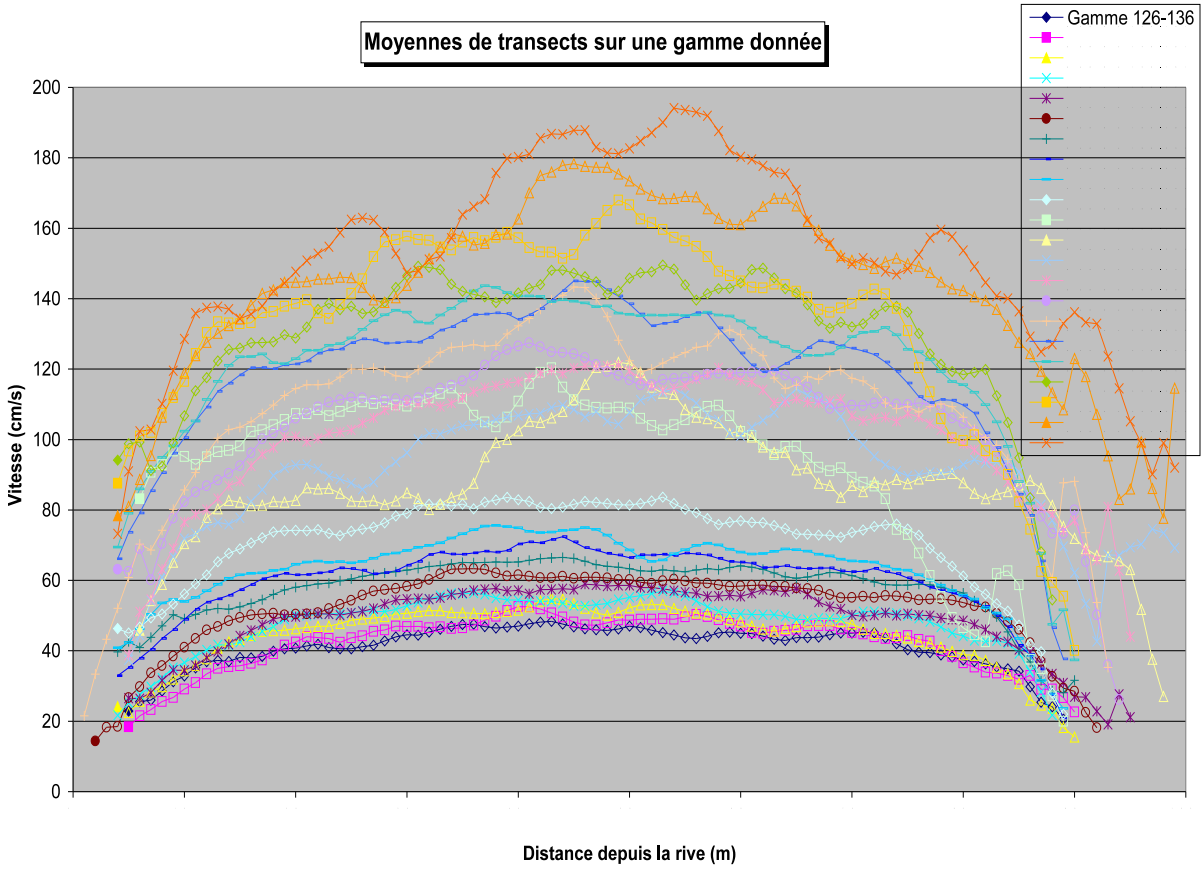

Figure B.1: Across-stream velocity profiles measured during ADCP gauging at Romans-sur-Isère for a range of discharge values. Figure is taken from *Pierrefeu* (2008).

BIBLIOGRAPHY

Ainslie, M. A., C. H. Harrison, and M. Zampolli, An analytical solution for signal, background and signal to background ratio for a low frequency active sonar in a Pekeris waveguide satisfying Lambert's rule, in *Proc. 4th International Conf. and Exhibition on Underwater Acoustic Measurements: Technologies and Results*, pp. 491 – 498, 2011.

Astrade, L., *La Saône en crue: dynamique d'un hydrosystème anthropisé (The flooding Saône: dynamics of an anthropized hydrosystem)*, Presses universitaires de Lyon, 2005.

Bero, A. S., and R. J. Gibbs, Mechanisms of pollutant transport in the Hudson estuary, *The Science of the Total Environment*, *97/98*, 9 – 22, 1990.

Bravard, J. P., *Le Rhône, du Léman à Lyon*, La Manufacture, Lyon, 1987.

Buschman, F. A., A. J. F. Hoitink, M. van der Vegt, and P. Hoekstra, Subtidal water level variation controlled by river flow and tides, *Water Resour. Res.*, *45*, W10,420, 2009, doi:10.1029/2009WR008167.

Campbell, F. B., and H. A. Bauder, A rating-curve method for determining silt-discharge of streams, *Trans. Amer. Geophys. Un.*, *21*, 603–607, 1940.

Campbell, J. R., Limitations in the laser particle sizing of soils, in *Advances in Regolith: Proceedings of the CRC LEME Regional Regolith Symposia*, edited by I. C. Roach, CRC LEME, 2003, p. 38 - 42.

Clay, C. S., and H. Medwin, *Acoustical Oceanography: Principles and Applications*, John Wiley and Sons, Toronto, 1977, p. 82.

Crawford, A. M., and A. E. Hay, Determining suspended sand size and concentration from multifrequency acoustic backscatter, *J. Acous. Soc. Am.*, *94*, 3312–3324, 1993.

Davis, B. J., P. Gough, and B. Hunt, Sea surface simulator for testing a synthetic aperture sonar, in *Impact of littoral environmental variability on acoustic predictions and sonar performance*, edited by N. G. Pace and F. B. Jensen, pp. 473–480, Kluwer Academic Publishers, The Netherlands, 2002.

Deines, K. L., Backscatter estimation using broadband acoustic Doppler current profilers, *Proc. IEEE, 6th Working Conf. on Current Measurement, San Diego, USA*, pp. 249–253, 1999.

Doppler, C., *Über das farbige Licht der Doppelsterne und einiger anderer Gestirne des Himmels* (On the Coloured Light from Double Stars and Other Stars of the Sky), *Abhandlungen der Königlich Böhmischen Gesellschaft der Wissenschaften*, *2*, 465 – 482, 1842.

Downing, J., Twenty-five years with OBS sensors: The good, the bad, and the ugly, *Cont. Shelf Res.*, 2006, doi:10.1016/j.csr.2006.07.018.

Droppo, I. G., and E. D. Ongley, Flocculation of suspended sediment in rivers of Southeastern Canada, *Wat. Res.*, *28*, 1799 – 1809, 1994.

Ellis, D. D., Solutions to range-dependent reverberation and sonar workshop problems using an adiabatic normal mode model, in *Proc. 4th International Conf. and Exhibition on Underwater Acoustic Measurements: Technologies and Results*, pp. 485 – 490, 2011.

Faran, J. J., Jr., Sound scattering by solid cylinders and spheres, *J. Acoust. Soc. Am.*, *23*, 405–418, 1951.

Fisher, F. H., and V. P. Simmons, Sound absorption in sea water, *J. Acoust. Soc. Am.*, *62*, 558 – 564, 1977.

Flammer, G. H., Ultrasonic measurement of suspended sediment, Geo. Survey Bull. No. 1141-A, 1962, (US GPO, Washington, DC, 1962).

Foster, I. D. L., R. Millington, and R. G. Grew, The impact of particle size controls on stream turbidity measurement; some implications for suspended sediment yield estimation, in *Erosion and Sediment Transport Monitoring Programmes in River Basins (Proceedings of the International Symposium in Oslo, Norway*, edited by J. Bogen, D. E. Walling, and T. J. Day, IAHS Publication No. 210, pp. 51 – 62, 1992.

Gartner, J. W., Estimating suspended solids concentrations from backscatter intensity measured by acoustic Doppler current profiler in San Francisco Bay, California, *Marine Geology*, *211*, 169 – 187, 2004.

Gostiaux, L., and H. van Haren, Extracting meaningful information from uncalibrated backscattered echo intensity data, *Journal of Atmospheric and Oceanic Technology*, *27*, 943–949, 2010.

Ha, H. K., J. P. Y. Maa, K. Park, and Y. H. Kim, Estimation of high-resolution sediment concentration profiles in bottom boundary layer using pulse-coherent acoustic Doppler current profilers, *Marine Geology*, *279*, 199 – 209, 2011.

Hach Lange, Solitax sc user manual, 2006.

Hay, A. E., On the remote acoustic detection of suspended sediment at long wavelengths, *J. Geophys. Res.*, *88*, 7525–7542, 1983.

Hay, A. E., Sound scattering from a particle-laden, turbulent jet, *J. Acoust. Soc. Am.*, *90*, 2055–2074, 1991.

Hay, A. E., and D. G. Mercer, On the theory of sound scattering and viscous absorption in aqueous suspensions at medium and short wavelengths, *J. Acoust. Soc. Am*, *78*, 1761–1771, 1985.

Hay, A. E., and J. Sheng, Vertical profiles of suspended sand concentration and size from multifrequency acoustic backscatter, *J. Geophys. Res.*, *97*, 15,661 – 15,677, 1992.

Hickling, R., Analysis of echoes from a solid elastic sphere in water, *J. Acoust. Soc. Am*, *34*, 1582–1592, 1962.

Hicks, D. M., and B. Gomez, *Tools in Fluvial Geomorphology*, chap. Sediment transport, pp. 425 – 461, John Wiley and Sons Ltd, 2003.

Hoitink, A. J. F., F. A. Buschman, and B. Vermeulen, Continuous measurements of discharge from a horizontal acoustic Doppler current profiler in a tidal river, *Water Resour. Res.*, *45*, 2009, doi:10.1029/2009WR007791.

Holdaway, G. P., P. D. Thorne, D. Flatt, S. E. Jones, and D. Prandle, Comparison between ADCP and transmissometer measurements of suspended sediment concentration, *Cont. Shelf Res.*, *19*, 421–441, 1999.

Howard, A., and R. Dolan, Geomorphology of the Colorado River in the Grand Canyon, *The Journal of Geology*, *89*, 269 – 298, 1981.

Huang, H., River discharge monitoring using Horizontal Acoustic Doppler Current Profiler (H-ADCP), 2006, teledyne RD Instruments, USA.

Hurther, D., P. D. Thorne, M. Bricault, J-. M. Barnoud, and U. Lemmin, A multi-frequency Acoustic Concentration and Velocity Profiler (ACVP) for boundary layer measurements of fine-scale flow and sediment transport processes, *Coastal Eng.*, *58*, 594 – 605, 2011.

Le Coz, J., G. Pierrefeu, J. F. Brochot, A. Paquier, B. Chastan, and M. Lagouy, Suspended-load dynamics during floods in the river Saône, France, in *Proc. 10th International Symposium on River Sedimentation*, Moscow, Russia, 2007.

Le Coz, J., G. Pierrefeu, and A. Paquier, Evaluation of river discharges monitored by a fixed side-looking Doppler profiler, *Water Resour. Res.*, *44*, W00D09, 2008.

Le Coz, J., G. Saysset, and G. Pierrefeu, Rapport d'essais – Régate ADCP 1. 3-4-5/02/2009, Vézère au pont de Garavet (Allassac, Corrèze), *Tech. rep.*, Groupe Doppler France (utilisateurs ADCP), 2009.

LePage, K. D., Real-time simulation of reverberation for moving platforms, in *Proc. 4th International Conf. and Exhibition on Underwater Acoustic Measurements: Technologies and Results*, pp. 471 – 478, 2011.

Lick, W., *Sediment and Contaminant Transport in Surface Waters*, CRC Press, Taylor and Francis Group, Boca Raton, FL, 2009.

Lohrmann, A., Monitoring sediment concentration with acoustic backscatter instruments, *Tech. rep.*, Nortek, AS, 2001.

Lord (J. W. Strutt) Rayleigh, *Theory of Sound*, vol. 2, 2nd ed., Dover, New York, 1945, 504 pp.

Ma, Y., K. Varadan, and V. V. Varadan, Application of Twersky's multiple scattering formalism to a density suspension of elastic particles in water, *J. Acoust. Soc. Am.*, *75*, 335–339, 1984.

Malvern, *Guide pratique de la granulométrie laser* (practical guide for laser grain sizing), C.D., 2005.

Middleton, G. V., *Topics in Mathematical Geology*, chap. The generation of lognormal size frequency distributions in sediments, pp. 34 – 42, Consultants Bureau, 1970.

Miller, C. R., Analysis of flow duration sediment rating curve method of computing sediment yield, *Tech. rep.*, US Bureau of Reclamation Report, 1951.

Moore, S., J. L. Coz, D. Hurther, and A. Paquier, On the application of horizontal adcps to suspended sediment transport surveys in rivers, *Continental Shelf Research*, pp. –, 2011.

Moore, S. A., J. Le Coz, G. Pierrefeu, C. Perret, D. Hurther, and A. Paquier, Measuring river flow using sidelooking acoustic Doppler current profilers : a comparison to vertically–oriented ADCP results, in *Proc. 33rd IAHR Congress: Water Eng. for a Sustainable Environment, Vancouver, Canada*, 2009.

Morel, A., and A. Bricaud, Inherent optical properties of algal cells, including picoplankton: Theoretical and experimental results, *Canadian Bulletin of Fisheries and Aquatic Science*, *214*, 521–559, 1986.

Morlock, S. E., Evaluation of acoustic Doppler current profiler measurements of river discharge, *Tech. Rep. Water-Resources Investigations Report 95-4218*, U.S. Geological Survey, 1996.

Morse, P. M., and K. U. Ingard, *Theoretical Acoustics*, Princeton University Press, Princeton, 1968.

Neubauer, W. G., R. H. Vogt, and L. R. Dragonette, Acoustic reflection from elastic spheres. I. Steady-state signals, *J. Acoust. Soc. Am*, *55*, 1123 – 1129, 1974.

NF ISO 13320-1, Particle size analysis: laser diffraction methods.

Nihei, Y., and A. Kimizu, A new monitoring system for river discharge with horizontal acoustic Doppler current profiler measurements and river flow simulation, *Water Resour. Res.*, *44*, W00D20, 2008, doi:10.1029/2008WR006970.

Oberg, K. A., In search of easy-to-use methods for calibrating ADCP's for velocity and discharge measurements, in *Proc., Hydraulic Measurements & Experimental Methods 2002*, edited by ASCE, Reston, VA, 2002.

Oberg, K. A., and D. Mueller, Validation of streamflow measurements made with acoustic Doppler current profilers, *Journal of Hydraulic Engineering*, *133*, 1421 – 1432, 2007.

Olson, D. R., A. P. Lyons, and D. C. Brown, Parameterization of very rough seafloors using high-resolution syntehtic aperture sonar, in *Proc. 4th International Conf. and Exhibition on Underwater Acoustic Measurements: Technologies and Results*, pp. 1637 – 1642, 2011.

Pierrefeu, G., *Journée utilisateurs Technitrade*, Oral presentation, 2008.

Rantz, S. E., Measurement and Computation of Streamflow. volume 2. Computation of discharge, *Water Supply Paper 2175*, U. S. Geological Survey, 1982.

RD Instruments, Acoustic Doppler Current Profiler Principles of Operation: a Practical Primer, 1996, second Edition for Broadband ADCPs.

RD Instruments, ADCP Coordinate Transformation: Formulas and Calculations, 2007.

RD Instruments, Workhorse H-ADCP Operational Manual, 2008, p. 87 and p. 158.

RD Instruments, Winriver II User's Guide, 2009.

Reichel, G., and H. P. Nachtnebel, Suspended sediment monitoring in a fluvial environment: Advantages and limitations applying an acoustic Doppler current profiler, *Water Research*, *28*, 751–761, 1994.

Ruhl, C. A., and M. R. Simpson, Computation of discharge using the index-velocity method in tidally affected areas, *Scientific Investigations Report 2005-5004*, U.S. Department of the Interior, U.S. Geological Survey, 2005.

Sassi, M. G., A. J. F. Hoitink, B. Vermeulen, and Hidayat, Discharge estimation from H-ADCP measurements in a tidal river subject to sidewall effects and a mobile bed, *Water Resour. Res.*, *47*, W06,504, 2011, doi:10.1029/2010WR009972.

Sengupta, S., Grain-size distribution of suspended load in relation to bed materials and flow velocity, *Sedimentology*, *26*, 63 – 82, 1979.

Sheng, J., Remote determination of suspended sediment size and concentration by multi-frequency acoustic backscatter, Ph.D. thesis, Memorial University of Newfoundland, 1991.

Sheng, J., and A. E. Hay, An examination of the spherical scatterer approximation in aqueous suspensions of sand, *J. Acoust. Soc. Am.*, *83*, 598–610, 1988.

Teledyne RD Instruments, Workhorse H-ADCP Specification Sheet, 2007, mM-1022.

Thevenot, M. M., T. L. Prickett, and N. C. Kraus, Tylers Beach, Virginia, dredged material plume monitoring project, 27 September to 4 October 1991, *Tech. Rep. DRP-92-7*, US Army Corps of Engineers, 1992.

Thorne, P. D., and D. M. Hanes, A review of acoustic measurement of small-scale sediment processes, *Cont. Shelf Res.*, *22*, 603–632, 2002.

Thorne, P. D., and P. J. Hardcastle, Acoustic measurements of suspended sediments in turbulent currents and comparison with *in-situ* samples, *J. Acoust. Soc. Am.*, *101*, 2603 – 2614, 1997.

Thorne, P. D., and R. Meral, Formulations for the scattering properties of suspended sandy sediments for use in the application of acoustics to sediment transport processes, *Cont. Shelf Res.*, *28*, 309–317, 2008.

Topping, D. J., S. A. Wright, T. S. Melis, and D. M. Rubin, High-resolution measurements of suspended-sediment concentration and grain size in the Colorado River in Grand Canyon using a multi-frequency acoustic system, in *Proc. 10th International Symposium on River Sedimentation. August 1–4, Moscow, Russia*, 2007.

Urick, R. J., The absorption of sound in suspensions of irregular particles, *J. Acoust. Soc. Am*, *20*, 283 – 289, 1948.

Walling, D. E., Limitations of the rating curve technique for estimating suspended sediment loads, with particular reference to British rivers, in *Erosion and Solid Matter Transport in Inland Waters, Proc. of a symposium held at Paris*, IAHS Publication No. 122, pp. 34 – 48, 1977.

Walling, D. E., B. W. Webb, and M. A. Russell, Sediment-associated nutrient transport in UK rivers, in *Freshwater Contamination (Proc. IAHS Rabat Symposium S4)*, edited by B. Webb, IAHS Publication No. 243, pp. 69 – 81, 1997.

Wedd, M. W., Determination of particle size distributions using laser diffraction, *Tech. rep.*, Educ. Reso. for Part. Techn., 2003.

Wood, M. S., Evaluation of sediment surrogates in rivers draining to Lower Granite Reservoir, ID and WA, in *Proc. 9th Federal Interagency Sedimentation Conf.*, Las Vegas, 2010.

Wood, P. A., Controls of variation in suspended sediment concentration in the River Rother, West Sussex, England, *Sedimentology*, *24*, 437 – 445, 1977.

Wright, S. A., D. J. Topping, and C. A. Williams, Discriminating silt-and-clay from suspended-sand in rivers using side-looking acoustic profilers, in *Proc. 9th Federal Interagency Sedimentation Conf.*, Las Vegas, 2010.

Xu, R., and O. A. Di Guida, Comparison of sizing small particles using different technologies, *Powder Technology*, *132*, 145–153, 2003.

Suivi des flux d'eau et de matières en suspension dans les cours d'eau par profileurs acoustiques Doppler horizontaux

Stephanie A. Moore

Résumé :

Cette thèse est une étude de l'applicabilité des profileurs acoustiques Doppler horizontaux (H-ADCP) pour le suivi des flux d'eau et de matières en suspension (MES) dans les rivières. Plus d'un an de données acquises avec des H-ADCP de 300, 600 et 1200 kHz sur quatre sites, sur le Rhône, l'Isère et la Saône, avec des géométries et des conditions de forçage contrastées sont analysées. Les résultats montrent qu'une profondeur de section limitée peut poser problème en raison de la diffusion d'une partie de l'énergie acoustique par la surface libre. De plus, quand l'intensité rétrodiffusée par les particules est trop faible, les mesures de vitesse sont sous-estimées ou plus dispersées par rapport aux mesures de référence. Des relations de vitesse indice sont toutefois établies en fonction de l'intensité et de la concentration afin de corriger les vitesses. La concentration en MES est déterminée à partir de l'atténuation acoustique qui est importante pour des suspensions concentrées de limons ($\gtrsim$ 100 mg/L). Les constantes d'atténuation sont obtenues par calage sur des mesures de turbidité ; elles sont proches des valeurs théoriques calculées pour les distributions granulométriques des particules primaires. Les mesures acoustiques de concentration sont en bon accord avec les mesures de référence et reproduisent finement la dynamique temporelle. En outre, l'évolution de la granulométrie est étudiée à partir des mesures multi-fréquences d'atténuation sous l'hypothèse que les distributions granulométriques sont lognormales. Cette étude montre qu'une fois que les conditions limites pour des mesures fiables sont bien établies, le H-ADCP est un outil performant pour le suivi des flux d'eau et de MES dans les rivières, surtout pendant des périodes de fortes concentrations telles que des crues.

Mots-clés : Mesures acoustiques multi-fréquences, flux de sédiments en suspension, H-ADCP, atténuation acoustique.

Monitoring fluxes of water and suspended sediment in rivers using side-looking acoustic Doppler current profilers

Abstract:

The work investigates the feasibility of using horizontal acoustic Doppler current profilers (H-ADCPs) to monitor fluxes of water and suspended sediment in rivers. Year-long data sets acquired with H-ADCPs operating at 300, 600 and 1200 kHz at four sites with varying geometries and flow forcing conditions on the Rhône, Saône and Isère rivers are analyzed. Findings show that limited depth can pose a problem due to scattering of a fraction of the acoustic energy from the air-water interface. A second problem arises when the backscattered intensity from the suspended sediment is too weak; this leads to underestimation or higher variability of the velocity estimates compared to reference values. Nevertheless, index-velocity relationships are established as a function of concentration and intensity in order to correct the velocity measurements. Concentrations of suspended sediment can be determined from the acoustic attenuation, which is substantial for silt-sized particles at concentrations $\gtrsim$ 100 mg/L. Attenuation constants obtained by comparison with turbidity data are in good agreement with the theoretical values calculated for the measured grain size distributions of the primary particles. The acoustic measurements of concentration are in good agreement with reference methods in terms of both amplitude and temporal resolution. Grain size is determined from multi-frequency attenuation data, accounting for lognormal grain size distributions. Our findings show that once the limits of accurate velocity measurements are well established for a given site and instrument, the side-looking ADCP can be a valuable tool for monitoring concentration and changes in grain size throughout high concentration events such as floods.

Keywords:

Multi-frequency acoustics, suspended sediment fluxes, H-ADCP, acoustic attenuation.